ERL2015

ERL2015

The 56th ICFA Advanced Beam Dynamics Workshop on Energy Recovery Linacs

June 7-12, 2015

Stony Brook University, Stony Brook, New York, USA

Topics

Operational Experience and Commissioning Results

New Applications and Projects

Electron Sources

Machine Optics and Beam Dynamics

Superconducting RF

Beam Instrumentation and Control

For more information please contact: **erl2015@bnl.gov**

http://www.bnl.gov/erl2015/

International Organizing Committee

S. Belomestnykh, BNL/SBU (Chairman)

S. Benson, JLab

I. Ben-Zvi, BNL/SBU

W. Fischer, BNL

R. Hajima, JAEA

G. Hoffstaetter, Cornell U.

E. Jensen, CERN

H. Kawata, KEK

K.-J. Kim, ANL and U. of Chicago

J. Knobloch, HZB

G. N. Kulipanov, BINP

S. Smith, STFC/DL/ASTeC

Local Organizing Committee

V. Ptitsyn, BNL/SBU (Chairman)

D. Kayran, BNL (IPC Chair)

P. Manning, BNL

A. Petway, BNL

C. Hoffman, BNL

BROOKHAVEN NATIONAL LABORATORY

U.S. DEPARTMENT OF ENERGY | Office of Science

ICFA

Stony Brook University


CHARLES B. WANG CENTER
ERL 2015

Contents

Preface **i**

Poster . . . i

Group Photo . . . ii

Contents . . . iii

Committees . . . iv

Papers **1**

MOPBTH003 – The Femto-Science Factory: A Multi-turn ERL Based Light Source . . . 1

MOPCTH010 – Design Work of the ERL-FEL as the High Intense EUV Light Source . . . 4

MOPDTH014 – Status and Commissioning Results of the R&D ERL at BNL . . . 10

TUIBLH2026 – LHeC ERL Design and Beam-Dynamics Issues . . . 15

TUIBLH2027 – Tracking Studies in eRHIC Energy-Recovery Recirculator . . . 20

TUICLH1030 – Improving the Smoothness of Multialkali Antimonide Photocathodes: An In-Situ X-Ray Reflectivity Study . . . 27

TUICLH2032 – Investigations on Transverse Beam Break Up Using a Recirculated Electron Beam* . . . 30

TUICLH2034 – Linear Microbunching Gain Estimation Including CSR and LSC Impedances in Recirculation Machines . . . 34

TUIDLH1038 – First Beam Characterization of SRF Gun II with a Copper Photocathode . . . 42

TUIDLH2040 – Transverse-emittance Preserving Arc Compressor: Sensitivity to Beam Optics, Charge and Energy 48

WEIALH2048 – Current Measurement and Associated Machine Protection in the ERL at BNL . . . 52

WEIBLH1049 – Current Status of the MESA Project . . . 58

WEIBLH2054 – Operational Experience of CW SRF Injector and Main Linac Cryomodules at the Compact ERL 63

WEICLH1058 – ERL for Low Energy Electron Cooling at RHIC (LEReC) . . . 67

WEICLH2062 – Development for Mass Production of Superconducting Cavity By MHI . . . 72

WEICLH2063 – Ultra-Fast Harmonic Resonant Kicker Design for the MEIC Electron Circular Cooler Ring . . . 75

WEIDLH1002 – The Optics of the Low Energy FFAG Cell of the eRHIC Collider Using Realistic Fields . . . 80

WEIDLH2066 – Performance of the Digital LLRF Systems at KEK cERL . . . 84

WEIDLH2068 – Using a 1.3 GHz 20 kW Solid State Amplifier as RF Power Supply for DC-SRF Photo-injector . 88

THIALH2069 – Diagnostic Test-Beam-Line for the MESA Injector . . . 91

THPTHL072 – CsK2Sb Photocathode Development for B*ERL*inPro . . . 97

THPTHL073 – Development of a Multialkali Photocathode Preparation System . . . 100

THPCTH075 – Summary of WG1 on Injectors - ERL 2015 . . . 103

THPCTH076 – ERL Beam Dynamics and Optics: A Summary of Working Group 2 at the ERL Workshop 2015 . 107

THPCTH077 – Summary of WG3 on Instrumentation, Controls, and Beam Losses - ERL 2015 . . . 111

THPDTH078 – ERL 2015 Summary of Workging Group 4 RF and Superconducting RF . . . 115

THPDTH079 – Summary of WG5 on ERL Applications - ERL 2015 . . . 121

Appendices **127**

List of Authors . . . 127

Institutes List . . . 131

Chair of Conference

Sergey Belomestnykh	BNL/SBU

Local Organizing Committee (LOC)

Sergey Belomestnykh	ERL2015 Chairman
Vadim Ptitsyn	LOC Chair
Pamela Manning	Administration
Anna Petway	Coordinator
Caitlin Hoffman	Editor
Dmitry Kayran	IPC Chair

International Organizing Committee (IOC)

Sergey Belomestnykh (ERL Chair)	BNL/SBU
Steve Benson	JLab
Ilan Ben-Zvi	BNL/SBU
Wolfram Fischer	BNL
Ryoichi Hajima	JAEA
Georg Hoffstaetter	Cornell
Erk Jensen	CERN
Hiroshi Kawata	KEK
Kwang-Je Kim	ANL & U. of Chicago
Jens Knobloch	HZB
Gennady N. Kulipanov	BINP
Susan Smith	STFC/DL/ASTeC

International Program Committee (IPC)

Dmitry Kayran (IPC Chair)	BNL
Michael Abo-Bakr	HZB
Deepa Angal-Kalinin	ASTeC
Andre Arnold	HZDR
Kurt Aulenbacher	Mainz U.
Ivan Bazarov	Cornell
Oliver Bruning	CERN
Andrew Burrill	HZB
Dave Douglas	JLab
Bruce Dunham	Cornell
Pavel Evtushenko	JLab
Carlos Hernandez-Garcia	JLab
Thorsten Kamps	HZB
Vladimir Litvinenko	SBU/BNL
Kexin Liu	Peking U.
Chris Mayes	Cornell
Nobuyuki Nishimori	JAEA
Takashi Obina	KEK
Vadim Ptitsyn	BNL/SBU
Hiroshi Sakai	KEK
Nikolay Vinokurov	BINP
Jiuqing Wang	IHEP

THE FEMTO-SCIENCE FACTORY: A MULTI-TURN ERL BASED LIGHT SOURCE*

T. Atkinson†, A. V. Bondarenko, A. N. Matveenko, Y. Petenev,
Helmholtz-Zentrum Berlin für Materialien und Energie GmbH (HZB), Germany.

Abstract

A conceptual design study for a future multi-turn ERL based light source at HZB is completed and presently under internal review. The Femto-Science-Factory (FSF) is a candidate for a 4th generation diffraction limited synchrotron light source. It will provide its users with ultra-bright photons of angstrom wavelength at 6 GeV. The FSF is intended to be a multi-user facility and offer a wide variety of operation modes. Presented in this paper is an overview of the conceptual design with respect to the facility layout, operation modes and the expectations of the beam parameters from the start-to-end simulations.

INTRODUCTION

This paper continues on from a recent feasibility study [1] for multi-turn ERL based light sources. The most recent additions to the optic are the numerous matching sections needed to geometrically optimize the machine layout into a single tunnel and the final deceleration recovery stage to dump the beam at 10 MeV.

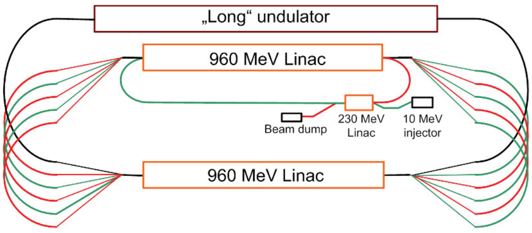

Figure 1: Schematic of the FSF. Green lines - acceleration, red - deceleration and black - 6 GeV final beam.

Figure 1 shows the layout of the light source and Table 1 summarizes the main parameters.

The difference in the two modes with regards to the lattice design occurs in the low energy section of the machine. For the High Brilliance Mode (HBM) a beam of higher charge is accelerated on crest in all of the linacs and circulates round isochronous arcs. The Short Pulse Mode (SPM) however relies on achromatic arcs for the telescopic compression technique removing the correlated energy spread due to the off-crest acceleration. The modes share common high energy arcs where radiation effects play an important role in emittance growth.

The vertical spreaders geometry has been designed so that the total length of the structure is restricted to 25 m.

Table 1: Main Parameters of the FSF Multi-turn ERL

Parameter	HBM	SPM
Energy (GeV)	6	6
$\langle I \rangle$ (mA)	20	5
Q (pC)	15	4
ε_n (mm mrad)	0.1	0.5
σ_t (fs)	2000	10
$\langle B \rangle$ (ph/(s mm^2 mrad^2 0.1%)	$8{\cdot}10^{22}$	$4{\cdot}10^{21}$
B_{peak} (ph/(s mm^2 mrad^2 0.1%)	10^{26}	10^{26}

The optic is isochronous, contains sextupoles to correct the second order for high energy spread beams, and the beta functions are minimized throughout. Due to these heavy demands, the 4 and 6 GeV spreaders bend in both transversal planes.

TWO STAGE INJECTION

The beam parameters achieved in the injector is essential for ultimate brilliance in both modes of the FSF. The 0.1 mm mrad goal of the transverse emittance is challenging and compensation techniques up to 50 MeV where space charge still dominates are required to preserve emittance. A Space Charge Optimizer (SCO) [2] program was used to numerically solve the Kapchinsky-Vladimirsky equations repetitively and to find the optimal setting for the quadrupoles for minimum emittance growth (2D emittance compensation). Modeling of the injector is comprehensively described in [3]. ASTRA was used to produce a realistic bunch starting simulations from the cathode, as shown in Fig. 2 which could be converted to Elegant and tracked onwards.

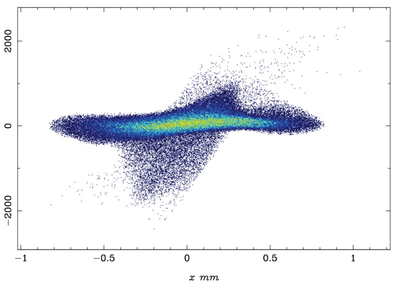

Figure 2: Typical beam distribution on injector exit.

The 230 MeV linac and the respective arc in the injection scheme are used to further accelerate the beam and provide intermediate bunch compression to 2 ps in both modes. In addition, energy staging considerations, transversal beam

---

* Work supported by German Bundesministerium für Bildung und Forschung, Land Berlin, and grants of Helmholtz Association VH NG 636 and HRJRG-214.

† terry.atkinson@helmholtz-berlin.de

break-up and micro-bunching instability studies have all contributed to the inclusion and layout of this two stage injection process.

HIGH BRILLIANCE MODE

The transverse emittance growth is kept to a minimum throughout the whole 8 km machine, to utilize the undulator radiation in all acceleration and deceleration sections in order to maximize user potential. Shown in Fig. 3 is the spectral brightness expectations of the FSF using the start-to-end beam parameters.

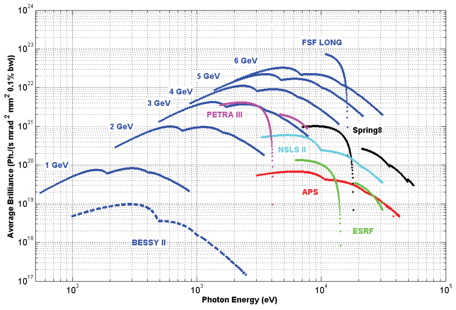

Figure 3: Comparison of the spectral brightness for the FSF and present 3rd generation light sources.

The average brilliance expectations of the FSF from 1 to 6 GeV plotted in blue, cover a broad wavelength and are a magnitude larger than present 3rd generation light sources. The comparison is made using realistic undulator parameters and common operational modes.

For the high brilliance mode, with all the suppression techniques described in place, the transversal emittance mainly grows due to incoherent radiation effects and can be analytically estimated in the 6 GeV arc as 0.04 mm mrad.

Table 2 summarizes the main beam dynamic parameters at various stages across the machine. The bunch is of great quality regarding minimal emittance from the 1st to the final user station on recovery.

Table 2: Start-to-end Beam Parameters for the 15 pC HBM

Pos.	ε_{nx} (mm mrad)	ε_{ny} (mm mrad)	σ_t (ps)	σ_E (10^{-3})	Energy (MeV)
Input	0.13	0.09	3.09	2.93	50
1st user	0.14	0.08	2.13	0.21	1000
Undulator	0.20	0.08	2.13	0.18	6000
Final user	0.28	0.09	2.13	0.66	1000
Dumpline	1.24	0.11	3.60	72.56	10

The 7.3 % output energy spread is foreseen as unproblematic for the future beam dump design.

SHORT PULSE MODE

Each off-crest acceleration followed by achromatic arcs constitute the telescopic compression scheme in the lower energy acceleration sections. The first two arcs up to a beam energy of 2 GeV have $\phi_1 = +10\,°$, $\phi_2 = -20\,°$ and positive $R56_1 = 20$ cm and $R56_2 = 8$ cm values. On recovery the linac phase is shifted $\phi_{1,2} \rightarrow \phi_{1,2} + 180\,°$ (ERL process) and the arcs have the corresponding symmetric negative $R56$ values. This telescopic scheme not only has the potential to produce ultra short bunch lengths but also helps remove the correlated energy spread from RF on acceleration. Figure 4 shows the SPM to have a larger relative energy spread compared with the HBM (Low Emittance Mode LEM).

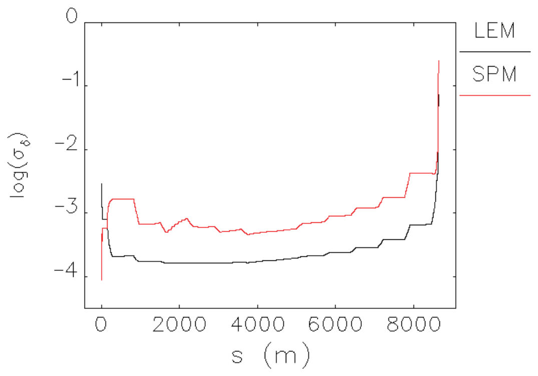

Figure 4: Log plot of the evolution of the energy spread throughout the FSF for both modes.

Sextupoles are required to combat the transverse emittance growth due to chromatic aberrations due to the high energy spread on recovery $s > 6$ km. As an alternative to computationally expensive particle tracking, key 2nd order terms were analytically found to reduce the transverse emittance growth.

$$\varepsilon_1^2 = \langle {x_1}^2\rangle\langle x'^2_1\rangle - \langle x_1 x'_1\rangle^2 \tag{1}$$

$$\varepsilon_1^2 = (T_{161}T_{262} - T_{162}T_{261})^2(\langle\delta_0^2 x_0^2\rangle\langle\delta_0^2 x'^2_0\rangle - \langle\delta_0^2 x_0 x'_0\rangle^2)$$

Suitable optic can be found where $T_{161}T_{262} = T_{162}T_{261}$ in a few seconds rather than the usual time scales associated with dedicated particle tracking codes. Without these additional corrections the beam degradation on recovery is too large and results in energy spreads far above the specification at the dump.

To complement this analytic 2nd order technique, a longitudinal emittance compensation scheme uses the higher order magnetic terms created in the arc Eq. 3 and the linac off-crest acceleration Eq. 2 to recover the longitudinal emittance of the injector Eq. 4.

$$\begin{aligned} \text{LINAC: } c\Delta t_1 &= c\Delta t_0 \\ \delta_1 &= \delta_0 + R_{65}c\Delta t_0 + T_{655}(c\Delta t_0)^2 \end{aligned} \tag{2}$$

$$\begin{aligned} \text{ARC: } c\Delta t_2 &= c\Delta t_1 + R_{56}\delta_1 + T_{566}\delta_1^2 \\ \delta_2 &= \delta_1 \end{aligned} \tag{3}$$

ISBN 978-3-95450-183-0

$$\varepsilon_2^2 = (T_{566}R_{65}^3 - T_{655})^2\langle(c\Delta t_0)^4\rangle\langle(c\Delta t_0)^2\rangle \qquad (4)$$

Figure 5 shows the positive implications of this method adapted for the two stage telescopic bunch compression, the vertical scale is logarithmic (log $10^{-14} \rightarrow 10$ fs). The longitudinal emittance, black line, is recovered after the first arc at 1 km. This allows the full potential for further compression in the following arc resulting in a 10 fs long bunch length shown in red. The longitudinal emittance then grows due to CSR effects producing unwanted energy spread. The bunch length at 2 GeV also increases to 25 fs at the entrance to the long undulator section at 6 GeV. On recovery the bunch is actively decompressed in preparation for the dump.

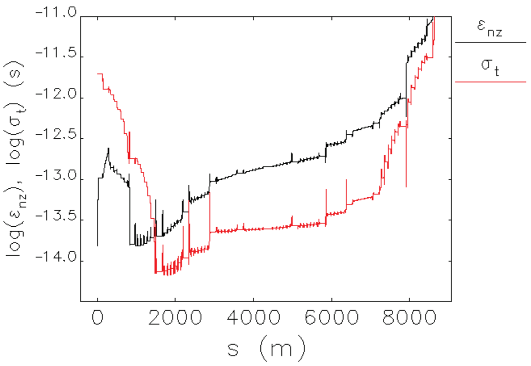

Figure 5: Normalized longitudinal emittance and bunch length in the FSF.

If one assumes that the compression scheme represents a limit for any given bunch charge, then the zero-charge bunch length can be deduced from the rectangular bunch model and the data (red crosses) from start-to-end simulations to be 5.6 fs. As the SPM is heavily dependent on CSR, this notion is extrapolated in Fig. 6 to form a boundary for feasible operation in the FSF. Bunch lengths below the boundary will induce distortions due to CSR that will be too large to recover the beam at 10 MeV.

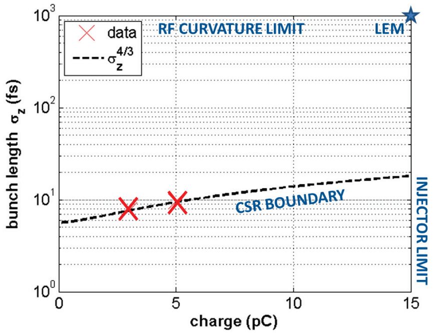

Figure 6: Boundary of minimum bunch length due to CSR effects in the FSF.

Above the boundary all machine settings are possible. The upper charge boundary of 15 pC is the limit from the injector studies for low emittance. The 1 ps long bunch extremity on the top of the figure is seen as a value that will not produce excessive longitudinal emittance growth during acceleration. Notably the LEM results would exist in the top right hand corner of the figure suggesting that the operation mode is well above the CSR limit and further bunch compression is possible, but will reduce the average brilliance.

Bunches of 1, 3 and 5 pC were used in the SPM start-to-end simulations. Table 3 summarizes the results for the 3 pC case. The bunch length remains below 50 fs throughout the user stages Low and High Energy Arcs (LEA and HEA) and the corresponding expectations of the peak brilliance is shown in Fig. 7.

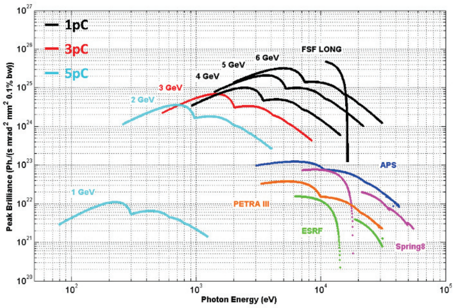

Figure 7: Comparison of the peak brilliance for the FSF and present 3rd generation light sources.

As the energy increases and the beam distortions grow depending on the bunch charge and length, the beam properties rise beyond the diffraction limit. This is apparent in Fig. 7 as the ultimate peak brilliance favors lower bunch charges at the final beam energy of 6 GeV.

Table 3: Start-to-end Beam Parameters for the 3 pC SPM

Pos.	ε_{nx} (mm mrad)	ε_{ny} (mm mrad)	σ_t (fs)	σ_E (10^{-3})	Energy (MeV)
Input	0.11	0.06	1990.09	0.46	50
LEA	0.18	0.06	7.39	0.71	2000
HEA	0.30	0.08	22.59	0.62	4000
Undulator	0.49	0.10	24.73	0.52	6000
HEA	1.00	0.23	48.70	0.92	4000
LEA	2.52	0.49	452.22	1.77	2000
Dumpline	32.88	0.64	4430.29	14.66 %	10

REFERENCES

[1] T. Atkinson et al., "Start-to-end Optic of the FSF Multi-turn ERL Project", IPAC2014, Germany.

[2] A. V. Bondarenko et al, "Implementation of 2D-emittance compensation scheme in the bERLinpro injector", FEL2011, China.

[3] A. Matveenko et al., "Multi-turn ERL-based Synchrotron Light Facility: Injector Design", IPAC2014, Germany.

ISBN 978-3-95450-183-0

DESIGN WORK OF THE ERL-FEL AS THE HIGH INTENSE EUV LIGHT SOURCE *

N. Nakamura, S. Chen, T. Furuya, K. Haga, I. Hanyu, K. Harada, T. Honda, Y. Honda,
E. Kako, Y. Kamiya, R. Kato, H. Kawata, Y. Kobayashi, T. Konomi, T. Kubo,
S. Michizono, T. Miyajima, H. Nakai, T. Obina, K. Oide, H. Sakai, S. Sakanaka,
M. Shimada, K. Tsuchiya, K. Umemori, M. Yamamoto,
KEK, Oho, Tsukuba, Ibaraki 305-0801, Japan
R. Hajima, N. Nishimori, JAEA, Tokai, Naka, Ibaraki 319-1195, Japan

Abstract

Energy recovery linac(ERL) based free electron lasers(FELs) are promising candidates of high-power EUV sources for lithography. We have designed a 10-kW class ERL-FEL operated at 13.5 nm and demonstrated the FEL power of more than 10 kW at the average current of less than 10 mA by using simulations. In this paper, we will present the design work of the ERL-FEL as the high-power EUV source.

INTRODUCTION

High-power EUV sources are required in the future for lithography. EUV FELs are becoming candidates of the EUV sources because the order of EUV-FEL size and cost can be acceptable. ERL-based FELs have merits of energy recovery, low dumped beam power and activation compared with those based on ordinary linear accelerators. We recently started the design study on the ERL-based FEL as a high intense EUV source for lithography applications. In this design work, the first target is 10-kW FEL power at 13.5 nm and the beam energy is fixed to 800 MeV. For the design, we use available technology without too much development and make the most of resources of the Compact ERL(cERL) at KEK[1].

INJECTOR DESIGN

Figure 1 shows layout of the injector system designed for the EUV source. The DC photocathode gun has the same structure of the 2nd gun developed at the cERL[2]. It succeeded in the HV conditioning up to 550 kV and 50-hour holding test of 500 kV. Two solenoid magnets and one buncher cavity are used like in the cERL injector. Two cERL injector cryomodules with six 2-cell superconducting (SC) cavities are used to increase the injection beam energy up to 10.511 MeV. A merger system is newly designed.

Injector parameters are optimized before the merger by using *GPT*[3] tracking and genetic algorithm. Figure 2 shows an example of the optimized normalized emittance and momentum spread as a function of bunch length for the bunch charge of 60pC. Taking account of the optimization results before the merger and transverse emittance growth due to the merger, we estimate the injector parameter values at the merger exit. The estimated parameter values are summarized in Table 1. These values are used as the initial parameter values for simulations including the bunch compression.

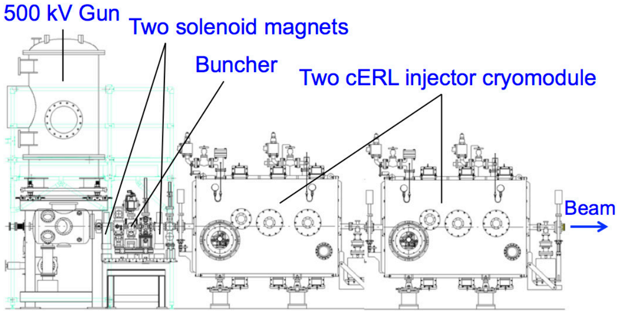

Figure 1: Layout of the injector system designed for the EUV source. The merger system is not included.

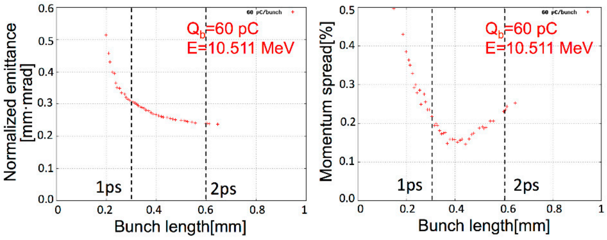

Figure 2: Optimized normalized emittance (left) and momentum spread (right) as a function of the bunch length at the bunch charge of 60 pC for the designed injector system before the merger.

Table 1: Estimated Injector Parameter Values at the Merger Exit

Bunch charge	σ_t* [ps]	$\varepsilon_n$$^{\#}$ (ε_{nx}=ε_{ny}) [mm·mrad]	σ_p/p† [%]
60 pC	1	0.60	0.25
60 pC	2	0.55	0.25
100 pC	1	0.80	0.35
100 pC	2	0.60	0.16

* Bunch length $^{\#}$ Normalized emittance † Momentum spread

---

*norio.nakamura@kek.jp

ISBN 978-3-95450-183-0

MAIN LINAC DESIGN

Cavity Design

The cERL main-linac cavities, called Model 2, are stably operated at about 8.5MV/m[4]. However the field emission of the cavities becomes significant above about 10 MV/m. Therefore we will use a different design called Model 1 for the EUV source. The Model-1 cavity[5] illustrated in Fig. 3 is a Tesla-type 9-cell cavity with a large-aperture HOM-damped beam pipe. This cavity has a smaller ratio of the peak to acceleration electric field as compared to Model 2. Therefore stable operation at 12.5 MV/m seems achievable. The detailed structure of the Model-1 cavity is under design and the large-aperture HOM-damped beam pipe may be applied to the other side.

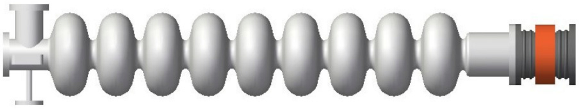

Figure 3: Illustration of the Model-1 cavity.

Table 2: Comparison of Model 1 and Model 2

	Model 1	Model 2
Frequency	1.3 GHz	1.3 GHz
R_{sh}/Q	1007 Ω	897 Ω
E_p/E_{acc}	2.0	3.0
Iris diameter	70 mm	80 mm

Main Linac Optics

The main linac has 64 cavities in 16 cryomodules to accelerate the beam up to 800 MeV. The acceleration electric field is about 12.5 MV/m. Figure 4 shows the main-linac optics for acceleration and deceleration. Quadrupole triplets are placed at every two cryomodules for the beam focusing. The horizontal and vertical betatron functions are optimized against transverse beam break-up (BBU) due to the cavity HOMs.

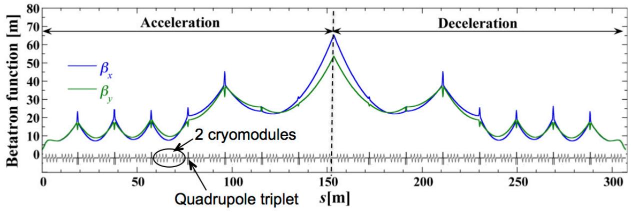

Figure 4: Horizontal and vertical betatron functions (β_x, β_y) of the main superconducting linac for the acceleration and deceleration phases.

HOM BBU and Heating

The BBU threshold current is calculated for the designed main-linac optics by using the simulation code *bi*[6]. The transverse HOM parameters of the Model-1 cavity are listed in Table 3. By scanning over the betatron phase and the return loop length, the minimum threshold current is calculated to be 195 mA without the HOM frequency randomization. It is well above the expected average current of the EUV source.

Table 3: HOM Parameters of the Model-1 Cavity

Frequency [GHz]	Q_e	R/Q [Ω/cm^2]	(R/Q) Q_e/f [Ω/cm^2/GHz]
1.866	7732	6.43	26659
1.874	11655	8.77	54526
1.879	18360	1.95	19089
2.575	4899	21.32	40557
3.082	33608	0.98	10676

The HOM heating of the main-linac cavity should be considered. The parasitic loss of the beam is given by the following equation:

$$P_{loss} = k_{loss} Q_b^2 f \ . \tag{1}$$

where the loss factor k_{loss} strongly depends on the bunch length. The parasitic loss is finally absorbed at the HOM damper. Therefore the maximum absorption power of the HOM damper restricts the bunch charge, length and frequency. Table 4 shows examples of estimated parasitic loss power for the Model-1 cavity. Our short-term target of the absorption power of the HOM damper is 30 W and the final goal is 100 W. In addition, the bunch frequency should be carefully selected so as to avoid heating resonant to monopole HOMs. Bunch frequencies of 130, 162.5, 260, 325 and 650 MHz are possible at least for the Model-1 cavity.

Table 4: Estimated Parasitic Loss of the Model-1 Cavity

Bunch length @cavity	**9.75mA x 2 60pC 162.5MHz**	**8mA x 2 100pC 81.25MHz**
1 ps	23.4 W	32 W
2 ps	17.6 W	24 W

FEL PARAMETERS

Here FEL parameters are briefly described. The FEL power P_{FEL} is roughly expressed by the product of the electron beam power $P_{electron}$ and Pierce parameter ρ_{FEL} as follows:

$$P_{FEL} = \rho_{FEL} P_{electron} \ . \tag{2}$$

The electron beam power is the product of the beam energy E and the average beam current I_{av}. The Pierce parameter is given by

$$\rho_{FEL} = \left[\frac{1}{16}\frac{I_p}{I_A}\frac{K^2[JJ]^2\lambda_u^2}{\gamma^3\sigma_x\sigma_y(2\pi)^2}\right]^{1/3}, \qquad (3)$$

where I_p, I_A, γ, σ_x, σ_y, K and λ_u are the peak current, Alfven current(17kA), horizontal and vertical beam sizes, the K-vaue and magnetic period of the undulators. $[JJ]$ is $J_0[\xi]$-$J_1[\xi]$ with $\xi=K^2/(4+2K^2)$ for planar undulators and unity for helical undulators. The horizontal and vertical beam sizes are proportional to the square root of the horizontal and vertical emittances, respectively. High peak current and low emittance are important for the FEL power.

BUNCH COMPRESSION AND DECOMPRESSION SCHEME

Bunch compression is essential for achieving high peak current and decompression for efficient energy recovery without significant beam loss.

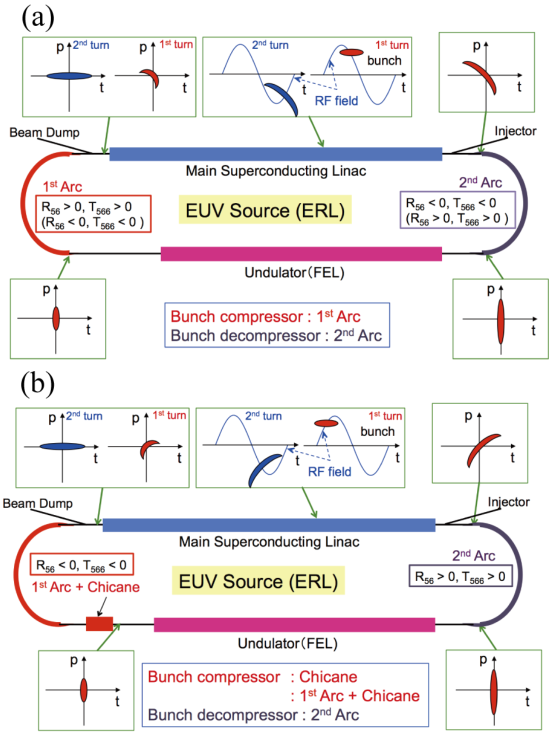

Figure 5: Bunch compression and decompression schemes: (a) The bunch compressor is the 1st arc. (b) The bunch compressor is only the chicane or combination of the 1st arc and chicane. For all the cases, the bunch decompressor is the 2nd arc.

The simplest scheme is that the bunch compressor is the 1st arc and the bunch decompressor the 2nd arc and illustrated in Fig. 5a. The 1st and 2nd arcs have the R_{56} and T_{566} values with different signs. The electron bunch from the injector is accelerated off crest in the main linac and compressed in the 1st arc with non-zero R_{56} optics. The sextupole magnets in the 1st arc optimize T_{566} in order to minimize the bunch length or maximize the Pierce parameter. The compressed bunch is used for the FEL in the long undulator section and then decompressed before the beam dump by using the optics of the 2nd arc and off-crest deceleration in the main linac.

Figure 5b shows two other bunch compression and decompression schemes using a chicane. One is that the bunch compressor is only the chicane and the other combination of the 1st arc and chicane. We try three different bunch compression schemes in our design study.

DESIGN OF ARCS AND CHICANE

Arc Sections

A 2-cell TBA lattice is used for design of the arc sections. Figure 6 shows the 2-cell TBA lattice and an example of the isochronous optics (R_{56}=0 m). The structure of the TBA cell is very similar to that of the cERL arcs. The bending radius and angle are 3 m and π/8 for each of the eight sector bending magnets. The lengths of the quadrupole and sextupole magnets are two times longer than that of the cERL because the beam energy is high. Optics matching of the two cells is done by four quadrupole magnets at the arc center. Eight sextupole magnets can be inserted in the arc to optimize T_{566}.

The R_{56} of the 2-cell TBA lattice is expressed with the bending radius ρ, the bending angle θ and the dispersion function η_c at the TBA-cell center as follows:

$$R_{56} = 4\rho(\theta - \sin\theta) + 2\eta_c \sin\theta\,. \qquad (4)$$

The 2-cell TBA optics with different R_{56} values of ±0.3 m and ±0.6 m can be designed in a similarly way to the isochronous optics. The 2-cell TBA lattice has a wide dynamic range of R_{56}. The momentum acceptance is estimated from the maximum dispersion function to be more than 4% for a possible horizontal half-aperture of about 5 cm and expected to tolerate a large momentum spread caused by the FEL.

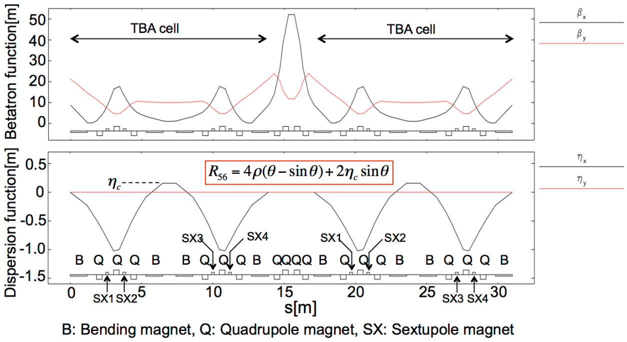

Figure 6: 2-cell TBA lattice and optics for the arcs. The betatron and dispersion functions of an isochronous optics (R_{56}=0 m) are shown in the upper and lower graphs.

Chicane

A chicane is designed with four rectangular bending magnets for the bunch compression. The R_{56} of this chicane is expressed by

$$R_{56} = -\frac{4L_B}{\cos\theta} - \frac{4L_B^2 L_D}{\rho^2 \cos^3\theta} + 4\rho\theta \,, \tag{5}$$

where ρ, θ, L_B, and L_D are the bending radius, the bending angle and the magnet length and interval. In the design, the magnet length of 1 m and the magnet interval of 0.51 m are used. Figure 7a is chicane optics with R_{56} of -0.3 m for the bunch compression by only the chicane and Figure 7b chicane optics with R_{56} of -0.15 m for the bunch compression by combination of the 1st arc and chicane. They are used for the bunch compression simulations.

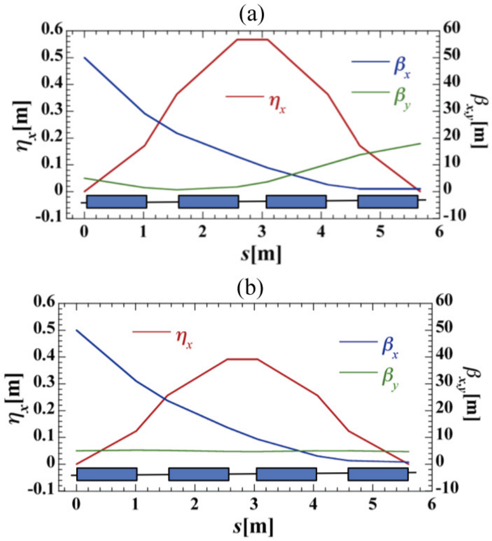

Figure 7: Dispersion function η_x and betatron functions (β_x, β_y) of the chicane for bunch compression (a) by only the chicane (R_{56}=-0.3 m) and (b) by the combination of the 1st arc and chicane (R_{56}=-0.15 m).

BUNCH COMPRESSION SIMULATION

The bunch compression simulation is performed for the three different schemes by using the simulation code *elegant*[7]. Figure 8 shows the simulation result of the bunch compression by the 1st arc, the chicane and their combination. In each of Figs. 8a to 8c, the upper graph shows optics from the entrance of the main linac to the exit of the 1st arc or the exit of the chicane. The 2-D longitudinal (time-momentum) distributions of the electron bunch at the entrance of the main linac, the entrance of the 1st arc and the exit of the 1st arc or the chicane are also shown. In the simulation, the initial distribution at the entrance of the main linac is assumed to be a 6-D Gaussian distribution with the injector parameter values estimated in the previous section. This is the case of the initial bunch length of 1ps and the bunch charge of 60 pC. The momentum spread is set to about 0.1 % after off-crest acceleration by the main linac.

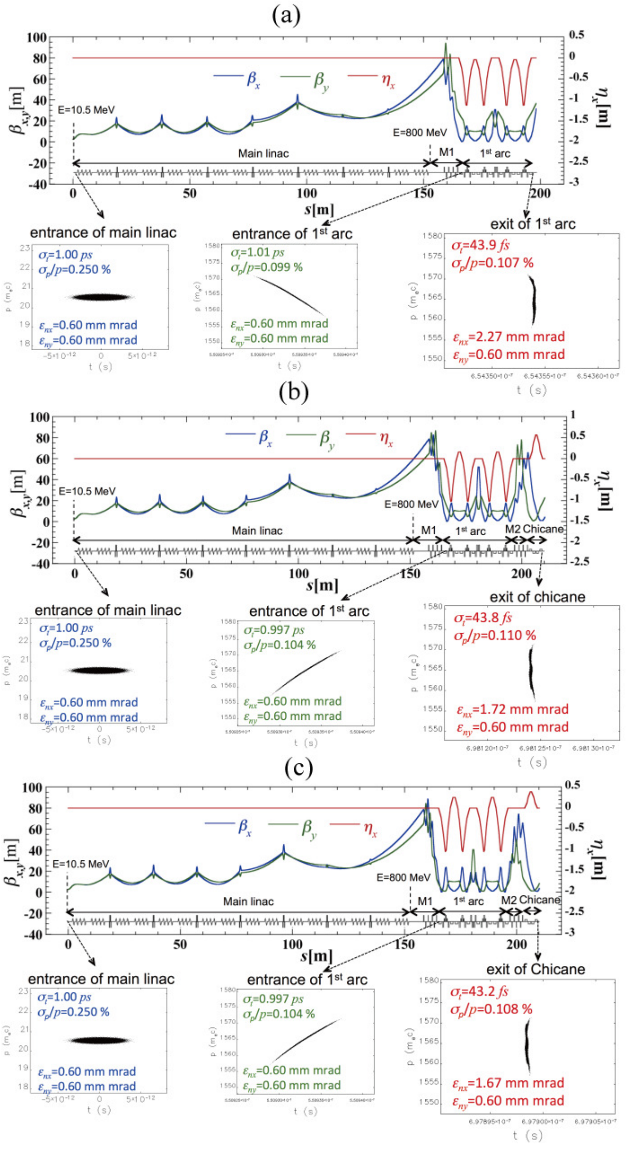

Figure 8: Optics from the main-linac entrance to the 1st arc exit or chicane exit and simulated time-momentum distributions at the main-linac entrance, the 1st arc entrance and the 1st arc exit or the chicane exit for the bunch compression by (a) the 1st arc, (b) the chicane and (c) their combination.

For the bunch compression by the 1st arc shown in Fig. 8a, the bunch length is compressed to about 44 fs by the 1st arc with R_{56}=0.3 m and the normalized horizontal and vertical emittances are 2.26 and 0.60 mm·mrad at the 1st arc exit. The normalized horizontal emittance is significantly increased by the CSR effects. In the case of the bunch compression by only the chicane in Fig. 8b, the 1st arc optics is isochronous (R_{56}=0 m) and the bunch is compressed by the chicane with the R_{56} value of -0.3 m. At the chicane exit after the bunch compression, the bunch length is almost the same as that of bunch compression by the 1st arc. On the other hand, the normalized horizontal emittance is reduced to 1.72 mm·mrad because the CSR effects are reduced by optics adjustment described later. Figure 8c shows the simulation result of the bunch compression by combination of the 1st arc and chicane. Both the 1st arc and chicane have the same R_{56} value of -0.15 m. At the chicane exit, the bunch has almost the same parameter values as that of the bunch compression by only the chicane. The parameter values after the bunch compression are summarized in Table 5.

For the two bunch compression schemes using the chicane, the CSR-induced emittance growth is reduced by matching the phase ellipse angle to the CSR kick angle at the chicane exit, as shown in Fig. 9. The Pierce parameter becomes almost maximum at this matching condition. Such adjustment of the phase ellipse angle is found to be difficult for the bunch compression by the 1st arc having achromatic TBA optics with a fixed R_{56} value. Therefore the normalized horizontal emittance is large compared to those of the other two schemes using the chicane.

Table 5: Beam Parameters after Bunch Compression

Bunch Compressor	σ_t* [fs]	σ_p/p# [%]	ε_{nx}, ε_{ny}† [mm·mrad]
1st arc	43.9	0.107	2.27, 0.60
Chicane	43.8	0.110	1.72, 0.60
1st arc + Chicane	43.2	0.108	1.67, 0.60

* Bunch length # Momentum spread † Normalized horizontal and vertical emittances

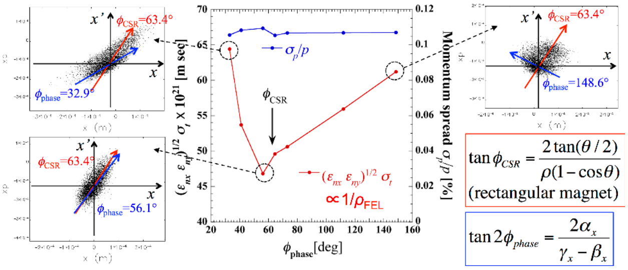

Figure 9: Maximization of the Pierce parameter by matching the phase ellipse angle ϕ_{phase} to the CSR kick angle ϕ_{CSR}=63.4 degrees. This is the case for the bunch compression by only the chicane at the bunch charge of 60 pC.

Figure 10 shows the peak current and normalized horizontal and vertical slice emittances in the bunch after the bunch compression for the three different bunch compression schemes. The slice emittances are more important for the FEL power than the projected ones listed in Table 5. The horizontal normalized slice emittance is lower at high slice peak currents than the projected one, especially for the two bunch compression schemes using the chicane.

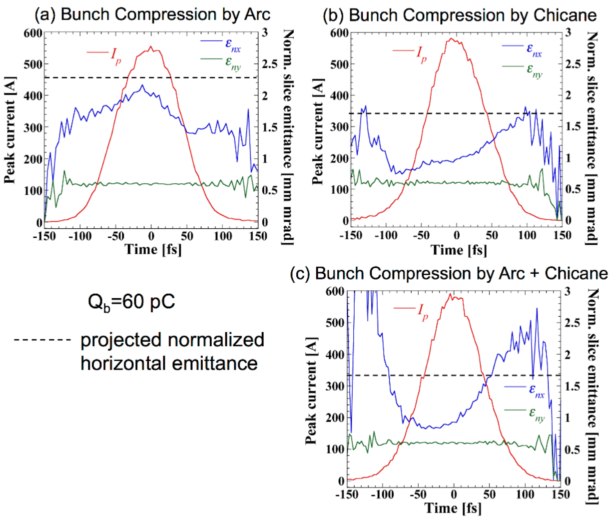

Figure 10: Peak current and normalized horizontal and vertical slice emittances in the bunch after the bunch compression for the three different bunch compression schemes. The broken line in each graph means the projected normalized horizontal emittance.

FEL PERFORMANCE

The FEL performance of the designed ERL-EUV source is calculated by using the FEL simulation code *Genesis*[8] and the simulation result of the bunch compression for the bunch charge of 60 pC. Helical undulators with the magnetic period of 28 mm are used for the FEL. Figure 11 shows the FEL pulse energy as function of the undulator section length, the FEL temporal profile and the FEL power spectrum for the bunch compression by combination of the 1st arc and chicane. The FEL pulse energy is 55.5 μJ without tapering and 67.6 μJ with 10% linear tapering at the undulator section length of 100 m. For the bunch frequency of 162.5/325 MHz, 9/18 kW FEL power is achieved at 9.75/19.5 mA without tapering and 11/22 kW at the same current with the 10% tapering.

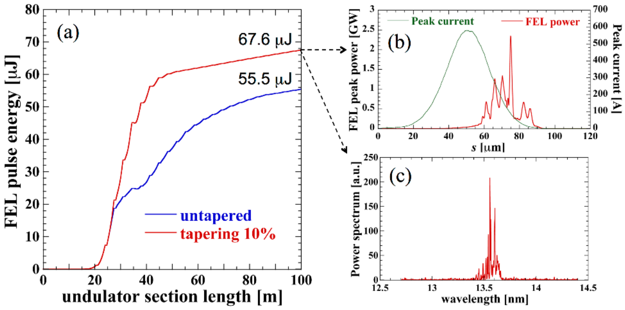

Figure 11: Calculated FEL performance of the designed ERL-based EUV source: (a) the FEL pulse energy as function of the undulator section length, (b) the FEL temporal profile and (c) the FEL power spectrum.

ISBN 978-3-95450-183-0

SUMMARY AND OUTLOOK

The design work on the ERL-based EUV source was recently started. The injector, main linac, arc sections and chicane have been designed. The bunch compression simulation has also been done. As a result, more than 10/20 kW FEL power is demonstrated at the average current of less than 10/20 mA. The present image of the designed EUV source is shown in Fig. 12. Further design work and optimization for the tapering, optics, beam and undulator parameters are expected to improve the FEL power. In addition, the bunch decompression simulation and finally S2E simulation from the gun to the beam dump should be performed.

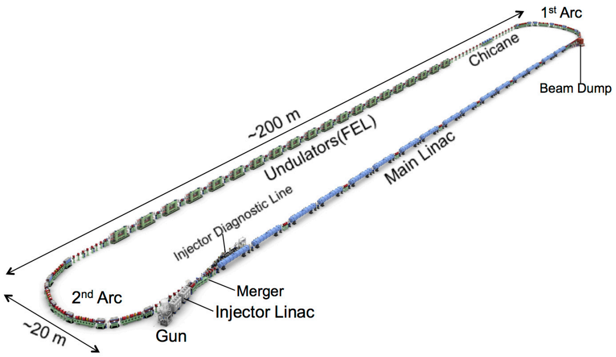

Figure 12: Present image of the designed ERL-based EUV source.

REFERENCES

[1] S. Sakanaka et al., MOPCTH07, ERL2015, Stony Brook, NY, USA.

[2] M. Yamamoto et al., TUIBLH1020, ERL2015, Stony Brook, NY, USA.

[3] *GPT*, http://www.pulsar.nl/gpt/index.html

[4] H. Sakai et al., WEIBLH2054, ERL2015, Stony Brook, NY, USA.

[5] H. Sakai et al., Proc. of ERL2007, Daresbury, UK, p.34 (2007).

[6] *bi*, http://www.lepp.cornell.edu/~ib38/bbu/

[7] *elegant*, http://www.aps.anl.gov/Accelerator_Systems_Division/Accelerator_Operations_Physics/manuals/elegant_latest/elegant.pdf

[8] *Genesis*, http://genesis.web.psi.ch

STATUS AND COMMISSIONING RESULTS OF THE R&D ERL AT BNL*

D. Kayran#,1,2, Z. Altinbas1, D. Beavis1, S. Belomestnykh1,2, I. Ben-Zvi1,2, S. Deonarine1,
D. M. Gassner1, R. C. Gupta1, H. Hahn1,L. R. Hammons1,2, Chung Ho1, J. Jamilkowski1,
P. Kankiya1, N. Laloudakis1, R. Lambiase1, V.N. Litvinenko1,2, G. Mahler1, L. Masi1, G. McIntyre1,
T. A. Miller1, J. Morris1, D. Phillips1, V. Ptitsyn1,2, T. Seda1, B. Sheehy1, L. Smart1, K. Smith1,
T. Srinivasan-Rao1, A.N.Steszyn1, T. R. Than1, E. Wang1, D. Weiss1, Huamu Xie1, Wencan Xu1,
A.Zaltsman1

1) Collider-Accelerator Department, Brookhaven National Laboratory, Upton, NY 11973, USA

2) Physics & Astronomy Department, Stony Brook University, Stony Brook, NY 11794, USA

Abstract

An ampere class 20 MeV superconducting Energy Recovery Linac (ERL) is presently under commissioning at Brookhaven National Laboratory (BNL) for testing of concepts relevant for high-energy coherent electron cooling and electron-ion colliders [1]. The injector subsystems tests and installation were finished in fall 2013. The injector includes: SRF photoelectron gun with 1 MW amplifier, 10W green drive-laser system, multi-alkaline cathode deposition system, cathode transport system, beam instrumentation and control. First beam test conducted in June 2014 only dark current observed during first beam test [2]. The first photo current from ERL SRF gun has been observed in fall 2014 after second attempt [3]. The ERL returning loop components installed. New cathode with Ta tip conditioned. QE 4% observed. Bunch charge 0.55 nC achieved with new cathode. After ERL commissioning in BLDG 912 the ERL will be relocated to RHIC IP2 to be used for LEReC.

INTRODUCTION

The R&D ERL facility at BNL aims to demonstrate CW operation of ERL with average beam current up to 0.3 ampere, combined with very high efficiency of energy recovery. The ERL is being installed in one of the spacious bays in Bldg. 912 of the RHIC/AGS complex. The intensive R&D program geared towards the construction of the prototype ERL is under way [4]: from development of high efficiency photo-cathodes [5], design, construction and commissioning SRF gun [6], to the development of new merging system compatible with emittance compensation technic [7]. The R&D ERL will test many generic issues relevant with ultra-high current continuously operation ERLs: 1) SRF photo-injector (704 MHz SRF Gun, photocathode, laser) capable of 300 mA; 2) preservation of low emittance for high-charge, bunches in ERL merger; 3) high current 5-cell SRF linac with efficient HOM absorbers [8]; 4) BBU studies using flexible optics; 5) stability criteria of amp class CW beams. BNL ERL design has one re-circulating loop with achromatic flexible optics [9]. Schematic layout is shown on Fig. 1. Electrons are generated and accelerated in superconducting half-cell gun to 1-2 MeV. Then electrons are injected into the ERL loop through the merging system, which incorporate emittance compensation scheme. The SRF linac accelerates electrons up to 20 MeV. Accelerated electron beam passes through two achromatic arcs and a straight section between them, and returns to the same linac. The path-length of the loop provides for 180 degrees change of the RF phase, causing electron deceleration in the linac (hence the energy recovery) down to injection energy. Decelerated beam is separated from the higher energy beam and is directed to the beam-dump.

Two operating modes will be investigated, namely the high current mode and the high charge mode. Beam parameters for each mode and recent tests results summarized at Table 1.

Table 1: ERL Beam Parameters

Parameter	High Charge	High Current	Measured
Gun energy	3 MeV	2.5 MeV	1.4 MeV
Max. Energy	20 MeV	20 MeV	1.4 MeV
Charge per bunch	5 nC	0.5 nC	0.55 nC
Current	50 mA	350 mA	6 μA
Laser Rep. Rate	9.38 MHz	350 MHz	9.38 MHz*
Laser Bunch Length	30 ps	8-20 ps	8.5, 22 ps
Norm. emittance	5 μm	1.4 μm	12 /.25 μm**
Energy spread	1%	0.35%	
Beam dump Power	150 kW	875 kW	8 W (@FC)

*) 5μsec train every 500μsec.

**) Full beam rms /20% core, preliminary results.

---

* This work is supported by Brookhaven Science Associates, LLC under Contract No. DE-AC02-98CH10886 with the U.S. DOE.
#dkayran@bnl.gov

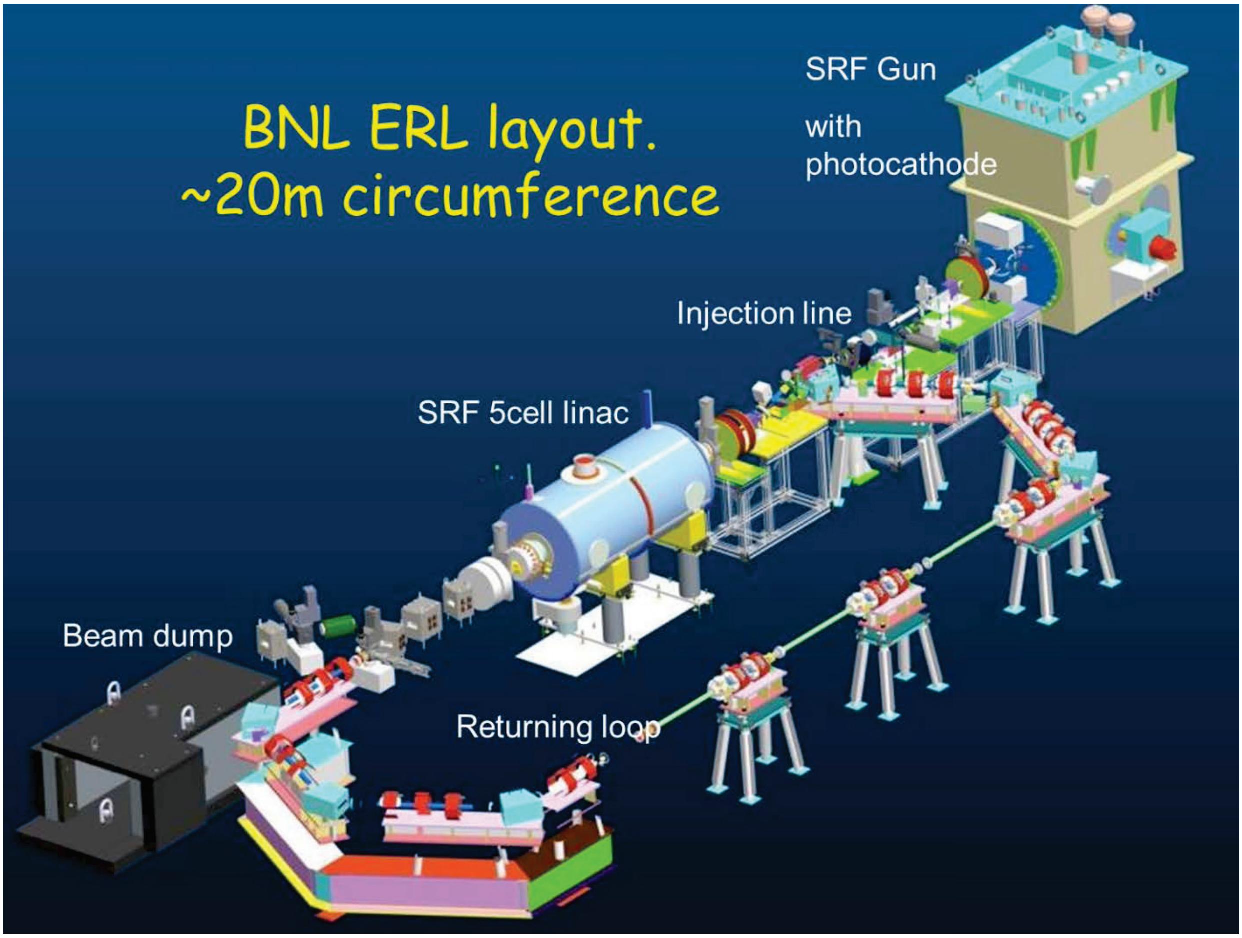

Figure 1: Schematic layout of the R&D ERL at BNL.

In the high current (0.3 A) mode ERL will accelerate electron 0.5 nC per bunch with 703 MHz rep-rate. In this case the energy gain of electrons at gun exit is limited to 2.0 MeV by the available RF CW klystron power of 1 MW. In the high charge mode, ERL will have electron beam with 5 nC per bunch and 10 MHz repetition rate, i.e. it will produce 50 mA average current. In this mode, the electrons energy at the gun exit could be pushed higher. The maximum voltage at the gun is 2.5 MV limited by power coupling design and available RF power.

SRF COMPONENTS

The most important element of BNL ERL is SRF photo-injector. BNL 704 MHz SRF gun has been designed with a short 8.5 cm cell. The short length was chosen to provide high electric field at the cathode at low accelerating voltage. In order to provide effective damping of high order mode (HOM) this gun has rather large iris radius of 5 cm. Ferrate dumpers are installed around ceramic break at the exit of the gun. Gun has been installed at ERL in 2012. SRF gun now routinely operates CW without the cathode at 2 MV accelerating voltage.

With new cathode stalk installed the gun operated at 1.25 MV [10] with good vacuum and no radiation. (See Fig. 2)

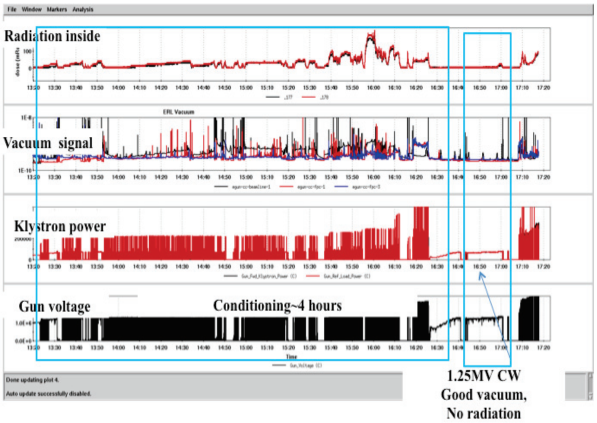

Figure 2: ERL 704MHz SRF gun performance during conditioning and CW operation with new cathode stalk. From top to bottom: radiation, beam-line vacuum, klystron power and gun voltage signals.

The heart of the ERL facility is 5-cell 704MHz SRF linac, which is designed for operating with ampere-class CW beam current [8]. The cavity was designed as a “single-mode” cavity, in which all Higher Order Modes (HOMs) propagate to HOM ferrite absorbers through the large beam pipe. This design provides for very low Q’s for HOMs and hence very high ERL stability.

Measurements of the damped Q and R/Q of the HOMs and simulations show that in nominal operation regime the cavity is stable to over 20 amperes in a one pass ERL and over 2 amperes for two passes ERL. The 5cell cavity has been commissioned in 2010. In cold emission tests high gradients are achieved for short period of time (as shown in Fig. 3).

A thermal problem has been discovered during commissioning SRF 5-cell cavity, which prevents CW operation at gradients above 12 MV/m. However, the prototype program can still be pursued if the cavity can be operated in a pulsed "quasi-cw' mode up to 20 MV/m, in which the cavity is on, with stable gradient, for a time long compared with the transit time through the ERL loop (10 nsec).

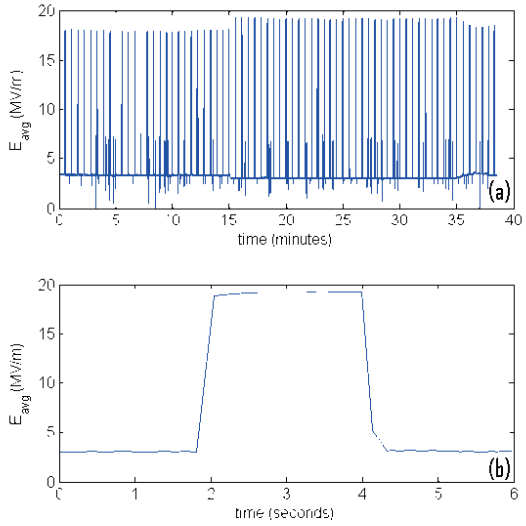

Figure 3: Five cell cavity performances during horizontal test. Pulses are 2 seconds long with a 30 second interval .

SRF PHOTOINJECTOR BEAM TEST SETUP

The beam commissioning has been started on June 2014. The first beam test schematic setup shown in Fig. 4. The ERL injection dipole is off during first beam test. The current coming from the gun goes straight to the faraday cup where current can be measured. Steering magnet is installed next to the laser cross. The beam profile monitor (YAG crystal) can be inserted before the faraday cup to measure beam size [11] (see Fig. 4).

For the first beam test, a Cs3Sb cathode was fabricated using copper substrate and QE has been measured at value of 2E-3 in deposition chamber. During cathode stalk transfer to the gun QE significantly degraded. Additional QE reduction has been observed when cathode has been used at liquid nitrogen temperature. Final QE measured was very low of 2.7e-5.

With maximum available laser power 4W we were able to extract only 7.7 pC charge per bunch. This first photocurrent was measured during the first ERL gun beam test [3] (see Fig. 5).

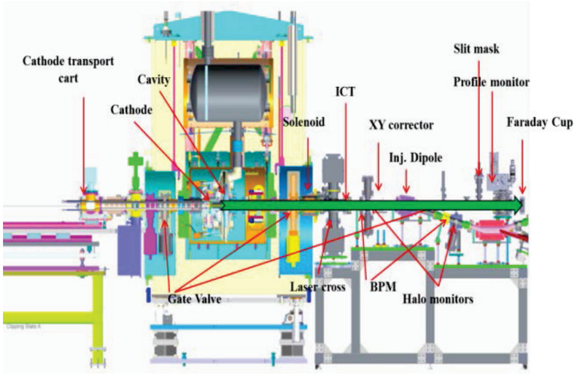

Figure 4: Schematic layout of the SRF injector at BNL R&D ERL.

Figure 5: Faraday cup (1MOhm termination) signal during first beam test of ERL 704 MHz SRF Gun. Top: laser shutter open 1.09V; bottom: laser shutter closed 38mV. It corresponds to dark current 38nA, photocurrent 1.09 mA.

RESULTS WITH NEW CATHODE STALK

New cathode stalk with Ta tip has been fabricated. We tested 3.8% QE K2CsSb cathode in the 704MHz SRF gun. The cathode survives well during the gun and stalk RF conditioning. The maximum cathode QE inside the gun (cold) measured 1%. We didn't see any QE degradation after two days of high bunch charge operation. The vacuum at the gun exit is at 10-9 scale during gun operation. After extracting the measured QE at room temperature is still 3.8% [12] (see Fig. 6).

During the beam tests bunch charge was measured by FC and ICT (Fig. 7). Both measurements agreed.

With initial laser spot size at the photocathode of 2 mm FWHM, we observed saturation of the extracted charge per bunch at 200 pC. Increasing spot size up to 4 mm allows us to extract more charge with the same gun voltage (see Fig. 8). With new photocathode 550pC charge per pulse has been achieved (see Fig. 9).

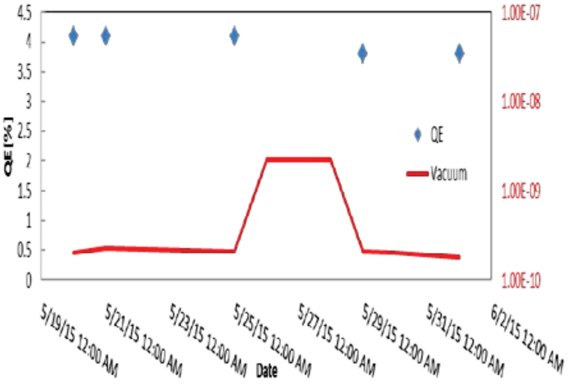

Figure 6: QE (blue diamonds) of K2CsSb cathode deposited to the new cathode stalk and vacuum (red trace) measured at room temperature before beam test 4% and after beam test 3.8%.

Figure 7: Straight beam line with beam diagnostics components (top). Dark current (slop) and photocurrent (spikes) measured one faraday cup (left bottom). Cross calibration charge measurements at ICT (right bottom).

UNEXPECTED ASTIGMATISM

Instrumentation beam line equipped with beam profile monitors YAG crystal. Several attempts have been made in order to measure emittance. The straight line is axial symmetric system except RF fundamental power couplers (FPC). During solenoid scan very strong astigmatism has been observed (see Fig 10.).

Based on these measurements we suspect that there is strong quadruple focusing in the system. One of the suspects is FPC. We estimate that focusing strength of quadrupole responsible for the same kick placed at FPC location is equal to 65cm. This required further investigation.

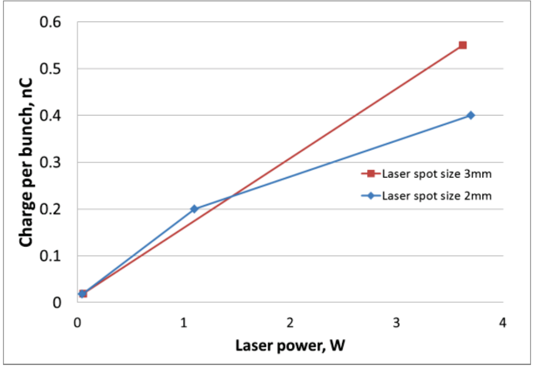

Figure 8: Charge per pulse vs laser average power. Due to space charge limitation some saturation has been observed at high average laser power (blue diamonds). Laser spot size has been increased to reach 550pC per bunch (red square).

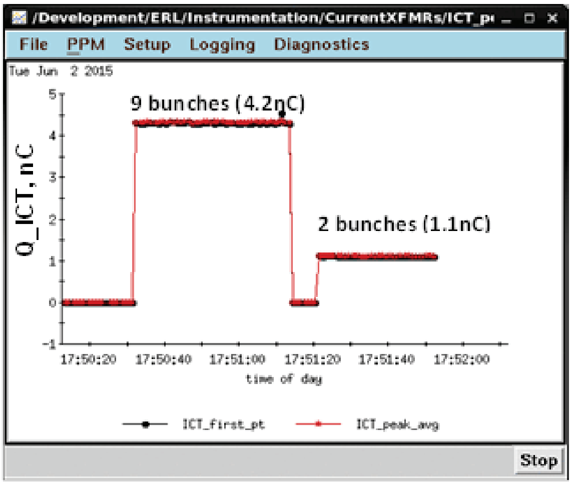

Figure 9: ICT signal during high charge operation of 704MHz SRF gun. Maximum charge per one bunch Q=550 pC.

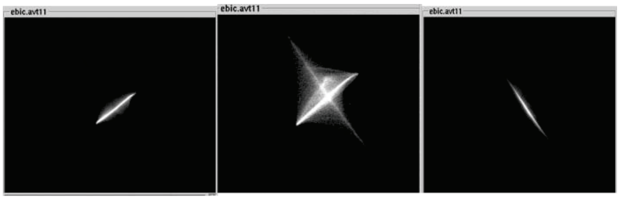

Figure 10: Beam image at beam profile monitor located before faraday cup for three different solenoid settings.

STATUS AND PLANS

An ampere class 20 MeV superconducting Energy Recovery Linac (ERL) is presently under commissioning at Brookhaven National Laboratory (BNL) for testing of concepts relevant for high-energy electron cooling and electron-ion colliders. Commissioning with beam started on July, 2014.

- Gun to dump commissioning has been approved. Full ERL loop commissioning approval is under its way.
- The first photo current from ERL SRF gun has been observed in November 2014 (1 mA per 500msec RF pulse). New "mulipactor free" Ta tip cathode stalks conditioned for CW operation in March, 2015. ERL returning loop components installation is completed in May, 2015. QE with Ta cathode tip: room temperature measured 4%, cold in gun 1%. May, 2015.
- Beam commissioning with new cathode started in June 2015. Some beam parameters measured: energy, emittance. The highest charge per bunch from SRF gun .55 nC has been demonstrated, max average current per 3 msec RF pulse 3.5uA. We started commissioning beam instrumentation with beam.
- After ERL commissioning in BLDG912 the ERL components will be relocated to RHIC IP2 to be used as low energy RHIC electron cooler [13].

REFERENCES

[1] I. Ben-Zvi et al., "Extremely High Current, High Brightness Energy Recovery Linac," In Proc. of PAC2005, pp. 2741-2743 (2005).

[2] D. Kayran et al., "First Test Results from SRF Photoinjector for the R&D ERL at BNL," In Proc. of IPAC'14, pp. 748-750 (2014).

[3] Wencan Xu et al., "First beam Commissioning at BNL ERL SRF gun," In Proc. of IPAC'2015, pp 1941-1943 (2015).

[4] D. Kayran et al., "Status of High Current R&D Energy Recovery Linac at BNL," In Proc. of PAC'11, pp. 2148-2150 (2011).

[5] E. Wang et al., "Fabrication of alkali antimonite photocathode for SRF gun," In Proc. of IPAC'14, pp. 742-744 (2014).

[6] Wencan Xu et al., Commissioning SRF gun for the R&D ERL at BNL, In Proc. of IPAC2013, pp. 2492-2494 (2013).

[7] V.N. Litvinenko, R. Hajima, D. Kayran, NIMA **557**, 165 (2006).

[8] B. Sheehy et al., "BNL 703 MHz Superconducting RF cavity testing", In Proc. of PAC'11, pp. 913-915 (2011).

[9] D. Kayran et al., "Optics for High Brightness and High Current ERL Project at BNL", In Proc. of PAC2005, pp. 1775- 1777 (2005).

[10] Wencan Xu et al., "Multipacting-free quarter-wavelength choke joint design for BNL SRF gun", In Proc. of IPAC'2015, pp 1935-1937 (2015).

[11] T.A. Miller et al., "Current Measurement and Associated Machine Protection in the ERL at BNL". WEIALH248, these proceedings ERL2015.

[12] E. Wang et al., "Characterization of Multi-alkali Antimonide Cathode at Cryogenic Temperatures and its Performance in SRF Gun". TUICLH1027, these proceedings, ERL2015.

[13] J. Kewisch et al., "ERL for Low Energy Electron Cooling at RHIC (LEReC)", WEICLH1058, these proceedings, ERL2015.

LHeC ERL DESIGN AND BEAM-DYNAMICS ISSUES

A. Bogacz, JLab, Newport News, VA 23606, USA
A. Latina, D. Schulte, CERN, Geneva, Switzerland
D. Pellegrini, EPFL, Lausanne, Switzerland and CERN, Geneva, Switzerland

Abstract

The LHeC study is a possible upgrade of the LHC that aims at delivering an electron beam for collision with the existing hadronic beam. The current baseline design for the electron facility consists of a multi-pass superconductive energy-recovery linac operating in a continuous wave mode. Here, we describe the overall layout of such ERL complex located on the LHC site. We present an optimized multi-pass linac optics enabling operation of the proposed 3-pass RLA in the Energy Recovery mode. We also describe emittance preserving return arc optics architecture; including layout and optics of the arc switch-yard. High current (~100 mA) beam operation in the linacs excites long range wake-fields between bunches of different turns, which induce instabilities and might cause beam losses. The impact of long-range wake-fields, synchrotron radiation, and beam-beam effects has been assessed in this paper.

INTRODUCTION

Two of the initially purposed options for the LHeC: the Linac-Ring and the Ring-Ring, both offered comparable performances. However, the Linac-Ring has recently been selected as the baseline; the choice mainly based on minimizing interference with the LHC operation. New sections of the lattice have been recently designed and a PLACET2 [1] simulation has been setup to validate the ERL operation.

The ERL based design for the LHeC electron facility is sketched in Fig. 1. Each of the two 1 km long superconducting linacs provide a total acceleration of 10 GeV. The injection energy is 500 MeV. In order to reach the collision energy of 60 GeV, the electrons are recirculated three times. Beams of different energies are directed into separate recirculation arcs via beam spreaders and recombiners placed at each end of the linacs. They allow to vertically separate the beams at the different energies routing them to the corresponding arcs. Arc2 and Arc4 are equipped with bypasses to avoid the interference with the detector.

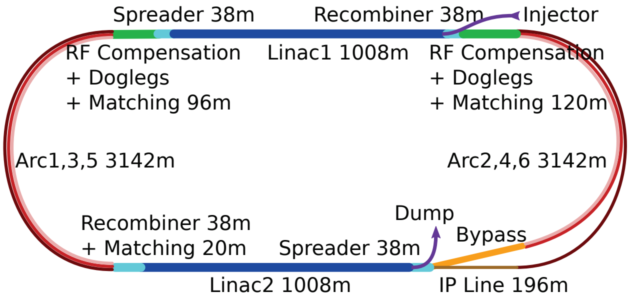

Figure 1: Scheme of the LHeC electron facility.

After the collision with the LHC proton or ion beam, the electron beam is decelerated in the subsequent three turns, allowing to increase the beam current and luminosity while limiting the power consumption [2]. The machine is operated continuously and bunches of different passes are interleaved in the linacs. An up-to-date beam parameter list can be found in [3].

LATTICE COMPONENTS

Linacs

The two linacs are about 1 km long and they consist of 18 FODO cells. Following each quadrupole two cryomodules are placed, each containing 8 cavities operating at 802 MHz, for a total of 576 cavities per linac. The phase advance per FODO cell is set to 130 °. In order to reuse the same arcs for both the acceleration and deceleration, the β functions before and after each linac must coincide. The only free parameters are then the optic functions at the injection. These can be optimised minimising the value of:

$$\left\langle \frac{\beta}{E} \right\rangle = \int \frac{\beta}{E} ds$$

which enhances the impact of imperfections and many collective effects. Figure 2 shows the evolution of the Twiss functions in the linacs, starting from the initial condition.

Arcs

To accomplish the multi-turn recirculation, six arcs are employed. They all share the same radius of 1 km. The lattice cell adopts a flexible momentum compaction layout which allows to tune each of them according to the impact of the Synchrotron Radiation at different energies. At the highest energy, it is crucial to minimise its emittance dilution tuning the cells to TME. At the lowest energy it is possible to compensate for the bunch elongation with a negative momentum compaction setup. The intermediate energy arcs are tuned to a DBA-like lattice, offering a good compromise. Fig. 3 shows the different tunings of the cells.

Spreader and Recombiner

The spreaders and recombiners separate the bunches at different energies coming from the linac, in order to route them to the corresponding arc, and recombine them to the same orbit before entering the next linac.

The CDR design employs a two-step vertical bending that simplifies the suppression of the vertical dispersion. It has been verified that this design causes a non negligible energy loss, especially for Arc4, moreover it raises the horizontal β function to very high values. A new single-step design

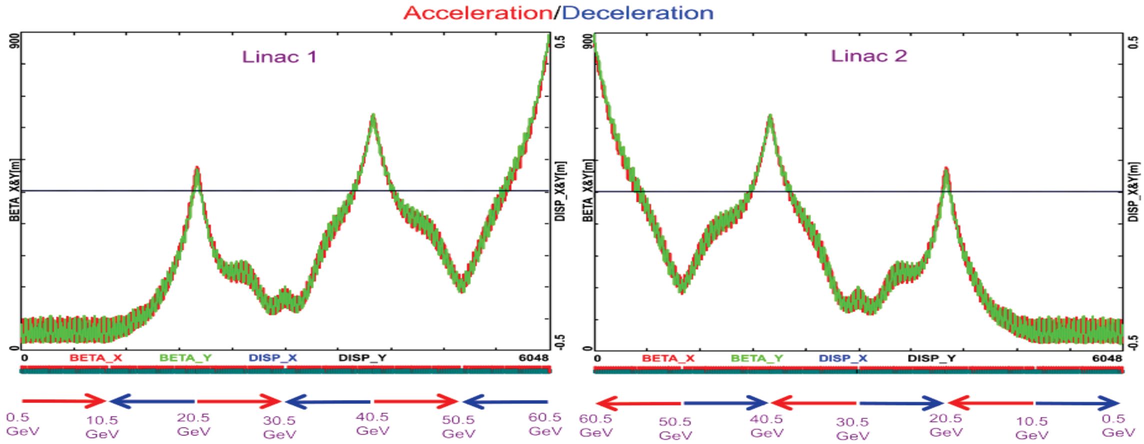

Figure 2: Optics functions in the linacs for the subsequent passages.

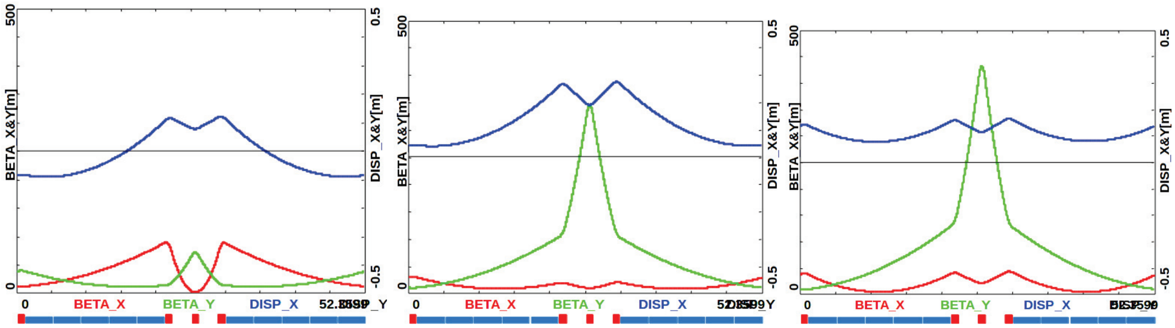

Figure 3: Cells for Arc1 and Arc2 (left), Arc3 and Arc4 (centre), Arc5 and Arc6 (right).

targets both. It employs seven quadrupoles to control the dispersion between the two bending dipoles. The energy loss is reduced by a factor 5 and at the same time both the dispersion and the β functions are reduced. The maximum quadrupole gradient of 80 T/m is not challenging adopting superconducting technology, but cannot be reached with warm magnets. The integrability of the systems needs to be verified with technical drawings. A comparison of the two design for the Arc2 spreader is shown in Fig. 4.

Bypasses

Following the spreader of linac2, that provides vertical separation, the 60 GeV beam goes straight to the IP; however, the lower energy beams need to be further separated to avoid the detector. This is accomplished by the bypass section that applies to Arc2 and Arc4. As shown in Fig. 1 and 5, the separation takes place in the horizontal plain, towards the inside of the racetrack. This allows one to minimise the required extra bending and therefore the impact of synchrotron radiation.

Ten arc-like dipoles, placed very close to the spreader, provide the initial bending, resulting in 10 m separation from the detector 150 m downstream. The straight section of the bypass is approximately 300 m long and may have many applications; such as diagnostic and path length adjustments. To connect with Arc6, ten of the sixty standard cells in Arc2 and Arc4, are replaced with seven higher field cells. This is a compromise between the field strength and length of the tunnel in which multiple-bore combined magnets [4] can be employed since the three arcs are vertically stacked.

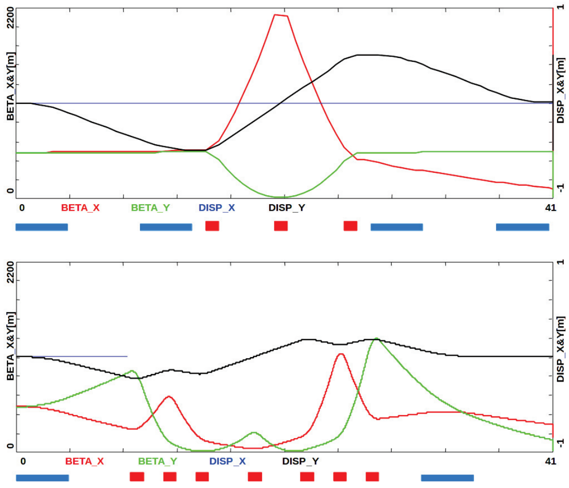

Figure 4: Optics functions for the two-steps vertical spreader (top) compared with the new design of a single-step spreader (bottom).

ISBN 978-3-95450-183-0

Figure 6 shows the Twiss functions at the beginning of Arc4. We chose to keep the same quadrupolar strengths in the junction and in the arc cells, this creates a little mismatch in the junction cells that is removed in the dispersion suppressor. In Arc2 the mismatch is more evident and it has been cured by adjusting the quadrupoles in the last junction cell and in the first regular cell.

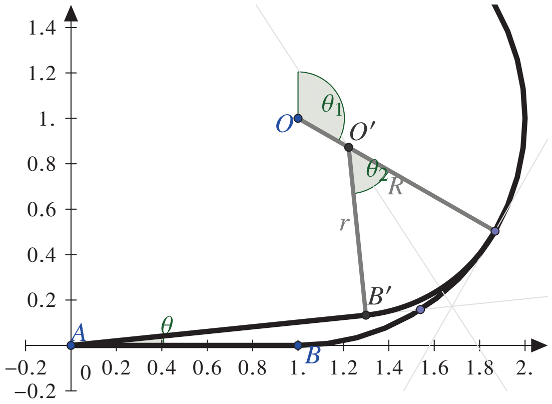

Figure 5: Scheme of the bypass geometry. The IP line, $\overline{AB}$, has been purposely stretched, being actually $\sim 1/5$ of the arc radius.

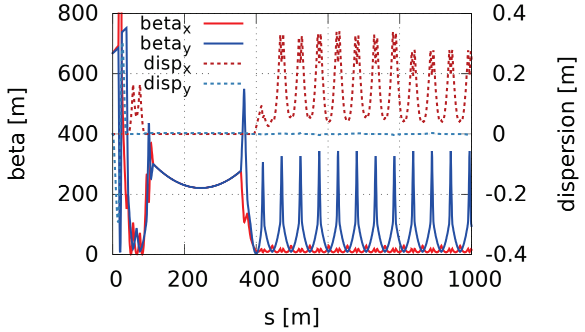

Figure 6: Beta functions and dispersion at the beginning of Arc4 with the detector bypass included. It features the vertical spreader, the initial horizontal bending, the straight section, the modified dispersion suppressor, seven junction cells, and four regular cells.

Compensating RF

The energy lost due to the synchrotron radiation has to be replenished into the beam so that at the entrance of each arc the accelerating and deceletating beams have the same energy. Compensating cavities are placed before the bending section of Arc1, Arc3 and Arc5 and after the bending section of Arc2, Arc4 and Arc6. As shown in Fig. 7, they employ the second harmonic RF frequency, so that each section can replenish the energy lost in the corresponding arc for both the accelerating and the decelerating beams.

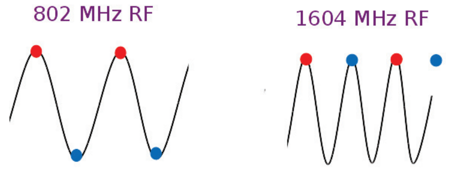

Figure 7: The second harmonic RF restores the energy loss both in the accelerating and decelerating passages.

TRACKING SIMULATIONS

The two linacs and the six arcs, properly connected together, have been imported in PLACET2 [5]. This code implements the recirculation in a realistic way. Each element is defined only once and its phase is computed accordingly to the beam time of flight. The beam-beam effect is computed by GUINEA-PIG [6]. It has been found that the synchrotron radiation has a big impact in the spreader and recombiner sections and in the doglegs for path length adjustments. For the time being, in order to proceed with this study, the above effects have been ignored. The second harmonic RF, required to re-integrate the synchrotron radiation energy loss, is currently modelled as a thin element.

Single-Bunch Tracking

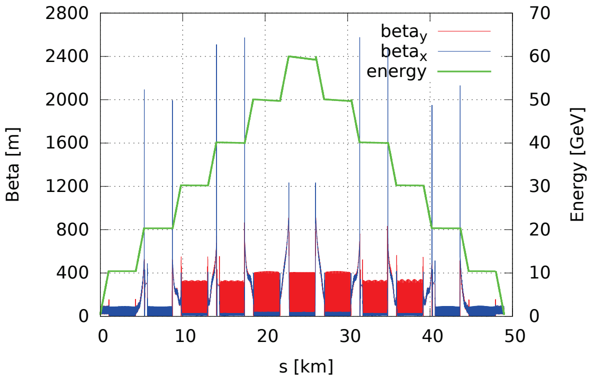

Figure 8: Beta functions and energy profile obtained following a bunch in the whole LHeC lattice.

The single bunch tracking allows to verify the beam transport. Figure 8 shows the Twiss parameters obtained following a bunch along its path along the whole machine. The linacs are easily identifiable by looking at the energy profile. In the arcs the energy stays almost constant, the only variation being caused by the synchrotron radiation. A small beta beating can be barely noted in the arcs: it is caused by the different model of the RF-focussing in the linacs between PLACET2 and OptiM, the program used for the matchings.

It is possible to note the different average values of the β functions in different arcs, deriving from their different tunings of the momentum compaction, as previously described.

The longitudinal phase space is shown in Fig. 9. It can be noted that while none of the arc is isochronous, their combined effects preserve the bunch length reducing the impact of the RF curvature. The beam parameters are summarised in Table 1 and Table 2 respectively at the IP and at the dump (after the deceleration). The beam is transported to the IP with a reasonable emittance growth. The impacts of beam-beam and SR in Arc6 are evident, but not detrimental to the deceleration. The beam envelop remains well within the aperture even at the end of the deceleration as shown in Fig. 10.

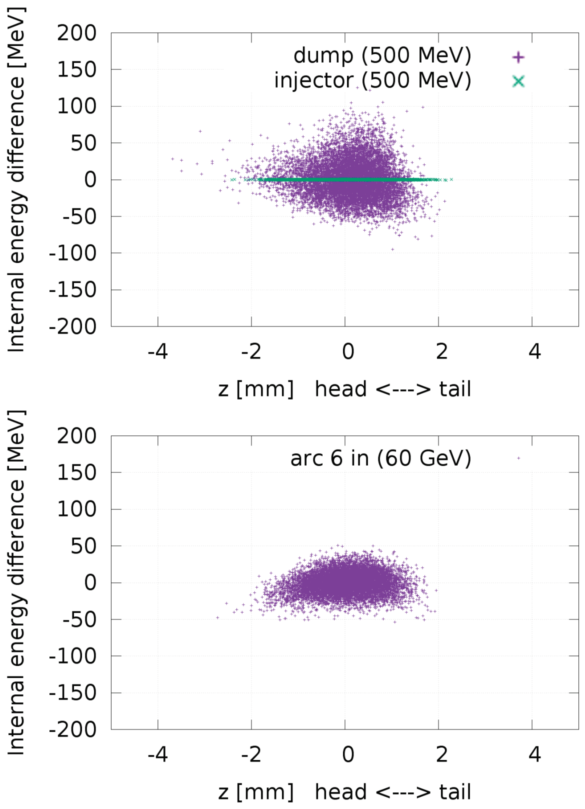

Figure 9: Longitudinal phase space at the injection and dump (top) and at the IP (bottom). The zero of the vertical axis is the value indicated in the key.

Table 1: Initial Beam Parameters Compared To The Ones At The IP In Presence Of Synchrotron Radiation

	initial/CDR	IP
ε_x [μm]	50	57.4
ε_y [μm]	50	50.8
δ	0.0020	0.0026
RMS x [μm]	7.20	7.66
RMS y [μm]	7.20	7.21
RMS z [mm]	0.600	0.601
RMS e [MeV]	1.00	15.4

Multi-Bunch Effects

PLACET2 allows to set up a train of bunches for tracking. It simultaneously propagates all the bunches in the machine preserving their time sequence in each beamline. This allows to compute multi-bunch effects even with complex lattice topologies. A model of transverse long-range wakefields (LRW) is currently implemented in PLACET2. LRW take place when a bunch passing through a cavity excites higher order modes (HOMs) of oscillation of the electromagnetic field; if the Q-value is big enough, the HOMs kick the subsequent bunches. High current and strong HOMs can establish a positive feedback leading to beam break up. The operation of the LHeC as an Higgs Factory requires high currents, up to 150 mA in the linacs [3], this posed a concern for the beam stability.

Table 2: Beam Parameters At The Dump, The Columns Shows The Values For SR Only, SR And Beam-Beam, SR And Beam-Beam With High-Lumi Parameters. The List Of Parameters Can Be Found In [3].

	Final SR	SR + BB	SR + BB-HL
ε_x [μm]	107	133	165
ε_y [μm]	87	125	158
δ	0.059	0.059	0.059
RMS x [mm]	1.52	1.67	1.86
RMS x’ [mrad]	0.08	0.09	0.10
RMS y [mm]	2.42	3.03	3.15
RMS y’ [mrad]	0.07	0.09	0.09
RMS z [mm]	0.66	0.66	0.66
RMS e [MeV]	29.7	29.5	29.6

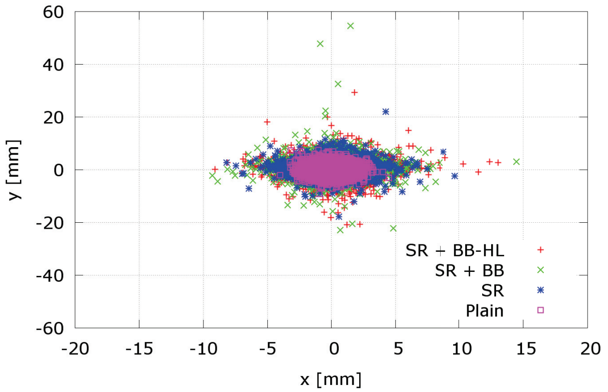

Figure 10: Beam transverse section at the end of the last linac, after the deceleration, including Synchrotron Radiation and Beam-Beam with standard and High Luminosity parameters. The beam contains 5000 macroparticles and the initial distribution is gaussian with no cuts.

For the multi-bunch simulation the same setup, as described before, was used. The tracking was performed using single particle bunches. The beam-beam computation GUINEA-PIG was substituted by an amplitude-dependent kick. The simplified beam-beam calculation overestimates the beam-beam effect as in reality the electrons oscillate around the proton beam and receive a smaller kick. The HOMs considered are the transverse dipole modes of the SPL cavity design, scaled to 802 MHz.

In order to evaluate the LRW impact the machine is completely filled with approximately 6000 single-particle bunches perfectly aligned. One misaligned bunch is then injected followed by many bunches again perfectly aligned. The perturbation introduced by the misaligned bunch is propagated to the others, as can be seen in Fig. 11. There are two important parameters: the slope of the tail, which determines if and how fast the perturbation is damped; and the F parameter that represents the total amplification of the beam action, defined as the squared sum of all the amplitudes [7]. This sum is convergent and mostly driven by the bunches that are close to the exciting one.

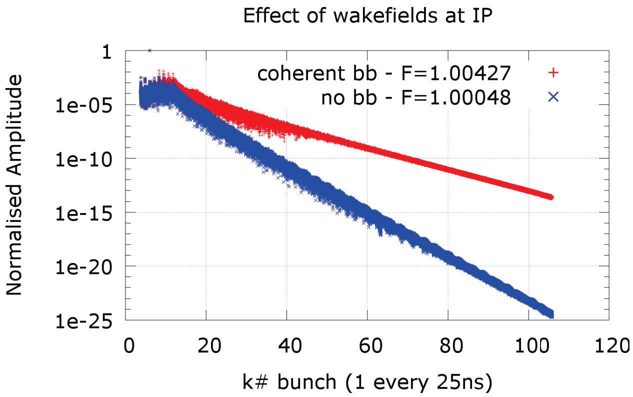

Figure 11: Normalised actions of the bunches at the IP. Only the bunch with action 1 carries an initial misalignment. All the other bunches are excited by LRW. Each bunch contains 4×10^9 electrons.

BUNCH RECOMBINATION PATTERN

The LHeC operation foresees continuous injection and multi-turn recirculation. In this scenario more bunches at different energies are interleaved in the linacs, appearing in periodic sequences. The spreader and recombiner design, employing fixed-field dipoles, do not pose timing constraints. This give us full control of the recombination pattern that can be selected adjusting the length of the return arcs to the required integer number of λ.

A good choice for the recombination pattern consists of almost equal spacing (compatibly with the RF) of the bunches in the RF buckets. In order to minimise the bunch cross talk is advantageous to maximise the separation between the bunches at the lowest energy: the ones at first and sixth turn. This is depicted in Fig. 12.

It has been verified that a pattern where bunches at first and sixth turn closely follow each other, reduces the BBU threshold current.

CONCLUSIONS AND OUTLOOK

The LHeC study is vigorously progressing both on the lattice design and on the beam dynamics simulations. In this paper we have reviewed the fundamental components of the LHeC lattice together with their optimisations. The machine layout, the linacs and the return arcs design have been summarised and new sections such as the detector bypass and the single-step spreader have been introduced.

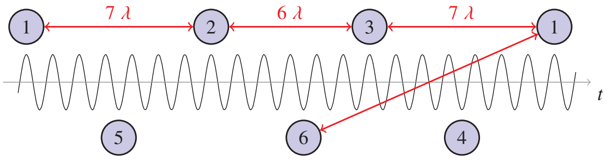

Figure 12: When the recirculation is in place, the linacs are populated with bunches at different turns (the turn number is indicated).

A comprehensive simulation has been setup using the newly developed tracking code: PLACET2. The impacts of synchrotron radiation, long-range wakefields and beam-beam effect have been evaluated and they are not detrimental for the deceleration. Investigation of cavity misalignment impact on beam trajectories has also been initiated.

The next major steps should target the full integration of the lattice with the interaction region. Realistic simulation of the ion cloud effect should also be performed. Furthermore detailed estimate of tolerances in terms of field quality and phase stability are required and may come with the experimental support of the CERN ERLF [8], currently in the design phase.

ACKNOWLEDGMENT

The authors would like to thank Edward Niessen for his help with the GUINEA-PIG computations of the beam-beam effect.

REFERENCES

[1] D. Pellegrini et al., “PLACET2: a Novel Code for Beam Dynamics in Recirculating Machines”, MOPJE068, Proceedings of IPAC’15, Richmond VA, USA (2015).

[2] J.L. Abelleira Fernandez et al., “LHeC Conceptual Design Report”, J. Phys. G: Nucl. Part. Phys. 39 075001 (2012).

[3] F. Zimmerman, O. Brüening, M. Klein, “The LHeC as a Higgs Boson Factory”, MOPWO054, IPAC’13, Shangai, China (2013).

[4] A. Milanese, “Warm magnets for LHeC / Test Facility arcs”, Talk at the LHeC workshop 2014, https://indico.cern. ch/ event/278903/session/6/contribution/41

[5] D. Pellegrini et al., “Single and Multi-bunch End-to-end Tracking in the LHeC”, MOPJE066, Proceedings of IPAC’15, Richmond VA, USA (2015).

[6] D. Schulte, “Beam-Beam Simulations with GUINEA-PIG“, ICAP’98, Monterey CA, USA (1998).

[7] D. Schulte, “Multi-Bunch Calculations in the CLIC Main Linac”, FR5RFP055, Proceedings of PAC09, Vancouver, BC, Canada.

[8] E. Jensen et al., “Design Study of an ERL Test Facility at CERN” TUOBA02, Proceedings of IPAC’14, Dresden, Ger-many (2014).

ISBN 978-3-95450-183-0

TRACKING STUDIES IN eRHIC ENERGY-RECOVERY RECIRCULATOR

F. Méot, S. Brooks, V. Ptitsyn, D. Trbojevic, N. Tsoupas
Collider-Accelerator Department, BNL, Upton, NY 11973

Abstract

This paper gives a brief overview of various beam and spin dynamics investigations undertaken in the framework of the design studies regarding the FFAG lattice based electron energy recovery re-circulator ring of the eRHIC electron-ion collider project.

INTRODUCTION

A Fixed Field Alternating Gradient (FFAG) doublet-cell version of the energy recovery recirculator of the eRHIC electron-ion collider [1] is being investigated [2, 3]. A pair of such FFAG rings placed along RHIC recirculate the electron beam through a 1.322 GeV linac (ERL), from respectively 1.3 to 6.6 GeV (5 beams) and 7.9 to 21.2 GeV (11 beams), and back down to injection energy. A spreader and a combiner are placed at the linac ends for proper orbit and 6-D matching, including time-of-flight adjustment.

FFAG LATTICE

The second, 11 beam, 21.2 GeV ring is considered in this discussion since it produces the major SR induced particle and spin dynamics perturbations. The cell is shown in Fig. 1, there are 138 such cells in each one of the 6 eRHIC arcs. The 6 long straight sections (LSS) use that very cell, with quadrupole axes aligned. In the twelve, 17-cell, dispersion suppressors (DS) the quadrupole axes slowly shift from their distance in the arc, to zero at the LSS.

Figure 2 shows the transverse excursion and magnetic field along orbits across the arc cell. Figure 3 shows the energy dependence of the deviation angle and curvature radius in the two quadrupoles, and the energy dependent tunes and chromaticities.

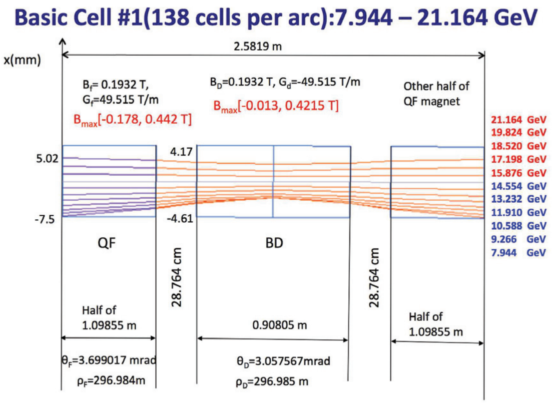

Figure 1 : Arc cell in the 7.944-21.16 GeV recirculating ring.

The y-precession of the spin over the six 138-cell arcs amounts to $6 \times 138 \times a\gamma\theta_{\rm cell} = a\gamma \times (2\pi - 0.688734)$ rad (with the difference to $a\gamma \times 2\pi$ corresponding to the contribution of the 12 DS), *i.e.*, from 18 precessions at 7.944 GeV to 48 at 21.164 GeV. ($a = 0.00116$ is the electron anomalous magnetic factor, γ the Lorentz relativistic factor).

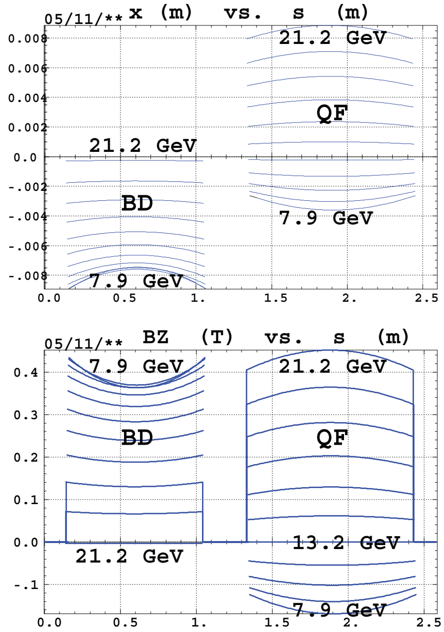

Figure 2: Transverse excursion in the quadrupole frame (hence artefact of trajectory discontinuity) (top) and hard-edged magnetic field (bottom) along the 11 orbits across the arc FFAG cell.

A Note on Dispersion Suppressors

The 12 dispersion suppressors are based on a “missing bend” scheme, where the relative displacement of the two cell quadrupoles (the origin of the dipole effect in the FFAG cell) is brought to zero over a series of cells. From orbit viewpoint, a quadrupole displacement is equivalent to a kick θ_k at entrance and exit [4] (see appendix).

Upon equivalent defect kicks due to the varying displacement of the quads (from their misalignment in the arc to aligned configuration in the straight) the orbit builds along the DS (with origin at upstream arc, end at downstream straight, or reverse) following

$$\frac{x_{\rm orb}(s)}{\sqrt{\beta(s)}} = \frac{x_{\rm orb}(0)}{\sqrt{\beta(0)}}\cos(\phi) + \qquad (1)$$

$$\frac{\alpha(0)x_{\rm orb}(0)+\beta(0)x'_{\rm orb}(0)}{\sqrt{\beta(0)}}\sin(\phi) + \sum_k \sqrt{\beta(s_k)}\theta_k\sin(\phi-\phi_k)$$

$$\frac{\alpha(s)x_{\rm orb}(s)+\beta(s)x'_{\rm orb}(s)}{\sqrt{\beta(s)}} = -\frac{x_{\rm orb}(0)}{\sqrt{\beta(0)}}\sin(\phi) +$$

ISBN 978-3-95450-183-0

$$\frac{\alpha(0)x_{\rm orb}(0)+\beta(0)x'_{\rm orb}(0)}{\sqrt{\beta(0)}}\cos(\phi)+\sum_k\sqrt{\beta(s_k)}\theta_k\cos(\phi-\phi_k)$$

with $x_{\rm orb}(0)$ and $x_{\rm orb}(0)$ the FFAG orbit coordinates in the arc→LSS case, while $x_{\rm orb}(0) = 0$, $x'_{\rm orb}(0) = 0$ in the LSS→arc case. Figure 4-top shows the orbit build-up from LLS to arc, ending up at the arc with (x,x') coordinates which do not *fully* coincide with the periodic orbit of the arc FFAG cell. The orbit build-up depends on the phase advance $\phi = \int_0^s \frac{ds}{\beta(s)}$, as a consequence it depends on cell tune, and thus on energy. Figure 4-middle shows the resulting orbit build-up in the arcs over 6 consecutive arcs at 5 different energies, 7.9, 9.3, 10.6, 11.9GeV and 13.2 GeV. In each case the starting coordinates (at $s = 0$ in the figure, *i.e.*, in the first LSS) are taken $(x, x') = (0, 0)$. Figure 4-bottom illustrates the tune dependence of the orbit amplification in the case of pass #4 - for simplicity energy is changed instead of tunes, with the correlation given in Fig. 3.

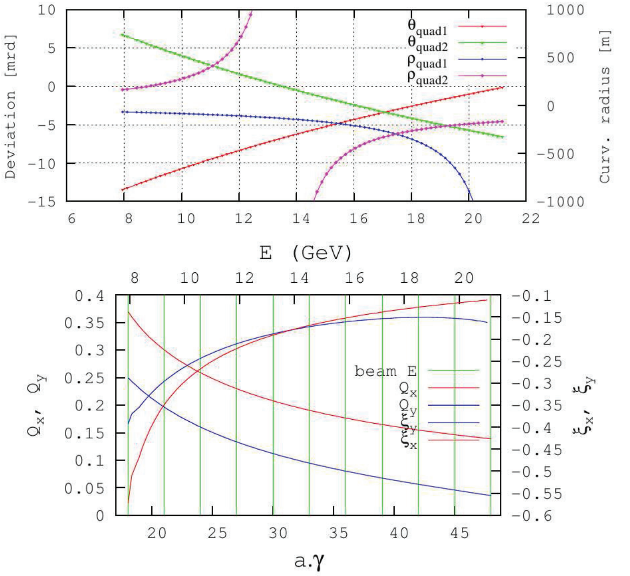

Figure 3: Top : energy dependence of deviation and curvature radius in arc cell quads. Bottom : cell tunes and chromaticities versus energy; the vertical bars materialize the 11 design energies.

SYNCHROTRON RADIATION

The SR induced energy loss relative to the the bunch centroid and the energy spread write, respectively

$$\frac{\overline{\Delta E}}{E_{\rm ref}} = 1.9\times10^{-15}\,\frac{\gamma^3\Delta\theta}{\rho},\quad \frac{\sigma_E}{E_{\rm ref}} = 3.8\times10^{-14}\,\frac{\gamma^{\frac{5}{2}}\sqrt{\Delta\theta}}{\rho} \tag{2}$$

with $\Delta\theta$ the arc length and $1/\rho$ the curvature, assumed constant. Taking for average radius, in the QF (focusing quad) and BD (defocusing quad) magnets respectively, $\rho_{\rm BD} \approx \frac{s_{\rm BD}}{\Delta\theta_{\rm BD}}$, $\rho_{\rm QF} \approx \frac{s_{\rm QF}}{\Delta\theta_{\rm QF}}$ (with $s_{\rm BD}$ and $s_{\rm QF}$ the arc lengths) and considering in addition, with $l_{\rm BD}$, $l_{\rm QF}$ the magnet lengths, $s_{\rm BD} \approx l_{\rm BD}$, $s_{\rm QF} \approx l_{\rm QF}$, and taking in addition $<(1/\rho)^2> \approx 1/<\rho^2>$, then one gets, per cell

$$\overline{\Delta E}[MeV] \approx 0.96\times10^{-15}\gamma^4\left(\frac{l_{\rm BD}}{\rho^2_{\rm BD}}+\frac{l_{\rm QF}}{\rho^2_{\rm QF}}\right) \tag{3}$$

$$\sigma_E \approx 1.94\times10^{-14}\gamma^{7/2}\sqrt{\frac{l_{\rm BD}}{|\rho^3_{\rm BD}|}+\frac{l_{\rm QF}}{|\rho^3_{\rm QF}|}}$$

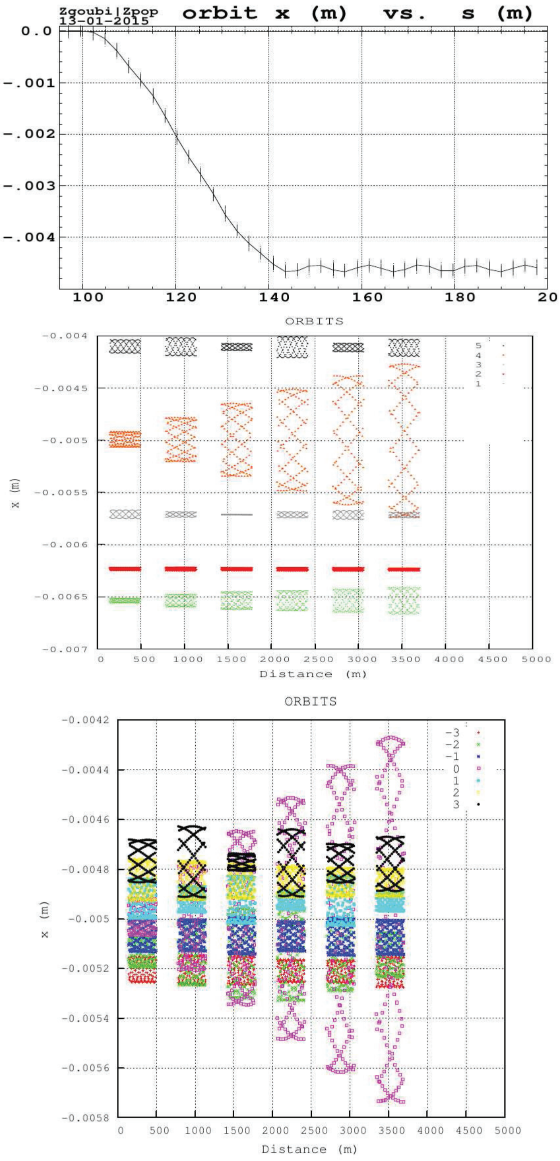

Figure 4: Top : Case of the 11.9GeV pass. The orbit is shown from end of first LSS to upstream region of first arc. Middle : Case of the 11.9GeV pass. The orbit is shown from end of first LSS (from where it starts with zero coordinates) to upstream region of first arc (140-200 m region). Bottom : The orbit is computed for 7 different energies $E + dE$ in the vicinity of $E = 11.9$GeV, namely for $dE/E = 0, \pm1, 2, 3\%$. The orbit build-up appears very small for $dE/E = 1\%$.

ISBN 978-3-95450-183-0

This is illustrated for a complete eRHIC turn (including LSS and DS sections) in Fig. 5, where it is also compared with Monte Carlo tracking, the agreement is at % level. The energy loss shows a local minimum in the $a\gamma = 30-35$ region, a different behavior from the classical γ^4 dependence in an isomagnetic lattice.

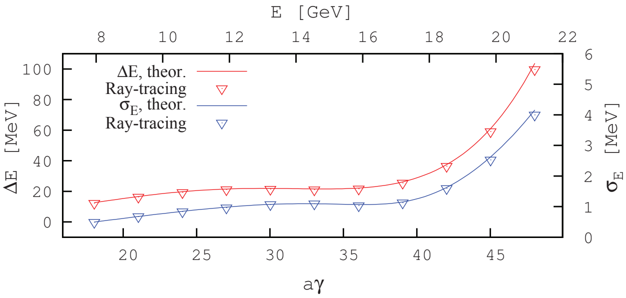

Figure 5: Energy loss and energy spread. Solid lines : theory (Eqs. 3) for a 6-arc ring. Markers : Monte Carlo, for a complete eRHIC ring (see sample tracking outcomes in Fig. 6).

The bunch lengthening over a $[s, s_f]$ distance, resulting from the stochastic energy loss, can be written [5],

$$\sigma_l = \left(\frac{\sigma_E}{E}\right)\left[\frac{1}{L_{\rm bend}}\int_s^{s_f}(D_x(s)T_{51}(s_f \leftarrow s)+ \right. \tag{4}$$

$$\left. D'_x(s)T_{52}(s_f \leftarrow s) - T_{56})^2\ ds\right]^{1/2}$$

with the integral being taken over the bends, D_x and D'_x the dispersion function and its derivative, T_{5i} the trajectory lengthening coefficient of the first order mapping ($i = 1, 5, 6$ stand for respectively x, δl, $\delta p/p$ coordinates).

The energy loss causes a drift of the bunch centroid, as well as an horizontal emittance increase, both can be computed from the lattice parameters in the linear approximation [5, 6, 7]. Figure 7 illustrates these effects over a 21.164 GeV recirculation (with bunch re-centering on the reference optical axis at each of the six LSS).

Cumulative effect of SR, over a complete 7.94→21.2→7.94 GeV cycle, is illustrated in Fig. 8 : (i) energy spread, $\sigma_E/E = 2.6\times10^{-4}$ at 21.1 GeV and $\sigma_E/E = 8.4\times10^{-4}$ back at 7.944 GeV ; (ii) bunch lengthening, $\sigma_l = 2$ mm at 21.1 GeV and $\sigma_l = 2.5$ mm back down to 7.944 GeV ; (iii) normalized horizontal emittance (from zero starting value), namely, $\epsilon_x = 20\ \mu$m at 21.1 GeV (with strong contribution from uncompensated chromatic effects), and $\epsilon_x = 8\ \mu$m back at 7.944 GeV.

Acceptance

The naturally large dynamical acceptance of the linear lattice shrinks with magnet alignment and field defects, this is illustrated in Fig. 9. SR is off in these DA computations, SR causes emittance growth thus reducing the space available for the beam at injection into a recirculation.

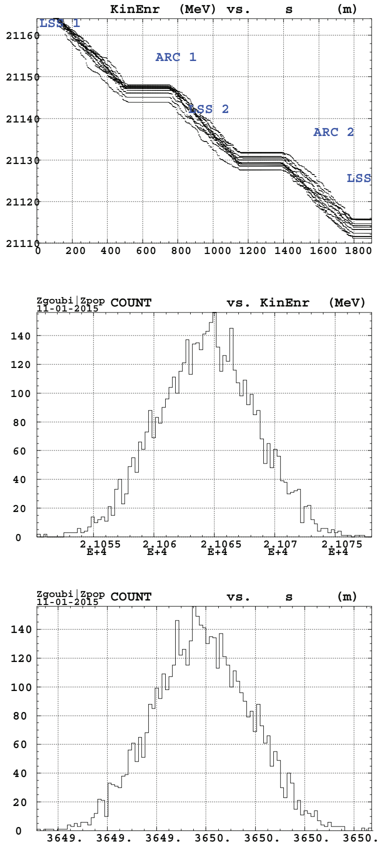

Figure 6: Top : stochastic energy decrease of a few particles over the first 3 arcs at$E_{\rm ref}$= 21.164 GeV. Middle: final spread a 5000 particle bunch after the 21.164 GeV pass, $\frac{\sigma_E}{E_{\rm ref}} = 1.9\times10^{-4}$ around $\frac{\Delta E}{E_{\rm ref}} = -4.7\times10^{-3}$ average energy loss (Eq. 2). Bottom : longitudinal bunch distribution (Eq. 4).

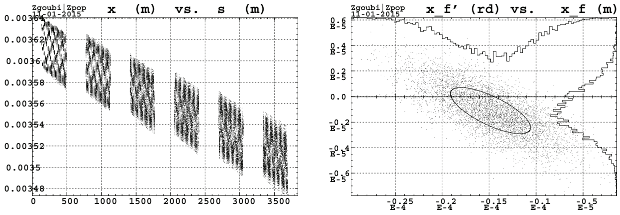

Figure 7: Left : SR loss induced x-drift along the 6 arcs, com-plete ring, $E = 21.164$ GeV, (shown are a few particles in a bunch launched on the LSS axis with zero initial 6-D emittance). Right : a 5000 particle bunch, horizontal phase space after that complete turn, featuring $\overline{x_f} = -15\ \mu$m, $\sigma_{x_f} = 4.3\ \mu$m, $\overline{x'}_f = -1.1.\ \mu$rad, $\sigma_{x'_f} = 1.8\ \mu$rad.

Multipole Defects

Figure 10 illustrates a different way of looking at tolerances, *e.g.* here in the presence of a dodecapole defect in all quadrupoles of the ring (*i.e.*, same working hypotheses as for the bottom Fig. 9) : a 5000-particle bunch is launched with $\epsilon_x \approx \epsilon_y \approx 50\,\pi\mu$m and 10^{-4} *rms* energy spread, for 21 circulations in a complete ring ($6\times\left[\frac{1}{2}{\rm LSS} - {\rm DS} - {\rm ARC} - {\rm DS} - \frac{1}{2}{\rm LSS}\right] + $ Linac).

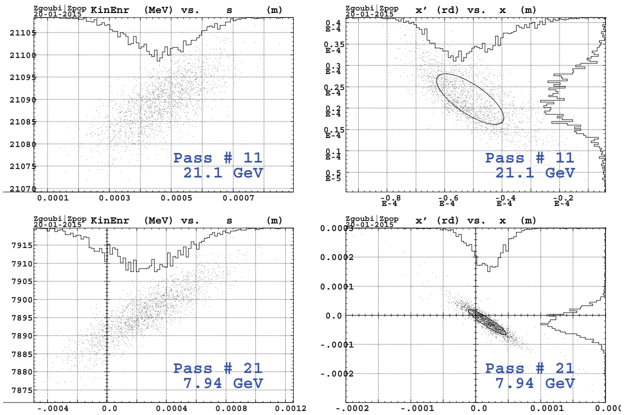

Figure 8: Cumulated effects of SR, in longitudinal (left) and radial (right) phase space, over 21 passes in eRHIC (from 7.944 GeV to 21.164 GeV, and back down to 7.944 GeV). Left plots : energy spread and bunch lengthening. Right plots : horizontal emittance growth

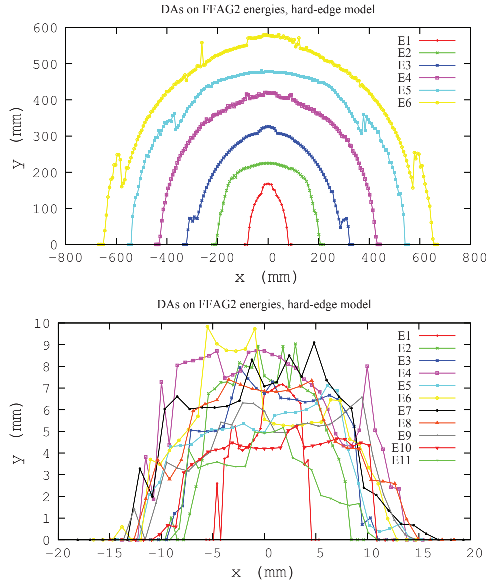

Figure 9: Available injection window into the ring at mid-LSS, for each of the 11 beams, observed at the center of an LSS. Top : defect-free lattice. Bottom : in the presence of dodecapole defect, ±3 Gauss at 1 cm, random uniform.

SR loss is summarily compensated at the linac, bunch position is assumed perfectly corrected at each LSS. Figure 10 shows the emittance evolution, pass after pass, from 7.94 to 21.16 and back to 7.94 GeV. This gives an indication of the maximum tolerable defect, depending on criteria of maximum tolerable emittance, *e.g.* at collision (pass 11) and/or extraction (pass 21).

POLARIZATION

Polarized electron bunch production is based on a Gatling gun, with a polarization of 85-90%. The electron bunch is re-circulated in eRHIC with longitudinal polarization. Spins precess at a rate $a\gamma$ per turn, with an increment of $a\Delta\gamma = 3$ at each 1.322 GeV linac boost, so ensuring the requested longitudinal spin orientation at the two IPs.

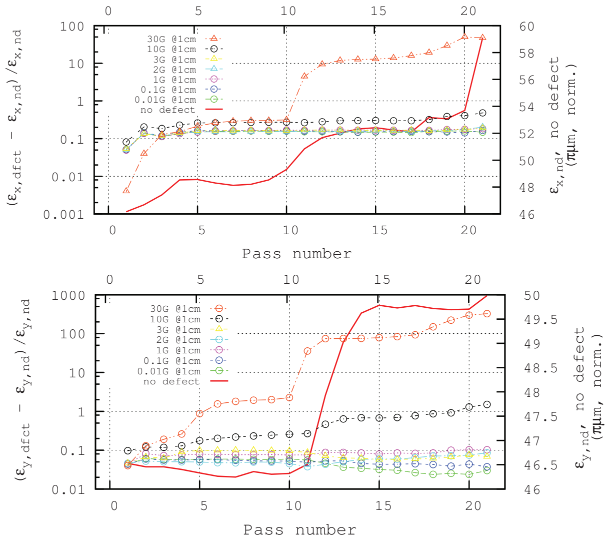

Figure 10: Pass-by-pass evolution of the emittances of a re-circulated bunch, for various dodecapole defect strengths (from 0, to 10 Gauss at 1 cm). Left axis and markers : defect cases. Right axis and red curve : defect-free ring. Top : horizontal, bottom : vertical emittances.

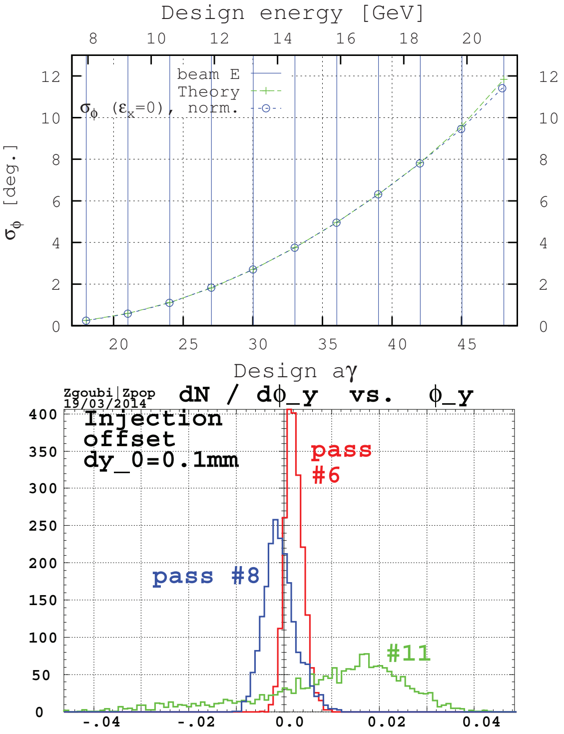

Figure 11: Polarization loss. Top : from energy spread, in-cluding theoretical expectation [8]. Bottom : vertical spin angle spread, in the presence of initial vertical beam jitter.

Depolarization mainly stems from energy spread (*e.g.*, a cumulated 2.5 10^{-4} at 21.2 GeV from SR contribution, see Fig. 8). Spin diffusion resulting from stochastic SR also causes polarization loss, of about 2% at 21.2 GeV. Non-zero vertical emittance, or vertical defects, cause spins to leave the median plane. This is illustrated in Fig. 11.

ISBN 978-3-95450-183-0

Figure 12 monitors the evolution of the polarization and of spin angle spreading, in the conditions of dodecapole error simulations discussed earlier ("Multipole defect" section and Fig. 10). Both quantities appear unchanged in this particular case, compared to the unperturbed optics (cf. σ_ϕ in Fig. 11-left).

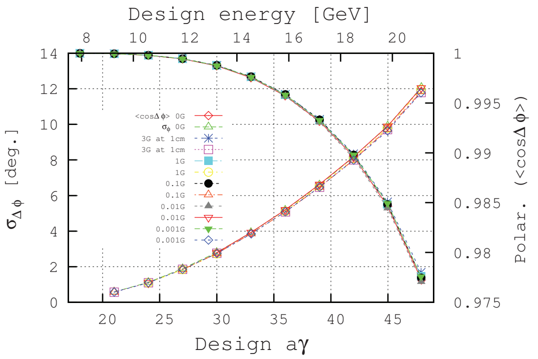

Figure 12: Polarization (right vertical axis) and spin angle spread (left axis) in the presence of dodecapole errors.

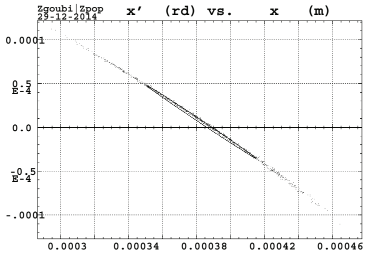

Figure 13: SR induced horizontal phase space portrait, for an initially zero 6-D emittance bunch, as acquired after an 11 GeV pass in the eRHIC ring.

CHROMATIC EFFECTS

Due to the large chromaticity (Fig. 3), any beam misalignment results in phase extent in phase space according to $\Delta\phi = 2\pi\xi\delta E/E$. SR is an intrinsic cause since it introduces both energy spread and beam shift [9], its effect is small however compared to nominal beam emittances, it is illustrated in Fig. 13 which shows the phase-space portrait acquired by a bunch launched with zero emittances and energy spread, after a single 11 GeV pass in the eRHIC ring, assuming a sub-millimeter beam misalignment in the DS regions. Note that here we introduce a measure (used in the following) of that chromaticity related effect in terms of the rms emittance, namely, *surface in phase space* $\epsilon_x = 4\pi\sqrt{<x^2><x'^2> - <xx'>^2}$ (same for (y, y') space), which is thus an *apparent* emittance, including momentum spread induced surface increase.

Since the chromaticity is not corrected in the eRHIC linear FFAG lattice, and given the natural beam energy spread σ_E/E in the 2×10^{-4} range, thus the emittance growth is prohibitive in the absence of orbit correction. This is illustrated, for the horizontal motion, in Fig. 14 which shows the phase space portraits of a 5000-particle bunch at the end of pass 11 (21.2 GeV, collision energy), and at the end of pass 21 (back to 7.944 GeV), whereas initial conditions at start, 7.944 GeV, were Gaussian *rms* $\epsilon_x \approx \epsilon_y \approx 50\,\pi\mu$m and $dE/E \in [-10^{-4}, +10^{-4}]$ (random uniform).

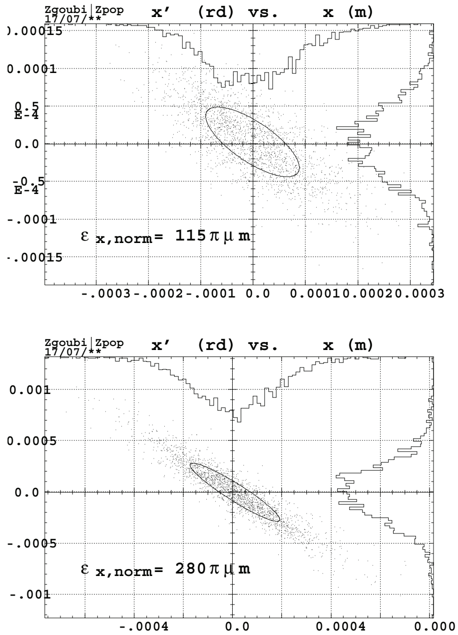

Figure 14: Horizontal phase space portrait of a bunch launched at 7.944 GeV with initial Gaussian *rms* $\epsilon_x \approx \epsilon_y \approx 50\,\pi\mu$m and $dE/E = 0$. Top : end of the 21.2 GeV pass (collision energy), bottom : end of the the decelerated 7.9 GeV last pass.

Fig. 15 summarizes the overall *apparent* emittance increase, over the 11 accelerated passes (from 7.944 to 21.16 GeV) followed by 10 decelerated passes (from 21.16 back to 7.944 GeV), for a bunch launched at 7.944 GeV with initial Gaussian *rms* $\epsilon_x \approx \epsilon_y \approx 50\,\pi\mu$m and $dE/E \in [-10^{-4}, +10^{-4}]$ (random uniform). In this simulation there is no vertical orbit defect whereas the bunch is (i) experiencing small misalignments in the dispersion suppressors that cause betatron oscillations in the mm range, and (ii) recentered on the theoretical reference orbit once per eRHIC turn, at the linac (*i.e.*, center of an LSS). Bunch distortion in phase space (similar to what is observed in Fig. 13) is at the origin of the steps (local apparent emittance increase) in the region $a\gamma \approx 27$ on the accelerating phase and $a\gamma \approx 38, 28$ on the decelerating phase.

Figure 16 shows the much reduced emittance growth in the presence of orbit control, namely here, bunch recentering at each LSS.

Figure 17 is obtained in the case of a vertical orbit defect caused by a small dipole error $a_0 \in [-1, +1]$Gauss, random uniform, injected in all the quadrupoles of the ring. The bunch in this case is recentered at the linac, in both transverse planes, at each turn.

Figure 18 displays the evolution of the polarization (the projection, $\cos(\Delta\phi)$, of the 5000 spins on the average spin direction) and of the spin angle spread σ_ϕ, in the previ-

ISBN 978-3-95450-183-0

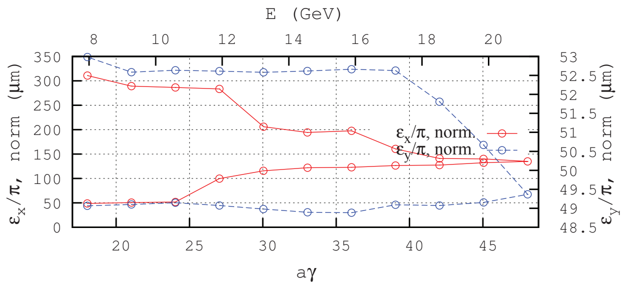

Figure 15: Emittances after each turn. The bunch is recentered once per turn, at the linac.

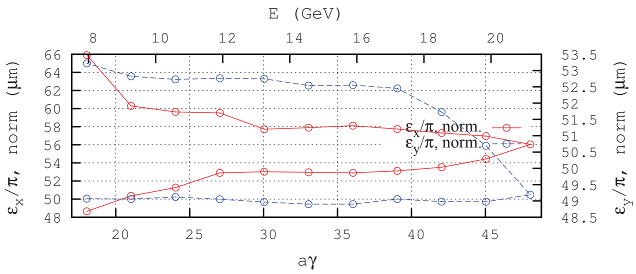

Figure 16: Emittances after each turn. The bunch is recentered at each of the six LSS.

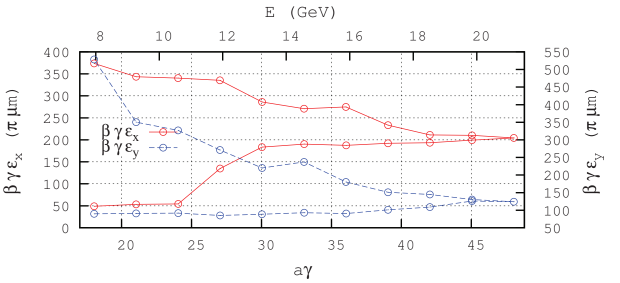

Figure 17: Evolution of the emittances in the presence of vertical orbit defect. Bunch recentered at linac only.

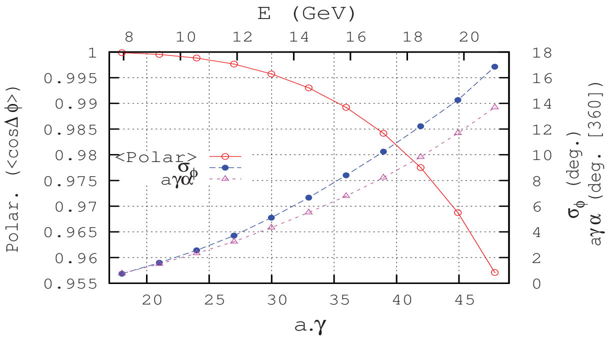

Figure 18: Polarization, spin angle spreading, precession, in the conditions of Figs. 15, 16.

ous conditions of orbit defects : the polarization appears marginally sensible to misalignment effects of this nature and at this level. Note that the number of precessions ($a\gamma$, right vertical axis) slightly differs from an integer value, this is just an indication of a residual effect in the present rough compensation of SR energy loss.

MULTIPLE-BEAM ORBIT CORRECTION

A first approach to multiple-beam orbit correction uses a matching procedure, in which the theoretical FFAG orbit is imposed on the bunch centroid in the arcs, for each energy. The constraint is imposed every 23 cells, this makes 6 such sections to be corrected in a 138 cell arc. That allows 23 variables (H-correctors at quadrupoles) for 22 constraints (x and x' for each one of the 11 energies, in one go). A 50 particle bunch is considered for the matching.

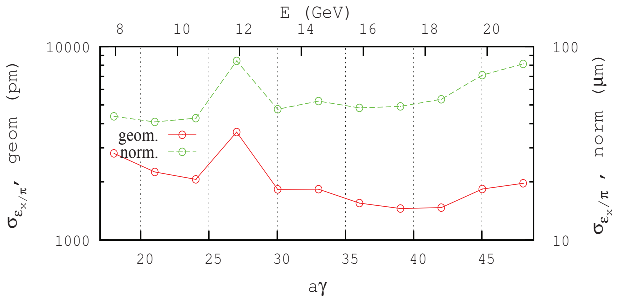

Figure 19: Turn-by-turn evolution of emittances, in the presence of a *corrected* $b_0 \in [-20, +20]$Gauss random defect.

As an illustration, a strong horizontal orbit defect is injected in the arc quadrupoles, namely, a vertical dipole error $b_0 \in [-20, +20]$Gauss (equivalent to misalignment $\Delta x = \pm 40\,\mu$m), random uniform. As a consequence the emittance growth in the absence of correction would be far beyond even what the earlier Fig. 15 shows. Figure 19 displays the evolution of the horizontal emittance after applying that orbit correction scheme in the arcs (orbit correction uses dipole correctors located in drifts between quadrupoles), given initial conditions, at 7.944 GeV, $\epsilon_x \approx \epsilon_y \approx 50\,\pi\mu$m and $dE/E = 0$. This result is promising (the surge at $a\gamma \approx 27$ is again an *apparent* emittance increase resulting from a surge in bunch off-centering at that particular pass/energy in the eRHIC ring).

An option in this method is to apply the constraint cell after cell, in a running mode all around the ring (in both planes in addition, in the presence of both horizontal and vertical multipole defects), until the residual orbit causes tolerable residual emittance growth.

A different type of constraint, rather than the theoretical FFAG orbits, is to request minimal bunch oscillation amplitude in the cells, leaving the average orbit free. This would have the merit of allowing a self-adjustment of the FFAG orbit on the actual bunch centroid energy (which is not the design one, due to SR for instance). This is an on-going study.

APPENDIX

CLOSED ORBIT DEFECTS

Dipolar type of errors due to magnet misalignments and dipole field defects, can be approximated by pairs of identical entrance/exit kicks [4], recalled in Tab. 1, such that

$\theta_{en}/\theta_{ex} = \Delta(Bl)/B\rho$, with $\Delta(Bl)$ representing the effect of the imperfection.

Table 1: Defect Equivalent Closed Orbit Kicks

	Formulas$^{(a)}$
Horizontal c.o.	
Dipole H kicks	
$\theta/\delta L/L$	$-\theta/(2\cos(\theta/2))$
$\theta/\delta B/B$	$-\tan(\theta/2)$
$\theta/\delta x$	$\sin(\theta/2-\alpha)/(\rho\cos(\alpha))$
$\theta/\delta s$	$\pm\cos(\theta/2-\alpha)/(\rho\cos(\alpha))$
θ/ϕ_z	$\mp\sin(\theta/2)\sin(\theta/2-\alpha)/\cos(\alpha)$
Quad H kicks	
$\theta/\delta x_F$	$K_F^{\frac{1}{2}}\tan(LK_F^{\frac{1}{2}}/2)$
$\theta/\delta x_D$	$-\lvert K_D\rvert^{\frac{1}{2}}\mathrm{th}(L\lvert K_D\rvert^{\frac{1}{2}}/2)$
θ/ϕ_{z_F}	$\pm(LK_F^{\frac{1}{2}}/2/\tan(LK_F^{\frac{1}{2}}/2)-1)$
θ/ϕ_{z_D}	$\pm(L\lvert K_D\rvert^{\frac{1}{2}}/2/\mathrm{th}(L\lvert K_D\rvert^{\frac{1}{2}}/2)-1)$
Vertical c.o.	
Dipole V kicks	
$\theta/\delta z$	$\tan\alpha/\rho$
θ/ϕ_x	$\sin(\theta/2)/\theta/2-\cos(\theta/2-\alpha)\cos\alpha$
θ/ϕ_s	$\sin(\theta/2)$
Quad V kicks	
$\theta/\delta z_F$	$-K_F^{\frac{1}{2}}\mathrm{th}(LK_F^{\frac{1}{2}}/2)$
$\theta/\delta z_D$	$\lvert K_D\rvert^{\frac{1}{2}}\tan(L\lvert K_D\rvert^{\frac{1}{2}}/2)$
θ/ϕ_{x_F}	$\pm(L(K_F)^{\frac{1}{2}}/2/\mathrm{th}(LK_F^{\frac{1}{2}}/2)-1)$
θ/ϕ_{x_D}	$\pm(L\lvert K_D\rvert^{\frac{1}{2}}/2/\tan(L\lvert K_D\rvert^{\frac{1}{2}}/2)-1)$

(a) ∓ and ± stand for entrance/exit kick signs, otherwise identical.

(b) Calculated for extreme values K=0.1 m^{-2} and length=1 m.

REFERENCES

[1] E.C. Aschenauer et als., “eRHIC Design Study, Electron-Ion Collider at BNL”, arXiv:1409.1633, Sept. 2014.

[2] D. Trbojevic, FFAG Lattice Design of eRHIC and LHeC, EIC 2014 workshop, Newport News (17-21 March 2014).

[3] D. Trbojevic et al., ERL with non-scaling fixed field alternating gradient lattice for eRHIC, IPAC15 Conf. Procs. (Richmond, 2015).

[4] D. Poirier, Etude des défauts de champ magnétiques de MIMAS et correction de la chromaticité de Super-ACO, PhD Thesis, Orsay, 1984.

[5] G. Leleux et al., Synchrotron radiation perturbation in transport lines, Part. Acc. Conf., San Francisco, May 6-9, 1991.

[6] https://oraweb.cern.ch/pls/hhh/code_website.disp_code?code_name=BETA

[7] F. Méot, J. Payet, Simulation of SR loss in high energy transport lines, Rep. CEA DSM DAPNIA/SEA-00-01 (2000).

[8] V. Ptitsyn, Electron Polarization Dynamics in eRHIC, EIC 14 workshop, JLab, 17-21/03/2014.

[9] F. Méot et al., End-to-end 9-D polarized bunch transport in eRHIC, IPAC15 Conf. Procs. (Richmond, 2015).

IMPROVING THE SMOOTHNESS OF MULTIALKALI ANTIMONIDE PHOTOCATHODES: AN IN-SITU X-RAY REFLECTIVITY STUDY

Z. Ding, E. Muller, Stony Brook University, Stony Brook, NY, 11794, USA
J. Xie, ANL, Lemont, IL 60439, USA
K. Attenkofer, M. Gaowei, J. Sinsheimer, J. Smedley, J. Walsh, BNL, Upton, NY, 11973, USA
J. Kuhn, Helmholtz-Zentrum Berlin, Berlin, 12489, Germany
S. Schubert, J. Wong, H. Padmore, LBNL, Berkeley, CA, 94720, USA
H. Frisch, University of Chicago, Chicago, IL, 60637, USA

Abstract

Multialkali antimonide photocathodes have been shown to be excellent electron sources for a wide range of applications because of high quantum efficiency, low emittance, good lifetime, and fast response. In recent years, synchrotron X-ray methods have been used to study the growth mechanism of K_2CsSb photocathodes. The traditional sequential growth of K_2CsSb has been shown to result in rough surface, which will have an adverse impact on the emittance of the electron beam. However, co-evaporation of alkali metals on the evaporated Sb layer and sputter deposition may offer a route to solving the roughness problem. Recent studies on K_2CsSb grown by these methods are presented and surface roughness is determined by X-ray reflectivity (XRR) and results are compared.

INTRODUCTION

During recent years, numerous studies have been carried out on the K_2CsSb photocathode as a promising candidate for high quality electron sources [1, 2]. The traditional growth method is to sequentially evaporate Sb, K and Cs onto the substrate. In-situ X-ray analysis on photocathodes grown by this traditional recipe indicates that the surface roughness to be ~ 25 nm rms for a 50 nm thick cathode [2], however a photocathode with this roughness would impact the intrinsic emittance in the high gradient fields used in most applications [3]. Studies have shown that for an emission field of 20 MV/m a roughness of less than 1 nm is required [4].

Previous studies have revealed the growth mechanism of the traditionally grown K_2CsSb photocathode [5, 6]. The evolution of crystalline Sb layer to a K-Sb compound and then to a crystalline K_3Sb significantly increases the roughness from the sub nm scale to more than 10 nm. In order to improve this process, we have developed a method in which multiple thin layers of the antimonide are grown. Sb is deposited in thickness that prevents the formation of crystalline antimony, followed by sequential evaporation of K and Cs [6].

In this work, X-ray reflectivity analysis on photocathodes grown by this method as well as two new approaches, co-evaporation of K and Cs and sputter deposition, will be discussed in details.

EXPERIMENTAL

In-situ synchrotron X-ray growth studies of K_2CsSb photocathodes were carried out at beam line G3, on the Cornell High Energy Synchrotron Source (CHESS), using a photon energy of 11.26 keV. Two Pilatus 100K pixel detectors were installed on the growth system and a Vortex detector was placed about 18 cm away from the sample, so that X-ray reflectivity (XRR), wide angle X-ray diffraction (WAXD), X-ray diffraction (XRD) and X-ray fluorescence (XRF) can be measured during the growth. The base pressure of the chamber during cathode growth was kept in the low 10^{-10} Torr range and partial pressure of water and oxygen were in the low 10^{-11} Torr range. A quartz crystal microbalance (QCM) was positioned alongside the sample holder, and the growth rate of all materials set controlled to be 0.2 Å/s. The temperature of the sample was kept at approximately 110℃.

The XRR data is fitted by the refinement program GenX [7], which uses Parratt's recursion and adopts the Nevot-Croce model for the calculation of roughness [8].

Sequential Evaporation

For sequential evaporation experiments, a first layer of 3nm Sb was deposited on a Si substrate, followed by K deposition until the photocurrent maximized. Cs was deposited finally to maximize the photocurrent. A second layer of 5nm Sb was deposited afterwards and the deposition of K and Cs was repeated. X-ray reflectivity analysis was done on the substrate and after each evaporation. Further details can be found in [6].

ISBN 978-3-95450-183-0

Co-evaporation

For co-evaporation experiments, a first layer of 1.5nm Sb, according to QCM, was deposited on the MgO substrate, K and Cs were then co-evaporated onto the Sb layer until the photocurrent reached a maximum. A second layer of Sb followed by co-evaporation of K and Cs was repeated. A final photocathode of 6 layers in total was grown.

Sputter Deposition

A radio-frequency (RF) sputter system was installed in the growth chamber. The K_2CsSb target was synthesized at Radiation Monitoring Devices (RMD), Inc. The detailed description of the sputter experiment can be found in [4]. Sputter deposition was carried out on MgO substrates, grown in 3 layers for a total thickness of 30 nm (sample F009) and on a Si substrate, where the film was grown in one layer of 30 nm thick (sample F010), with final Cs deposition on both samples.

RESULTS

Sequential Evaporation

XRR simulation result for the sample grown by sequential evaporation is shown in Fig. 1 (left). The Si substrate has a roughness determined by fitting the simulation model of 3.1 Å. The first evaporation of Sb has a thickness of 35 Å and a roughness of 2.9 Å. The next step of K evaporation results in a 141 Å thick layer which has 10.5 Å roughness due to the recrystallization process. The cesiation process produces a photocathode that is 5 times as thick as the Sb layer. The fitted roughness for the first layer of cathode is 13.2 Å.

XRR analysis on the final photocathode reveals that the thickness is 469 Å and the roughness is 32 Å, which is approximately an order of magnitude lower than that of the traditionally grown sequential photocathodes. The quantum efficiency at the 532 nm wavelength is measured to be 4.9%.

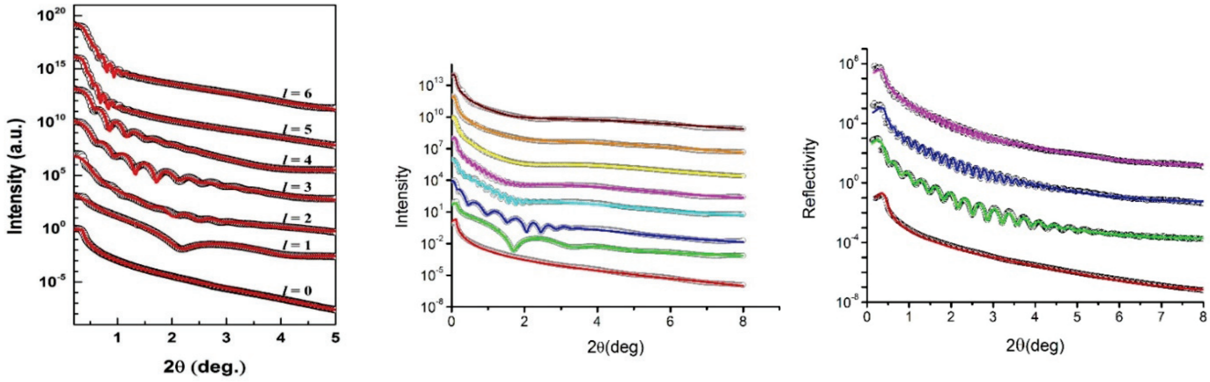

Figure 1: XRR fitting results, simulations are fitted to experimental data. Open circles stand for measured data; Colored curves stand for simulation. Left: Sequential evaporation; Middle: Co-evaporation; Right: Sputter deposition (F009).

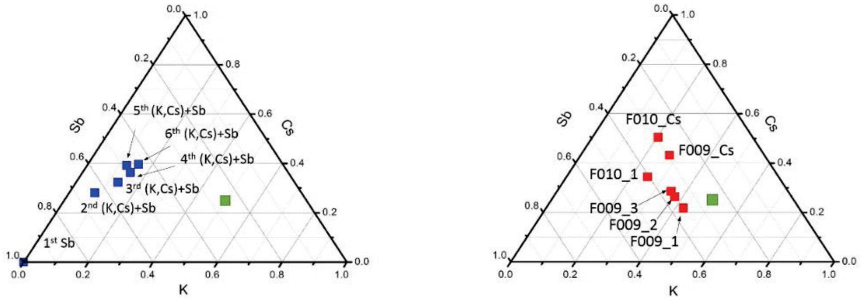

Figure 2: Calculated stoichiometry of each layer of the photocathodes. Left: Co-evaporation sample; Right: Sputtered sample.

Co-evaporation

With the real-time stoichiometry taken into account, the XRR data can be precisely fitted and the result is shown in Fig. 1 (middle). Figure 2 (left) shows the calculated stoichiometry for each layer of the co-evaporation cathode. For the final cathode, more than enough Sb has been deposited while the amount of K remains deficient while compared to the standard K_2CsSb marked green in the figure.

The first Sb layer shows a thickness of 36.7 Å and 5.2 Å roughness. After evaporating K and Cs, the thickness increases to 159.3 Å and the roughness rises to 9.22 Å. As the growth continues, the surface roughness of this photocathode roughly stays at around 10 Å, while the thickness increases to 489 Å after three layers have been deposited. Further evaporation of Sb and co-evaporation of alkalis doesn't improve the QE substantially and results in a final photocathode with a thickness of 725 Å and 24.9 Å roughness. The final QE at a wavelength of 532 nm is 4.5 %.

Sputter Deposition

The fitted XRR data with stoichiometry taken into account is shown in Fig 1 (right). From the calculated stoichiometry for sputtered cathode shown in Fig. 2 (right) it can be concluded that the sputtered cathode is slightly deficient in K compared to the standard stoichiometry. It can be observed from the curve that the surface roughness become relatively small as demonstrated by the fact that there are intensity oscillations up to a very high angle, showing the coherence of the substrate and surface interfaces . The surface roughness for sample F009 after 3 layers of sputtering is about 6.87 Å and the thickness is fitted to be 512 Å. XRR fitting result on sample F010 after Cs deposition reveals that the surface roughness is about 7.56 Å, with a final thickness of 776 Å. The simulated electron density which is related to the model used for the best fit indicates that the sputtered layer has a uniform density. The spectral response measurement for two sputtered cathode shows the quantum efficiency of both cathodes is approximately 1% at 532 nm wavelength. Figure 3 shows the comparison of surface roughness vs. thickness between photocathodes grown by these three growth methods.

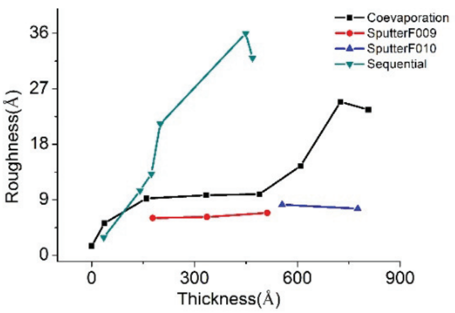

Figure 3: Comparison of surface roughness vs. thickness between photocathodes grown by sequential evaporation, co-evaporation and sputter deposition.

CONCLUSION

In order to produce a CsK_2Sb photocathode with high quantum efficiency and a smooth surface, it is essential to prevent the initial Sb layer from crystallization. The photocathode grown by alternating deposition of a thin Sb layer and alkali metals has been verified to result in a smoother surface than obtained by sequential deposition. A series of experiments on alternating deposition of Sb followed by sequential evaporation and co-evaporation of alkali metals have been carried out. XRR analysis show that surface roughness of these photocathodes is approximately an order of magnitude lower than sequentially produced photocathodes, with acceptable quantum efficiency of about 4% at 532 nm wavelength.

Sputter deposition can result in an even smoother photocathode with sub nm surface roughness according to the XRR analysis but with a lower quantum efficiency of 1% at 532 nm wavelength due to loss of K.

ACKNOWLEDGMENT

The authors would like to thank John Walsh (BNL) for his continuous technical support and Arthur Woll as well as other CHESS staff for their prompt beam line assistance.

REFERENCES

[1] A. H. Sommer, Photoemissive Materials: Preparation, Properties and Use (John Wiley & Sons Inc., 1969).
[2] T. Vecchione et al., APL, vol 99, 034103, 2011.
[3] S. Schubert et al., APL Materials 1, 032119 (2013).
[4] T. Vecchione et al., Proc. of IPAC12, 655 (2012).
[5] J. Smedley et al., "Sputter growth of alkali antimonide photocathodes: an in-operando materials analysis", IPAC'15, Richmond, USA (2015).
[6] M. Ruiz-Osés et al., APL Materials 2, 121101 (2014).
[7] J. Xie et al., "Synchrotron X-ray study for a low roughness and high efficiency K_2CsSb photocathode during film growth", manuscript submitted, (2015).
[8] J. Appl. Cryst. (2007). 40, 1174–1178.

ISBN 978-3-95450-183-0

INVESTIGATIONS ON TRANSVERSE BEAM BREAK UP USING A RECIRCULATED ELECTRON BEAM*

T. Kürzeder#, M. Arnold, M. Gros, F. Hug, L. Jürgensen, J. Pforr, N. Pietralla
TU Darmstadt, Darmstadt, Germany

Abstract

The recirculating superconducting accelerator S-DALINAC provides electron beams of up to 130 MeV for nuclear physics experiments at the University of Darmstadt since 1991. It consists of a 10 MeV injector and a 40 MeV main linac and reaches its final design energy using up to two recirculation paths. The superconducting main linac houses eight 20-cell SRF cavities operated at 3 GHz and 2 K. The very low threshold current of only a few µA for the occurrence of beam break up in addition with the recirculating linac design gives a unique opportunity to the ERL community for testing different strategies of avoiding beam break up experimentally at this accelerator and to benchmark beam dynamics simulations concerning this topic. To minimize the impact of HOMs on the recirculating electron bunches we will place skew quadrupole and sextupole magnets in our accelerator and test their effect on the threshold current. We will report on the status of beam dynamics simulations concerning their use in the accelerator and present actual calculations for the positioning of the skew quadrupoles. An outlook on the future activities at the S-DALINAC will be given.

INTRODUCTION

Transverse beam break up (BBU) is one of the main problems of modern superconducting energy recovery linacs. A theory of BBU instability in ERLs was shown in [1]. It occurs when an electron bunch travelling through an accelerating cavity excites higher order dipole modes (HOM) in it. These HOMs can have a large quality factor and thus a long lifetime in superconducting cavities. The bunch will be deflected by the electro-magnetic field of the mode. In a recirculating design this gets even worse as the same bunch can be deflected by the same HOM in the same direction. Thereby the maximum beam current which can be transported and accelerated is limited in every recirculating linac. This limit is called the BBU threshold current. For ERLs worldwide which are planned or already under constructions this is a crucial parameter as they yield for beam currents of 10-100 mA and above.

On the contrary in early SRF linacs only a few µA of beam current were possible because of BBU [2,3]. Also the S-DALINAC [4] is limited in its beam current when operated in recirculating mode. The highest stable current achieved so far in a long term experiment accounts for 5 µA [5], which was well below the design value of 20 µA but convenient for the experiments carried out. The low threshold currents at the S-DALINAC allow to carry out experiments on transverse beam break up without the risk of damaging the accelerator.

S-DALINAC

The Superconducting Darmstadt LINear Accelerator (S-DALINAC) provides electron beams for nuclear- and astrophysical experiments at the University of Darmstadt. It consists of a superconducting 10 MeV injector and a 40 MeV linac. With two recirculation beam lines the main linac can be used up to 3 times. As electron sources a thermionic and a photo gun, which can also produce polarized electrons [6], can be chosen. This layout was originally designed to provide beam energies of up to 130 MeV and beam currents of either 60 µA in single pass mode or 20 µA when recirculated twice. But as mentioned above, the design beam current in recirculating operation could not be achieved so far.

For acceleration of the beam twelve 20-cell SRF cavities are used on an operation frequency of 3 GHz. These cavities have been produced in the 1990s and have never been optimized with regard to HOM suppression. Furthermore no HOM couplers can be used as most HOMs are trapped within the middle cells of these long 20-cell cavities.

In August 2015 the installation of an additional recirculation beam line will begin and is scheduled to be finished in January 2016 [7]. A floor plan of the S-DALINAC is shown in Fig. 1. In the current setup with only two recirculations the power dissipated by the cavities to the helium bath was too high when used at maximum gradient as the quality factor of the cavities is smaller than originally planned [8]. The upgrade is done in order to reach the design energy of 130 MeV in c.w.-operation with a smaller accelerating gradient per cavity

BBU SUPPRESSION

Many efforts have been made and are still going on to raise the BBU threshold currents. There are two strategies to address the problem. As a basis, cavities of ERLs are designed to damp the higher order modes. Also HOM couplers will be used. The second approach is matching the optics of the beam transport system. We are planning to increase the low threshold current of the S-DALINAC by manipulating the beam optics in the recirculation loops.

Variation of the Transverse Phase Advance

In [9] it is proposed to match the transverse phase advance in an ERL in a way that a negative feedback of the HOM excitation is provided which can increase the

---

*Work supported by BMBF through 05K13RDA

#kuerzeder@ikp.tu-darmstadt.de

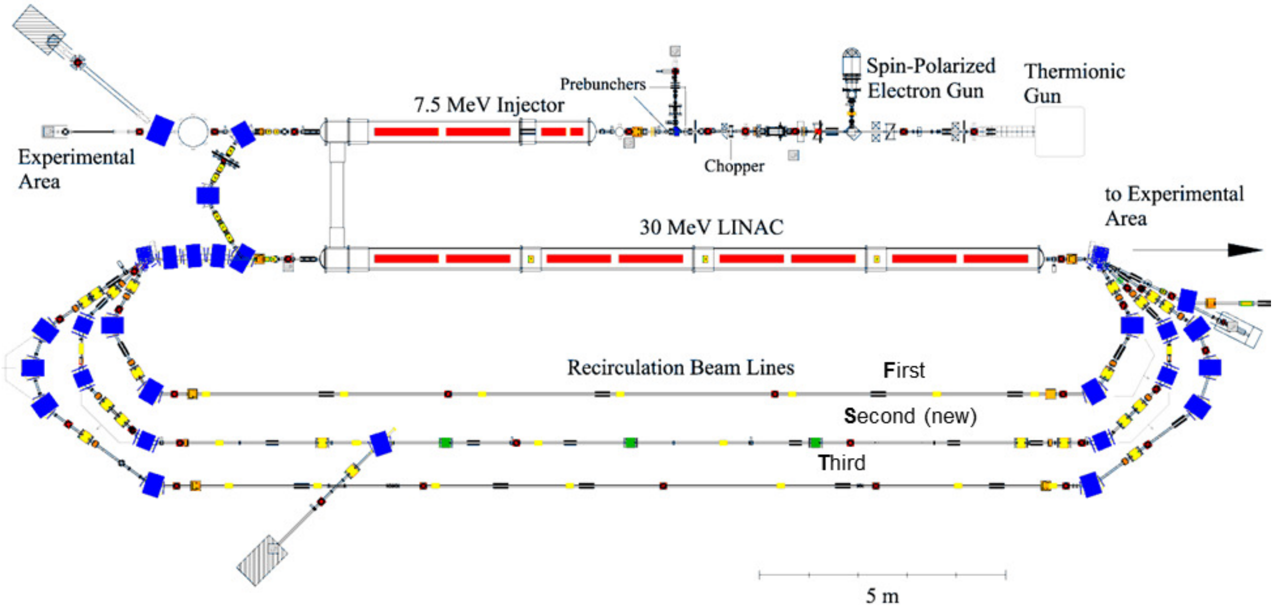

Figure 1: Floor plan of the S-DALINAC with planned upgrade. Skew quadrupole magnets are shown in green in the strait section of the new (Second) recirculation. Sextupoles will be positioned in the arcs (shown in orange)

threshold current. In addition simulations in [9] show that a coupling of the x and y planes of transverse motion could increase the threshold current even further.

We will test these approaches and try to reach for higher currents when running the S-DALINAC as a single or three times recirculating linac in 2016. The exchange of the complete phase space will be done in the second recirculation path. Therefore three skew quadrupole magnets need to be implemented in our FODO lattice. In order to achieve the exchange of vertical and horizontal phase spaces a 4x4 rotation matrix is needed.

Such a matrix can be calculated analytically like in [10]. For our case we chose a lattice, which fits best into our regular lattice. The three skew quadrupoles are distributed in a way that between half of their distance to each other respectively one conventional quadrupole (first focussing, second defocussing) will be positioned (SFSDS).

The positions of the skew quadrupoles are marked green in Fig.1. The analytical solution (thin lens approximation) for such a system [10] provides the refractive power for the skew quadrupoles of $\delta_s = 1/s\sqrt{2}$ and for the conventional quadrupoles of $\delta_{F/D} = \pm\sqrt{2}/s$. With a beam energy of 68.85 MeV and a drift of $s = 1.981$ m between each magnet's focal plane the gradients easily can be calculated to $G_s = 0.4184$ T/m and $G_{F/D} = \pm 1.4206$ T/m then. Finally a numerical optimization using the *elegant* code [11] has been carried out in order to find the exact values for the 5 magnets of the rotation system (see Table 1).

Table 1: Optimized Quadrupole Gradients for the Phase Space Rotation System

Focussing/Defocussing Quadrupoles	±1.082 T/m
Skew Quadrupole 1&3	0.4408 T/m
Skew Quadrupole 2	0.4347 T/m

The skew magnets have been manufactured already and are currently undergoing tests in the first recirculation of the S-DALINAC (see Fig. 2). They will be used for first experiments on BBU in summer 2015 and then be relocated to their optimized positions during installation of the new recirculation beamline.

Figure 2: Three skew quadrupole magnets in the first recirculation of the S-DALINAC. They will be relocated in the second loop in the described SFSDS lattice above.

Variation of Chromaticity

In [12] it is shown that a recirculation beam line with high enough chromaticity ξ let electrons "forget" the kick obtained by any dipole mode. The condition which has to be fulfilled for that behaviour is also given in [12]:

$$|\Delta E/E \cdot \xi| >> 1 \qquad (1)$$

With its typical energy spread $\Delta E/E$ of about 10^{-3} to 10^{-4} the natural chromaticity of <100 in the recirculation beam lines is not big enough to test this theory with the S-DALINAC. Therefore two sextupole magnets will be installed in each arc of a recirculation at positions of high dispersion in order to increase ξ. In total there will be 12 sextupoles (four per recirculation beam line).

ISBN 978-3-95450-183-0

The magnets were constructed from 1 mm sheets of mu-metal (see Fig. 3). The magnets with 35 windings per coil were tested in continuous operation showing no significant heating operated with 7 A. At that current the field gradient was determined to be 109 T/m^2 (see also Fig. 3). While the geometric length of the yoke amounts 7.5 cm the magnetic length was found to be 9 cm.

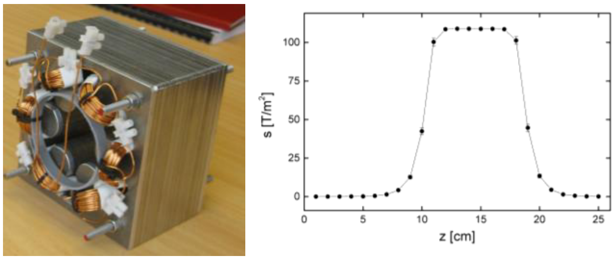

Figure 3: Photo of a sextupole magnet and results of a field gradient measurement on it.

So far simulations of the beam dynamics with the *elegant*-code [11] showed, that the sextupole magnets can increase the chromaticity per turn to values of 1000 and higher, when one uses a larger energy spread of $2.5 \cdot 10^{-3}$. Fulfilling the condition in [12] is thereby possible but nevertheless one has to watch carefully the emittance growth caused by such a setting [13,14]. In Figure 4 the envelope of the first recirculation beam line is shown with and without using the sextupole magnets in it.

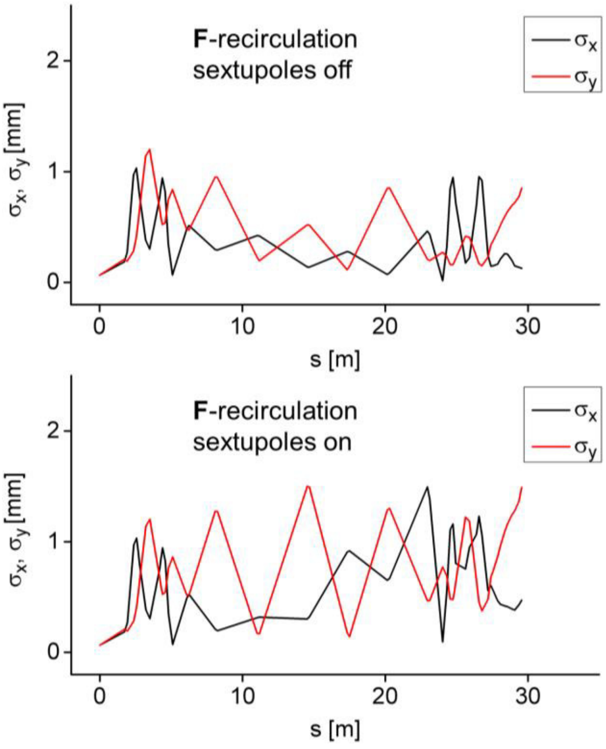

Figure 4: Beam envelope in x and y direction of the first recirculation beam line with sexupoles switched off and on (E = 38 MeV and ΔE/E = $2.5 \cdot 10^{-3}$).

The quadrupole magnets were set in a way, that they compensate already for negative effects caused by the sextupoles, while we tried to reach the needed chromaticities. In the shown example we got ξ_x and ξ_y of about 1000 but the emittance increased by a factor of 20 for ε_x and a factor 12 for ε_y. A proper beam transport gets challenging with an emittance growth like that. So far we think of testing the effect of chromaticity to the BBU threshold current by only recirculating once and then dump the beam or recirculate many times but only activate the sexupoles in a specific turn finding a setting which also provides a proper beam transport.

FUTURE ACTIVITIES

After testing the strategies for BBU suppression with the 3 times recirculated electron beam, we plan to commission the S-DALINAC as a single and double turn ERL. The major preparations for this are already done. Within the arcs of the new beamline, dipole magnets can be moved by stepper motors on their table in order to allow a change of the pathlength by about 10 cm. This represents a complete rf-wavelength and will allow to change the mode of operation from an accelerating multi-turn linac to an ERL. The separation magnet together with its vacuum chamber were designed and built to allow the extraction of a decelerated beam at injection energy (see Fig. 5). In future it will be possible to either steer the beam directly after the first linac pass into the second recirculation beamline and decelerate it afterwards or to use the main linac twice by bringing the beam first in the F-recirculation before performing the 180° phase shift in

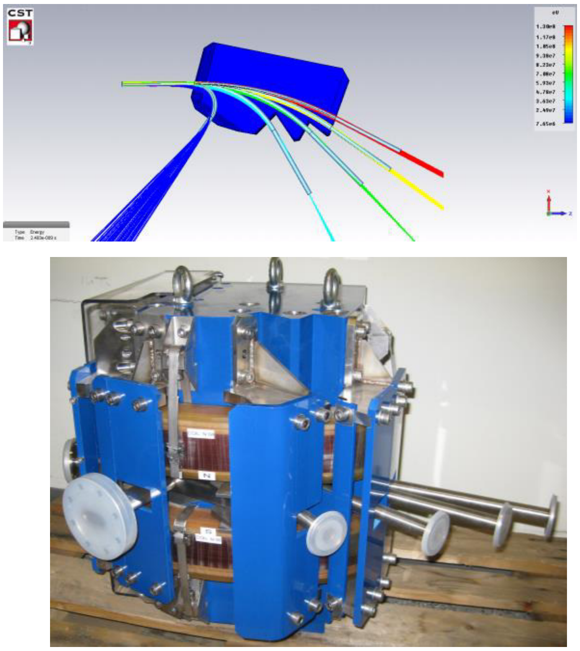

Figure 5: Separation magnet for the S-DALINAC upgrade providing possibility to extract the electron beam at injection energy for ERL mode. A picture taken from CST [15] simulation and a photo of the recently delivered magnet with vacuum chamber are shown.

ISBN 978-3-95450-183-0

the second recirculation and decelerate the beam twice before extraction at injection energy. The use of the third recirculation will not be possible in ERL-mode. A schematic of a possible ERL setting is shown in Fig. 6.

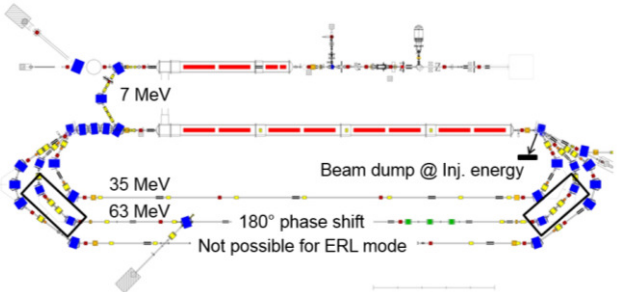

Figure 6: Possible energy configuration for the S-DALINAC in ERL operation. The dipole magnets inside the rectangles will be moveable to allow the necessary shift of the pathlength.

So far, there is no ERL operation for users planned. It will be used for research in accelerator physics, e.g. further tests on BBU, LLRF control, diagnostics and other ERL related questions. Junior accelerator scientists will have the opportunity to work and learn with this machine running in ERL mode. The ongoing research program on basic questions in nuclear structure physics will strongly benefit from the operation of the S-DALINAC in the upcoming triple-recirculation scheme.

SUMMARY AND OUTLOOK

The S-DALINAC is a recirculating linac were BBU occurs already at a few µA. Strategies of increasing the threshold current by manipulating the beam optics in the recirculation loops can be tested. After the upgrade of the S-DALINAC with a third recirculation beam line we plan to check the influence of chromaticity by using sextupole magnets. The variation of the transverse phase advance will be investigated as well. Skew quadrupoles can be used to perform a complete phase space exchange. In the future those devices can be used as well when we will operate the S-DALINAC as a single or double turn ERL.

REFERENCES

[1] G.H. Hoffstaetter et al., Phys. Rev. STAB **7** (2004) 054401.
[2] C.M. Lyneis et al., Trans. Nucl. Sci. **B** (1979).
[3] P. Axel et al., Trans. Nucl. Sci. **26** (1979). [2]
[4] A. Richter., EPAC ’96, Sitges (1996) 110. [2]
[5] O. Yevetska et al., Nucl. Instr. Meth. A **618** (2010) 160.
[6] Y. Poltoratska et al., J. Phys.: Conf. Ser. **298** (2011) 012002.
[7] M. Kleinmann et al., IPAC ’12, New Orleans (2012) 1161.
[8] R. Eichhorn et al., LINAC ’12, Victoria (2008) 395.
[9] Y. Petenev et al., IPAC'11 San Sebastian, (2011) 718.
[10] L. R. Evans, CERN/SPS-DI (MST)/80-2 (1980).
[11] M. Borland, APS LS-287 (2000).
[12] V. Litvinenko, Phys. Rev. STAB **15** (2012) 074401.
[13] V. Litvinenko, Phys. Rev. STAB **18** (2015) 039901.
[14] T. Raubenheimer, Phys. Rev. STAB **3** (2000) 121002.
[15] CST Studio Suite, http://www.cst.com/

ISBN 978-3-95450-183-0

LINEAR MICROBUNCHING GAIN ESTIMATION INCLUDING CSR AND LSC IMPEDANCES IN RECIRCULATION MACHINES*

C. -Y. Tsai#, Virginia Tech, Blacksburg, VA 24061, USA
D. Douglas, R. Li, and C. Tennant, Jefferson Lab, Newport News, VA 23606, USA

Abstract

It is known that microbunching instability (MBI) has been one of the most challenging issues with the design of magnetic compressor chicanes for FEL or linear colliders, as well as the transport lines for recirculating or energy recovery linac machines. To more accurately quantify MBI in a single-pass or few-passes system and for more complete analyses, we extend our previously developed linear Vlasov solver [1, 2] to incorporate more relevant impedance models, including transient and steady-state coherent synchrotron radiation (CSR) and longitudinal space charge (LSC) impedances. Then the linearized Vlasov equation is numerically solved for the microbunching gain amplification factor. With application of this code to two specially designed transport arcs and a circulator cooling ring design of MEIC at Jefferson Lab, the resultant gain functions and spectra are presented and some results are compared with particle tracking simulation. We also discuss some underlying physics with inclusion of these collective effects. It is anticipated this more complete analysis can further improve the understanding of the MBI mechanisms and shed light on how to suppress or compensate MBI effects in such lattice designs.

INTRODUCTION

The beam quality preservation is of a general concern in delivering a high-brightness beam through a transport line or recirculation arc in the design of modern accelerators. Microbunching instability (MBI) has been one of the most challenging issues associated with such beamline designs. Any source of beam performance limitations in such recirculation or transport arcs must be carefully examined in order to preserve the beam quality, such as the coherent synchrotron radiation (CSR), longitudinal space-charge (LSC) and/or other high-frequency impedances that can drive microbunching instabilities.

To accurately quantify the direct consequence of microbunching effect, i.e. the gain amplification factor G (which shall be defined later), we further extend our previously developed semi-analytical simulation code [1, 2] to include more relevant impedance models, including both CSR and LSC impedances. The LSC effect stems from (upstream) non-uniformity of an electron beam and can accumulate an amount of energy modulation when a beam traverses a long section of a beamline. Such energy modulation can then convert to density modulation via momentum compaction R_{56} downstream the beamline. In addition, along the beamline, CSR due to electron radiation emission out of bending dipoles can have a significant effect on further amplifying such density to energy modulation. The accumulation and conversion between density and energy modulations can possibly cause serious microbunching gain amplification (or, microbunching instability).

In this paper, we would first summarize the impedance models used in our semi-analytical simulations. Then, we briefly introduce the methods of microbunching gain calculation: a kinetic model based on (linearized) Vlasov equation [3, 4], including direct and iterative approaches, and particle tracking by ELEGANT [5, 6]. In the same section, we devise a method to quantify the contribution of microbunching gains from individual stages based on the concept proposed in Ref. [4]. After that, we illustrate the calculated gain functions and spectra for our example lattices, including two comparative high-energy transport arcs and a circulator cooling ring (CCR) design for Medium-energy Electron Ion Collider (MEIC) project at Jefferson Lab [7]. Finally we discuss the underlying physics and summarize our observations from the simulation results. We hope this further accurate and complete consideration of microbunching gain estimation can be compared with currently experimental investigation [8, 9] and help shed light on how to further improve future lattice designs.

IMPEDANCE MODELS

For a (ultra-)relativistic electron beam traversing an individual dipole, CSR can have both steady-state and transient effects. In addition, when a beam goes through a long transport line, LSC can also have a significant effect on accumulating energy modulations. Here we quote the resultant analytical expressions for CSR and LSC impedances without further derivation:

Free-space Steady-state Non-ultrarelativistic CSR Impedance

For a relativistic electron beam ($\beta = 1, \gamma < \infty$) traversing a bending dipole, the free-space steady-state CSR impedance per unit length can be expressed as [10]:

$$\mathrm{Re}\left[Z_{CSR}^{s.s.NUR}(k(s);s)\right] = \frac{-2\pi k(s)^{1/3}}{|\rho(s)|^{2/3}}\mathrm{Ai}'\left(\frac{(k(s)|\rho(s)|)^{2/3}}{\gamma^2}\right) + \frac{k(s)\pi}{\gamma^2}\left(\int_0^{(k(s)|\rho(s)|)^{2/3}/\gamma^2}\mathrm{Ai}(\varsigma)\mathrm{d}\varsigma - \frac{1}{3}\right) \tag{1}$$

$$\mathrm{Im}[Z_{CSR}^{s.s.NUR}(k(s);s)] \simeq \frac{2\pi k(s)^{1/3}}{|\rho(s)|^{2/3}}\left\{\frac{1}{3}\mathrm{Bi}'(x) + \int_0^x \begin{bmatrix}\mathrm{Ai}'(x)\mathrm{Bi}(t)\\ -\mathrm{Ai}(t)\mathrm{Bi}'(x)\end{bmatrix} dt\right\}$$

---

* This material is based upon work supported by the U.S. Department of Energy, Office of Science, Office of Nuclear Physics under contract DE-AC05-06OR23177.

#jcytsai@vt.edu

where $x=\left(k(s)\left|\rho(s)\right|\right)^{2/3}/\gamma^2$, k = 2π/λ is the modulation wave number, $\rho(s)$ is the bending radius, and Ai and Bi are Airy functions. Under ultrarelativistic approximation ($\gamma\to\infty$), Eq. (1) is reduced to the well-known expression [11, 12]:

$$Z_{CSR}^{s.s,UR}\left(k(s);s\right)=\frac{-ik(s)^{1/3}A}{\left|\rho(s)\right|^{2/3}} \tag{2}$$

where the constant $A=-2\pi\left[\mathrm{Bi}'(0)/3+i\mathrm{Ai}'(0)\right]$.

Entrance Transient CSR Impedance

Prior to reaching steady-state interaction, the beam entering a bend from a straight section would experience the so-called entrance transient state, where the impedance per unit length can be obtained by Laplace transformation of the corresponding wakefield [13, 14, 15]:

$$Z_{CSR}^{ent}\left(k(s);s\right)=\frac{-4}{s^*}e^{-4i\mu(s)}+\frac{4}{3s^*}\left(i\mu(s)\right)^{1/3}\Gamma\left(\frac{-1}{3},i\mu(s)\right) \tag{3}$$

where $\mu(s)=k(s)z_L(s)$, s^* is the longitudinal coordinate measured from dipole entrance, $z_L=\left(s^*\right)^3/24\rho^2$, and Γ is the upper incomplete Gamma function.

Exit Transient CSR Impedance

There are also exit CSR transient effects as a beam exits from a dipole. For the case with fields generated from an upstream electron (at retarded time) propagating across the dipole to downstream straight section, i.e. Case C of Ref. [15], the corresponding impedance per unit length can be similarly obtained by Laplace transformation:

$$Z_{CSR}^{exit}\left(k(s);s\right)=\frac{-4}{L_b+2s^*}e^{\frac{-ik(s)L_b^2}{6\left|\rho(s)\right|^2}\left(L_b+3s^*\right)} \tag{4}$$

where s^* is the longitudinal coordinate measured from dipole exit and L_b is the dipole length.

For the impedance expression with the case of fields generated from an electron (at retarded time) within a dipole propagating downstream the straight section, we use the following expression for the exit transient impedance [16]:

$$Z_{CSR}^{drif}(k(s);s)\approx\begin{cases}\frac{2}{s^*},\ \text{if}\ \rho^{2/3}\lambda^{1/3}\le s^*\le\lambda\gamma^2/2\pi\\ \frac{2k(s)}{\gamma^2},\ \text{if}\ s^*\ge\lambda\gamma^2/2\pi\\ 0,\ \text{if}\ s^*<\rho^{2/3}\lambda^{1/3}\end{cases} \tag{5}$$

where s^* is the longitudinal coordinate measured from dipole exit. This expression assumes the exit impedance comes primarily from coherent edge radiation in the near-field region (i.e. $z<\lambda\gamma^2$), and in our simulation we only include transient effects [Eq. (4) and (5)] right after a nearby upstream bend. Here we note that these CSR models are valid only when the wall shielding effect is negligible. The wall shielding effect becomes important when the distance from the beam orbit to the walls h is to satisfy $h\le\left(\rho\lambda^2\right)^{1/3}$.

Longitudinal Space Charge Impedances [17]

Below we present two slightly different LSC impedance expressions implemented in our code. The first one is on-axis model, which assumes a transversely uniform density with circular cross section of radius r_b,

$$Z_{LSC}^{on-axis}(k(s);s)=\frac{4i}{\gamma r_b(s)}\frac{1-\xi K_1(\xi)}{\xi} \tag{6}$$

where $\xi=\frac{k(s)r_b(s)}{\gamma}$ and the transverse beam sizes can be obtained by the fitted result $r_b(s)\approx\frac{1.747}{2}\left(\sigma_x(s)+\sigma_y(s)\right)$ [18].

The second LSC model is the average model, which integrates the radial dependence [17,19],

$$Z_{LSC}^{ave}(k(s);s)=\frac{4i}{\gamma r_b(s)}\frac{1-2I_1(\xi)K_1(\xi)}{\xi} \tag{7}$$

where ξ is defined above the same way.

NUMERICAL METHODS

To quantify the MBI in a transport or recirculation arc, we estimate the microbunching amplification factor G (or, bunching factor) by two distinct methods. The first one, based on a kinetic model, is to solve a (linearized) Vlasov equation [3,4] using given impedance models [e.g. Eqs. (1-7)]. This method is of our primary focus in this paper. The second one, served as a benchmarking of the first method, is based on particle tracking (here we use ELEGANT [5,6]). For the former, after mathematical simplification of the linearized Vlsaov equation, we actually solve a general form of Volterra integral equation [3,4] in terms of the bunching factor. In our semi-analytical code, to facilitate us in simulating ERL-based lattices which usually contain spreaders/recombiners, we extend the existing formulation [3,4] to include both transverse horizontal and vertical bends. Below summarizes the governing equation for bunching factor g_k,

$$g_k(s)=g_k^{(0)}(s)+\int_0^s K(s,s')g_k(s')ds' \tag{8}$$

where the kernel function can be particularly expressed as

$$K(s,s')=\frac{ik}{\gamma}\frac{I(s)}{I_A}C(s')R_{56}(s'\to s)Z\left(kC(s'),s'\right)\times[\text{Landau damping}] \tag{9}$$

for the [Landau damping] term

$$[\text{Landau damping}]=\exp\left\{\frac{-k^2}{2}\left[\begin{array}{l}\varepsilon_{x0}\left(\beta_{x0}R_{51}^2(s,s')+\dfrac{R_{52}^2(s,s')}{\beta_{x0}}\right)\\ +\varepsilon_{y0}\left(\beta_{y0}R_{53}^2(s,s')+\dfrac{R_{54}^2(s,s')}{\beta_{y0}}\right)+\sigma_\delta^2R_{56}^2(s,s')\end{array}\right]\right\} \tag{10}$$

with

$$\begin{aligned}R_{56}(s'\to s)&=R_{56}(s)-R_{56}(s')+R_{51}(s')R_{52}(s)-R_{51}(s)R_{52}(s')\\&\quad+R_{53}(s')R_{54}(s)-R_{53}(s)R_{54}(s')\end{aligned} \tag{11}$$

and $R_{5i}(s,s')=C(s)R_{5i}(s)-C(s')R_{5i}(s')$ for i = 1, 2, 3, 4, 6.

Here the kernel function $K(s,s')$ describes relevant collective effects, $g_k(s)$ the resultant bunching factor as a function of the longitudinal position given a wavenumber k, and $g_k^{(0)}(s)$ is the bunching factor in the absence of collective effect (i.e. from pure optics effect). We particularly note that the above formulation can be applicable to the case with focusing in combined-function dipoles.

ISBN 978-3-95450-183-0

In the above formulation, we have made the coasting beam approximation, i.e. the modulation wavelength is assumed much shorter compared with the whole bunch duration. The transport functions $R_{5i}(s)$ (i = 1, 2, 3, 4, 6) are adopted from ELEGANT with slight modification to account for "non-ultrarelativistic" contribution $R_{56}(s) \rightarrow R_{56}(s) + \frac{s}{\gamma^2}$ where s is the longitudinal coordinate along the beamline. Here we define the microbunching gain function at $k = 2\pi/\lambda$ as $G(s) \equiv \left| g_k(s) / g_k^{(0)}(0) \right|$ and the gain spectral function at the exit of a lattice as

$$G_f(\lambda) \equiv G(s = s_f) \qquad (12)$$

We note that the impedance term in Eq. (9) is of our primary interest. With given impedance models [Eqs. (1-7)], we can estimate the microbunching gain through a beamline. Since the calculation is fast (compared with tracking simulation), it can be used to make quick estimation or optimize the microbunching gain development in a lattice design.

For Eq. (8), we solve it by two approaches: one is the *direct* solution, and the other resorts to the *iterative* solution. For the latter approach, at the first step, we express Eq. (8) in vector forms for $g_k(s)$ and $g_k^{(0)}(s)$, and in a matrix form for $K(s,s')$. Then we arrive at the following equation

$$\mathbf{g}_k = \left(\mathbf{I} - \mathbf{K}\right)^{-1} \mathbf{g}_k^{(0)} \qquad (13)$$

provided the inverse matrix of $\left(\mathbf{I} - \mathbf{K}\right)$ exists.

At the second step, to introduce the stage gain concept, motivated by Ref. [4], we try to define the first-order iterative solution by expanding Eq. (13) as: $\mathbf{g}_k^{(1)} = \left(\mathbf{I} + \mathbf{K}\right)\mathbf{g}_k^{(0)}$ and the second-order iteration to be $\mathbf{g}_k^{(2)} = \left(\mathbf{I} + \mathbf{K} + \mathbf{K}^2\right)\mathbf{g}_k^{(0)}$. In general, to n^{th} order iterative solution, we have

$$\mathbf{g}_k^{(n)} = \left(\sum_{m=0}^{n} \mathbf{K}^m\right)\mathbf{g}_k^{(0)} \qquad (14)$$

It can be seen that, in Eq. (14), the sum to infinite order should give an equivalent result of Eq. (13) [or, Eq. (8)], provided the sum converges. Therefore, these two approaches, Eq. (8) and Eq. (14), can be proven equivalent. Here we note that the convergence of Eq. (14) is held in a single-pass (or, finite-pass) system, e.g. the transport or recirculation arcs, for CSR effects. For a storage ring or for LSC effects which are ubiquitous along the beamline, the convergence would not be held, which is however beyond the scope of this paper [20]. For CSR-induced microbunching gain, the advantage of using numerical iterative approach, Eq. (14), is that it can give us a further insight to see how different orders of iterative solutions contribute to the different physical amplification stages. Also, Eq. (14) facilitates us exploring up to which stage the overall CSR-induced microbunching development can be described, by comparing with the direct solution [1]. Hereafter we dub the solutions of Eq. (13) as *direct* solutions, and those of Eq. (14) as *iterative* solutions. Note that the definition of gain function with respect to Eq. (8) [i.e. Eq. (12)] can now be generalized to define the staged gain function, with respect to Eq. (14), as $\tilde{G}^{(n)}(s) = \mathbf{g}_k^{(n)}(s) / \mathbf{g}_k^{(0)}(0)$ with $G^{(n)}(s) = \left|\tilde{G}^{(n)}(s)\right|$ and, similar to Eq. (12), the stage gain spectral function,

$$G_f^{(n)} \equiv G^{(n)}(s = s_f) \qquad (15)$$

To further compare the CSR microbunching gains contributed from individual stages, we devise in this subsection a method to quantitatively characterize the microbunching amplification in terms of stage orders. We note that Eq. (15) can in general be expanded in a series of polynomial of the beam current as [see also Eq. (14) and (9)]

$$\tilde{G}_f^{(M)} = \tilde{G}^{(M)}(s = s_f) = \tilde{G}_0 + \tilde{G}_1 I_b + \ldots + \tilde{G}_M I_b^M = \sum_{m=0}^{M} \tilde{G}_m I_b^m \qquad (16)$$

up to a certain order M.

In order to extract the net effects caused by the lattice optics and beam phase space spreads for Landau damping, the above expression Eq. (16), together with knowledge of Eq. (9), can be further formulated as

$$\tilde{G}_f^{(M)} = \sum_{m=0}^{M} A^m d_m^{(\lambda)} \left(\frac{I_b}{\gamma I_A}\right)^m \qquad (17)$$

where A is defined in Eq. (2), γ is the relativistic factor and $d_m^{(\lambda)}$ is the dimensionless coefficient (given a certain modulation wavelength) which now reflects the properties from lattice optics at m^{th} stage (m = 0, 1, 2,…), as well as Landau damping through finite beam emittances and energy spread [see Eqs. (10)]. For our interest in the following discussion, λ is chosen to correspond to the maximal CSR gain, denoted as λ_{opt}. Here we point out that Eq. (38) of Ref. [4] can be a special case of Eq. (17) for $M = 2$ in a typical bunch compressor chicane.

Obtaining the coefficients $d_m^{(\lambda)}$ of Eq. (17) can be straightforward. Here we remark the close connection between Eq. (9) and Eqs. (14, 15). For now, we can define the *individual* stage gain, which shall be convenient for our further discussion,

$$\mathcal{G}_f^{(m)} = \left| A^m d_m^{(\lambda)} \left(\frac{I_b}{\gamma I_A}\right)^m \right| \qquad (18)$$

Note the difference between Eq. (17) and (18).

As our second model to calculate the microbunching gains, we use ELEGANT [5,6], based on the particle tracking, as our benchmarking against the results by our semi-analytical Vlasov solver for the following example lattices.

SIMULATION RESULTS

High-energy Transport Arcs (Example 1 and 2)

In this section we take two 1.3 GeV high-energy transport arcs as our comparative examples (hereafter dubbed Example 1 and Example 2 lattice). The detailed description of the two example lattices can be found in Ref. [21, 22]. Table 1 summarizes some initial beam parameters for use in our simulations. Here, Example 1 lattice is a 180° arc with large momentum compaction (R_{56}), as well as a second-order achromat and being globally isochronous with a large dispersion modulation across the entire arc. In contrast to the first example, Example 2 is again a 180° arc with however small momentum compaction. This arc is also a second-order achromat but designed to be a locally isochronous lattice within superperiods. Local isochronisity ensures that the bunch length is kept the same at phase homologous CSR emission sites. The lattice design strategy was originally aimed for CSR-induced beam emittance suppression, while our simulation results show that it appears to work for microbunching gain suppression as well. Figure 1 shows the Twiss functions and transport functions $R_{56}(s)$ (or, the momentum compaction functions) across the arcs. Note that $R_{56}(s)$ for Example 2 (Fig. 1d) is much smaller in amplitude than that for Example 1 (Fig.1c) due to local isochronicity.

Table 1: Initial Beam and Twiss Parameters for the Two High-energy Transport Arcs

Name	Example 1 (large R_{56})	Example 2 (small R_{56})	Unit
Beam energy	1.3	1.3	GeV
Bunch current	65.5	65.5	A
Normalized emittance	0.3	0.3	µm
Initial beta function	35.81	65.0	m
Initial alpha function	0	0	
Energy spread (uncorrelated)	1.23×10^{-5}	1.23×10^{-5}	

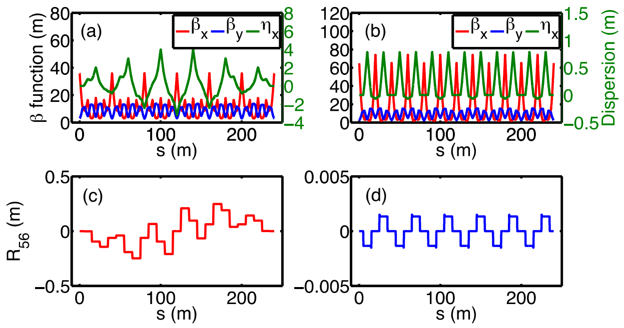

Figure 1: Lattice and transport functions for 1.3 GeV high-energy transport arc: (a)(c) with large momentum compaction function R_{56} (Example 1); (b)(d) with small momentum compaction function R_{56} (Example 2).

Microbunching gains for the two transport arcs are shown in Figs. 2 and 3. Figure 2 shows the gain spectra $G_f(\lambda)$ at the exits of the lattices as a function of modulation wavelength, from which one can obviously see a significant difference between them: Example 1 is vulnerable to CSR effect while Example 2 is still laid a very low level.

One can observe that microbunching gain with the inclusion of both steady-state CSR and entrance transient effects is slightly lowered from the case of steady-state CSR alone. This is because the CSR impedances including entrance transient effect become a bit reduced near a dipole entrance where the beam enters a bend. One can also observe that, with the inclusion of all relevant CSR impedances, including exit transients, the microbunching gain increases up to 200 % compared with that of steady-state case. It can be also expected that the additional inclusion of LSC can further degrade the longitudinal beam quality. Note that, for this lattice (Example 1), all the dipoles only occupy less than 5% of total beamline length, so without optical compensation the CSR-drift transient can cause a further significant effect. Yet with optical compensation, even with the same ratio of dipoles over the beamline, Example 2 is not subject to CSR-induced MBI. This highlights the impact of lattice design for transport or recirculation arcs on microbunching gain. We remind that, due to extremely high gain of Example 1 lattice with inclusion of all relevant CSR impedances, those ELEGANT results are averaged over the initial amplitudes 0.01-0.04% and 70×10^{6} macroparticles are used in the simulation with extensive convergence studies done before ELEGANT production [23].

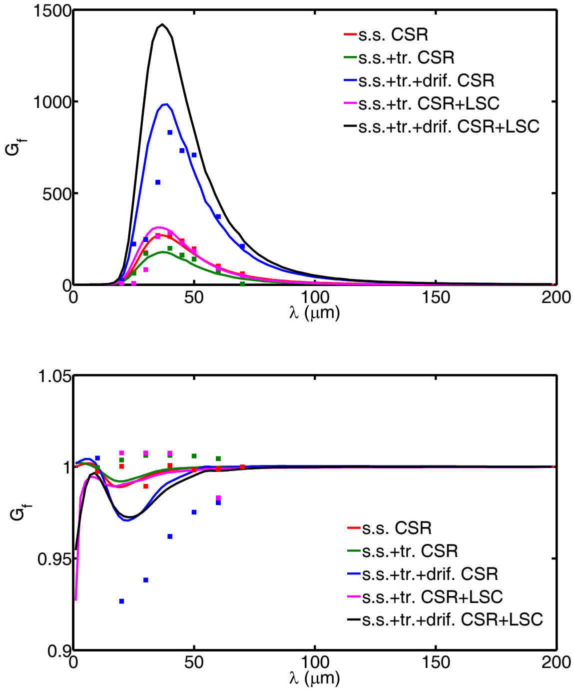

Figure 2: Microbunching gain spectra as a function of initial modulation wavelength for Example 1 (top) and Example 2 (bottom) lattice. Here, for ELEGANT tracking of Example 1, we vary the initial density modulation

ISBN 978-3-95450-183-0

amplitudes from 0.04 % to 0.1 % for various modulation wavelengths in order to obtain the converged results.

Figure 3 demonstrates the evolution of microbunching gains as a function of *s* for several different combination of impedances at optimal wavelengths (λ_{opt} = 40 μm for Example 1; λ_{opt} = 20 μm for Example 2). One can see in Fig. 3, with inclusion of CSR drift, the gain greatly accumulates at the second half of Example 1, while Example 2 (with local isochronicity) is free from the gain amplification. With further inclusion of LSC, the gain increases more, but primary contribution to the overall gain comes from CSR effect.

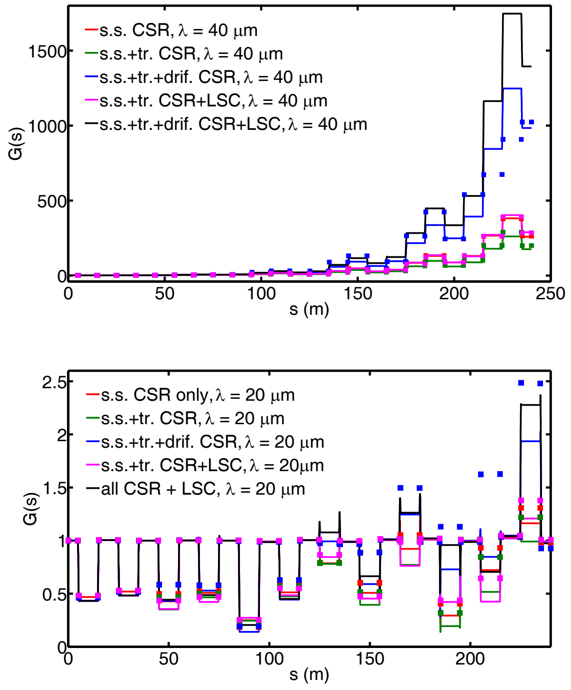

Figure 3: Microbunching gain functions G(s) for Example 1 (top) and Example 2 (bottom) lattice. Note here that we impose an initial density modulation amplitude 0.05 % on a flattop density distribution in ELEGANT simulations for Example 1.

To further examine the features of multi-stage gain amplification, we continue to take the two high-energy transport arcs (Example 1 and 2) as examples to extract the coefficients $d_m^{(\lambda)}$ [defined in Eq. (17)] so that we can quantify and compare optics impacts on the CSR microbunching gains (for simplicity, here we consider only steady-state CSR effect). Provided a set of $d_m^{(\lambda)}$ are given for different stages (i.e. different *m*), Fig. 4 shows the bar charts representing the individual staged gains $\mathcal{G}_f^{(m)}$ as functions of beam current and stage index for both Examples. Here we have two observations in Fig. 4: first, given a specific stage index, as the beam current increases, $\mathcal{G}_f^{(m)}$ also increases; second, for the same beam current, as the stage order increases, $\mathcal{G}_f^{(m)}$ does not necessarily increase accordingly. This is because the stage gain coefficient's behavior is lattice dependent. Since $d_m^{(\lambda)}$ are independent of beam current and beam energy, they can be used to obtain the maximal gain as a function of the beam current provided $d_m^{(\lambda)}$ are given. Figure 5 compares the overall gain from Eq. (17) and Eq. (12) for different currents for Example 1 and 2, at a selected wavelength close to maximal gain. As can be seen, $M = 6$ can well describe the current dependence of the CSR microbunching gain in Example 1 lattice. For Example 2 case, the nominal beam current (65.5 A) is well described by M = 6; however, if at further high current scale, it needs to take higher stage orders into account.

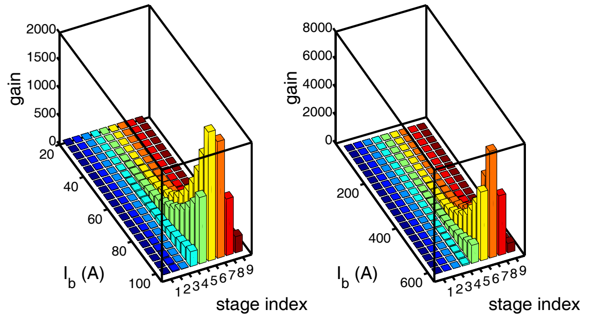

Figure 4: Bar chart representation of the individual staged gains [Eq. (18)] at the exits of the Example 1 and 2 lattices for several different beam currents. (Left) Example 1 (λ = 36.82 μm); (right) Example 2 (λ = 19 μm).

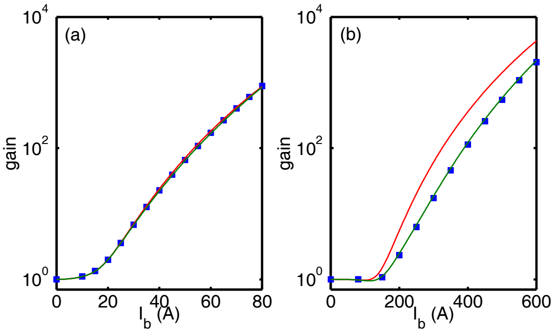

Figure 5: Current dependence of maximal CSR gain for the two high-energy transport arc lattices: (a) Example 1; (b) Example 2. Solid red line from Eq. (12) with M = 6, solid green line from Eq. (12) with M = 9 and blue square dots from Eq. (17).

To further illustrate how the multi-stage amplification physically contributes to and how the lattice optics impacts on the microbunching development, we create in Fig. 6 the "quilt" patterns $R_{56}(s'\to s)$ [defined in Eq. (11)] for the two example lattices in order to clearly identify the enhancement or suppression of microbunching along the beamline by lattice optics. For a planar and uncoupled lattice, Eq. (11) is reduced back to $R_{56}(s'\to s)=R_{56}(s)-R_{56}(s')+R_{51}(s')R_{52}(s)-R_{51}(s)R_{52}(s')$. The upper left area in the figures vanishes due to causality. It is obvious that in Example 1 (left figure) those block areas with large amplitude, particularly the bottom right deep red blocks, can potentially accumulate the CSR gain. To be specific, for Example 1, energy modulation at s' = 15 m can cause density modulation at s = 60 m, where CSR can induce further energy modulation at the same location. Then such modulation propagate by $R_{56}(s'\to s)$ from s' = 60 m to s = 100 m, and so on. It is this situation that causes multi-stage CSR amplification. Here we note that more complete analysis needs to take Landau damping factor into account and we refer the interested reader to Ref. [24]. In contrast, the situation for Example 2 (right figure) is more alleviated because of much smaller amplitudes of $R_{56}(s'\to s)$.

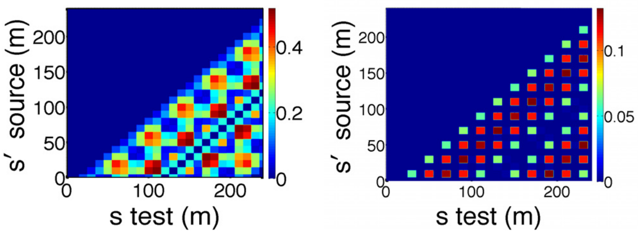

Figure 6: $R_{56}(s'\to s)$ quilt patterns for the two Example lattices: Example 1 (left) and Example 2 (right).

The third example is based on the circulator cooling ring (CCR) for MEIC [7]. Maintaining excellent phase space quality for the electron beam is known crucial to the electron cooling efficiency. This preliminary design is based upon the topological structure of figure-8 collider ring. Such design of an ERL-based electron cooler ring is characteristic of two 30-m cooling solenoids cross the center of the electron collider ring and composed of horizontal dipoles around the four corners and vertical bending dipoles around the two non-diagonal corners to meet the requirement of 3 stacked figure-8 rings [7]. Note here that the transverse beam dynamics in horizontal and vertical planes are coupled in the cooling solenoids, though our theoretical formulation [Eq. (8)] assumes no coupling. Note however that the first-order transfer matrix of a solenoid does not couple the transverse degrees of freedom to the longitudinal motion. Therefore, we remove the solenoid sections out from our simulations without affecting the CSR microbunching dynamics within the framework [25]. Table 2 lists the initial beam and Twiss parameters for MEIC CCR [7].

Table 2: Initial Beam and Twiss Parameters for MEIC CCR [7]

Name	**Value**	**Unit**
Beam energy	54	MeV
Beam current	60	A
Normalized emittances	3 (in both planes)	μm
Initial beta functions	10.695/1.867	m
Initial alpha functions	0 (in both planes)	
Energy spread (uncorrelated)	1.0×10^{-4}	

Microbunching gain spectra $G_f(s)$ from Eq. (8) for different combinations of impedance models are demonstrated in Fig. 7 where we found the microbunching gains with λ ≈ 350 μm reach the maximal. Unlike Example 1 and 2, LSC shows a detrimental effect on MEIC CCR, due to (relatively) low beam energy and high bunch charge. Figure 8 shows the gain evolution $G(s)$ along the ring, where we can see the microbunching gain starts to build up at the second arc ("10-o'clock arc"), continually develop at the third arc, and eventually increase to a huge level when the beam is sent back to the beam exchange system.

Our study indicates that the preliminary design of CCR for high-energy electron cooling is at risk of microbunching instability; an improved design is required to suppress such instability and/or alternative beam transport scheme would be considered in order to compensate and to circulate the electron beam as many turns as possible [7] while maintaining high phase space quality of the electron beam required by sufficient electron cooling efficiency.

We emphasize here that, for MEIC CCR, due to its high bunch charge (~ 2 nC) as well as low energy spread (~ 10^{-4}), as expected, microbunching, greatly accumulates along the beamline and over a broad spectral range of density modulation.

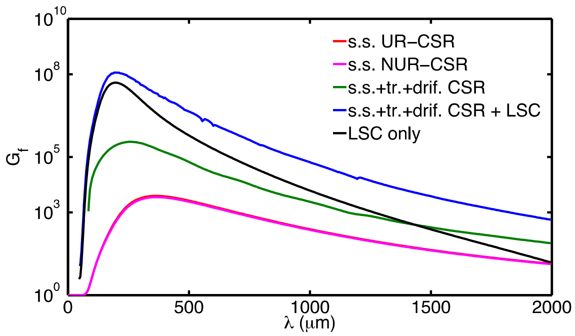

Figure 7: Microbunching gain spectra as a function of initial modulation wavelength for MEIC CCR lattice. Note that, due to ultrahigh gain, we do not benchmark these results directly, but we do for a case with 10 times larger the transverse emittances and have confirms the validity of our simulation results [24].

ISBN 978-3-95450-183-0

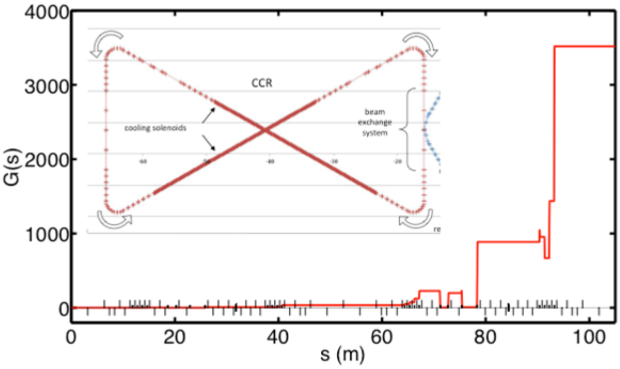

Figure 8: Microbunching gain functions G(s) for MEIC CCR lattice; here λ = 350 μm. The inset illustrates schematic layout of the circulator ring.

SUMMARY AND CONCLUSION

In this paper, we have first summarized relevant impedance models for microbunching instability study, including CSR and LSC, and outlined the theoretical formulation based on (linearized) Vlasov equation by treating this problem in frequency domain. The solution to the governing equation [Eq. (8)] can be self-consistently obtained (i.e. direct solution) or found through numerical iteration (i.e. iterative solution). With introduction of stage gain concept, the individual iterative solutions can be connected through the lattice optics $R_{56}(s' \to s)$ in a physical way. Moreover, the stage gain coefficient [defined in Eq. (17)] can be applied to make quick estimation for the maximal CSR gain provided a lattice is given (Fig. 5).

Then, we have illustrated, based on two comparative high-energy transport arcs, the optics impact on the microbunching gain development using the developed stage gain concept. We also presented the microbunching gain analysis for a circulator cooling ring design of MEIC and concluded that such preliminary design is subject to both CSR and (primary) LSC induced microbunching instability.

Finally, it is interesting that although the emittance preservation is of original/primary consideration for the proposed Example 2 design [21, 22], it also works well for microbunching gain suppression.

ACKNOWLEDGMENT

The author (C. -Y. T.) would like to express his sincere thanks to his advisors, Mark Pitt and Rui Li for their kind support and many fruitful discussions. We also thank Steve Benson for bringing many motivating issues for our studies. This work is supported by Jefferson Science Associates, LLC under U.S. DOE Contract No. DE-AC05-06OR23177.

REFERENCES

[1] C. -Y. Tsai et al., Theoretical investigation of coherent synchrotron radiation induced microbunching instability in transport and recirculation arcs, International FEL Conference 2014 (THP022)

[2] C. -Y. Tsai et al., CSR induced microbunching gain estimation including transient effects in transport and recirculation arcs, IPAC'15 (MOPMA025)

[3] S. Heifets et al., Coherent synchrotron radiation instability in a bunch compressor, Phys. Rev. ST Accel. Beams 5, 064401 (2002) and its erratum paper

[4] Z. Huang and K. -J. Kim, Formulas for coherent synchrotron radiation microbunching in a bunch compressor chicane, Phys. Rev. ST Accel. Beams 5, 074401 (2002) and its erratum paper

[5] M. Borland, elegant: A Flexible SDDS-Compliant Program for Accelerator Simulation, APS Light Source Note LS-287, September 2000

[6] M. Borland, Modeling of microbunching instability, Phys. Rev. ST Accel Beams 11, 030701 (2008)

[7] MEIC Design Summary, available at http://arxiv.org/abs/1504.07961

[8] Y. Roblin et al, Experimental studies of optics schemes at CEBAF for suppression of coherent synchrotron radiation (CSR), JLab LDRD (2014)

[9] R. Li et al., Experimental investigation of LSC and CSR induced microbunching instability using LERF, JLab LDRD, submitted (2015)

[10] R. Li and C. -Y. Tsai, CSR impedance for non-ultrarelativistic beams, IPAC'15 (MOPMN004)

[11] J. Murphy et al., Longitudinal wakefield for an electron moving on a circular orbit, Part. Accel. 1997, Vol. 57, pp. 9-64

[12] Ya. S. Derbenev et al., Microbunch radiative tailhead interaction, TESLA-FEL-Report 1995-05

[13] D. Zhou, An alternative 1D model for CSR with chamber shielding, IPAC'12 (MOOBB03)

[14] C. Mitchell et al., Effects of transient CSR wakefields on microbunching in a bunch compressor, IPAC'13 (TUPWA057)

[15] E. L. Saldin et al., On the coherent radiation of an electron bunch moving in an arc of a circle, NIMA 398, 373 (1997)

[16] R. Bosch et al., Longitudinal wake of a bunch of suddenly accelerated electrons within the radiation formation zone, Phys. Rev. ST Accel. Beams 10, 050701 (2007)

[17] M. Venturini, Models for longitudinal space charge impedance for microbunching instability, Phys. Rev. ST Accel. Beams 11, 034401 (2008)

[18] J. Wu et al., Analytical Analysis of longitudinal space charge effects for a bunched beam with radial dependence, Phys. Rev. ST Accel. Beams 11, 040701 (2008)

[19] M. Venturini et al., Dynamics of longitudinal phase-space modulation in an RF compressor for electron beams, Phys. Rev. ST Accel. Beams 13, 080703 (2010)

ISBN 978-3-95450-183-0

[20] R. Warnock, private communication (2014)
[21] D. R. Douglas et al., Control of coherent synchrotron radiation and microbunching effects during transport of high brightness electron beams, arXiv: 1403.2318v1 [physics.acc-ph]
[22] D. R. Douglas et al., Control of synchrotron radiation effects during recirculation, IPAC'15 (TUPMA038)
[23] C.-Y. Tsai and R. Li, Simulation of coherent synchrotron radiation induced microbunching gain using ELEGANT, JLAB-TN-14-016
[24] C. -Y. Tsai et al., (to be published)
[25] Numerical tracking simulation confirms that such artificial removal of solenoid sections does not affect CSR-induced microbunching gains; however, we believe LSC can have an additional effect due to such long cooling sections.

ISBN 978-3-95450-183-0

FIRST BEAM CHARACTERIZATION OF SRF GUN II WITH A COPPER PHOTOCATHODE

J. Teichert[#], A. Arnold, P. Michel, P. Murcek, R. Xiang, HZDR, Dresden, Germany
P. Lu, H. Vennekate, TU Dresden & HZDR, Dresden, Germany

Abstract

An improved SRF gun (ELBE SRF Gun II) has been installed and commissioned at HZDR. This new gun replaces the first SRF gun at the superconducting linear accelerator ELBE which had been in operation since 2007. The new SRF gun II has an improved 3.5-cell niobium cavity and a superconducting solenoid is integrated into the gun cryostat. The first beam test has been carried out with a Cu photocathode. Using the standard high repetition rate laser system, this delivers low bunch charges of a few pC only. The beam parameters for this low charge beam have been measured, and the first beam has been guided into the ELBE accelerator.

INTRODUCTION

A high-brightness electron source is one of the key elements of an energy recovery linac (ERL) as it has been proposed for future light sources, or other application in high energy particle physics. Since ERLs are usually designed for high current and continuous wave (CW) operation, their electron sources require both properties: low emittance and high average current. At present, there are three electron source types in operation at ERLs or their application is planned: electron sources with a static high voltage (DC guns), normal conducting radio frequency (RF) electron sources, and superconducting RF electron sources (SRF guns). All three types are photoelectron injectors utilizing powerful lasers and photo cathodes for electron beam generation. DC guns present the most developed technology and have demonstrated high repetition rate and high average current operation at several CW accelerators. The DC gun of the Cornell injector holds the world record in CW current and in transverse emittance [1, 2], and recently the specifications for CLRS could be successfully demonstrated [3]. SRF guns are still in the development phase but they offer the potential of significant higher acceleration fields and should therefore be able to deliver smaller emittances for high bunch charges [4].

THE ELBE SRF GUN II

In May 2014 the second SRF gun (ELBE SRF Gun II) was installed at the ELBE superconducting linear accelerator facility. The basic design of this new gun is similar to that of the former SRF Gun I [5], but it has a new 3.5-cell cavity made of fine grain niobium. Beside several smaller modifications, the new cavity has a different acceleration field distribution, i.e. a peak field ratio of 80% to 100% between half-cell and TESLA cells. Benefit from a higher gradient, beam dynamic simulation showed reduced emittance and bunch length.

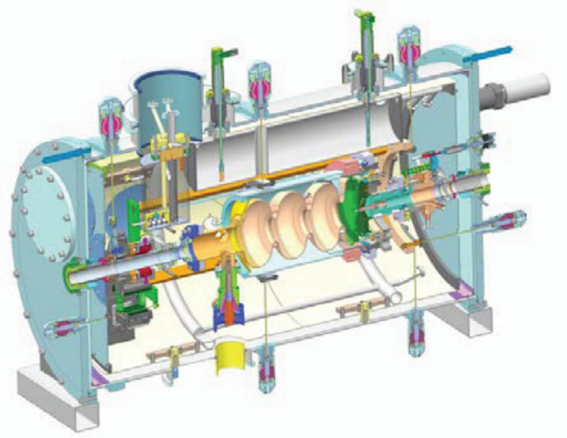
Figure 1: CAD view of the SRF Gun II cryomodule.

The design of the new cryomodule for SRF gun II is shown in Fig. 1. The 1.3 GHz Nb cavity consists of three TESLA cells and a specially designed half-cell. Another superconducting cell, called choke filter, prevents the leakage of the RF field towards the cathode support system. A normal conducting (NC) photocathode is installed in this system, which is isolated from the cavity by a vacuum gap and cooled with liquid nitrogen.

A new feature is the integration of a superconducting SC) solenoid in the cryomodule for emittance preservation purposes. Compared to the NC solenoid of SRF gun I which was placed downstream of the gun, the new design is much more compact and the distance to the cathode is smaller. The SC solenoid is placed on a remote-controlled x-y table to align its center to the electron beam axis. The cryogenic design of the assembly is sophisticated: The solenoid is cooled with 2 K He by means of a bypass from the cavity. The in-vacuum step motors and translation tables are on 77 K to reduce the heat load to the liquid He bath. Additional μ-metal shields keep the solenoid remanence field and the step motors fields on a 1 μT level near the cavity. Details of the SC solenoid design and testing are published in ref. [6].

Compared to the primary setup of SRF Gun I described in [5] there are several modification in the RF system of the gun. Now the RF main power with a frequency of 1.3 GHz is delivered by a solid state amplifier with a CW power of 10 kW [7]. The previous plastics (Rexolite) warm window is replaced by a fused silica window with higher thermal stability. A three stub tuner in the wave guide allows a variation of the band width. The analog low-level RF control system und the coaxial ELBE main power coupler with fixed coupling are still in use.

[#] j.teichert@hzdr.de

The drive laser for the SRF gun is a two-channel system developed by MBI Berlin and can deliver both laser pulses at 13 MHz with 3 ps FWHM and at 500 kHz (optionally 250 and 100 kHz) with 10 ps FWHM. These two channels support the two planned operation modes of the SRF gun. Both channels produce temporally Gaussian shaped pulses, and the average power at 258 nm can reach about 1 W. The laser consists of a Nd:glass oscillator at 52 MHz, a pulse picker generating the 13 MHz with an electro-optical modulator, a fiber-laser preamplifier for the 13-MHz-channel, a regenerative preamplifier for the 500-kHz-channel, a multipass final amplifier for both channels, and two frequency conversion stages with LBO and BBO crystals. The laser spot is transversally shaped to a round flat-top by an aperture on the laser table and then imaged onto the photo cathode with a four-lens telescopic system.

For the electron beam characterization the existing diagnostics beamline [8] has been utilized. An insertable Faraday cup delivers the beam current, five screen stations equipped with YAG(Ce) screens serve for beam profile measurements, and a 180° dipole magnet is used for energy and energy spread measurements. For transverse phase space measurements a movable slit scan system is installed.

MEASUREMENTS

Cavity Performance

Cavity performance results for the ELBE SRF Gun II together with a comparison to SRF Gun I are presented in Fig. 2. After commissioning of the gun and several checks, RF measurements in August 2014 give an intrinsic quality factor of $>10^{10}$ and a maximum acceleration gradient in CW of 10 MV/m (25.6 MV/m peak field) was obtained. More details of the RF related measurements and results of performance tests of components are published in ref. [9]. In the following commissioning period electron beam was produced with the Cu photocathode with acceleration gradients up to 9 MV/m. Later the photocathode transfer system was installed and Cs_2Te photocathodes were prepared. A first test with a Cs_2Te photocathode was performed in February 2015. Unfortunately it turned out after insertion that this photocathode was bad, i.e. the quantum efficiency was very low and very strong field emission was observed, increasing the He consumption as well as the dark current. The bad photocathode was taken out and the performance of the cavity was measured again. It was found that the cavity had been polluted. The helium consumption due to field emission was still significantly higher than before and the same for the dark current. A high power RF processing of the cavity could reduce the dark current but did not improve the cavity performance. Thus in the following beam time the acceleration gradient was restricted to 7 MV/m.

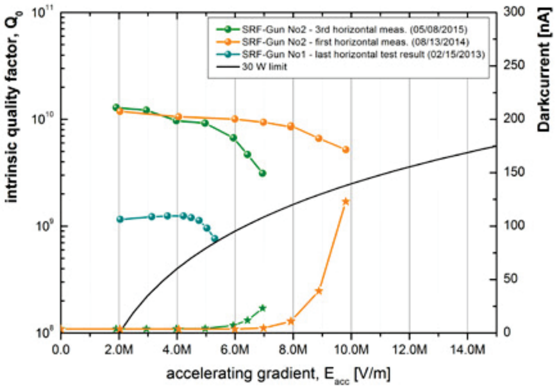

Figure 2: Measured cavity performance of ELBE SRF Gun II (intrinsic quality factor versus acceleration gradient) and comparison with the previous SRF Gun I.

Gun and Laser Parameter

Electron beam was produced and characterized in CW with acceleration gradients of 6, 7, 8, and 9 MV/m which belong to peak fields from 15.5 to 23 MV/m. The photo cathode was biased with a DC voltage of -5 kV. The dark currents during measurements were about 50 nA or less.

The photocathode was solid, polycrystalline Cu which was mirror-like polished. Before assembled in the vacuum it was dipped in citric acid and cleaned with acetone. A further in-situ processing, like laser cleaning, was not carried out. A quantum efficiency of about $2x10^{-5}$ was measured. Thus CW beam currents between 3 and 300 nA were produced and the corresponding maximum bunch charge was 3 pC at 100 kHz pulse repetition rate.

The UV drive laser at 258 nm wave length had a power between 200 and 800 mW on the laser table. Due to the cutting aperture, vacuum window, and mirror losses the laser power at the cathode was about 5 – 10% of this value. The transverse flat-top laser was adjusted to 1 and 2 mm diameter on the cathode, and the longitudinal profile was Gaussian with 3 ps FWHM (13 MHz) or 10 ps FWHM (100 kHz).

Beam Based Alignment

Laser Phase Scan: The alignment procedure start with the fixing of the laser pulse arrival time at the cathode with respect to the RF phase which is called the laser phase in the following and measured in degrees of the RF wave. For the RF time-dependence we assume a sine function $E_z(z,t) = E_0(z)\sin(2\pi f_{RF} t + \phi_l)$ with the laser phase ϕ_l and the center of the laser pulse arrives the cathode at t = 0. In the measured phase scan, presented in Fig. 3, in which the beam current is measured using a Faraday cup about 0.5 m downstream the gun, the left-side slope defines the zero value of ϕ_l, since for $\phi_l<0$ the RF field direction is inverse and electrons are not emitted. The phase width in the current increase is determined by the laser pulse length und further broadened by phase jitter or other instabilities. The DC bias of the cathode shifts the slope to lower laser phase values. Therefore the bias was switched off for the laser scan curve used for calibration.

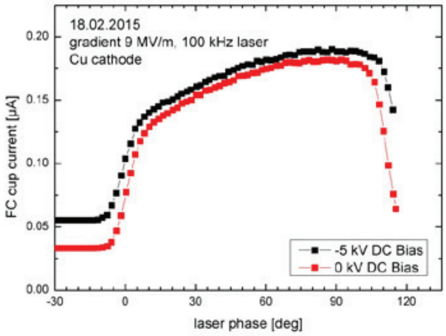

Figure 3: Laser phase scan for phase for zero-point adjustment.

Adjustment of Laser Spot on Photocathode: The next step of the alignment procedure was to center the laser spot on the cathode. The method we used is similar to a current scan for solenoid or quadrupole alignment. But the scan variable is the laser phase and the position of the electron beam spot on a screen downstream is observed. All optical components between the cavity and the screen, i.e. the solenoid, the quadrupoles, the dipole and the correction coils were switched off. The laser spot was moved across the photocathode in horizontal and vertical direction in order to find the position, where the phase scan caused the minimal beam spot shift on the screen. Figure 4 shows the results of the alignment. Beginning with the initial position of the laser spot (in black) with coordinates (0,0) on the virtual cathode, the laser spot was changed to the position (-0.2 mm, 0.8 mm) giving the minimal shift of the electron beam with laser phase. The accuracy of the laser spot alignment is about 100 µm.

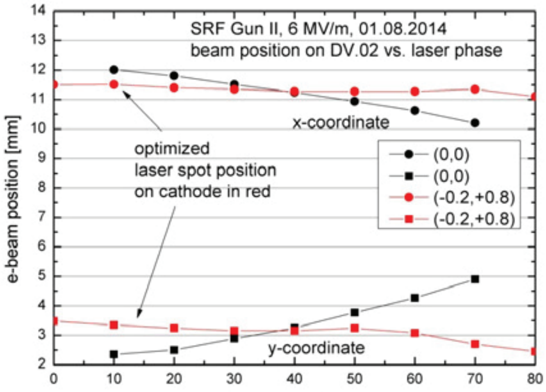

Figure 4: Laser spot centering on the photo cathode. For different laser spot positions the beam position on screen DV02 was measured as function of the laser phase.

Cavity Alignment: During installation the cryomodule of the SRF gun was mechanically aligned in the warm state with respect to the existing ELBE accelerator beam lines considering the shrinking of the cold mass after cool-down. Nevertheless a misalignment was found guiding the electron beam through the first beamline section with the quadrupole triplet. Assuming that the triplet defines the beam line axis, a difference up to 3 mm between the electron beam defining the gun cavity axis and the beam line axis at the quadrupole was found. By means of the beam corrector coils, the screens upstream and downstream the quadrupoles, and by scanning the quadrupole currents, it was possible to determine the differences in position and tilt between these two axes. Then the cavity position and tilt were corrected by the micrometer movers at the gun cryomodule. Repeating this process of cavity realignment and beam based measurement several times, an agreement between the two axes with an accuracy of 50 µm was achieved.

Solenoid Alignment: The SC solenoid can be moved remotely controlled in horizontal and vertical direction with step motors. As the laser spot is centred on the cathode, the electron beam axis defines the target for the solenoid alignment. The solenoid is first switched off and then excited with the nominal current, the centre positions on the first view screen is measured, and the solenoid moved until both positions agreed. Since the beam spot moves on a small circular path when the current is increasing, it seems that there is still a small angle misalignment of the solenoid which cannot be corrected.

Beam Parameter Measurement

Beam Energy and Energy Spread: The energy and energy spread of the beam was measured with the 180° dipole magnet in the diagnostics beamline [7]. The arrangement of the screens DV04 in forward direction downstream the dipole and DV05 in the 180°-direction allows a beam spot size correction of the energy spread measurement, and thus to measure up to very small values. The kinetic energy as function of laser phase for different acceleration gradient is presented in Fig. 5. With increasing gradient the energy maximum in the curves moves towards higher laser phases. Since the gun´s working point is near to this maximum, a higher gradient act twofold on the electron launch field strength. The slope of the curve determines the correlated energy spread produced by the gun.

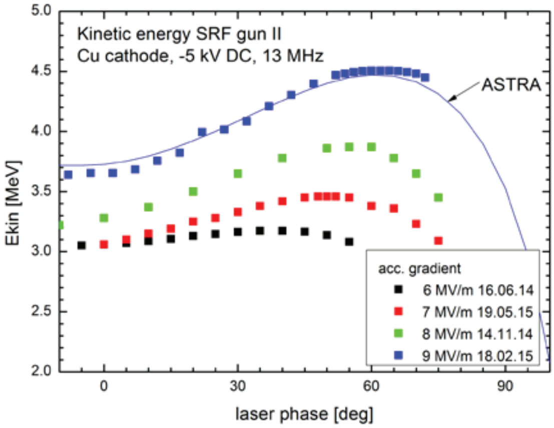

Figure 5: Kinetic energy as function of the laser phase for different acceleration gradients.

ISBN 978-3-95450-183-0

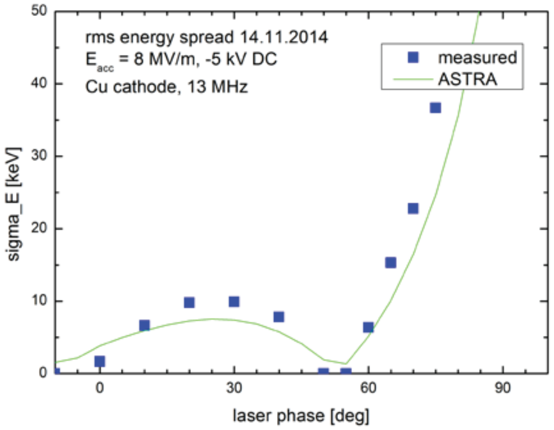

Figure 6: Results of the rms energy spread vs. laser phase for short-pulse laser (3 ps FWHM).

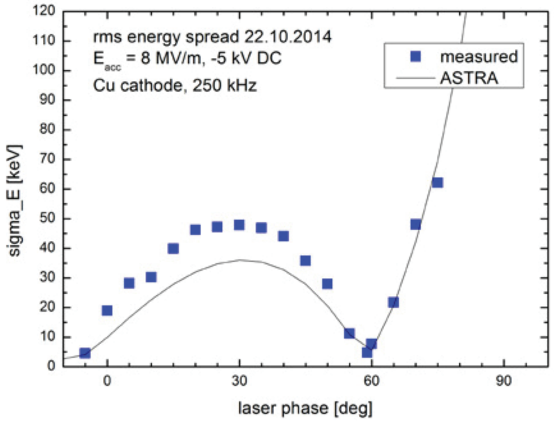

Figure 7: Results of the rms energy spread vs. laser phase for long-pulse laser (10 ps FWHM).

In the case of very low bunch charge, the energy spread is proportional to $dE/d\phi_l$ and to the laser pulse length as the measured curves show in Figs. 6 and 7. The sign of the correlated energy spread is like that the bunch has a high energy tail for the smaller laser phases. The long pulse laser, Fig. 7, produces an about five times higher energy spread than the shorter one. The discrepancy with respect to the ASTRA simulation can be caused by an in reality about 20% longer laser pulse than it was specified.

Transverse Emittance: The transverse emittance measurements were carried out using the quadrupole scan and the moving slit scan technique. Results of both measurements are shown in Fig. 8 for a laser spot between 1 mm and 1.5 mm in vertical and horizontal direction. In general, there are three contributions to the total emittance: thermal emittance, RF field effects, and space charge effects. Here the RF field effect is small and the space charge effect is negligible. The dominant thermal emittance is proportional to the rms laser spot size and in a wide range independent of the laser phase as it is predicted by the ASTRA simulation.

Bunch Length: First results of the bunch length were obtained applying the phase scan method. Thereto the beam from the gun was guided through the dogleg beamline section into the first linac module of the ELBE accelerator. In the module the phase of the second cavity C2 was modulated and the following first chicane magnet together with a YAG screen in the 45°-beamline serve as energy spectrometer. The phase scan method has been described in [10].

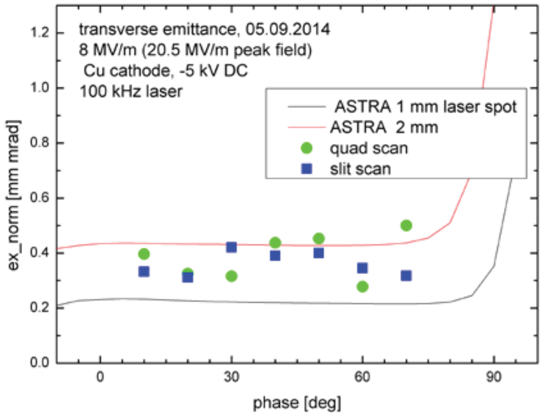

Figure 8: Results of the transverse emittance from moving slit scan method (vertical) and quadrupole scan (horizontal).

Figure 9 presents the ASTRA simulation for the long pulse laser (10 ps FWHM, 100 kHz) and for the short pulse laser (3 ps FWHM, 13 MHz), as well as the measurement values for the short pulse laser at different laser phases. As it can be seen from the simulation the bunch length increases with the laser phase monotonously. Therefore the shortest bunch length appears near to zero laser phase, where indeed a value of 480 fs was measured. The results are preliminary and a correction with respect to beam transport effects from the gun to the linac, especially due to the R_{56} of the dogleg and the drift ($1/\gamma^2$-term), is still required.

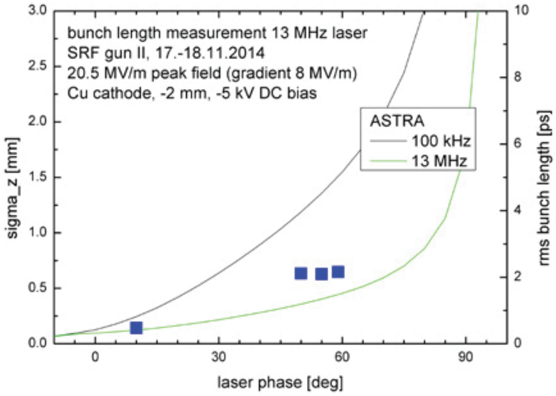

Figure 9: ASTRA results for the rms bunch length vs. laser phase for the 10 ps laser (100 kHz) and the 3 ps laser (13 MHz) and experimental results for the 3 ps laser obtained with the cavity phase scan method.

Dark Current

For normal conducting RF photo injectors dark current is a serious issue and previous results indicate that the mitigation of dark current requires attention for SRF guns too [11]. The sources of dark current are field emitters within the cavity field of the gun which produce electrons escaping the gun. Depending on its properties the dark current can partially gain energy in the accelerator and can be further transported through its beamlines producing beam loss, can increase the measurement background of experiments, or can damage accelerator components. A typical picture of photo electron beam and dark current of the SRF Gun is shown in Fig. 10. For characterization of the dark current we measured its dependence on the acceleration gradient and its energy spectrum.

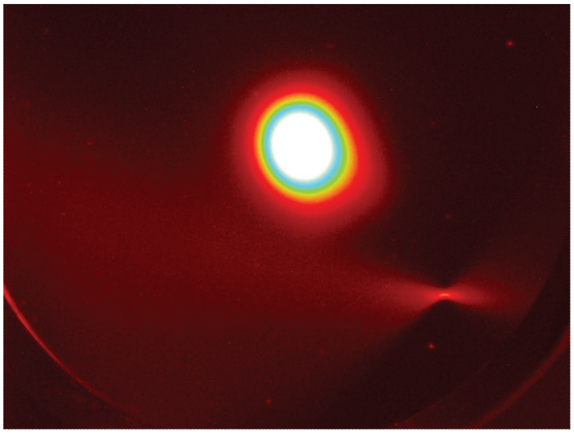

Figure 10: Screen image with photo electron beam spot (200 nA) and the dark current (53 nA) without any focusing by solenoid or quadrupole.

Figure 11 presents a comparison of the dark current for SRF gun II and the previous SRF gun I. Both measurements are performed for clean and polished metal cathodes without photo emission layers, e.g. the field emitters are situated at the cavity surface. It is visible that the onset of field emission is much higher for SRF gun II. At the working point of 18 MV/m the dark current is about 20 nA. The dark current spectrum, presented in Fig. 12, has one single dominant peak at 2.8 MeV whereas the kinetic energy of the photo current beam is at 3.6 MeV. This energy of the dark current is outside the energy acceptance of the dogleg. Still an open question is, to what extend the photo emission layers like Cs_2Te contribute to dark current.

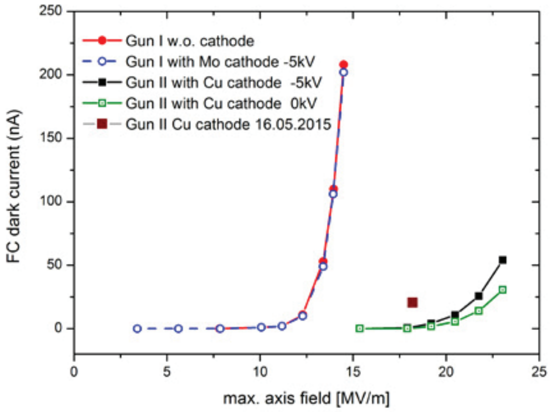

Figure 11: Comparison of dark current measurements as function of peak acceleration field for SRF Gun I and II.

Both results are for clean metallic photocathode without photo emission layers.

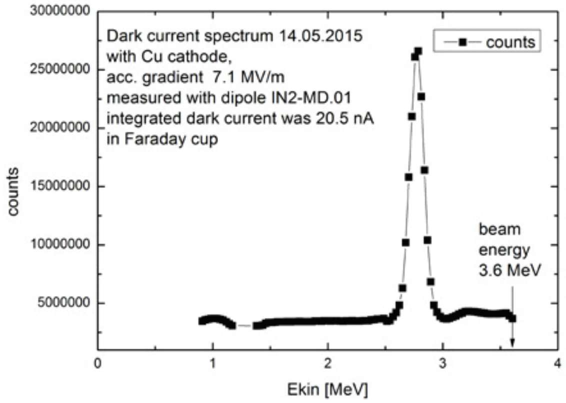

Figure 12: Dark current spectrum of SRF Gun II measured after the test with the bad Cs_2Te photo cathode.

SUMMARY AND OUTLOOK

The ELBE SRF Gun II has been commissioned and beam parameters have been measured with a copper photocathode. A first test with a Cs_2Te photocathode failed and polluted the cavity. Thus the future operation of the gun is limited to about 7 MV/m whereas an acceleration gradient of 10 MV/m was achieved in the first RF tests. The dark current measured to 20 nA is low enough that it will not disturb user operation.

Simulations with actual performance parameters of the SRF Gun II confirm that the gun will be useful for future user operation. Especially higher bunch charges up to 0.5 nC will improve the experimental prospects at ELBE. The crucial point at present is the quality and cleanness of photocathodes. The latest experiences showed that exchange of photocathodes exhibits the highest risk for cavity contamination.

ACKNOWLEDGMENT

We would like to thank the whole ELBE team for their help and assistance with this project. The work is supported by the European Community under the FP7programme (EuCARD-2, contract number 312453, and LA3NET, contract number 289191) and by the German Federal Ministry of Education and Research (BMBF) grant 05K12CR1.

REFERENCES

[1] C. Gulliford et. al., Phys. Rev. ST Accel. Beams 16, 073401 (2013).
[2] B. Dunham et. al., Appl. Phys. Lett. 102, 034105 (2013).
[3] C. Gulliford et. al., Appl. Phys. Lett. 106, 094101 (2015).
[4] A. Arnold and J. Teichert, Phys. Rev. ST Accel. Beams 14, 024801 (2011).
[5] A. Arnold et. al., Nucl. Instrum. Methods Phys. Res. A 577, 440 (2007).
[6] H. Vennekate et al., “Emittance Compensation for an SRF Photo Injector”, Proceedings of SRF’13, Paris, France (2013).
[7] H. Büttig et al., Nucl. Instrum. Methods Phys. Res. A 704, 7 (2013).

[8] T. Kamps et al., Review of Scientific Instruments 79 (2008) 093301.
[9] A. Arnold et al., "Commissioning Results of the 2nd 3.5 Cell SRF Gun for ELBE", Proceedings of LINAC´14, Geneva, Switzerland (2014).
[10] D.H. Dowell et al., Nucl. Instrum. and Methods Phys. Res. A 507, 331 (2003).
[11] R. Xiang et al., Phys. Rev. ST Accel. Beams 17, 043401 (2014).

ISBN 978-3-95450-183-0

TRANSVERSE-EMITTANCE PRESERVING ARC COMPRESSOR: SENSITIVITY STUDY TO BEAM OPTICS, CHARGE AND ENERGY*

S. Di Mitri[#], Elettra Sincrotrone Trieste, 34149 Basovizza, Trieste, Italy

Abstract

Magnetic compression of ultra-relativistic electron bunches in a 180 deg periodic arc, made of identical double bend achromats, has recently been proposed [1]; its performance surpasses, to the author's knowledge, that of any past studies on the subject, by reaching higher compression factors at larger bunch charges, and by upper-limiting the normalized transverse emittance growth to 0.1 µm level. Chromatic aberrations and nonlinearity in the particle longitudinal dynamics are reduced with sextupole magnets. Coherent synchrotron radiation-induced emittance growth is minimized with a proper choice of beam optics and compression factor per cell. The design is supported by analytical considerations that found confirmation in particle tracking results. In this article, we study the dependence of beam final emittance on optics, charge and mean energy. The range of validity of the linear optics approach is discussed, together with limits of applicability of the lattice under consideration.

BACKGROUND

Bunch length magnetic compression is routinely used in high brightness electron linacs driving free electron lasers (FELs) and particle colliders in order to shorten the bunch, that is increase the peak current of the injected beam from few tens to kilo-Amperes (see, e.g., [2] and references therein). To date, magnetic compression is performed in dedicated insertions made of few degrees bending magnets inserted on the accelerator straight path; the compression factor is limited by the degradation of the beam transverse emittance owing to emission and absorption of coherent synchrotron radiation (CSR). In a recent paper [1], we show through analytical and numerical results, that a 500 pC charge beam can be time-compressed by a factor of up to 45, reaching peak currents of up to 2 kA, in a periodic 180 deg arc at 2.4 GeV beam energy, while the normalized emittance is rather immune to CSR, namely its total growth does not exceed the 0.1 µm rad level. To achieve such emittance control, we reformulated the known concept of CSR-driven optics balance [3] for the more general case of varying bunch length, and found that it works for bending angles larger than previously thought advisable and practical. The proposed solution applies adiabatic compression throughout the arc. Optical aberrations and longitudinal nonlinearities are controlled with sextupole magnets.

In the past, several energy recovery linac (ERL) designs [4–6] have attempted to use recirculating arcs for bunch length compression in the energy range 0.2–7 GeV, while keeping the normalized emittance growth below approximately 0.1 µm rad. Double and triple bend achromatic cells were tested for compression factors C < 30. The highest beam charge compatible with the target emittance control was set at 150 pC at the highest energy, and at 77 pC at 3 GeV. While in [5, 6] some degree of optics control was exercised in order to minimize the CSR effect following the optics prescriptions given in [7], in all those designs CSR was mainly neutralized by a low beam charge.

In comparison with the existing literature, our solution allows larger compression factors at high charges, simplifies ERL lattice designs (since, in principle, no dedicated chicane is anymore needed for compression as the arc acts both as final stage of recirculation *and* compressor) and paves the way for repeated compressions at different stages of acceleration, i.e., at different energies. Although it finds an immediate application to ERLs, the proposed CSR-immune arc compressor promises to be applicable to more general accelerator design, thus offering the possibility of new and more effective layout geometries of single-pass accelerators and of new schemes for beam longitudinal gymnastic, both in electron-driven light sources and colliders.

ARC COMPRESSOR DESIGN

The 180 deg arc compressor is made of 6 modified Chasman-Green achromats (one cell shown in Fig.1) separated by drift sections that allow optics matching from one DBA to the next one. The arc is 125 m long (40 m long radius) and functional up to 2.4 GeV. The bending angle per sector dipole magnet is $\theta = 0.2618$ rad and the dipole arc length $l_b = 1.4489$ m. R_{56} of one dipole is 17.2 mm, while that of the entire arc is 207.1 mm. If, for example, a total compression factor C = 45 were required at the end of the arc (1.9 per DBA cell), an energy chirp $h = \left(\frac{1}{C} - 1\right)\frac{1}{R_{56}} \approx 4.7 m^{-1}$ would be needed at its entrance, which corresponds roughly to a fractional rms energy spread of $\sigma_{\delta,0} \approx h\sigma_{z,0} = \frac{1}{E}\frac{dE}{dz}\sigma_{z,0} \approx 0.3\%$ for a 3 ps rms long bunch. Figure 2 shows the nominal optics functions along the arc.

According to the analysis in [1], the normalized emittance growth in the bending plane and in the presence of CSR for a *single* DBA cell can be estimated by (using the same notation than in [1]):

$$\Delta\varepsilon_{nf} = \varepsilon_{nf} - \varepsilon_{n0} \cong \varepsilon_{n0}\left(\sqrt{1 + \frac{\gamma J_3}{\varepsilon_{n0}}} - 1\right), \qquad (1)$$

---

*Work supported by the FERMI project and the ODAC project of Elettra Sincrotrone Trieste.

#simone.dimitri@elettra.eu

ISBN 978-3-95450-183-0

where the single particle Courant-Snyder invariant *2J₃* is:

$$2J_3 = \beta_2 x_3'^2 + 2\alpha_2 x_3 x_3' + \left(\frac{1+\alpha_2^2}{\beta_2}\right)x_3^2 = \tag{2}$$

$$\cong \left(\frac{k_1\rho^{1/3}\theta^2}{2}\right)^2 \left\{\left[\sqrt{\beta_2}\left(C^{4/3}+1\right) - \frac{\alpha_2}{\sqrt{\beta_2}}\left(\frac{l_b}{6}\right)\left(C^{4/3}-1\right)\right]^2 + \left[\frac{1}{\sqrt{\beta_2}}\left(\frac{l_b}{6}\right)\left(C^{4/3}-1\right)\right]^2\right\}$$

It is worth noticing that $(k_1\rho^{1/3}\theta)$ is the rms value of the fractional energy spread induced by CSR in the first dipole magnet of a DBA cell, and that its evolution along the cell (thus the arc), as well as that of the bunch length, is taken into account by the cell compression factor C. The invariant reaches a minimum for $\beta_2 \cong \beta_{2,\min} = \frac{l_b}{6}\left(\frac{C^{4/3}-1}{C^{4/3}+1}\right)$; β_2 is the betatron function inside the dipole magnet, where the beam size is forced to a waist. In the lattice under consideration, $l_b \geq \beta_2$, thereby we should consider average values of β_2 and α_2 inside the magnet; we expect to have minimal CSR effect on the emittance for $\beta_{2,\min} \sim 0.2$ m.

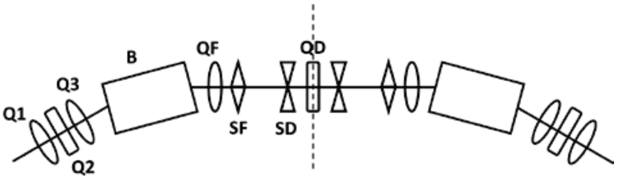

Figure 1: Sketch (not to scale) of the arc compressor DBA cell. Dipole magnets (B), focusing (QF, Q1 and Q3) and defocusing (QD, Q2) quadrupole magnets, focusing (SF) and defocusing sextupole magnets (SD) are labelled. The geometry and the magnets' arrangement is symmetric with respect to the middle axis (dashed line) [1]. Copyright by Europhysics Letters.

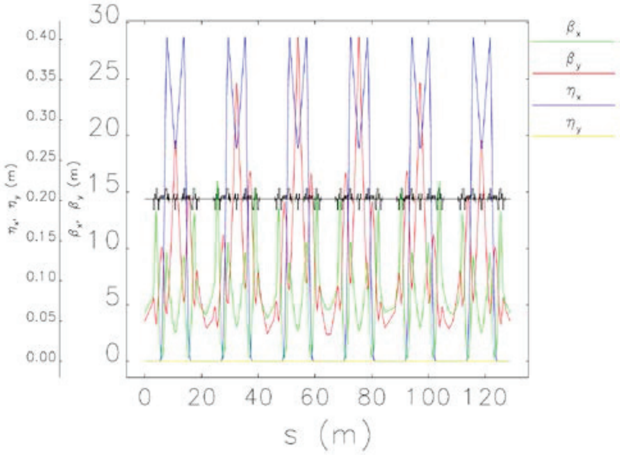

Figure 2: (Colour on-line) Linear optics functions along the 180 deg. arc compressor. Optics functions are quasi-symmetric in each DBA cell of the arc compressor, and totally symmetric with respect to the middle axis of the arc. The minimum β_x is in the dipole magnets, and it ranges from 0.14 m to 0.26 m over the six cells.

In summary, in order to minimize the CSR-induced emittance growth in a periodic 180 deg. arc compressor, we prescribe the use of several symmetric DBA cells with linear compression factor not far from unity in most of the cells. We also impose a beam waist in the dipoles of all the DBAs and find that, unlike in a magnetic chicane [8], there is an optimum value for β_2 inside the dipoles that minimizes the chromatic emittance growth due to CSR.

SENSITIVITY STUDY

The dependence of the final horizontal emittance on the optics, charge and mean energy is investigated through Elegant [9] simulations and compared with analytical predictions based on linear optics analysis. The nominal values of beam and arc parameters are listed in Tab.1. When beam charge and energy is varied, all the other parameters are meant to remain the same. For each charge and energy value, the beam Twiss parameters at the entrance of the arc are varied in order to be matched to the optics periodic solution. This way, the minimum value of β_x in the dipoles is scanned. Being the optics fully symmetric w.r.t. the arc central axis, but only quasi-periodic inside each DBA cell, the betatron phase advance between the DBA dipoles slightly deviates from π. This, together with dipole magnets finite length, CSR transient field at the dipoles' edges and in drift sections, is expected to generate some deviations from the analytical predictions based on Eqs.1 and 2.

Table 1: Beam and Arc Compressor Parameters

Parameter	**Value**	**Units**
Charge	0.1 – 1.0	nC
Mean Energy	0.5 – 2.4	GeV
Initial Bunch Duration, FWHM	10	ps
Linear Energy Chirp	-4.7	m^{-1}
Initial Norm. Emittance, RMS	0.8	μm
Number of Arc DBA Cells	6	
Total Compression Factor	45	

Varying the Optics Parameters

Figure 3 shows, for each charge value, the normalized emittance at the arc end at different simulation steps, each step corresponding to a different optics and thereby to a different value of β_2 (see Eq.2). Since the initial bunch length and the total compression factor are fixed, the final peak current is different for the three charge values (final peak current is 1.5 kA for 0.5 nC; it scales almost linearly with the charge for all the other cases). The initial emittance is also kept the same, for direct comparison of the behaviour of the final emittance in the presence of CSR.

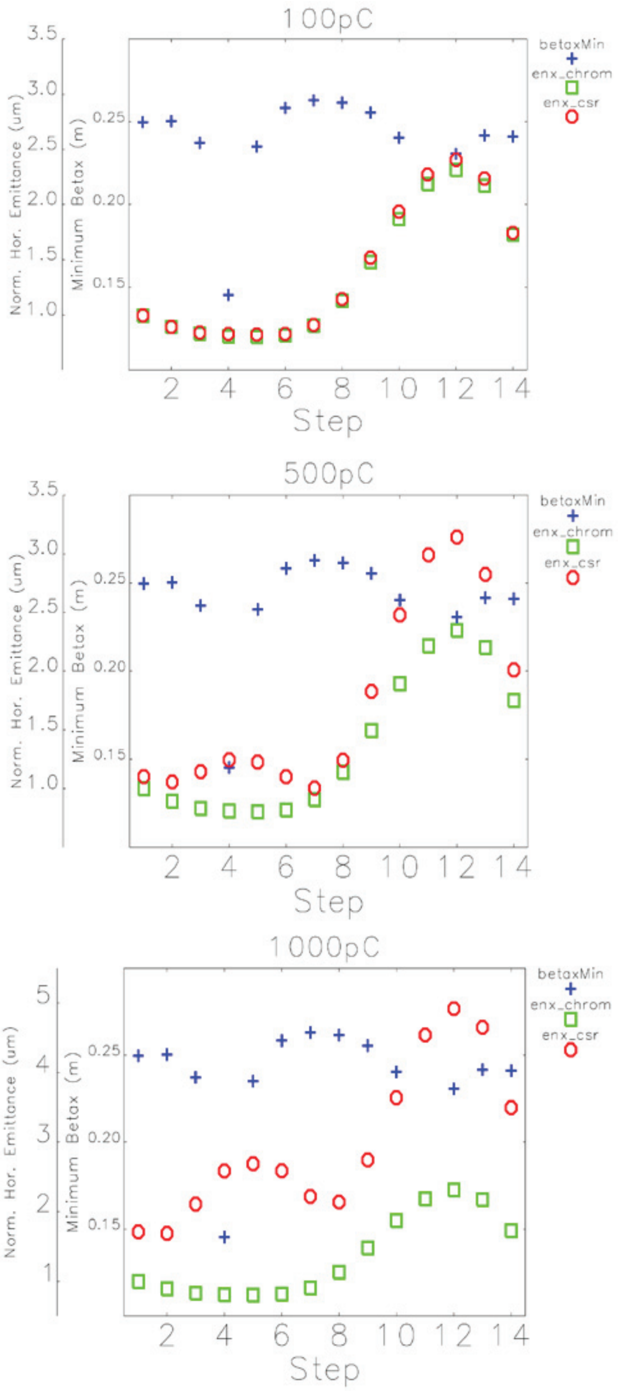

Figure 3: (Colour on-line) Normalized rms emittance and minimum betatron function in the arc dipoles, in the bending plane, at different simulation steps. Each step corresponds to a different periodic optics along the arc (Q1 strength is varied, see Fig.1). Bunch charge is 0.1, 0.5 and 1.0 nC from top to bottom; all other beam parameters are fixed (see Tab.1). Emittance is computed with (*enx_csr*) and without CSR (*enx_chrom*). Optical aberrations up to an including 3rd order and incoherent synchrotron radiation are computed in all simulations. CSR transient field and in drift sections following dipole magnets are included when CSR is turned on.

At 0.1 nC, the CSR effect is negligible over the entire range of β_2 considered; the emittance growth is dominated by chromatic aberrations (sextupole strengths are kept fixed during the scan, thereby aberrations are not corrected at each step).

At the higher charge of 0.5 nC, CSR starts degrading the emittance. The maximum CSR effect (in the figure, this is the distance between *enx_chrom* and *enx_csr*) corresponds to the lowest β_2's value over the scan. The CSR effect is almost fully suppressed at the optimum value of $\beta_2 = 0.26$ m, which is close to the theoretical expectation discussed above. There is a clear correlation between β_2 and the emittance value. It is a remarkable result that smallest β_2 values do not lead to optimum CSR suppression, in agreement with the analytical (and somehow counterintuitive) prediction of Eq.2.

At 1.0 nC, the CSR effect on emittance is visible at all values of β_2, as there is no exact cancellation of CSR kicks at any of the steps considered. The correlation between β_2 and the final emittance is apparent as in the 0.5 nC case.

Varying the Beam Energy

The same lattice considered above has been investigated for different beam mean energies, as shown in Fig.4. We assume that the field of the magnetic elements scale linearly with the beam energy. The difference of the final-minus-initial projected emittance (rms value) with CSR turned on and off is shown for beam charges of 0.1, 0.3 and 0.5 nC. Control of emittance growth at the 0.1 µm level is allowed at energies $E \geq 0.5$ GeV for 0.1 nC, at $E \geq 1$ GeV for 0.3 nC, and at $E > 2$ GeV for 0.5 nC.

For comparison, the analytical prediction based on Eqs.1–2 is shown in Fig.4. In this case, Eq.2 had to be evaluated for each DBA cell. At each cell, the rms energy spread due to CSR and the corresponding emittance increase is summed in quadrature with the energy spread and the emittance at the cell's entrance. After six cells, the difference between the final emittance and the emittance simulated without CSR is computed and plotted in Fig.4. It is worth noticing that for all charges considered, the rms energy spread induced by CSR in the first arc dipole magnet was assumed to be 1/3 of the energy spread predicted by the CSR steady-state emission of a longitudinal Gaussian charge distribution [10]. That value fits well all simulation results, and is supported by a current profile smoother than a Gaussian: it actually resembles a flat-top profile with Gaussian tails at the edges.

ISBN 978-3-95450-183-0

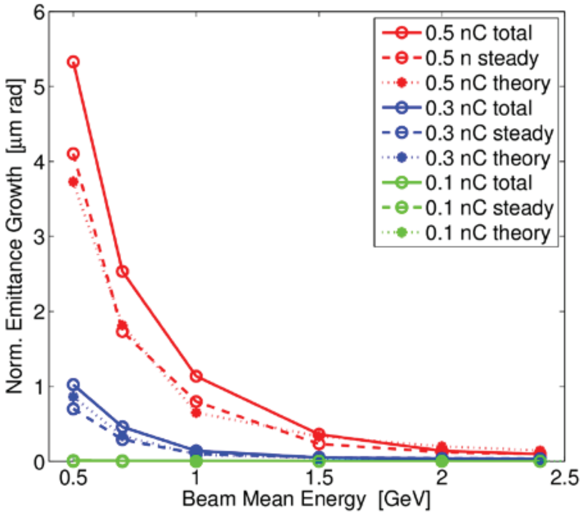

Figure 4: (Colour on-line) Quadratic difference of final-minus-initial normalized emittance (rms values) with CSR turned on and off, at different beam mean energies and bunch charges.

CONCLUSIONS

Linea transfer matrices associated to 1-D steady-state theory of CSR emission allow an estimation of chromatic emittance dilution due to CSR kicks in a multi-bend, 180 deg arc compressor, in a reasonable agreement with Elegant simulation results. The same theoretical background was used to design a compressor arc quasi-immune to CSR-induced emittance growth. The sensitivity of the compressed beam final emittance to optics, beam charge and mean energy has been investigated, and found to be in agreement with analytical expectations.

The simulation of finite dipoles' length, thus of variation of Twiss parameters in the dipoles, of transient CSR fields and CSR in drifts, all effects not included in the theoretical model, together with a partial cancellation of the CSR kicks along the lattice, lead to residual CSR-induced emittance growth at 1 nC (see Fig. 3), whereas it is still neutralized at 0.5 nC. A discrepancy as large as 20% in the final emittance value is found between theory and simulation at the highest charges and lowest beam energies. Nevertheless, the analytical prediction remains close to the numerical results when only CSR steady-state emission in dipoles is considered (see Fig. 4).

The most remarkable result is, in our opinion, the evidence of a correlation between β_2 and the final emittance value, and that the smallest β_2's value does not lead to optimum CSR suppression, in agreement with the analytical (and somehow counterintuitive) prediction of Eq.2. In conclusion, non-steady state CSR effects do not substantially affect the validity of the analysis; this can be used as a guidance for lattice design, possibly further improved by numerical optimization algorithms.

ACKNOWLEDGMENT

The author acknowledges M. Cornacchia (Elettra) for useful discussions and a careful reading of this article.

REFERENCES

[1] S. Di Mitri, M. Cornacchia, Europhys. Letters **109**, 62002 (2015).
[2] S. Di Mitri, M. Cornacchia, Physics Reports **539** (2014) 1–48.
[3] S. Di Mitri, M. Cornacchia and S. Spampinati, Phys. Rev. Letters, **110**, 014801 (2013).
[4] J.H. Wu, J.B. Murphy, V. Yakimenko, I. Ben-Zvi, W. Graves, E. Johnson, S. Krinsky and T. Shaftan, in Proc. of the 2001 Part. Accel. Conf., RPAH012, edited by P.W. Lucas and S. Webber, Chicago, IL, U.S.A. (2001).
[5] M. Shimada, K. Yokoya, T. Suwada and A. Enomoto, Nucl. Instrum. Meth. Phys. Research, Sect. A **575**, 315 (2007).
[6] M. Borland and V. Sajaev, in Proc. of the 24th Linear Accel. Conf., TUP023, edited by B. Laxdal and P.W. Schmor, Victoria, BC, Canada (2008).
[7] R. Hajima, Nucl. Instrum. Meth. Phys. Research, Sect. A **528**, 335 (2004).
[8] S. Di Mitri, M. Cornacchia, Nucl. Instr. Meth. Phys. Res. A **735** (2014) 60–65 and references therein.
[9] M. Borland, Advanced Photon Source LS-287 (2000).
[10] E. L. Saldin, E. A. Schneidmiller, and M. V. Yurkov, Nucl. Instrum. Meth. Phys. Research, Sect. A **398**, 373 (1997).

CURRENT MEASUREMENT AND ASSOCIATED MACHINE PROTECTION IN THE ERL AT BNL*

T. Miller[†], D.M. Gassner, J. Jamilkowski, D. Kayran, M. Minty, J. Morris, B. Sheehy
Brookhaven National Lab, Upton, NY 11973, USA

Abstract

The R & D Energy Recovery LINAC (ERL) at Brookhaven National Laboratory (BNL) requires accurate and precise current measurements for logging and for machine protection. In this paper we present techniques used to measure the beam charge and current during commissioning in pulsed and CW operating modes. The strategy for ramping up the total beam current is discussed, including the motivation for developing different operating modes with specific pulse structures, tailored by the constraints imposed by the operating limits of the instrumentation. The electronics packages used for integration and digitization are presented along with methods of synchronization. Finally, results of measurements made during the first beam tests are presented.

INTRODUCTION

The ERL is operated in a wide variety of operating modes; where the beam parameters, such as pulse structure, charge, and average current, vary widely from one mode to another. This presents a challenge to accurately measure the charge and current of the beam under all conditions. The two most prevalent operating modes are the “High Charge” and “High Current” modes [1]. The operating parameters for these modes are summarized in Table 1. An “Instrumentation” mode (not shown in the table) is also used with a repetition rate of only 1 Hz and where the total charge deposited on insertion instruments is limited and protected by the machine protection system (MPS).

Table 1: Operating Modes

Parameter	High Charge	High Current
Energy	2.0 – 20 MeV	
Current	50 mA	500 mA
Charge	0.05 – 5 nC	0.7 nC
Bunch Rep. Rate	9.38 MHz	704 MHz
Bunch Length	30 ps	20 ps
Macrobunch Rep.	5 kHz	5 kHz
Macrobunch Length	0 – 7 μs (ICT) up to CW (DCCT)	
Train Rep. Rate	1 Hz	
Train Length	0 – 900 ms	

Instrumentation is required to report the beam charge and/or current while operating in these modes. Table 2 summarizes the requirements that are met by using multiple instruments and tailoring the operating modes to work within the limitations of each instrument.

Table 2: Measurement Requirements

Parameter	**Current**	**Bunch Charge**
Range	50 μA – 500 mA	10 pC – 5 nC
Accuracy	1 %	5 %
Resolution	0.1 % (at I=500 mA)	0.1 % (at 5 nC)

Among the dense population of instrumentation on the beam line [2], a Faraday Cup is mounted to the end of a diagnostic beam line for direct measurement of beam charge. The high-power beam dump is isolated and also used as a Faraday Cup. Nondestructive charge measurements are made by an Integrating Current Transformer (ICT), located just downstream of the gun. Measurements with the ICT are limited to beam pulses under 7 μs at a repetition rate of less than 10 kHz. For pulse trains longer than 100 μs, the average current is measured in two places by DC Current Transformers. The locations of these instruments are shown in the symbolic layout of the machine in Fig. 1.

CURRENT MEASUREMENT

Faraday Cup

The two Faraday Cups, one on the diagnostic beam line and one at the beam dump, are unbiased and directly connected to ¼-inch Heliax cables (Andrews LDF1-50) that bring the signals back to integrating electronics. A BNL designed amplifier is used with High and Low gain settings for both Pulsed & DC modes. The calibration in Pulsed mode corresponds to 9 μA/V and 90 μA/V for the High and Low gain settings respectively. The amplifier output is fed to a BNL designed 8-channel integrator with Reset and Gate functions controlled by the ERL Timing System to correspond with the beam pulse structure. The integrator’s output is digitized by a VMIC3123 digitizer that is triggered at the beginning of the beam pulse train.

Preliminary commissioning of the beam with the Faraday Cup (FC) in the diagnostic beam line was made with a direct connection to an oscilloscope. The voltage signal induced by the impinging beam is slowed by capacitance in the system. This capacitance was calculated from the discharge portion of the FC response to dark current produced during a 10 ms RF pulse, as shown in Figure 2.

[†] tmiller@bnl.gov

*Work supported by Brookhaven Science Associates, LLC under Contract No. DE-AC02-98CH10886 with the U.S. DOE

ISBN 978-3-95450-183-0

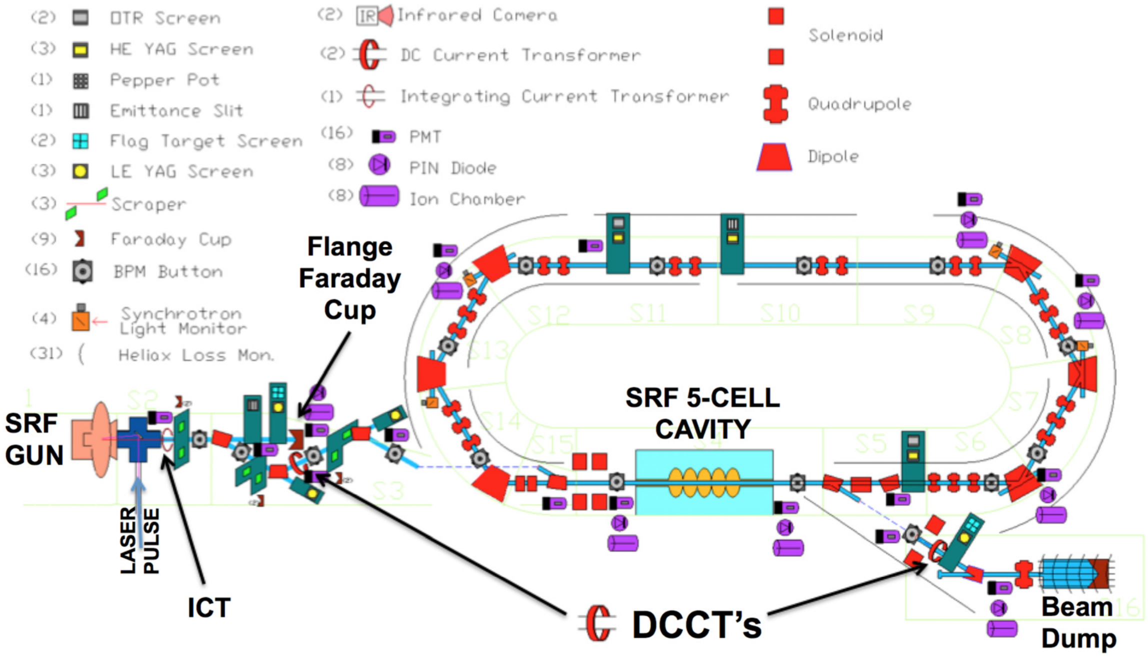

Figure 1: Symbolic layout of ERL with instrumentation.

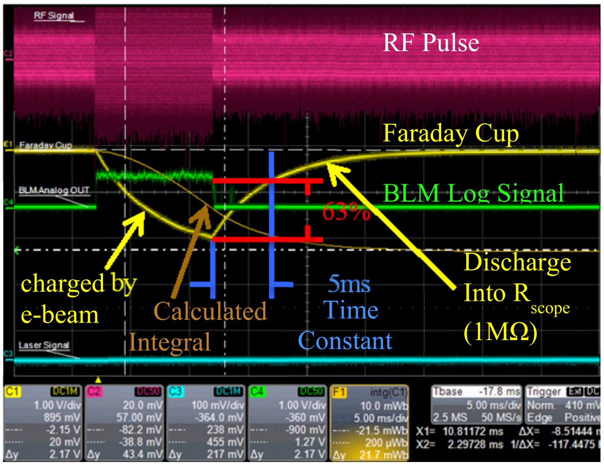

Figure 2: Faraday cup signal with pulsed beam – dark current.

The FC signal dropped by 63 % (one time constant) in 5ms as the capacitance discharged. Using equation 1 below with 1 MΩ from the scope input impedance and the measured 5 ms time constant;

$$\tau = RC \tag{1}$$

the system capacitance was found to be 5nF. Equation 2 below gives the total charge deposited by the dark current during the 10 ms pulse.

$$Q = \int I(t)dt = \frac{1}{R}\int V(t)dt\,. \tag{2}$$

Using equation 3 with equation 2 for Q, R=1 MΩ from the scope input impedance, T=10ms duration of the beam during the RF pulse, and the integrated voltage of 21.7 mV-s from the scope function;

$$\bar{I} = \frac{Q}{T} = \frac{1}{RT}\int V(t)dt \tag{3}$$

the average dark current during the RF pulse was found to be 2 μA, similar to measurements presented earlier [3]. Using the system capacitance, the charge from the photocurrent was found from Q=CΔV; where ΔV is the peak-to-peak change in voltage during the photocurrent pulse and C is the system capacitance of 5nF. This was measured in Fig. 3 to be 158 mV; giving a charge of 0.8 nC per pulse, considerably higher than measurements presented earlier [4]. Figure 3 shows three consecutive photocurrent pulses superimposed on the slow curve from

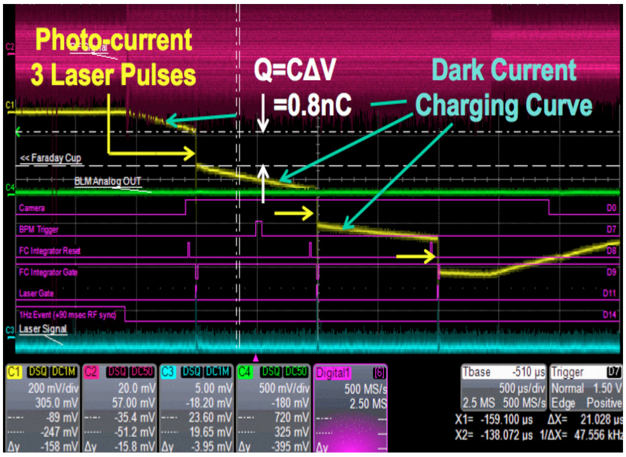

Figure 3: Faraday cup signal with photo current.

the dark current that contribute to the FC signal with each photocurrent pulse.

Integrating Current Transformer

For nondestructive charge measurement of the beam, an integrating current transformer is installed just downstream of the gun. It is installed in an in-flange type 6-inch Conflat® that includes an internal uncoated ceramic break. Made by Bergoz Instrumentation [5], its part number is ICT-CF6-60.4-070-05:1-H-UHV-THERMOE with a turns ratio of 5:1. Although the target vacuum level of 5×10^{-9} torr was met without the need for bake-out of the beamline, provisions for bake-out were made in the system design in the event it becomes necessary. Consequently, an internal type E thermocouple was included for temperature monitoring. This non-standard feature was developed on request for the ERL. The bake-out must be monitored as irreversible modifications to the toroid are expected to occur when the magnetic core is heated beyond 100 °C, with an immediate consequence of a loss of magnetic permeability. Experience of the manufacturer shows that while no loss is expected at 100 °C; at 168 °C, there can be as much as 50 % irreversible loss, resulting in an increase in output droop. The extent of the output droop depends on the transformer's turns ratio. With a 5:1 turns ratio, the droop is estimated to be about 6 %/µs. With a 50 % loss of permeability, the droop is expected to double to 12 %/µs.

This ICT is used in conjunction with a Beam Charge Monitor (BCM) electronics module, from Bergoz, that provides an Integrate-Reset-Hold (IHR) function. The device is triggered just before a beam pulse such that its adjustable integration window (0 – 7 µs) spans the beam pulse. Due to this limited range of integration window, only beam pulses shorter than 7µs can be measured. The BCM can be retriggered at a repetition rate of up to 10 kHz. There are 7 gain settings providing full-scale ranges of 0.8 to 40 nC. The sensitivity of the ICT + BCM-IHR is given in equation 4.

$$n/Q = \left(\frac{V_{FS}}{Q_{FS}}\right)_{BCM} * \left(\frac{n_{FS}}{V_{FS}}\right)_{Digitizer} \qquad (4)$$

Thus for the most sensitive scale (40 dB gain), we find n/Q = 655 counts/nC; where the BCM full-scale output voltage $(V_{FS})_{BCM}$ is ±10V, the BCM full-scale charge $(Q_{FS})_{BCM}$ is 0.8 nC, the digitizer full-scale input voltage $(V_{FS})_{Digitizer}$ is ±10V, and the full-scale number of counts for the 16-bit digitizer $(n_{FS})_{Digitizer}$ is 65,553 counts.

As it is important for the timing of the IHR integration window to span the beam pulse (or "macrobunch" of pulses), the machine operating procedures call for a verification of the timing alignment on an oscilloscope, at the start of each operating shift, as shown in Fig. 4.

The measured beam pulse, or macrobunch shown in Fig.4, consisted of 9 photocurrent pulses at 9.38 MHz repetition rate. The total integrated charge within the 7 µs window was 1.68 nC. Thus the charge per pulse was 0.19 nC/pulse.

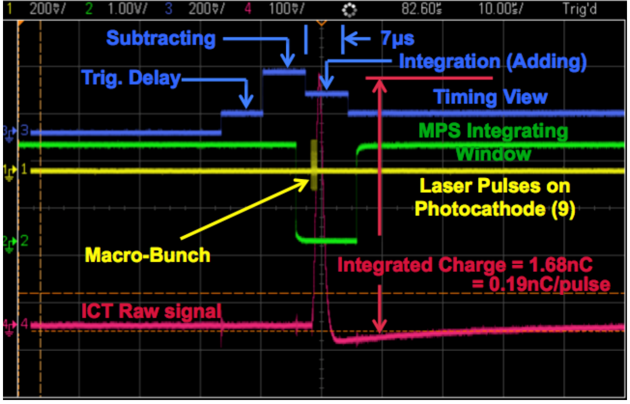

Figure 4: ICT measurement & timing signals.

DC Current Transformer

For beam pulse trains longer than 100 µs, two DC current transformers (DCCT), model NPCT (New Parametric Current Transformer) made by Bergoz are installed in the Zig-Zag injection section and in the extraction beam line. Installed over an uncoated ceramic break, this device is also sensitive to bake-out temperatures over 80 °C. Therefore, a custom cooling coil was fabricated and installed between the bake-out heating blanket (over the ceramic break) and the DCCT to prevent the core from overheating. The DCCT with its matched electronics package from Bergoz has four output scales ranging from ±20 mA to ±20 A. A ±10 V analog output voltage is provided by the amplifier module delivered with the transformer. The 70 µs rise time response of the DCCT gives about 50 us of flat-top with a 100 µs long macrobunch. Only the flat-top portion of the signal is considered as valid data during the digitization process.

Digitization

A VMIC3123 [6] digitizer handles macrobunch level data acquisition for the Faraday Cup and ICT signals. Sampling at 100 kHz, it is triggered at the start of a train of macrobunches and collects up to 320 ms of data. The digitizer may be upgraded once the ERL begins operating with pulse trains longer than 320 ms. The data is then processed in the VME Front End Computer (FEC) to pick out a peak value for each macrobunch. The signals are held long enough by the integrating electronics to ensure that a peak value will be captured in one of the 100 KHz samples for every macrobunch.

The VMIC3123 system (including Front End Computer software) can digitize and deliver up to 320 ms of data once per second. Configuration of the system involves setting the variable "dataArraySizeS" for the train length, "samplesPerPeakPeriodS" for the time between macro-bunches, and "peakThresholdS" for the minimum level recognized as a macrobunch peak. An upgrade to the ERL Timing Control Manager is planned that will update these values as the ERL timing changes.

An algorithm processes the Faraday Cup data each second to mask transients in the integrator's output caused by timing triggers that interfere with the peak-finding algorithm. As proper suppression of these transients requires a redesign of the integrator, a mask signal is generated, coincident with the offending integrator-timing signal, and is digitized at 100 KHz along with the integrator's output signal. Only data outside of the mask signal is used in the peak-finding algorithm. The filtered peak-finding software is currently being run on a Linux system using raw data signals delivered from the VMIC3123 in the FEC.

The analog output of the DCCT's NPCT electronics is digitized at 625 kHz by a National Instruments PXI-6289 data acquisition module. Work is underway to implement a triggered acquisition of the DCCT's measurement of the beam current of macrobunches longer than 100 µs. The system will average samples taken over the flat-top portion of the macrobunch measurement. In order to measure only the signal's flat-top, the digitizer will begin sampling the DCCT signal at the start of a pulse train (at 1 Hz) and also sample a gate pulse that defines the useable portion of the signal. Only the DCCT data that falls within the windows defined by the gate signal is averaged to report the current at the end of the train. The gate signal is delayed to account for the 70 µs of rise time and ends at the end of the macrobunch. Figure 5 shows the response of the DCCT (Ch1) to a 200 µs train of pulses (Ch3) at 9.32 MHz.

Figure 5: DCCT response to 200 µs long macrobunch; DCCT signal on yellow trace, pulse train on blue trace.

TIMING & PULSE STRUCTURE

In order to measure the charge and/or current proficiently in pulsed mode, the beam pulse structure is tailored by the limiting parameters of the ICT; which can measure only a 7 µs window at a repetition rate of up to 10 kHz. First beam tests were made with a single ~30 ps laser pulse on the photocathode at a 1 Hz repetition rate. Ramping up average current consists of additional pulses being grouped together into a macropulse. The repetition rate of the pulses within the macropulse is driven by the laser clock frequency at 9.38 MHz. The pulse count per macrobunch can be increased up to 65 pulses to fill the 7 µs maximum window of the ICT. However, to ensure that the macrobunch fits reliably within the ICT integration window, a maximum of 50 pulses is chosen. A maximum charge of 550 pC/pulse was demonstrated from the 703 MHz SRF Photoinjector in the most recent beam tests of June 2015 [7] yielding a maximum possible charge per 50-pulse macrobunch of 27.5 nC. Although these high charge pulses were demonstrated, early commissioning techniques utilized pulses of under 200 pC to minimize space charge effects; thereby resulting in a maximum of 10 nC per 50-pulse macrobunch.

For low power commissioning of the beam line, a technique of ramping up the current was devised, as shown in Fig. 6, that keeps a steady average current over the length of the RF pulse. Recent commissioning of the

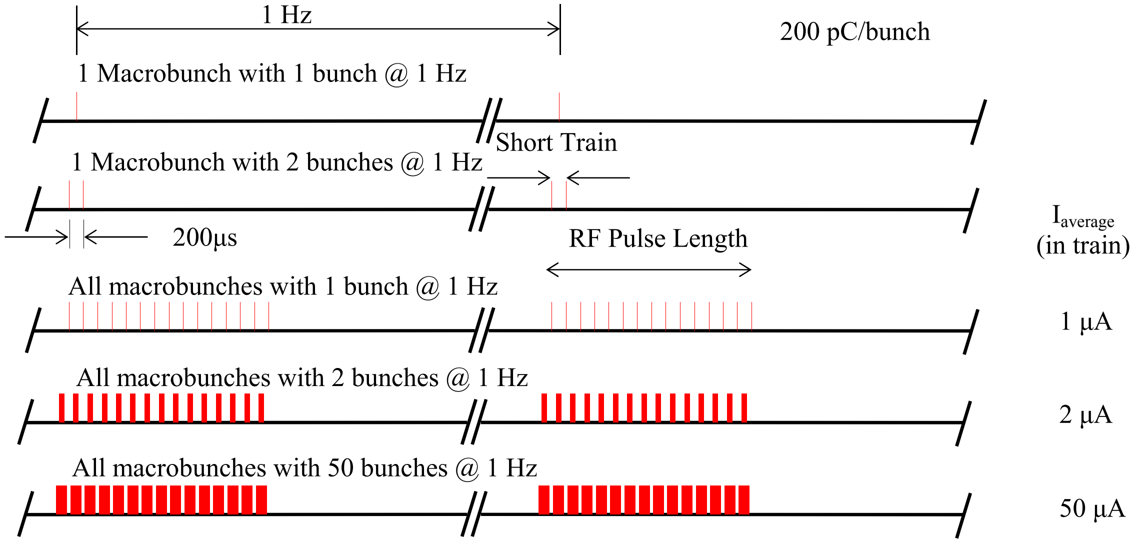

Figure 6: Pulse Train Structure for ramping up total beam current. $I_{average}$ is based on 200pC/bunch.

ISBN 978-3-95450-183-0

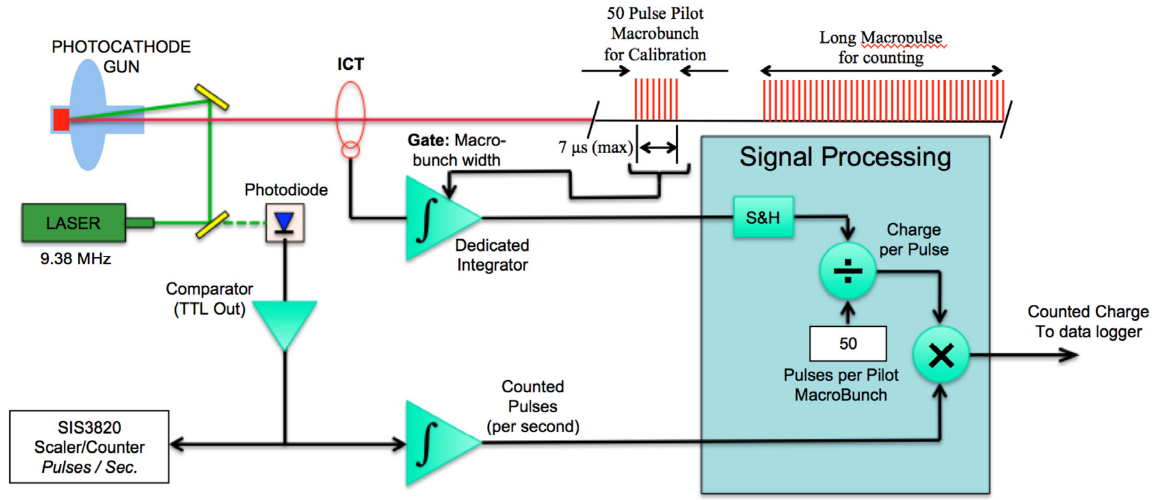

Figure 7: Pulse counting scheme with pilot pulse timing structure.

SRF gun required limiting the SRF cavity pulse to <10 ms due to vacuum excursions. The duty factor is planned to increase as the cathode is conditioned over time. To keep the average current steady, a continuous train of macro-bunches was produced for the length of the RF pulse. Although the BCM electronics are capable of 10 kHz, a dedicated integrator used to process the ICT signal for the MPS functions up to 5 kHz only. Therefore, a train of macrobunches was formed at 5 kHz. Beginning with a single 200 pC bunch in each macrobunch results in an average current of 1 µA (200 pC × 5 kHz) within the train. Further increases in current are made by adding bunches to each macrobunch in the train up to 50, resulting in an adjustable in-train current of 1 – 50 µA. The total average current then depends on the duty factor of the RF pulse.

PULSE COUNTING

To reach high average currents, the macrobunch length will eventually have to grow beyond the limited 7 µs maximum integration window of the ICT. To extend the charge measurement to accommodate these longer macrobunches, a pulse counting technique is used to count the number of laser pulses every second.

A photodiode (Thorlabs DET 36 A, 14 ns rise time) samples the laser beam striking the first turning mirror after the laser exit. A comparator (Pulse Research Labs PRL-350 TTL, 0 mV threshold) converts the analog photodiode pulses to TTL pulses that are counted by a scaler/counter. The response time of the photodiode is long enough to trigger the comparator, but short compared to the laser repetition period of 106 ns. The scaler (SIS 3820, from Struck Innovative Systeme) is reset every second and reports the total pulses/sec counted to the Control System.

Using the pulse count to predict the total charge requires an accurate calibration of the charge per pulse. A pulse structure implementing a “pilot pulse” is proposed, as shown in Fig. 7, with long pulse trains to allow the ICT to measure a sample of the pulse train and provide a calibration.

MACHINE PROTECTION

In addition to measuring and logging beam current, the ICT is also used to report macrobunch charge to the machine protection system (MPS) to shut down the beam in the event that measured charge levels exceed thresholds for insertable destructive instrumentation. A dedicated integrator is used to process the BCM output labeled “Signal View” (ICT signal before integration). An amplifier is used to buffer the output and add an offset adjustment to drive the integrator’s input. Although the electronics is capable of 10 kHz operation, this dedicated integrator is limited to operation at 5 kHz. The charge reported by the ICT is compared to four individual thresholds for the following groups of instruments: Profile Monitor, Dipole Profile Monitor, Emittance Slit Mask, & Halo Monitors. The insertion of an instrument enables the corresponding group threshold for comparison to the measured charge. Operation in a mode called “Instrumentation Mode” will limit all macrobunch lengths to under 7 µs (optimally only 50 pulses).

Figure 7 shows a proposed scheme to sample and hold the integrated charge measured from one “Pilot Macrobunch”. Although a platform on which to implement the scheme shown has not been specified, it would divide the pilot macrobunch charge by the number of bunches to arrive at a calibration coefficient (charge/bunch) that would be multiplied by the total number of counted pulses (bunches) in one second; thereby calculating the total beam charge per second, or average beam current.

CONCLUSION

Current measurements at the BNL ERL are accomplished with three instruments, Faraday Cup (FC), Integrating Current Transformer (ICT), and DC Current

Transformer (DCCT). The FC provides destructive charge measurement at the end of the diagnostic beam line; while the ICT provides operational measurement of the beam charge, but limits the beam duty factor to < 3.15% (7 µs × 5 kHz × 90 %). A laser pulse counter provides a check of the total pulses per second and a scheme to derive total beam charge is proposed.

The beam pulse structure is tailored to fit within the timing constraints of the ICT and associated electronics. For longer pulse trains, the DCCT provides average current measurement over 1 second at two places: zig-zag injection beam line and the extraction beam line. The MPS offers protection of the insertion instruments against over exposure to beam charge with separate thresholds for four different instrument groups.

Future Plans

A technique of alerting the MPS in an event that more than 50 pulses are generated per macrobunch while operating in the "Instrumentation Mode" needs to be implemented. Work is ongoing to implement a differential DCCT current measurement [8] between injection and extraction beam lines with an interface to the MPS.

ACKNOWLEDGEMENTS

The authors acknowledge the contributions of Ilan Ben-Zvi, W. Xu and other members of the Accelerator R&D Division, Instrumentation Systems Group, Accelerator Components & Instrumentation Group especially C. Dawson, C. Degen, L. Desanto, S. Jao, the Controls Group especially P. Harvey, P. Kankiya, the Vacuum Group, the Collider Mechanical Support group especially S. Seberg, and members of the Design Room.

REFERENCES

[1] D. Kayran, et al., "Status of High Current R&D Energy Recovery LINAC at Brookhaven National Lab", THP006, PAC2011, New York, NY, USA

[2] D. Gassner, et al., "Status of the BNL ERL Instrumentation", PS11, proceedings of the ERL2013 Workshop, Novosibirsk, Russia

[3] D. Kayran, et al., "First Test Results from SRF Photoinjector for the R&S ERL at BNL", MOPRI064, proceedings from IPAC2014, Dresden, Germany

[4] W. Xu, et al., "First Beam Commissioning at BNL ERL SRFG", TUPMA049, proceedings from IPAC2015, Richmond, VA, USA

[5] Bergoz Instrumentation, http://www.bergoz.com/

[6] VMIC, a GE Fanuc company, http://www.geautomation.com/download/vme-3123a/5385

[7] D. Kayran, et al., "Status and Commissioning of the R&D ERL at BNL", MOPDTH014, ERL2015, Stony Brook, NY, USA, these proceedings.

[8] P. Cameron, "Differential Current Measurement in the BNL Energy Recovery Linac Test Facility", C-A/AP/#203, C-A Dept., BNL, Aug. 2005.

CURRENT STATUS OF THE MESA PROJECT*

R. Heine†
Institut für Kernphysik, Johannes Gutenberg-Universität, D-55099 Mainz, Germany

Abstract

Most of the components of MESA are approaching a finalised design. Issues concerning beam dynamics, cryomodule operation and adaptations of the existing building constraints will be discussed. The current status will be presented.

INTRODUCTION

The Mainz Energy-recovering Superconducting Accelerator (MESA) is a low energy CW recirculating electron linac for particle physics experiments to be built at the Institut für Kernphysik (KHP) of the Johannes Gutenberg University of Mainz (JGU). MESA will be operated in two modes: the first is the external beam (EB) mode; the beam is dumped after being used with the external fixed target experiment P2. The current required for P2 is 150 μA with polarised electrons at 155 MeV. The second mode is energy recovery (ER). The experiment served in this mode is an (pseudo) internal fixed target experiment named MAGIX. It demands an unpolarised beam of 1 mA at 105 MeV. In a later stage-2 the ER-mode current shall be upgraded to 10 mA.

MAIN ACCELERATOR LATTICE

The accelerator has to fit into the existing building of the KPH. The place foreseen for MESA has been used by the P2 predecessor experiment, which has ended data taking in 2012 and the caves have been emptied recently to prepare the place. Designing an accelerator to fit into an existing building imposes many constraints to the lattice, rather due to civil engineering requirements, than accelerator physics.

The lattice design of the accelerator is a double sided recirculating linac with vertical stacking of the return arcs (see Fig. 2), which is a very compact set up in lateral dimensions. A similar design is planned for the LHeC ERL test facility [1]. The EB mode optics is that of a simple recirculating linac. In ER mode the beam will pass the main linac modules twice on the accelerating phase and also twice on the decelerating phase. Afterwards the beam is dumped at injection energy of 5 MeV. The lattice consists of:

- four spreader sections for vertically separating and recombining the beam,
- five 180° arcs for beam recirculation,
- two chicanes for the injection and extraction of the 5 MeV beam,

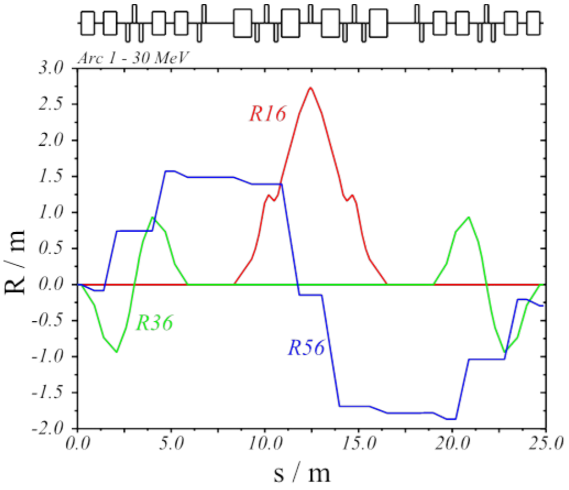

Figure 1: Dispersion and momentum compaction of the 30 MeV arc including the beam spreaders.

- an 180° bypass arc for ER mode incorporating the MAGIX experiment
- and a beam line to the P2 experiment.

The accelerated and the decelerated beam share the same arcs, therefore special care has to be taken on the optics of the low energy recirculations to avoid beam loss. To push the beam break up limits for ER-mode towards 1 mA the beta functions inside the main linac modules have to be of the order of magnitude of the length of the modules itself and have to be the same for all passes. The arcs are made of two double bend elementary cells, with a maximum of horizontal dispersion in the middle of the arc (Fig. 1). The arcs are as a whole achromatic. The momentum compaction R56 of each arc can be adjusted from 0.5 cm/% to -0.5 cm/% to allow for isochronous as well as non-isochronous operation. The optics of an arc is only slightly depending on the R56 and can be readjusted easily. The non-isochronous operation is needed to deliver a beam with low energy spread to the external experiment P2. The energy recovery shall also take place with phase focussing.

The design tools used for lattice design are, besides an in-house matrix optics program “beam optics”, which features an online preview of the optical functions, MAD-X [2] for the automatic optimisation routine and PARMELA [3] to allow for space charge and pseudo damping of the main linac cavities by using field data obtained from SuperFish. Due to the low injection energy and the large dynamic range of the beam current, the influence of space charge effects on the optics is strong and has to be considered.

The PARMELA tracking simulations of the ER-mode (Fig. 3) show a strongly peaked horizontal beta function in the 2nd arc, which is even stronger for the decelerated beam.

---

* Work supported by the German Science Foundation (DFG) under the Cluster of Excellence “PRISMA”

† rheine@uni-mainz.de

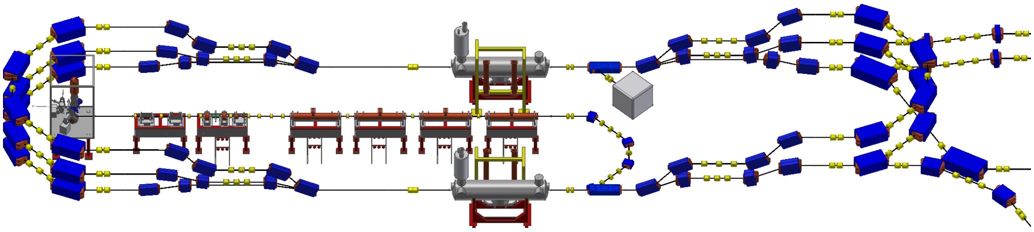

Figure 2: Overview of the MESA lattice. The experiments, as well as the energy-recovery arc, that continue to the right of the picture, have been cropped to enhance visibility.

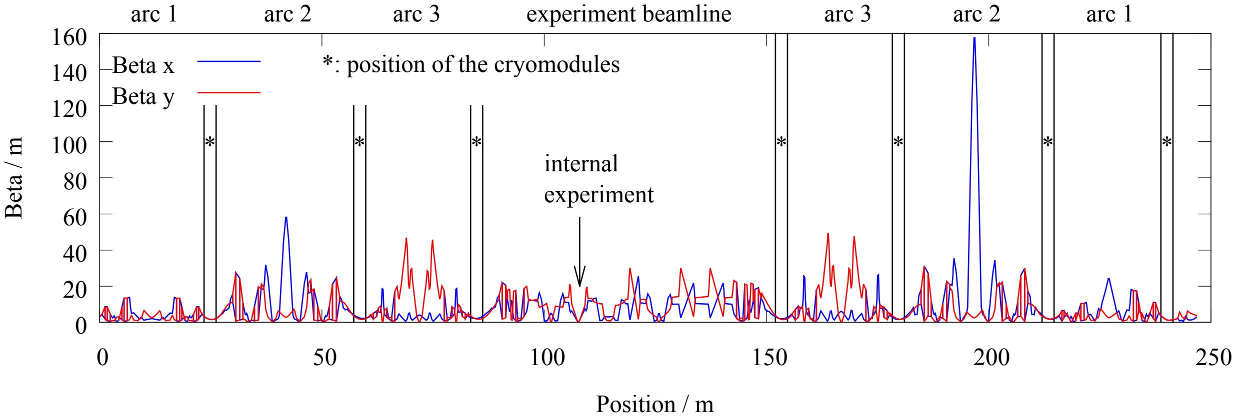

Figure 3: Beta functions of the ER mode lattice obtained from tracking simulation with PARMELA. The simulation starts after the first pass of the first cryomodule and ends at the beam dump. The injector and the first pass of the cryomodule are excluded. The simulation assumes a beam current of 150 μA.

This may lead to beam loss, deteriorating the efficiency of the energy-recovery. Optimisation of this arc is ongoing.

Optics for both EB and ER mode have been successfully tracked in PARMELA, the results as well as the development of the lattice can be followed in [4, 5].

MAIN LINAC MODULES

As can be seen in Fig. 2 the main linac will have two ac-celerating modules. In [6] several accelerator modules have been considered for their suitability for MESA. The modifi-cations necessary to the chosen ELBE-Rossendorf cryomod-ules [7] to fit the needs of MESA result in the MEEC module (MESA Enhanced ELBE Cryomodule). The changes to the HZDR design are as follows:

- sapphire feedthroughs for the couplers of higher order mode dampers, which shall enhance the thermal stability of the cavity in CW operation,
- the Rossendorf tuner is replaced by XFEL tuner which incorporates piezo actuators to fight against microphonics,
- alteration of the liquid helium (LHe) tank and of the interior of the cryostat to fit in the above

All adaptations will be planned and executed by the manufacturer RI Research Instruments GmbH, Bergisch-Gladbach. The cavities will undergo the preparation process according to European XFEL specification. More information can be found in [8]. Besides these adaptations RI will also provide cold boxes and control system for the 2K/4K LHe production. So KPH only has to provide the interfaces from the 4K LHe supply and the sub-atmospheric pumping units.

INJECTOR LINAC

The normal conducting linac MilliAMpere BOoster (MAMBO) is the injector for MESA. It has a start energy of 100 keV and a final energy of 5 MeV. Since the beam currents range from 150 μA to 10 mA, the RF sections have to cope with a large dynamic range of beam loading. At low energy space charge has a strong influence on the beam dynamics, so providing a sufficient beam quality under all conditions is challenging.

The concept of MAMBO is derived from the MAMI injector linac ILAC [9]. MAMBO has a circular chopper, a harmonic buncher system and four bi-periodic standing wave RF-structures for beam preparation and acceleration. The RF structures have a frequency of 1.3 GHz providing an energy gain of 1.25 MeV each. The first structure is a graded-β with $\beta_1 = 0.55 \ldots 0.96$, the following sections have no β-profile, but $\beta_2 = 0.98$ and $\beta_{3,4} = 1$. The beam dynamics design has been carried out with PARMELA using the 3D space charge routine with 300,000 particles to have enough statistics and also research the effect of halo particles.

ISBN 978-3-95450-183-0

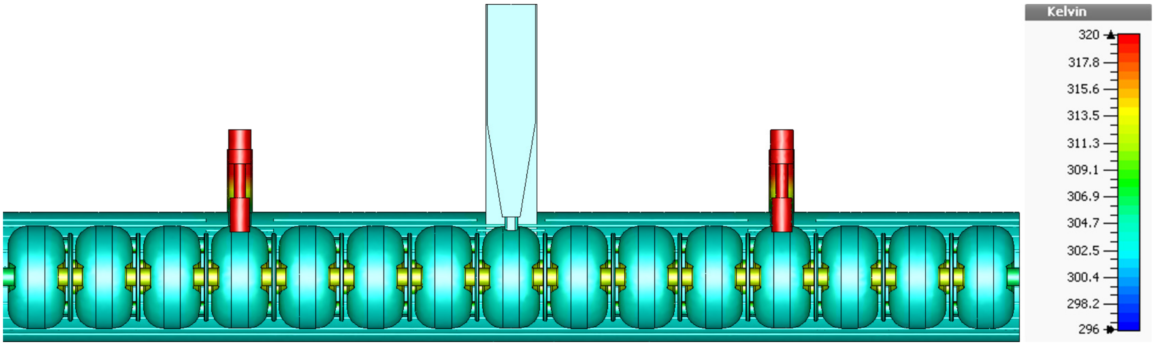

Figure 4: Thermal design of the MAMBO $\beta = 1$ section as presented in [12].

The basic RF-design was started with SuperFish and later improved with CST Studio [10]. Thermal design was also done with this software (Fig. 4). An in deep presentation of the development of the injector can be found in [11, 12].

Circular Chopper

The principle of the circular chopper is shown in Fig. 5. The beam is forced onto a conical area by a transverse deflecting resonator. The TM_{011} mode of the resonator is modified by Z-like grooves inside the caps, so the field pattern is superposed by a magnetic field component perpendicular to that of the undisturbed mode. The resulting force induces the circular deflection. A solenoid bends the beam back onto the beam axis and a second circular deflecting resonator placed at the crossing of the axis closes the orbit bump. At the point of maximum deflection, i.e. inside the solenoid, one places a collimator, to separate the accelerated from the rejected beam phase. Two movable scrapers can be used to select the bunch length of the chopped beam via the width of the arising slit between them.

The deflecting cavity was redesigned from the MAMI design [13] for f=1.3 GHz in course of a Diploma thesis and an Al low power and a Cu high power prototype were built and measured [14]. The Cu prototype was set into operation at the test bed photo source PKA2 in course of a Bachelor's thesis [15]. The circular deflection was monitored on a luminescence screen (see Fig. 5 bottom right). To achieve a sufficient deflection less than 100 W RF-power is needed. Currently the chopper set up is completed by master students in course of their theses [16, 17].

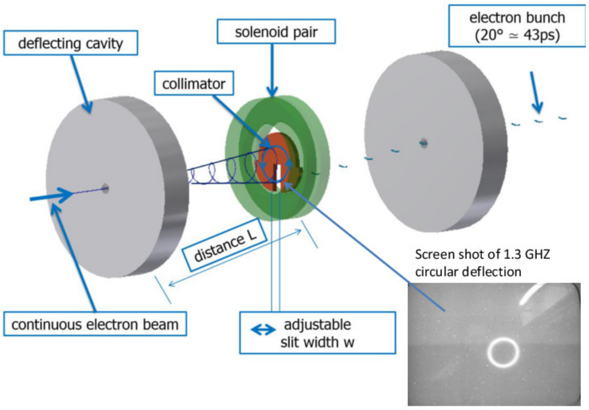

Figure 5: Sketch of a circular chopper system as used for MAMBO. On the bottom right a picture of the circularly deflected beam as seen on a luminescent screen is shown.

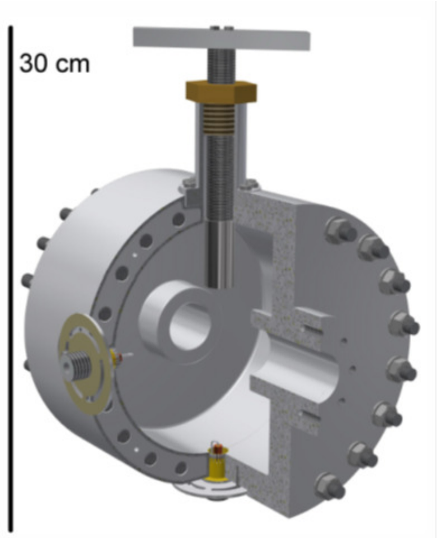

Figure 6: Prototype of the fundamental buncher cavity.

Harmonic Buncher

The harmonic buncher system of MAMI is described in [18]. It is used to increase the capture efficiency of the linac when the photo source is operated. Since the life time of a photo cathode is correlated to the amount of charge extracted, one is interested in not wasting too many particles. The harmonic buncher consists of two cavities, one at the fundamental frequency and one at the first harmonic. The resonators are separated by a drift space. The harmonic cavity acts as a debuncher on the beam, so energy spread is reduced. Further the superposition of the RF-fields generates a linear potential near the bunch centre, so less halo is produced. The drift space is a half-integer multiple of the fundamental wavelength, so the third harmonic is introduced with the proper algebraic sign, generating a good approximation of a linear potential.

The design of the buncher is currently adapted to the MESA frequency [19]. The RF-design of the fundamental and the harmonic cavity is finished. A low power prototype of the fundamental cavity (Fig. 6) has been produced and measured on a bead pull system. The high power prototype is currently in production, as well as the low power prototype of the harmonic resonator.

RF POWER SYSTEMS

At HZDR solid state amplifiers (SSA) have been proven to be a reliable choice for generating RF-power [20]. Therefore all RF-power transmitters of the MESA facility will be based on solid state technology. Scalability and redundancy are the main arguments for SSA, besides the ceasing availability of tube based power sources and a lack of tubes in the right power range for MAMBO. For MESA power sources of some 100 W (Chopper/Buncher), 10-15 kW (MEEC) and 45-75 kW (MAMBO) are needed.

In the low power range an in house solution is available for 1.3 GHz and 2.45 GHz. Both frequencies are actually used at the test photo sources PKA2 and PKAT at KPH [21]. In the kilowatt regime a commercial solution is favoured.

PARTICLE SOURCES

MESA will have a 100 keV GaAs photo source for polarised and non-polarised electrons. The gun to be used for MESA is PKA2 (Fig. 7), a copy of the well proven MAMI design [22] currently used as test bed. Although the restriction to 100 keV beam imposes strong space charge forces during the high current non-polarised beam operation, it is of high benefit for the control of the spin at low current polarised operation and e.g. the insertion length of the spin diagnostic and manipulation devices, such as Wien-filters, scales with the beam energy.

At MAMI the gun is used with a DC beam, the PKA2 has been equipped with an RF-synchronised pulse laser [21]. So a short bunch can be generated already at the gun, the chopper is only needed to cut away tails generated from e.g. stray light, dark currents or delayed emission. The amount of charge wasted is decreased significantly, improving cathode life time and radiation levels.

As an upgrade during stage-2 a new photo source the “Small Thermalised Electron source Mainz” (STEAM) is designed [23] based on the JLAB inverted gun [24]. The technical design of STEAM is finished (Fig. 8) and production of the parts has started. It is constructed for 200 keV beam energy, but also operation at 100 keV is possible. As the accelerating field of STEAM at 100 keV is still higher than compared to PKA2, the energy spread of the emitted electrons is smaller, leading to a better acceleration of a high current beam in MAMBO. Alternatively the low energy section of MAMBO including the graded-β could be redesigned for stage-2.

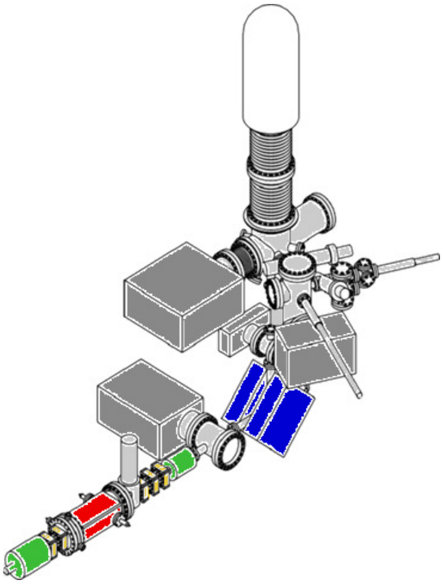

Figure 7: Technical drawing of the 100 keV photo source PKA2, which is currently used as test bed for MAMBO components.

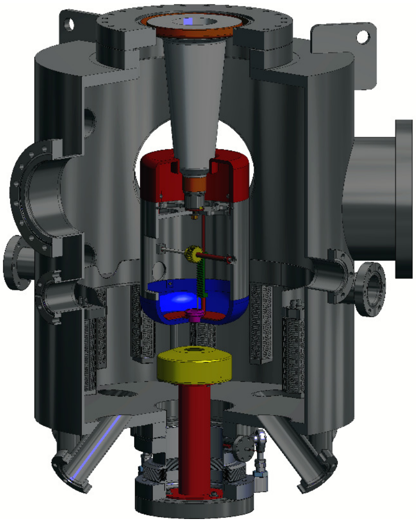

Figure 8: Technical drawing of the 200 keV photo source STEAM.

SUMMARY

The MESA project is well on the way. The core components are designed or their design is close to completion. First subcomponents are either in stage of production or testing. Assembly and commissioning of the low energy beam transport line of MAMBO is planned for 2016.

ACKNOWLEDGEMENT

The author would like to thank all members of the MESA accelerator working group for giving input on the current results of their work.

ISBN 978-3-95450-183-0

REFERENCES

[1] A. Valloni, et al., "Strawman Optics Design For the LHeC ERL Test Facility", IPAC2013, Shanghai, China, TUPME055, p. 1694-1696, (2013).

[2] W. Herr, F. Schmidt, "A MAD-X Primer", Geneva, Switzer-land, CERN-AB-2004-027-ABP, (2004).

[3] L.M. Young, "PARMELA", Los Alamos, USA, LA-UR-96- 1835, (2005).

[4] R. Heine, D. Simon, et al., "Lattice and Start to End Simulation of the Mainz Energy Recovering Superconducting Accelerator MESA", IPAC'14, Dresden, Germany, p. 346 (2014), MOPRO108.

[5] D. Simon, R. Heine, et al., "Lattice and Beam Dynamics of the Energy Recovery Mode of the Mainz Energy-recovering Superconducting Accelerator MESA", IPAC'15, Richmond, USA (2015), MOPWA046.

[6] F. Schlander, et al., "Investigation of Cryomodules for the Mainz Energy-recovering Superconducting Accelerator MESA", IPAC'14, Dresden, Germany, p 2505 (2014), WEPRI013.

[7] J. Teichert, et al., Nucl. Inst. and Meth. A **557** (2006) 239.

[8] F. Schlander, et al.,"1.3 GHz SRF Cryomodules for the Mainz Energy-recovering Superconducting Accelerator MESA" , IPAC'15, Richmond, USA (2015), WEPMA041.

[9] H. Euteneuer et al., "The Injector Linac for the Mainz Microtron", EPAC88, Rome, Italy, p. 550 (1988).

[10] CST - Computer Simulation Technology, Darmstadt, Germany.

[11] R. Heine et al., "Injector Linac for the MESA Facility", IPAC'13, Shanghai, China, p. 2150 (2013), WEPWA011.

[12] R. Heine et al.,"Further Investigations on the MESA injector", IPAC'15, Richmond, USA, (2015), TUPWA045.

[13] H. Braun et al., "The Gun/Chopper System for the MAINZ Microtron", EPAC88, Rome, Italy, p. 997 (1988).

[14] V. Bechtold, "Eine Deflektor-Kavität für den MESA Beschleuniger", Diploma thesis, JGU Mainz, Germany (2013).

[15] B. Ledroit, "Hochfrequenzmessungen am Chopperresonator für MESA", Bachleor's thesis, JGU Mainz, Germany (2014).

[16] B. Ledroit, "Aufbau und Test des MAMBO-Chopper", Master's thesis, JGU Mainz, Germany, in preparation.

[17] C. Stoll, "Bau und Test von Solenoiden für MAMBO", Master's thesis, JGU Mainz, Germany, in preparation.

[18] V.I. Shvedunov et al., "Design of a Prebuncher for Increased Longitudinal Capture Efficiency of MAMI", EPAC96, Sitges, Spain, p.1502 (1996).

[19] P. Heil, "Design und Test eines harmonischen Buncher für MAMBO", Master's thesis, JGU Mainz, Germany, in preparation.

[20] H. Büttig, et al., "Two Years Experience with the Upgraded ELBE RF-System Driven by 20 kW Solid State Amplifier Blocks (SSPA)", IPAC'15, Dresden, Germany, p 2257, WEPME003.

[21] I. Alexander, "Diagnostic Test-Beam-Line For The MESA Injector", ERL2015, Stony Brook, USA, (2015), THIALH2069.

[22] K. Aulenbacher, et al., AIP Conf. Proc. **675** (2002) 1088

[23] S. Friederich, K. Aulenbacher, "Test electron source for increased brightness emission by near band gap photoemission", IPAC'15, Richmond, USA, (2015), TUPWA044.

[24] P.A. Adderley, et al., Phys. Rev. ST-AB **13** (2010) 010101.

OPERATIONAL EXPERIENCE OF CW SRF INJECTOR AND MAIN LINAC CRYOMODULES AT THE COMPACT ERL

H. Sakai[#], K. Enami, T. Furuya, E. Kako, Y. Kondo, S. Michizono, T. Miura, F. Qiu, M. Satoh, K. Shinoe, T. Shishido, K. Umemori, K.Watanabe, Y. Yamamoto, KEK, Tsukuba, Ibaraki, Japan
M. Sawamura, JAEA, Tokai, Naka, Ibaraki, Japan
E. Cenni, The Graduate University for Advanced Studies, Tsukuba, Ibaraki, Japan

Abstract

We developed ERL injector cryomodule and main linac for Compact ERL (cERL) project. The injector cryomodule includes three 2-cell L-band superconducting cavities. The main linac cryomodule includes two 9-cell L-band superconducting cavities. After construction of cERL injector and recirculation loop, beam operation was started with 20 MeV beam and after precise beam tuning, energy recovery operation was achieved with more than 80uA. Injector and main linac cavity were stable for ERL beam operation with Digital LLRF system. Field emission is the severe problem for main linac and heating of HOM coupler is the problem for injector. We mainly describe the cavity performances of two cERL cryomodules during long-term beam operation.

COMPACT ERL PROJECT

Compact ERL (cERL)[1, 2] is a test facility, which was constructed on the ERL Test Facility in KEK. Its aim is to demonstrate technologies needed for future multi GeV class ERL. One of critical issues for ERL is development of the superconducting cavities.

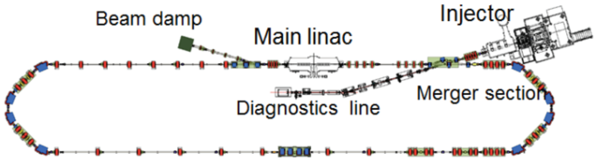

Figure 1: Conceptual layout of the cERL project.

Conceptual layout of the cERL is shown in Figure 1. The cERL main linac cryomodule was assembled and placed inside cERL radiation shield at fall of 2012. First high power test of cryomodule was carried out at December of 2012.

After commissioning of injector parts, recirculation ring was constructed during the summer and fall of 2013. Following the second high power test of main linac cryomodule, beam commissioning was started from December of 2013.

Its main parameters are shown in Table 1. Although the target beam parameters are 35MeV and 10mA for the first stage of cERL, current operation is limited to 20MeV and 10 μA. The beam energy was restricted because of severe field emission of main linac cavities [3]. The beam current was limited due to safety reason. In this paper, we present performance of injector and main linac cryomodule under the cERL beam operation.

Table 1: Main Parameters for cERL Project

Beam energy	35 MeV
Beam current	10 mA (initial)– 100 mA (final)
Normalized emittance	0.1 – 1 mm mrad
Bunch length	1 – 3 ps (usual) 100 fs (bunch compression)

INJECTOR CRYOMODULE

The left figure 2 shows a schematic view of the injector cryomodule [4]. The injector cryomodule consists of three 2-cell cavities and each cavity is fed RF power by twin couplers. At the injector cryomodule, 100 mA of electron beam is planned to accelerated up to 10 MeV. Thus, total of 1MW RF power should be passed to the beam. Still, one input coupler should pass the high power of 167 kW. This is most challenging task in the injector part.

Another important issue is cooling of HOM coupler. It is well known that original TESLA-type HOM coupler has a heating problem in the CW operation. Design of HOM coupler was modified and also cooling ability was strengthened.

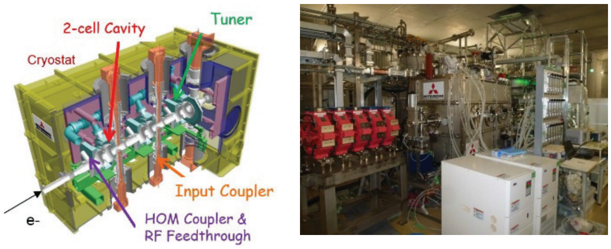

Figure 2: Schematic view of cERL injector cryomodule (left) and the one placed inside the cERL radiation shielding room (right).

MAIN LINAC CRYOMODULE

The left of Figure 3 shows a schematic view of the main linac cryomodule [3], which contains two 9-cell KEK ERL model-2 cavities [5] mounted with He jackets. Beampipe-type ferrite HOM absorbers [6] are connected at both sides of cavities, to strongly damp HOMs. The HOM absorbers are placed on 80K region. Coaxial input couplers [7] with double ceramic windows feed RF power to the cavities. Frequency tuners [8] control cavity resonant frequencies. Cooling pipes of 80K, 5K and 2K are extended throughout the cryomodule. The 80K line was cooled by Nitrogen, and 5K and 2K lines were cooled by Helium. After filling with

---

[#] hiroshi.sakai.phys@kek.jp

4K liquid He, insides of the He jackets were pumped down and the cavities were cooled down to 2K.

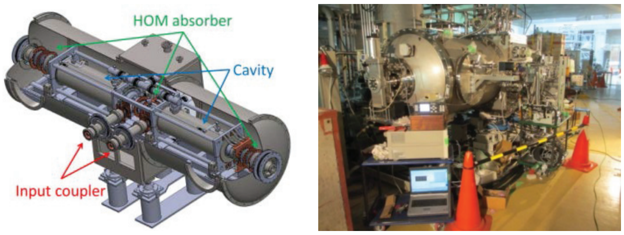

Figure 3: Schematic view of ERL main linac cryomodule (left) and the one placed inside the cERL radiation shielding room (right).

CERL BEAM OPERATION

Injector Cryomodule Performance

After injector cryomodule was cooled down to 2K, we start the high power test in Feb. 2013. The RF conditioning of the three cavities was started in a pulsed operation and an accelerating gradient of 15 MV/m was successfully achieved.[9] By changing CW operation, We measured dynamic heat loads in three cavities. An estimated heat load in case of $E_{acc} = 8$ MV/m and $Q_o = 1.5 \times 10^{10}$ is about 1 W at 2 K, However, the observed heat load was 10~15 W at 8 MV/m. This means one order lower Q_o values. The reason for the large dynamic heat load was due to heat up at RF feedthroughs of HOM couplers. Improvement of an efficient cooling at the RF feedthroughs is an essential issue to reduce the heat load.

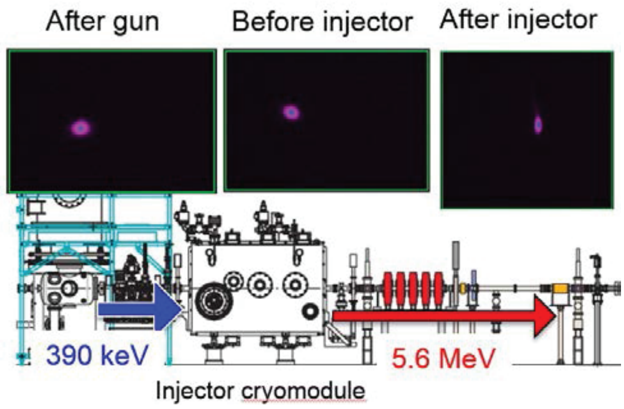

Figure 4: Measured beam profile of screen monitor before and after 5.6 MeV acceleration by injector cryomodule.

During the beam commissioning of injector part at February of 2013, 5.6MeV acceleration was achieved with 1 μA beam by applying the almost 7 MV/m to three cavities of injector cryomodule as shown in Figure 4.

Main Linac Cryomodule Performance

Main linac cryomodule was connected to He refrigerator system and cooled down to 2K. Figure 5 shows typical example of cryogenic operation, at December of 2013. The cryomodule was cooled down with cooling rate of less than 3K/hour, in order to avoid thermal stress to the ferrite HOM absorbers.

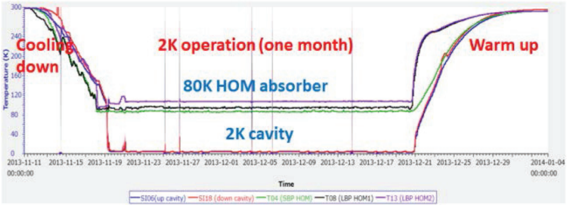

Figure 5: Example of cryogenic operation for the run at December of 2013. Temperatures of cavities are shown by red and blue lines.

At the second high power tests, one of main topics was preparation of the digital LLRF system [10]. Cavity frequencies are controlled by the digital feedback system using the piezo tuners. Also RF amplitude and phase on the main linac cavities are stabilized by the digital feedback system. RF stability of 0.01 % R.M.S. for amplitude and 0.01 degree R.M.S. for phase were achieved. These values satisfied the requirement to the not only cERL operation but also multi-GeV ERL plan. Microphonics was also well suppressed.

Unfortunately, main linac cavity performance was not so good. Severe field emission was observed from low fields, for both cavities. Operation voltage was limited to 8.6 MV for each cavity, to avoid the problem caused by the heavy radiation. Therefore operation energy of cERL beam was limited to 20 MeV; 2.9 MeV at injector part and 8.6 + 8.6 MeV at main linac part.

cERL Beam Operation with Recirculation Loop

Beam commissioning of cERL recirculation ring started at December of 2013. At first, main linac cavities were detuned and the electron beam passed the cavities. After that, low field was applied to the upper cavity, and acceleration phase was searched. For this aim screen monitors were used. The left of Figure 6 shows example of beam profile at the first arc section. The right of Figure 6 shows beam position; energy, dependence on RF phase. On crest RF phase can be found from this scan and also acceleration voltage can be checked with the field strength of the bending magnets.

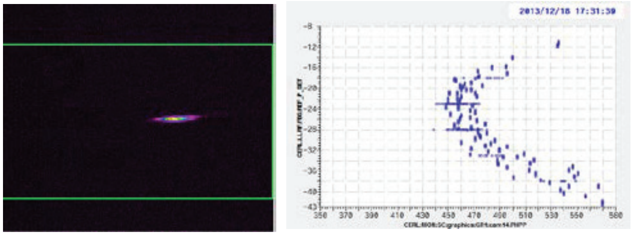

Figure 6: Beam profile observed by a screen monitor at the first arc section (left) and the RF phase scan to find acceleration phase (right).

Precise and dedicated beam tuning had been carried out and electron beam could successfully circulate the ring and reached to the beam dump. For the ERL, adjustment of recirculation loop length is important for energy recovery.

Deceleration phase of main cavities were investigated from the position of the screen monitor and the field strength of bending magnet at the beam dump section, while changing the length of recirculation loop by adjusting chicane or arc sections.

Figure 7 shows trials of energy recovery experiment. In the "Beam loading test", electron beam of 6.5 μA CW was accelerated by the upper cavity and then decelerated by the lower one. The beam loading effect can be seen in the figure as the variation of difference between input and reflection power. It is noted that the sign of this variation is opposite between two cavities. On the other hand, in the "Energy recovery test", no variation can be seen within measurement precision. This means energy recovery is successfully performed. Finally, in 2015 energy recovery was done by more than 80 μA CW beam.

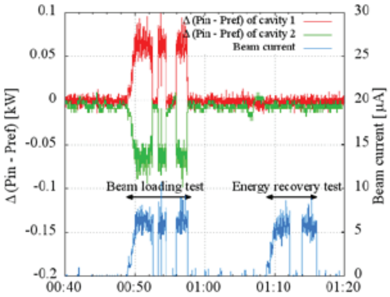

Figure 7: Energy recovery trial. Beam loading effect cannot be seen on "Energy recovery test". In the Beam loading test, upper and lower cavity only accelerates and decelerates electron beams.

LONG TERM CAVITY PERFORMANCE

For the superconducting cavities, especially for CW accelerators, field emission is one of big issue against stable operation. In order to monitor real time radiation status, Si PIN diodes and ALOKA radiation monitors were used. As shown in the left of Figure 8, Sixteen sensors were set like a ring, around the beampipe at each side of each cavity. Total 64 sensors were used for monitoring. The right of Figure 8 shows typical radiation distribution measured by Si PIN diodes. They are sensitive to angle information of field emissions. Monitoring this distribution, we can get some information about emitter locations. Two ALOKA monitors were located both end of cryomodule, at almost beamline height, and used also to see radiation information.

For the cERL operation, we selected acceleration voltage of 8.6MV for each cavity. This is higher than radiation on-set for both cavities. Thus, our cavities have been operated with field emissions. Even during beam operation, sometimes increases of radiation were observed. Increases of signals were seen both of Si PIN diodes and ALOKA monitors. One radiation history taken by ALOKA monitors is shown in Figure 9. Increase of radiation is observed at February 14.

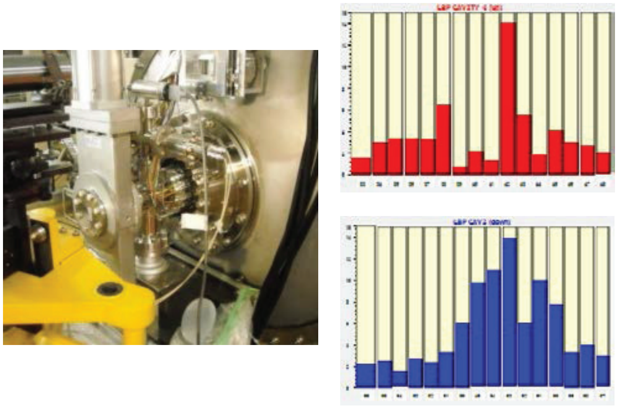

Figure 8: (Left) Si PIN diodes located around beam pipes and (right) example of radiation data taken by those Si PIN diodes.

Q-values of cavities were several times measured. Results are shown in Figure 10. Although radiation existed and Q-values were low from the first high power test at 2012, after some period of beam operation, Q-values became further worse. Finally, we kept same performance within error-bars after degradation from May 2014 to Mar. 2015. At present, Reason why field emission became worse and stopped is not clear. We will continue measuring the cavity performances.

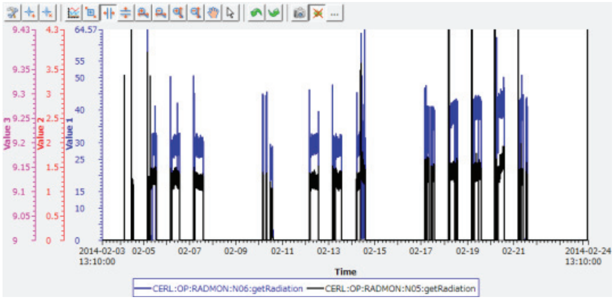

Figure 9: History of radiation status, monitored by ALOKA monitors, during cERL beam operation for three weeks at February of 2014. Radiation increased at February 14. Spikes at the beginning of dairy operation are due to RF aging.

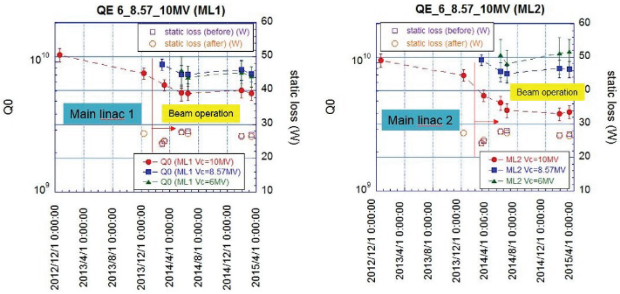

Figure 10: Measurement of the cavity performances of 6, 8.57 and 10 MV cavity voltage during long-term beam operation including high power test of Main linac 1(left) and 2 (right).

ISBN 978-3-95450-183-0

As one trial to suppress field emissions, pulse processing method was applied. Several milliseconds of additional few MV pulses were added to nominal 8.6MV CW RF field. Figure 11 shows the trial of pulse processing to the upper cavity. Figure 11 (a) shows RF field applied on the cavity and (b) shows its pulse structure. Figure 11 (c) shows variations of radiation signals monitored by Si diodes during processing. Time period of Figure (a) and (c) are same. It can be seen that several radiation signals became smaller during processing. Radiation becomes about half. Thus, Pulse processing method is considered to be effective to suppress field emissions.

At moment, field emission limits main linac cavity performance. To recover the design acceleration field of 15 MV, it is essential to eliminate it. Our ideas of countermeasure against field emission are as following; (a) apply more sophisticated pulse processing, (b) apply He processing, (c) disassemble the cryomodule, apply HPR to the cavities and reassemble it.

It is noted that suppression of field emission is of course essential for CW operation of superconducting cavities, but also recovery method from heavy field emission is important. If an effective recovery method is realized, possibly without disassembling the cryomodule, it is desirable.

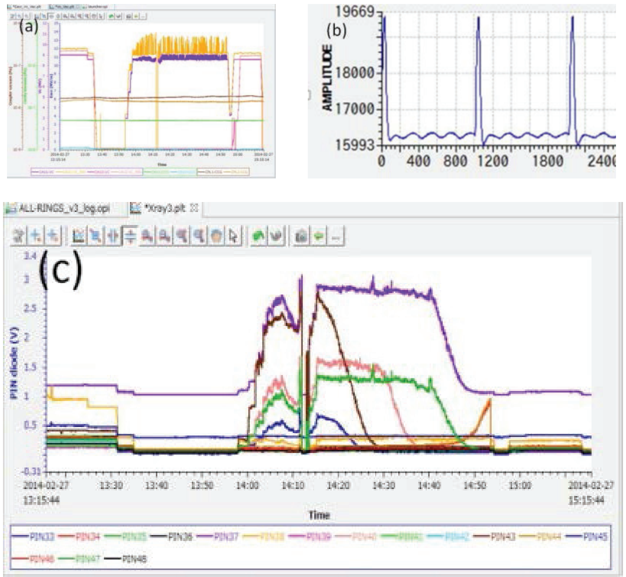

Figure 11: (a) RF field during pulse processing and (b) its magnification. (c) Decrease of radiation signal, observed by Si PIN diodes, during pulse processing.

SUMMARY AND FUTURE PLAN

The compact ERL in KEK was constructed and beam commissioning has been carried out for recirculation loop. Operation voltage of main linac cavities was restricted to 8.6 MV per cavity. So beam energy was limited up to 20 MeV. After beam tuning, energy recovery operation was successfully performed. RF stability of cavities were enough good for cERL beam operation. Field emission of main linac cavity is one of big issues for CW operation of ERL cavities. During beam operation, increases of radiation were sometimes observed. Pulse processing method was efficient to suppress field emissions.

We continue to see the cavity performance during the CW beam operation up to more than 10 mA. And we plan to make the new cryomodule with for 9c-cell cavities to overcome field emission problem with higher gradient and prepare the mass production.

REFERENCES

[1] R. Hajima *et al.* (ed.), KEK Report 2007-7/ JAEA-Research 2008-032 (2008) [in Japanese]

[2] N. Nakamura *et al.*, “Present status of the Compact ERL at KEK”, IPAC’14, Dresden, Germany, June 2014, p.2450 (2014).

[3] K. Umemori *et al.*, “Construction of main linac cryomodule for Compact ERL project”, IPAC’13, Shanghai, China, May 2013, p.2349 (2013)

[4] K. Watanabe *et al.*, “Development of the superconducting rf 2-cell cavity for cERL injector at KEK”, Nuclear Instruments and Methods In Physics Research A, Vol. 714 p.67 (2013).

[5] K. Umemori *et al.*, “Design of L-band superconducting cavity for the energy recovery linacs”, APAC’07, Indore, India, Feb 2007, p.570 (2007)

[6] M. Sawamura *et al.*, “Cooling properties of HOM absorber model for cERL in Japan”, SRF’2011, Chicago, July, 2011, p.350(2011)

[7] H. Sakai *et al.*, “High power tests of KEK-ERL input coupler for main linac under liquid nitrogen condition”, SRF’2011, Chicago, July, 2011, p.356(2011)

[8] S. Noguchi *et al.*, “New tuners for ILC cavity application”, SRF’07 Beijing, Oct, 2007, WE303.

[9] E. Kako *et al.*, “High Power Tests of Injector Cryomodule for Compact-ERL”, IPAC’13, Shanghai, China, May 2013, p.2340 (2013).

[10] T. Miura *et al.*, “Performance of RF system for Compact-ERL Main Linac at KEK”, IPAC’14, Dresden, Germany, June 2014, p.2450 (2014).

ISBN 978-3-95450-183-0

ERL FOR LOW ENERGY ELECTRON COOLING AT RHIC (LEReC)*

J. Kewisch, M. Blaskiewicz, A. Fedotov, D. Kayran, C. Montag, V. Ranjbar
Brookhaven National Laboratory, Upton, New York

Abstract

Low-energy RHIC Electron Cooler (LEReC) system is presently under design at Brookhaven National Laboratory. The electron cooling system needed should be able to deliver an electron beam of adequate quality in a wide range of electron beam energies (1.6-5 MeV). Since acceleration of electron beam is provided by the 704 MHz RF system the electron beam must be bunched and space-charge effects must be considered. An increase of electron beam temperatures by space-charge forces should be carefully avoided. We discuss the layout of the cooler and present the results of optics calculations using the computer code PARMELA.

INTRODUCTION

The nuclear physics program for the Relativistic Heavy Ion Collider (RHIC) for the 2019 and 2020 run periods concentrates on the search for the QCD phase transition critical point. While measurements at the energies of $\sqrt{s_{NN}}$ = 7.7, 11.5, 14.6, 19.6, 27 GeV have been performed in the 2010, 2011 and 2014 runs, a significant luminosity improvement at energies below $\gamma = 10.5$ is required, which can be achieved with the help of an electron cooling upgrade called Low Energy RHIC electron Cooler (LEReC) [1].

Table 1: Electron Beam Kinetic Energies and Bunch Charges

Energy [MeV]	Gamma	Charge per bunch [pC]	Bunches per train	Beam Current [mA]
1.58	4.10	100	30	30
2.04	5.10	100	30	30
2.65	6.18	150	24	33
3.48	7.80	200	21	40
4.85	10.50	300	18	50

In order to cover the range of ion beam energies electron bunches must be produced with an energy range between 1.6 and 5 MeV. Table 1 lists the beam energies and beam currents required for electron cooling. Table 2 lists the ion parameters for the highest and lowest energy.

Table 2: Ion Parameters at the Highest and Lowest Energy

Gamma	4.1	10.7
RMS bunch length	3.2 m	2 m
Number of ions	$0.5 \cdot 10^9$	$2 \cdot 10^9$
Peak Current	0.24 A	1.6 A
Frequency	9.1 MHz	9.34 MHz
Cooling section beta function	30 m	30 m
RMS bunch size	4.3 mm	2.7 mm
RMS angular spread	140 μrad	90 μrad
Cooling sections	2x20 m	2x20 m

The LEReC will be the first electron cooler using a bunched electron beam. This allows the use of RF cavities to accelerate the electron beam and removes the limitation of the beam energy of the cooled ions caused by the availably of DC voltage sources. The ERL concept allows accelerating a sufficiently large electron current to fulfil the cooling requirements.

The LEReC will be built reusing the SRF gun and five-cell cavity of Brookhaven's Energy Recovery Linac. Both devices are designed for the frequency of 704.75 MHz with a wave length of 42.6 cm. The electron bunches have a RMS length up to 3.5 cm, much less then the ion bunches which will use a 9 MHz RF system. Sufficient cooling will be obtained by merging electron bunch trains with up to 30 electron bunches with each ion bunch. The friction force acting on the ions scales near the force maximum as

$$\vec{F} = -\frac{4\pi\, Z^2 e^4 n_e L}{m} \frac{\vec{v}_i}{\beta^3 c^3 \left((\gamma\sigma_{r'e})^2 + \sigma_{pe}^2 + (\gamma\sigma_{r'i})^2 + \sigma_{pi}^2\right)^{3/2}}$$

where $\sigma_{r'e}$ and σ_{pe} are the angular and momentum spread of the electron beam in the laboratory system. In a bunched system both of these parameters are degraded by the space charge forces. Table 3 lists the electron beam requirements.

---

*Work supported by the U.S. Department of Energy.

Table 3: Electron Parameters at the Highest and Lowest Energy

Gamma	4.1	10.7
Charge per ion bunch	3 nC (30x100pC)	5.4 nC (18x300pC)
RMS norm. emittance	< 2.5 μm	<2 μm
RMS energy spread	$<5\cdot10^{-4}$	$< 5\cdot10^{-4}$
RMS angular spread	<150 μrad	<100 μrad

DESIGN OF THE LEReC

The electron bunches will be created using a DC photo-cathode electron gun to be built for LEReC by Cornell University which will operate at 400 kV. A similar gun at Cornell University has already delivered beams of the required quality (300 pC, 50 mA, ε_n=1μ). The SRF gun used in the Brookhaven ERL will be transformed into a cavity (then called "SRF booster") and will provide an energy boost between 1.2 and 1.6 MeV. The power couplers of the SRF booster can provide enough power for the two lowest electron energies to operate without energy recovery. This mode of operation will be used in Phase I of the project. Figure 1 shows the layout for the Phase I of the LEReC project.

The SRF booster (as well as the five-cell cavity used in Phase II) is too tall to be installed in the RHIC tunnel. It has to be placed in the 2 o'clock experimental hall. A transport beam line will bring the electrons to the "warm section" of RHIC.

Because a low energy spread is an important requirement for the electron cooling a warm cavity operating at 2111 MHz (3rd harmonic, located next to the SRF booster) removes the curvature of the bunch shape in the longitudinal phase space.

The SRF booster will not only accelerate the electrons, but also introduce an energy chirp, which causes ballistic stretching of the bunch as it drifts through the transport beam line. A warm 700 MHz cavity removes the energy chirp before electron and ion beams are merged in the cooling section.

The electron bunches are used to cool both RHIC ion beams. After passing through the first cooling section the electron beam is turned around in a single 180 degree dipole and is dumped after traversing the second cooling section.

The merging dog leg is achromatic, using two solenoids to match the dispersion function. The solenoids have opposing polarity and introduce only local vertical dispersion.

At the end of the first cooling section the electron beam turns around in a single 180 degree magnet and is merged with the counter-rotating ion beam. This turn-around is not achromatic. It turns out that the degradation of the transverse emittance by the unmatched dispersion is smaller than the degradation through space charge forces when strong focusing is employed to match the dispersion function.

Both cooling sections include eight solenoids, spaced 3 meters apart. They are used to keep the beam size constant and minimize the angular spread.

In the final configuration (Phase II) the beam will be accelerated to the final energy by the 700 MHz five-cell cavity, which is operated in ERL mode. Figure 2 shows the Phase II layout.

In the transition from Phase I to Phase II the five-cell cavity and an additional 3rd harmonic cavity will be installed. A 9 MHz warm cavity is added, which corrects the beam energy variation caused by beam loading by the

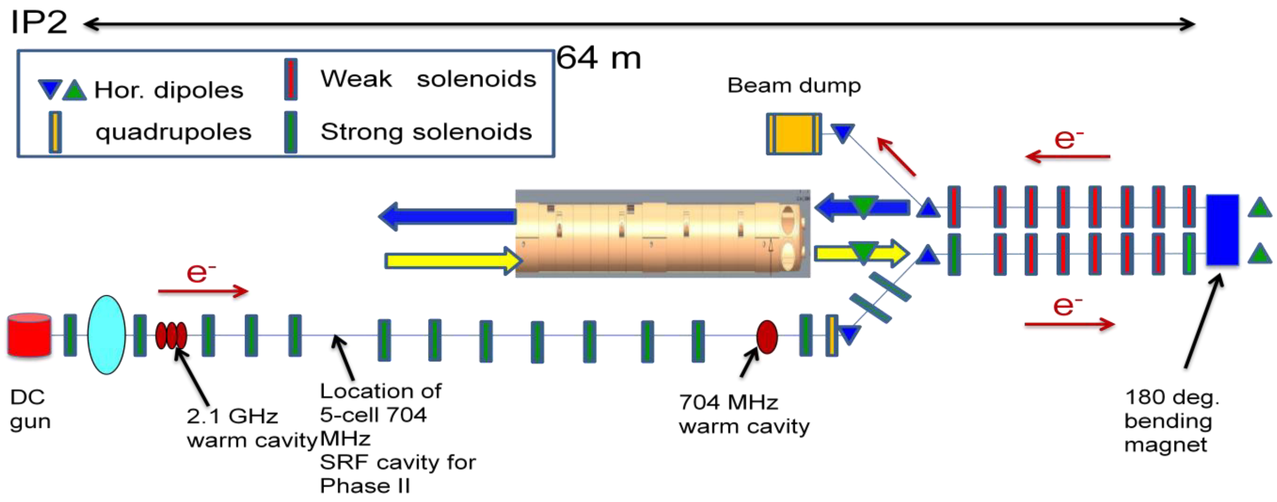

Figure 1: Layout for Phase I.

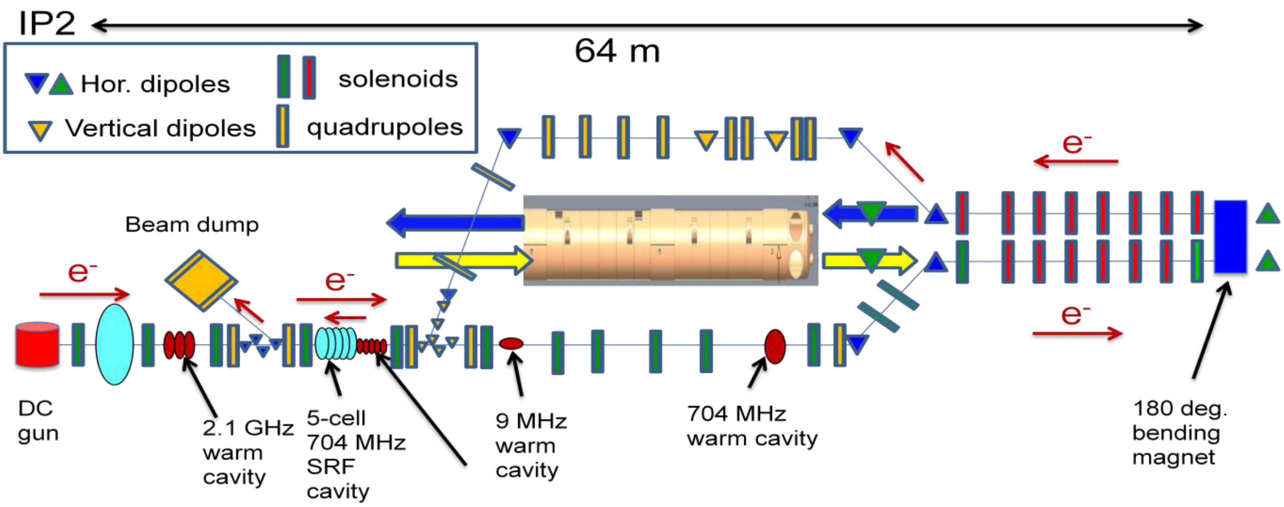

Figure 2: Layout for Phase II.

bunch trains. The beam transport for energy recovery including two zig-zag merging systems [2] for the energy recovery are installed and the beam dump is moved.

LEReC differs from most existing ERLs in that it operates in "push-pull" mode, i.e. the electrons move in the opposite direction through the cavity when the energy is recovered. This is possible since the gaps between the bunch trains are big enough to avoid collisions of the outgoing and incoming bunches.

The push-pull layout simplifies the merging systems on both sides of the 5 cell cavities, since it allows a fixed merger geometry while the ratio of the beam energies of the low and high energy electrons can be chosen independently for all ion energies.

SIMULATIONS

All simulations presented in this paper were made using the computer code PARMELA[3]. PARMELA is a 2-D program that assumes a round beam for the space charge calculations, which is the case for the LEReC.

A multi-threaded optimization program (written at BNL) was used which launches PARMELA for the function evaluation.

In the following results we take advantage of the fact that electrons that are too hot (i.e. have a too high velocity in the co-moving frame) do not contribute to the cooling but do not harm either. For the calculation at 1.6 MeV 130 pC bunches are tracked, and 100 pC (electrons with the lowest energy deviation) are used for the evaluation of the beam parameters expected in the cooling sections.

Since the set of electrons used for the calculation of the result is evaluated at each point of the curves the functions jumps when a cavity or space charge changes the energy distribution.

RESULTS FOR 1.6 MeV

Figure 3 shows the beam envelope for the Phase I accelerator and Figure 4 shows the projected emittance. The electron beam, generated in the DC gun, is focused with two solenoids to have a waist in the SRF booster so that the emittance is not degraded. Since the beam energy after the booster is still relatively low the projected emittance oscillates throughout the accelerator. The focusing in the transport section is chosen so that the average emittance in the cooling section is minimized.

The beam size in the cooling sections matches the size of the ion beams.

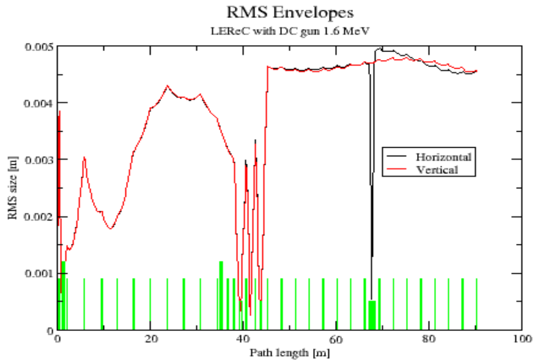

Figure 3: Beam envelope along entire electron beam transport through both cooling sections at 1.6 MeV.

ISBN 978-3-95450-183-0

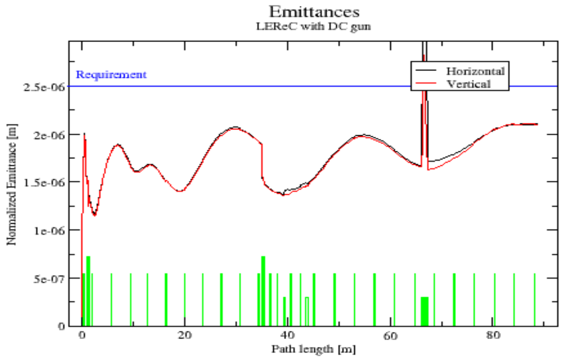

Figure 4: Projected beam emittance at 1.6 MeV. The wave in the emittance is caused by the differences of focusing of the longitudinal slices of the bunch.

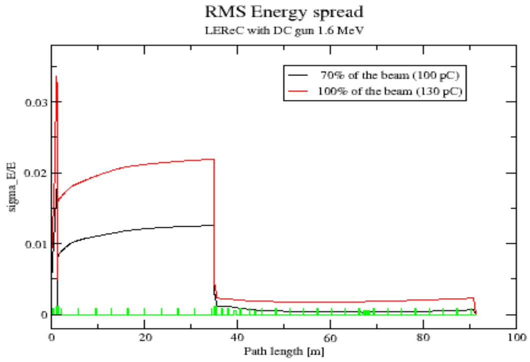

Figure 5: The red curve shows the energy spread of the whole beam (130 pC), the black curve shows the energy spread when only 70% (100 pC) are evaluated.

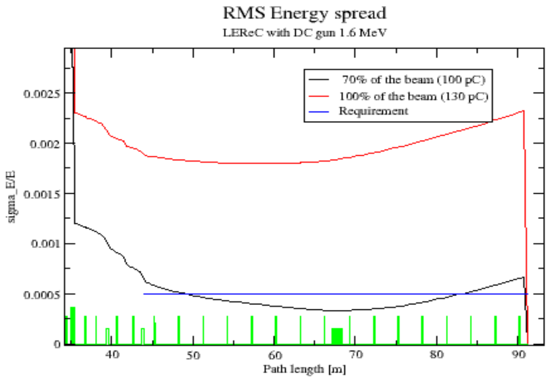

Figure 6: Energy spread in the cooling sections. The requirement is fulfilled.

Figures 5 and 6 show the energy spread of the beam and illustrate how the RMS values are dominated by the tails of the bunch. The intentional energy chirp in the transport section is removed by the warm 700 MHz cavity. Because space charge introduces an additional chirp as the electrons pass through the cooling section a small negative chirp is introduced by the cavity so that the energy spread is symmetric in both cooling sections. Figure 6 zooms into the cooling sections.

RESULTS FOR 5 MEV

The Phase-II, the LEReC will operate in ERL mode for energies 2.6-5 MeV. This Phase of the project is presently under design with preliminary results for 5 MeV shown in Figures 7 to 9. After the booster and 3rd harmonic cavity the beam passes through a zig-zag merging section into the the 5-cell SRF cavity for additional acceleration.

We found it necessary to place a 3rd harmonic cavity after each accelerating cavity. Otherwise the quadratic shape of the bunch in longitudinal phase space will be distorted by the momentum compaction of the mergers and the energy spread cannot be removed later on.

A second zig-zag merger allows the beam to return through the 5 cell cavity for energy recovery.

The beam size in the cooling sections is adapted to the smaller ion beam size.

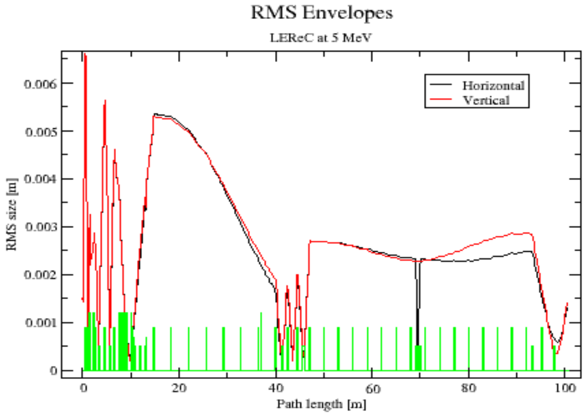

Figure 7: Beam envelope for 5 MeV operation.

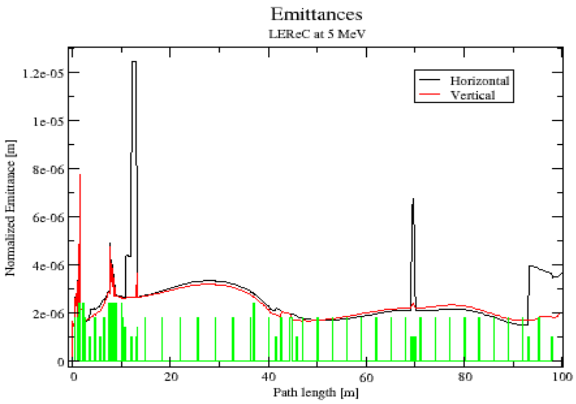

Figure 8: Normalized rms emittances. The spike in the horizontal emittance at the path length of 12 m is caused by the dispersion of the zig-zag merger.

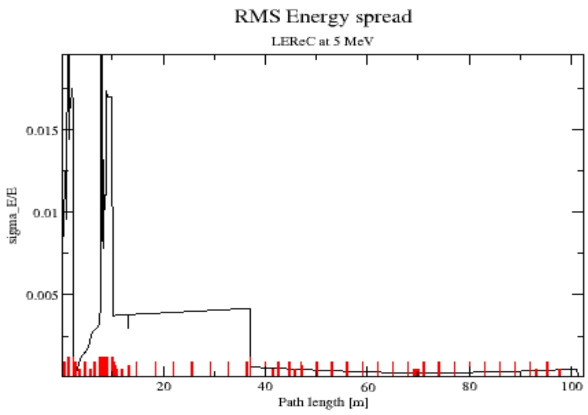

Figure 9: The energy spread calculated from tracking 330 pC charge and using 90% of the beam for the evaluation.

TIME LINE

Phase I of our project has been approved. The DC gun will be constructed by Cornell University in 2015 and commissioned at Cornell in 2016. Also in 2015 the cooling sections will be installed. The installation of the gun, SRF and RF components and beam dump in RHIc tunnel will be done in 2017. The system commissioning will start 2017 with electron beam commission to start in early 2018.

The RHIC Run-19 BES-II physics program (Phase I commissioning of cooling with Au ion beams) starts in October 2018, RHIC Run-20 BES-II (Phase II) at the end of 2019.

REFERENCES

[1] A. Fedotov, "Bunched beam electron cooling for Low Energy RHIC operation", in ICFA BeamDynamics letter No. 65, p. 22 (December 2014).

[2] D.Kayran, V.N.Litivnenko, "Novel Method of Emittance Preservation in ERL Merging System in the Presence of Strong Space Charge Forces", Proceedings of 2005 Particle Accelerator Conference, May 16-20, 2005, Knoxville. TN, USA.

[3] L.Young, J.Billen , PARMELA, LANL Codes.

DEVELOPMENT FOR MASS PRODUCTION OF SUPERCONDUCTING CAVITY BY MHI

K. Kanaoka, H. Hara, K. Okihira, K. Sennyu, T. Yanagisawa,
Mitsubishi Heavy Industries, Ltd., Mihara, Hiroshima, Japan
R. Matsuda, Mitsubishi Heavy Industries, Ltd., Takasago, Hyogo, Japan

Abstract

Mitsubishi Heavy Industries (MHI) has developed the manufacturing process of superconducting cavities for a long time. In this paper, recent progress of our work will be reported.

INTRODUCTION

MHI has improved our superconducting technology to take part in the production design and manufacturing of the cryomodules including the superconducting cavities. Figure 1 shows the schematic view of cERL in KEK. MHI produced the injector module of cERL shown in figure 2 which contains three 9-cell cavities. We performed the production design and fabrication of the parts and assembly of the cryomodule at KEK. We also fabricated the main accelerator module for cERL shown in figure 3. The assembly of the cryomodule was also performed by MHI at KEK except the assembly in the clean room. These cryomodules conform to Japanese high pressure gas safety law [1][2][3].

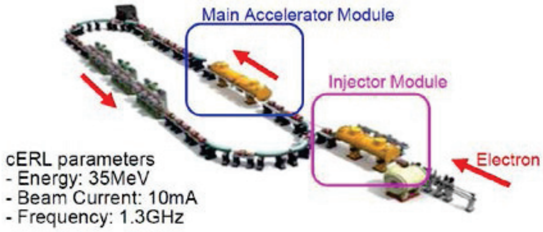

Figure 1: Schematic view of cERL in KEK.

Figure 2: Injector module of cERL in KEK.

Figure 3: Main accelerator module of cERL in KEK.

The high intensity electron gun will be requested for the next generation ERL. As a plan for the future, we have developed SRF electron gun in collaboration with KEK [3]. We designed the 1.3GHz 1.5-cell elliptical cavity for the superconducting RF electron gun. The spec and the electric field distribution of the gun are shown in figure 4. As the first step, we designed the shape of the cavity and analysed the electric field distribution by SUPERFISH.

Drive frequency	:1.3GHz
Beam Energy	:2MeV
Beam current(ave.)	:100mA
Electric field(Esp)	:<50Mv/m
Normalized emittance	:<1πmm mrad
Spread of Beam energy	:<2 keV (<0.1 %)
Number of the cell	:1.5 cell

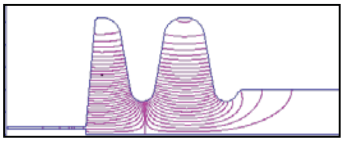

Figure 4: Spec(left) and electric field distribution (right) of superconducting RF electron gun.

Figure 5 shows the simplified schematic and the photos of the parts before assembly.

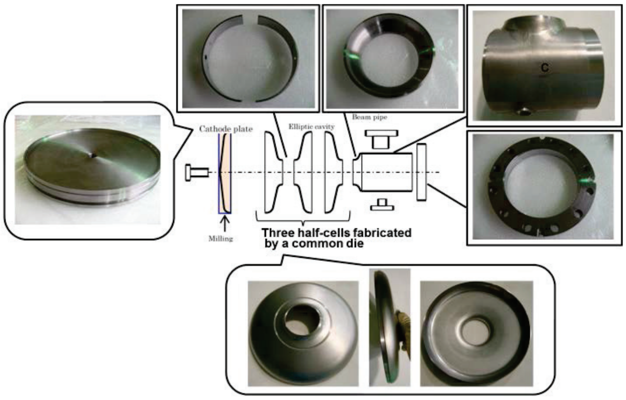

Figure 5: Manufacturing procedure of the half-cells.

We fabricated the Prototype#1 shown in figure 6. This cavity is under the preparation of the vertical test in KEK. The result will be reported soon. Now, we are studying the

ISBN 978-3-95450-183-0

choke structure and the coupling calculation of the input coupler and so on.

Figure 6: Prototype#1.

Cu plating for the input coupler requires high intensity electric conductivity to suppress RF resistance and low thermal conductivity to supress the heat transfer. Thin copper plating film on the stainless steel plate and high RRR are required.

We are developing the manufacturing method of high power input coupler for the purpose of low RF loss for high power and low heat penetration in collaboration with KEK. We fabricated the Cu plating sample by periodic reverse copper electroplating. And, we measured RRR of the Cu plating on the stainless steel bars. 3 samples (t=10,20,30μm Cu plating on t=1mm stainless steel plate) were prepared and measured RRR of each sample. However, it is difficult to measure directly the resistivity of the Cu plating. So we measured both Cu plated/unplated samples and calculated RRR. Heat treatment also has an influence on the resistivity. Therefore, we measured both with/without heat-treated(800℃) samples.

Figure 7 shows the cross section of the samples. We measured the thickness of the sample by the laser microscope.

Figure 8 shows the results of the measurement. We found RRR of Cu plating without heat treatment satisfied the requirement. On the other hand, the heat treatment decreases RRR of Cu plating on stainless steel. We are preparing the measurement of the chemical composition of the Cu layer.

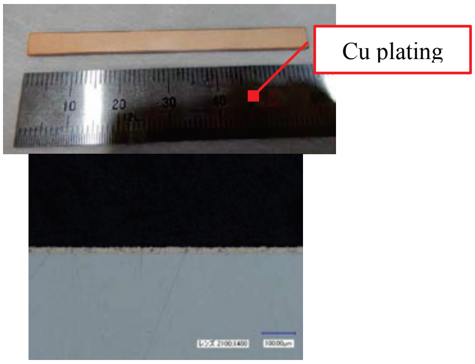

Figure 7: Sample (left), Cross section of the samples (right).

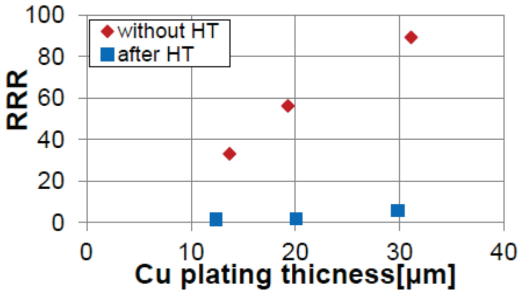

Figure 8: Result of the measurement.

DEVELOPMENT OF FABRICATION METHOD FOR MASS-PRODUCTION

In future, the mass production of the superconducting cavities will be required for the main linac of ERL. MHI has planned to have the factory to manufacture 200 cavities in 3 years. From now on, the activities of mass production performed by MHI will be introduced.

MHI's Development Histories of the Cavity Fabrication Methods

Table 1 shows our development histories of the cavity fabrication methods. Our technical developments are shown as below: [3][4][5]

- Welding process for stiffener from EBW to LBW.
- Welding process for baseplate EBW and LBW.
- Number of the cavity for final welding per 1 chamber from 1 cavity to 4 cavities.
- Seamless dumbbell applied to 2-cell cavity.
- Unification monitor port and flange

Table 1: Development Histories for Mass-production

Phase	Cavity No.	Welding process for stiffener	Welding process for baseplate	Number of the cavity for final welding per 1 chamber	New process
R&D	MHI-A 9-cell	LBW	EBW	1	
	MHI-B 2-cell	-	-	1	Seamless dumbbell
	MHI-C 9-cell	LBW	LBW	1	9seam/ 1batch
	MHI-D 9-cell	LBW	EBW	1 +3 dummy	Unification of monitor port and flange
STF 2-a	#23-26	LBW	EBW	2	Using retainer ring for monitor port
STF 2-b	#27-30	LBW	EBW	2	

LBW for the Welding Process for Stiffener

Figure 9 shows the laser welding machine which is applied to the welding of the stiffener rings. Laser generated by the oscillator is switched by the beam switch and directed to the welding station through the fiber. This laser welding machine can be used for the welding in this station and also other stations continuously [3][4][5].

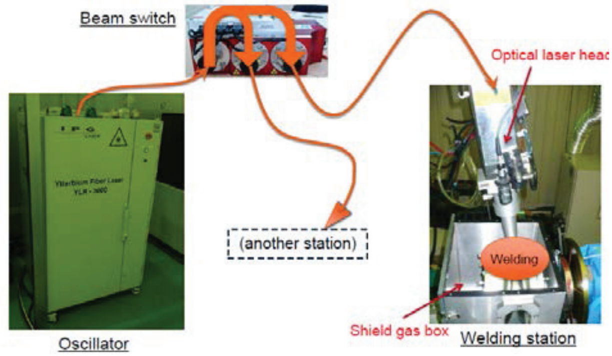

Figure 9: Composition of LBW machine.

Seamless Dumbbell

Figure 10 shows the process of the manufacture of the seamless dumbbell. The seamless pipe is made by deep drawing from a Niobium sheet and cut both end. We use spinning for the forming but not use hydroforming. We can process from "Set of the pipe" to "Turning for stiffener" without grip-changing. We fabricated the 2-call superconducting cavity called MHI-B by using the seamless dumbbell, and performed the vertical test in JLab in collaboration with JLab and KEK. This cavity reached 32.4[MV/m] [3][4][5].

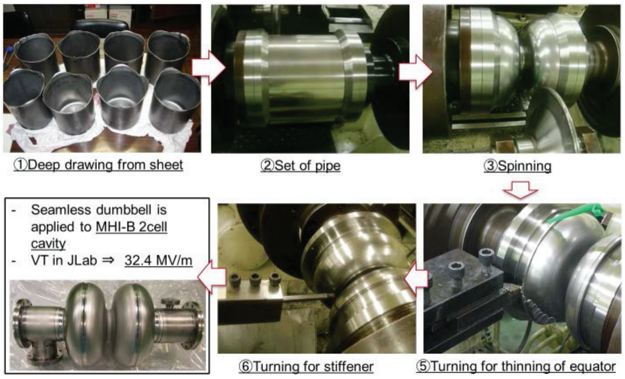

Figure 10: Process of the manufacture of the seamless dumbbell.

Unification of Monitor Port and Flange

Figure 11 shows the superconducting cavity called MHI-D. We succeeded to reduce 3 parts and 3 welding line by the combination of pick up port and flange. We changed the materials for pick up port from Niobium Titanium alloy and pure Niobium to ASTM Gr-2 Niobium. We performed the leak test for it at 2K and confirmed there was no leak [4][5].

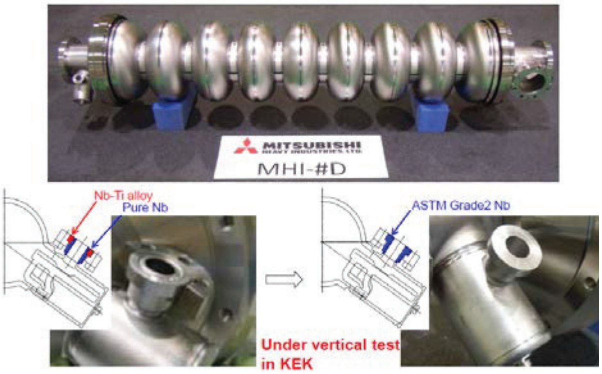

Figure 11: Result of the measurement.

Batch Process

MHI has the EBW machine which can contain four 9-cell cavities by vertical position and weld them in one batch. We succeeded in welding all seams of equator of four cavities in one batch (see Fig. 12). One of these cavities reached 34.9[MV/m] by the vertical test in KEK [4][5].

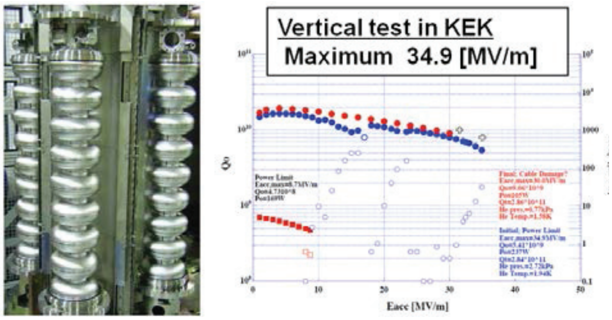

Figure 12: Batch process.

SUMMARY

- MHI fabricated "Injector module", "Main accelerator module" for KEK cERL
- MHI has improved mass-production method shown as below.
  - Laser beam welding
  - Seamless dumbbell
  - Changing the material of HOM coupler
- MHI is currently developing "SRF electron gun", "Coupler" now.

REFERENCES

[1] F. Inoue, et al., "The Development of Cryomodule for c-ERL at MHI", ERL2013, Novosibirsk, Russia, 2013, PS15
[2] T. Yanagisawa, et al., "Development for Mass Production of Superconducting Cavity by MHI" IPAC2015, Richmond, VA, USA, July 2015, WEPMA048.
[3] H. Hitomi, et al., "Fabrication of Superconducting RF cavity at MHI", ERL2011, Tsukuba, Japan, 2011, WG3002.
[4] H. Hara, et al., "SRF activities at MHI," TTC Meeting, Tsukuba, Japan, December 2014, WD4 Id86.
[5] K. Sennyu, et al., "Industrialization of ILC from a view point of industry", 4th IPAC13, Shanghai, China, 2013, WEIB203.

ULTRA-FAST HARMONIC RESONANT KICKER DESIGN FOR THE MEIC ELECTRON CIRCULAR COOLER RING*

Y. Huang#,[1,2], R.A. Rimmer[1], H. Wang[1], S. Wang[1], J.Guo[1]
1. Jefferson Lab, Newport News, VA 23606, USA
2. Institute of Modern Physics, Chinese Academy of Sciences, Lanzhou 730000, China

Abstract

Electron cooling is essential for the proposed Medium energy Electron Ion Collider (MEIC) to attain low emittance and high luminosity. To achieve a very high electron beam current for bunched beam cooling in the future high luminosity upgrade, we adopt a circulator ring to reuse the electron bunches. The electron bunches will recirculate for 25 turns, thus the current in the ERL can be reduced by a factor of 25. An ultra-fast kicker is required for this circulator ring, with pulse width less than 2.1 ns (1/476.3 MHz) and high repetition frequency of 19.052 MHz (1/25 of 476.3 MHz). JLab started an LDRD proposal to develop such a kicker. Our approach is to generate a series harmonic mode with RF resonant cavities, electron bunches passing through the cavity will experience an integral effect of all the harmonic fields, thus every 25th bunch will be kicked while all the other bunches un-kicked. Here we present a design of a simplified prototype with every 10th bunch kicked, using 4 cavities to generate 10 harmonic modes. Cavity structure is optimized to get the highest shunt impedance, thus the total power dissipated on 4 cavities for copper material is only 87.72 W, two to three orders of magnitude lower than a strip-line kicker.

INTRODUCTION

Cooling of ion beams is critical in delivering high luminosities for the proposed MEIC [1]. Low ion beam emittance is required to deliver a small beam spot at the interaction point. The present MEIC design utilizes a scheme of multi-stage cooling. In each stage, the velocity of the electron beam needs to be matched with the ion beam. In the booster, the required electron energy is less than or just about 1 MeV, a DC cooler is used to assist accumulation of injected positive ions and reduce the beam emittance at the low energy. In the ion collider ring, higher energy electron bunches is needed, for example, to cool 100 GeV protons, the required electron energy is 55 MeV. An electron cooler utilizing high energy bunched beam will be responsible for cooling the medium energy ions to suppress intra-beam scattering (IBS) and maintain emittance during collisions.

In the baseline design, a single turn ERL cooler is used, as shown in Fig.1 [2]. After being accelerated to 55 MeV in the SRF linac, the electron bunches will merge with the ion beam and continuously cool the ion bunches in a long cooling channel immersed in a strong solenoid field, then return to the linac for energy recovery, and finally be delivered to the beam dump. The bunch repetition frequency is 476.3 MHz, and the beam current is 0.2 A, which should be achievable with reasonable R&D effort.

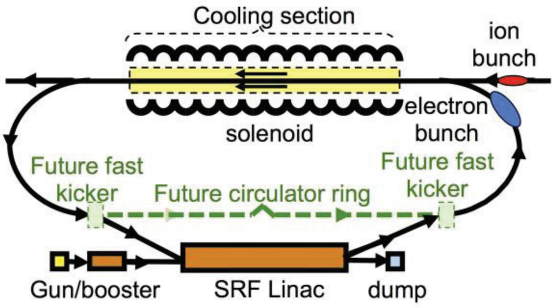

Figure 1: Schematic of bunched beam cooler with option for future recirculation.

In the future high luminosity upgrade, high intensity electron beam is needed. High current (~1.5 A) not only brings the difficulties to build the electron gun and the SRF linac, but also requires high RF power. A great idea to solve this problem is to add a circulator ring to reuse the electron bunches, as shown in Fig. 1 (green). Electron bunches will circulate 25 turns in the circulator ring, and then back to the ERL. In this scheme the beam current and bunch repetition frequency in ERL can be reduced by a factor 25 (0.06 A, 19.052 MHz).

A critical component in this scheme is the ultra-fast kicker that periodically switches electron bunches in and out of the circulator ring from and to the driver ERL. When the electron bunches are kicked into the Circulator Ring (CR) (476.3 MHz), every bunch in the ERL (19.052 MHz) is kicked; when kicked out, every 25th bunch is kicked and other 24 bunches are, ideally, undisturbed. Assuming 55 MeV electron beam energy and a kick angle of 1mrad, the kick voltage would be 55 kV. To avoid the interference to the undisturbed bunches, the pulse width should be very short (less than 2.1 ns for a 476.3 MHz bunch train). In the R&D design, we just prototype a simplified version that kicks every 10th bunch. The ideal kick voltage pulse and the bunch train structure are shown in Fig.2.

GENERATION OF KICK VOLTAGE WITH FINITE HARMONIC MODES

The periodical square kick voltage pulse can be described mathematically as a Fourier series expansion in compact trigonometric form [3]:

$$V_t = V_0 + \sum_{n=1}^{\infty} V_n \cos(n\omega_0 t + \varphi_n) \qquad (1)$$

---

*Work supported by Jefferson Science Associates, LLC under U.S.DOE Contract No. DE-AC05-06OR23177

#yulu@jlab.org

ISBN 978-3-95450-183-0

V_t is the total kick voltage, the constant term V_0 represents a DC offset, ω_0 is bunch repetition frequency in ERL, V_n and φ_n are amplitude and phase terms of these harmonics. Reconstructing the voltage pulse with the first 10 harmonics, and adjusting the DC offset and amplitudes to satisfy the design kick voltage, the reconstructed kick voltage pulse can be seen in Fig. 2 (black). The kicked bunches experience a kick voltage of 55 kV, while the centers of each un-kicked bunch will experience zero kick voltage. The waveform fluctuates between adjacent bunches, generating a head-tail difference in the kick each bunch sees. For the kicked bunches, a flat top kick can be obtained by adjusting the pulse width before FFT; and for the un-kicked bunches, the head and tail difference can be cancelled by an 180^0 betatron phase advance between two kickers.

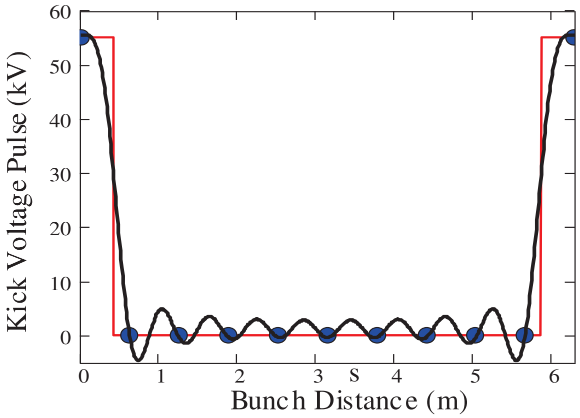

Figure 2: Ideal kicker voltage pulse (red solid line) and bunch train scheme (blue point) to kick every 10th bunch, and the reconstructed kicker pulse with the first 10 harmonic modes (black).

Adjust the Pulse Width to Get a Flat Top

Consider a normalized periodical pulse voltage of width b, amplitude 1, in one period $(-b/2,\ 2\pi-b/2)$, the square pulse can be expanded as the following form:

$$F(s,b,x)=\frac{b}{2\pi}+\frac{2}{\pi}\cdot\sum_{n=1}^{s}\frac{1}{n}\sin(n\cdot\frac{b}{2})\cos(n\cdot x) \qquad (2)$$

s is the harmonic number, x is variable. If we consider +/- 3σ of (σ=2cm) electron bunches, for 10 harmonics, we can solve the following equation to optimize the width b.

$$F(10,b,0)=F(10,b,0.06) \qquad (3)$$

A series b is get from this equation, as can be shown in Fig. 3.We define the flatness as:

$$flatF\,(s,b,x)=\frac{\max F(s,b,x)-\min F(s,b,x)}{F(s,b,0)} \qquad (4)$$

Here $maxF(s,b,x)$ and $minF(s,b,x)$ is the maximum value and minimum value of $F(s,b,x)$ in Interval $[0,x]$.

Calculate the flatness for several widths, we can get:

$$flatF\,(10,0.859324,0.06)=9.504\times10^{-5} \qquad (5)$$

$$flatF\,(10,1.474168,0.06)=3.4308\times10^{-5} \qquad (6)$$

$$flatF\,(10,2.079633,0.06)=1.6348\times10^{-5} \qquad (7)$$

Larger b gives better flatness, but also requires larger amplitude and power for each mode, and a wider pulse also has effect on the un-kicked bunch. Thus in this case, minimum b is enough.

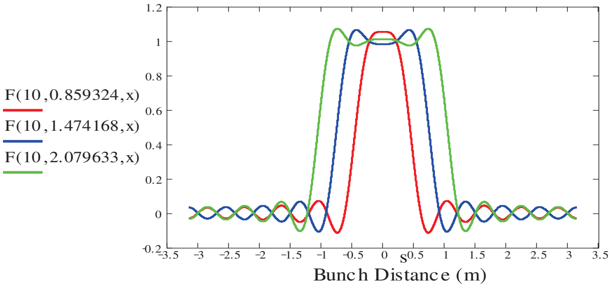

Figure 3: Pulse top flatness with different pulse width.

Cancelation of the Head and Tail Difference for the Un-kicked Bunch

For a single particle in a bunch, a transverse kick will change its transverse momentum. As the particle proceeds along the orbit, the transverse momentum and position follows the betatron oscillation. If two kickers are separated of a distance with exactly 180 degree betatron phase advance, particles experience a positive kick will experience another positive kick and then return to its original orbit. The particles experience a negative kick will be the same to return to the original bunch elliptical phase space orbit after the second kicker. The residual kick left due to the voltage difference between two kickers will be cancelled out after 25 turns in the CR due to pulse shape symmetry in time structure as illustrated in Fig. 2. The first cancelation scheme can be illustrated in Fig. 4. Total cancellation hypothesis could be confirmed by the tacking simulation study.

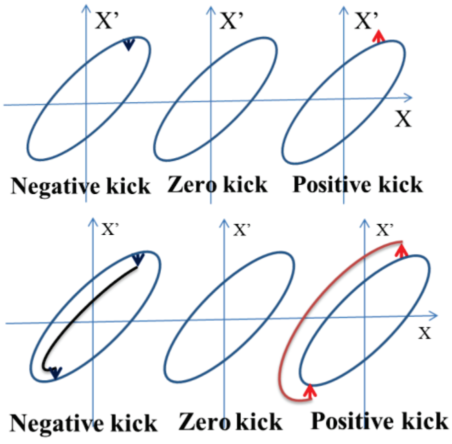

Figure 4: Cancelation of the head and tail difference for the un-kicked bunch.

Build the Kick Voltage with Less Harmonic Modes

In Figure 2, we construct the kick voltage with 10 harmonic modes, and every 10th bunch is kicked. If we want to construct a waveform that kicks every 25th bunch

ISBN 978-3-95450-183-0

using this method, the required harmonic number will be 25, which may impose difficulties for the cavity design. However, with *n* modes, the number of variables in equation (1) is *2n+1* (1 DC offset, *n* amplitudes, *n* phases). If the waveform has *2n+1* constraints in a period, i.e. zero at the *2n* un-kicked bunches and V_t at the kicked bunch, in most cases we should be able to find a set of solution constructed with about *n* modes, reducing the number of modes by half. We have found such a solution with all the phase set to 0, if

$$V_1 = V_2 = \ldots = V_n = 2V_0 \tag{8}$$

This waveform kicks every (2n+1)th bunch in an odd position at the amplitude of $(2n+1)V_0$.

To construct a waveform that kicks every 2nth bunch in the even position, it requires the V_n is half of lower frequency modes:

$$V_1 = V_2 = \ldots = V_{n-1} = 2V_n = 2V_0 \tag{9}$$

Figure 5 compares the waveforms generated by the constraint method with the FFT method. Both waveforms can kick every 25th bunch. The main difference is the flatness for the kicked bunch. To improve the flatness in the constraint method, one or two more harmonic modes can be added.

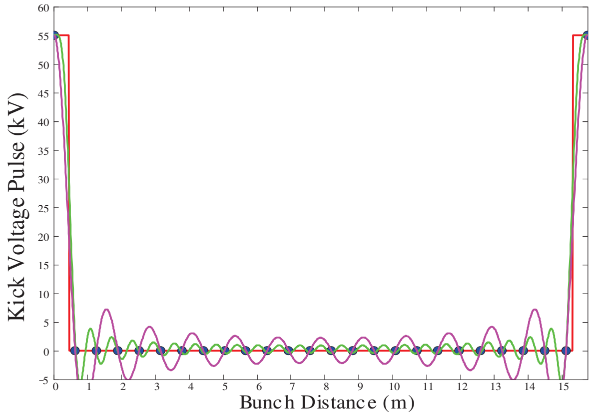

Figure 5: Comparison between the ideal kick voltage (red), reconstructed the kick voltages with 25 harmonics (green) and 12 harmonics (magenta).

CAVITY DESIGN

The cavity model used to generate harmonic modes is quarter wave transmission line shorted at one end and capacitive loaded at the other end, as shown in Fig. 6. Here *b* and *a* are the radius of outer and inner conductor, and *g* is the end gap. Beam passes through the gap and is deflected primarily by a transverse electric field.

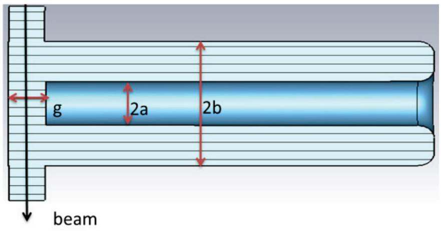

Figure 6: Cavity model.

Because of the boundary conditions of this type cavity, the higher order modes in one cavity can be only odd-harmonics of the fundamental mode of the cavity. Thus to generate the first 10 harmonics of the beam frequency, 4 cavities are needed, as shown in Fig. 7.

The relationship between cavity number M and maximum harmonic number N can be supported as

$$2^M - 1 \le N \tag{10}$$

The maximum harmonic modes N distributed in M cavities can be demonstrated in Tab.1 as an example for M=4, N=15, f_0=476.3MHz, calculated by the base frequencies of f_0/N $2f_0/N$, $4f_0/N$, $8f_0/N$.

Table 1: Harmonic Modes in Each Cavity

Cavity #1	Cavity #2	Cavity #3	Cavity #4
$(2n_1+1)\frac{f_0}{N}$	$(2n_2+1)\frac{2f_0}{N}$	$(2n_3+1)\frac{4f_0}{N}$	$(2n_4+1)\frac{8f_0}{N}$
n_1=0~7	n_2=0~3	n_3=0~1	n_4=0

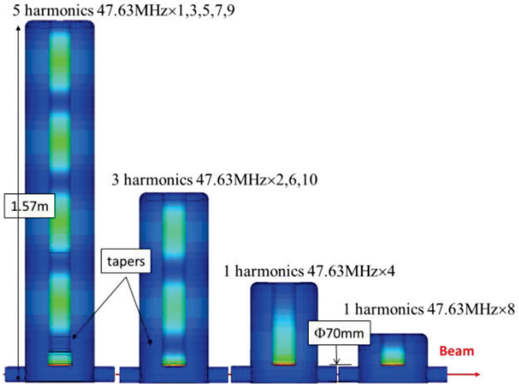

Figure 7: Harmonic modes in four cavity system with the highest harmonic electric field distribution shown in each cavity.

Cavity model is optimized to get the maximum shunt impedance in Microwave Studio CST, with the amplitude and phase from FFT, we can get the dissipated power of each mode on 300 K copper walls, as shown in Tab. 2.

Total power for all modes is 87.72W, two to three orders of magnitude lower than a strip-line kicker [4]. The equivalent transverse shunt impedance for the kicker system can be defined as,

$$R_t = \frac{V_t}{P_{total}} = \frac{V_0 + \sum_{n=1}^{N} V_n \cos(n\omega_0 t + \varphi_n)}{\sum_{n=1}^{N} P_n} \tag{11}$$

Stub Tuner Design

It is crucial to make sure every mode is on its target frequency. From the numerical simulations above, we can calculate the bandwidth of each mode for the room temperature copper wall material. As shown in Table 3, Q_0 for each mode is calculated for 300 K copper. Fundamental mode in each cavity is critically coupled; higher modes in the 5 modes and 3 modes cavities are slightly over coupled. Then the bandwidth for one coupler system:

ISBN 978-3-95450-183-0

$$\Delta f_n = \frac{f_n}{Q_{0n}}(1+\beta_n) \qquad (12)$$

Here f_n, Q_{0n}, β_n and Δf_n is the frequency, quality factor, coupling strength and bandwidth of n^th mode.

Table 2: Kick Voltage, Shunt Impedance and Dissipate Power for Each Mode

Mode (MHz)	FFT Kick Voltage (kV)	CST Trans. Shunt Impedance (Ω)	Dissipated Power for 300K Copper (W)
47.63	13.711	7.13E6	26.37
95.26	12.462	1.14E7	13.62
142.89	10.532	4.09E6	27.12
190.52	8.1290	1.35E7	4.89
238.15	5.5030	3.14E6	9.64
285.78	2.9170	6.09E6	1.40
333.41	0.6300	2.65E6	0.15
381.04	-1.2090	1.65E7	0.09
428.67	-2.4320	2.40E6	2.46
476.3	-3.0110	4.57E6	1.98
DC	8.2760		
Total	55.508	3.56E7	87.72

It is also shown in Tab.3, when we design the cavity, with an optimized tapering shape design on the cavity inner conductor, harmonic frequencies without tunings can be controlled within the bandwidths of operation modes. However, geometry change due to fabrication error or thermal/mechanical deformation may cause the cavity harmonic frequency deviations more than the natural bandwidths. This fabrication error can be corrected by stub tuners inserted into the cylinder wall. For the cavity with N modes, N stub tuners are needed since they are interacting with each other. Here we use the 3-mode cavity as an example. A small cylinder of 5mm in height, 20mm in diameter is used to find the most sensitive tuning position for each mode along the cavity outer wall. 3 positions are chosen to make sure every mode can be tuned in both positive and negative directions as can be shown in Fig.8.

When the tuner position is confirmed, we can adjust the insertion height of each tuner to get the function of frequency shift and the insertion height. Then we can get a tuning matrix (dependence of each mode on each tuner) and invert it to get the cavity spectrum tuned.

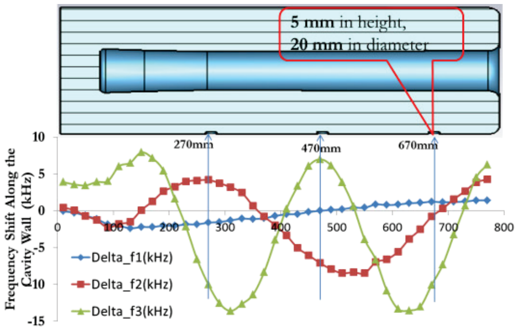

Figure 8: Tuner position simulation for the 3 harmonic modes cavity with a small cylinder perturbation.

Loop Coupler Design

For each cavity, we can use one common power coupler for all the modes. This coupler is inserted into the high magnetic field area near the cavity short end. The coupler optimum position can be simulated by moving a rectangular coupler loop along the cavity. The fundamental mode always has the lowest coupling strength. We can adjust the loop size, rotating angle and the position to make sure the fundamental mode is critically coupled, and the higher modes are over-coupled with minimum coupling [5].

CONCLUSIONS

An ultra-fast (2.1 ns pulse width), high repetition rate kicker was conceptual developed, with great power efficiency (87.72 W for 55kV kick voltage) and cost-effective (just copper or copper plated stainless steel cavities in room temperature). The conceptual design of the RF cavity, stub tuner and input loop coupler has been done for simple cavity case. Further optimization to reduce the number of harmonic modes, strategy to get more efficient tuning scheme is under study. Beam dynamics tracking, mechanical design, HOM damping will be studied further. A prototype cavity will be made; RF bench measurement and the possible vacuum device development for the beam experiment will be done in the future.

Table 3: Bandwidth of Each Mode for 300K Copper

Cavity	Operation Frequency (MHz)	Q_0 for 300K copper	β	Bandwidth for 300K copper (kHz)	Designed Frequency with Taper (MHz)	Error Frequency by Design (kHz)
Five Modes Cavity	47.63	8586	≈1	≈11.09	47.62991	-0.09
	142.89	14689	>1	>19.46	142.8915	0.15
	238.15	18973	>1	>25.10	238.153	3
	333.41	22472	>1	>29.67	333.4117	1.7
	428.67	25536	>1	>33.57	428.6718	1.8
Three Modes Cavity	95.26	12002	≈1	≈16.04	95.26267	2.67
	285.78	20784	>1	>27.50	285.7868	6.8
	476.3	27056	>1	>35.21	476.3087	8.7
One Mode Cavity	190.52	15298	≈1	≈24.91	190.5267	6.7
One Mode Cavity	381.04	19435	≈1	≈39.21	381.0361	3.9

ISBN 978-3-95450-183-0

REFERENCES

[1] MEIC Design Summary. January 12, 2015.
[2] R. A. Rimmer et al., “RF System Requirements for a Medium-Energy Electron-Ion Collider (MEIC) at JLab”, proceedings, IPAC’15, Richmond, USA (2015).
[3] B. Roberts et al, Phys. Rev. ST Accel. Beams 15, 122802 (2012).
[4] J. Guo, H. Wang, First Estimate of the Require Power for the Stripe-line RF Kicker, JLAB-TN-15-020
[5] Y. Huang et. al., “Harmonic Resonant Kicker Design for the MEIC Electron Circular Cooler Ring”, proceedings. IPAC’15, Richmond, USA (2015).

THE OPTICS OF THE LOW ENERGY FFAG CELL OF THE eRHIC COLLIDER USING REALISTIC FIELDS*

N. Tsoupas, S. Brooks, A. Jain, G. Mahler, F. Méot, V. Ptitsyn, D. Trbojevic, BNL, NY, USA
M. Severance, SBU, NY, USA

Abstract

The proposed electron accelerator of the eRHIC complex [1] will use a 1.32 GeV Energy Recovery Linac (ERL) to accelerate electron bunches to a top energy of 21.2 GeV, and subsequently will collide with hadron bunches. The electron bunches will attain the 21.2 GeV energy after passing through the ERL 16 times while they recirculate in two FFAG rings [1] which are placed alongside the RHIC hadron accelerator. The two rings are made of periodic cells and each cell is made of one focusing and one defocusing permanent magnet quadrupoles. In this paper we present the electromagnetic calculations of the 2D and 3D models of a cell which is comprised of two modified Halbach quadrupoles [2], and the optical properties of the cell. The magnetic measurements of a modified Halbach quadrupole will also be presented and compared with the model calculations.

INTRODUCTION

The mission and the design of the electron-ion collider (eRHIC) to be used in the electron-Ion-Collisions (EIC) physics program are described in a published report [1]. The eRHIC which is shown schematically in Figure 1 will make use of the existing Relativistic Heavy Ion Collider (RHIC) hadron accelerator which provides various hadronic species having maximum energies ranging from 250 GeV polarized protons to 100 GeV/u Uranium ions. The electron accelerator of the eRHIC complex will be built alongside the hadron accelerator and will provide electrons with maximum energy of 21.2 GeV. The electron accelerator shown as two red rings in Figure 1 will be built alongside the existing hadron accelerator which is shown as a blue ring in Figure 1. Polarized electron bunches will be injected at an energy of 12 MeV and will receive an energy increase of 1.32 GeV of each time they pass through the ERL a cryomodule of which is shown as an insert at the right-top of Figure 1. The electron bunches will recirculate in the two FFAG rings sixteen times to achieve the maximum energy of 21.2 GeV. The "low energy" electron ring will circulate the bunches with five energies, 1.32, 2.64, 3.96, 5.29, and 6.61 GeV and the "high energy" ring will circulate 11 beams with energies ranging from 7.93 GeV to 21.2 GeV. Each ring is based on the Fixed Field Alternating Gradient (FFAG) principle and consists of FODO cells. Each FODO cell is comprised of one focusing and one defocusing quadrupole.

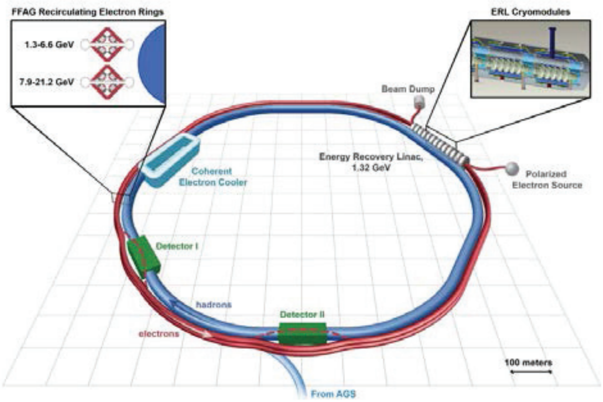

Figure 1: Schematic diagram of the eRHIC.

One of the proposed designs of the FODO cell's quadrupoles is a Halbach type permanent magnet quadrupole which is modified to prevent the interaction of the permanent magnet material with the synchrotron radiation emitted by the circulating electron bunches. This paper will present some information on the cell's beam optics which is based on computed field maps of the cell's quadrupoles.

THE FFAG CELL

One of the possible cell designs to be used for the low energy arcs of the electron accelerator is shown in Figure 2. The cell quadrupoles have aperture of radius 2 cm and are separated transversely by 5.4 mm. The low energy ring consists of 6x212 cells therefore each low energy cell focuses and bends the electron bunches by 4.9396 mrad (0.2830º). The remarkable property of the FFAG cell is indicated in Figure 2 which shows the trajectories of the electron bunches in the large energy range from 1.334 GeV to 6.622 GeV to be contained within a transverse space of 16.9 mm.

---

* Work supported by Brookhaven Science Associate, LLC under Contract No. DE-AC02-98CH10886 with the U.S. Dept. of Energy.

ISBN 978-3-95450-183-0

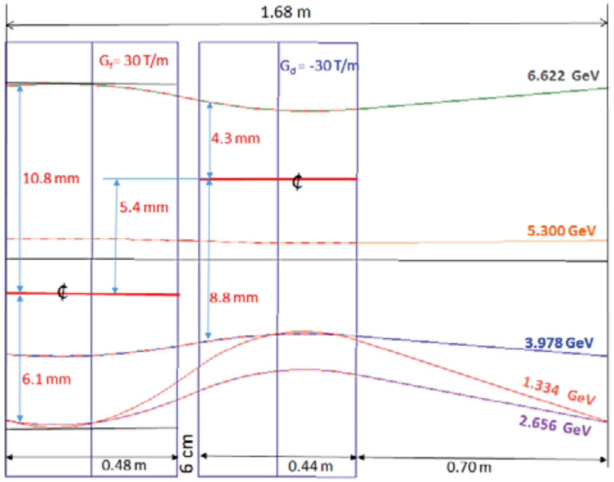

Figure 2: Schematic diagram of the 1.68 m long low energy FFAC cell.

MODELING AND ELECTROMAGNETIC DESIGN OF THE CELL

The electromagnetic design of the cell is done in two steps, first the 2D design followed by the 3D design. Both cell quadrupoles have the same cross section which is shown in Figure 3. The modification of the Halbach design consists in removing two permanent magnet wedges from left and right (see Figure 3) to prevent their damage from the synchrotron radiation, and also remove the two wedges from top and bottom to keep the four fold symmetry. A SmCo-R26SH BH curve has been used in both the 2D and 3D calculations [3].

The 2D Design

The 2D design establishes the cross section of each quadrupole to achieve the required gradient, and also minimize the 12pole multipole by varying the direction of the easy axis of blue-shaded wedges shown in Figure 3.

The 3D Design

The 6 cm longitudinal separation of the quadrupoles in the cell and the proximity between the cells justifies the 3D electromagnetic modeling. To obtain the field map of a cell we modelled three sequential cells using the OPERA computer code [4]. Details on the modelling as well as on other aspects of this paper appear in Ref [3].

An isometric view of the cell's two quadrupoles is shown in Figure 4. The 3D calculations provided the field map of the cell on a rectangular grid. The field map was used to calculate the optical properties of the cell.

MAGNETIC MEASUREMENTS OF A SINGLE QUADRUPOLE

To establish confidence on the calculated field maps we built a 6 cm long model of the quadrupole shown in Figure 5. The housing of the permanent magnet wedges is made by a 3D printer. The cross section of the built quadrupole is identical to that shown in Figure 3, the direction of the easy axis of the wedges of the built model was different from that which minimized the 12pole multipole [3].

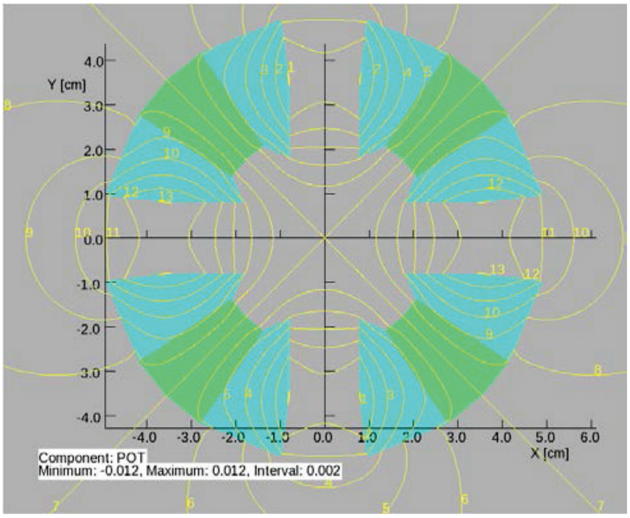

Figure 3: The cross section of the modified Halbach quadrupole.

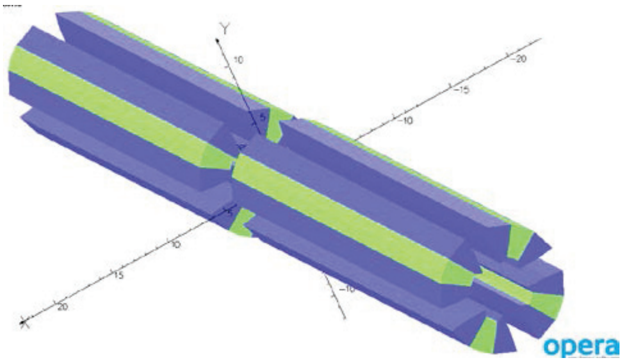

Figure 4: Isometric view of the cell's two quadrupoles.

Table 1 shows the integrated strengths of the quadrupole and 12pole at a radius of 1 cm. From Table 1 we can calculate that the difference between the calculated and measured 12pole is ~9x10^{-4} cm^{-4} at a radius of r=1 cm relative to the quadrupole strength. This discrepancy is within our tolerances as the optics calculations show.

Table 1: Measured and Calculated Strengths of the Quad

Quad	**Int. Quad [Gauss]**	**Int. 12pole [Gauss.cm^{-4}]**
Calculations	18730.5	337.4
Measurements	18650.0	350.6

Quadrupole correctors, will be included with the quad.

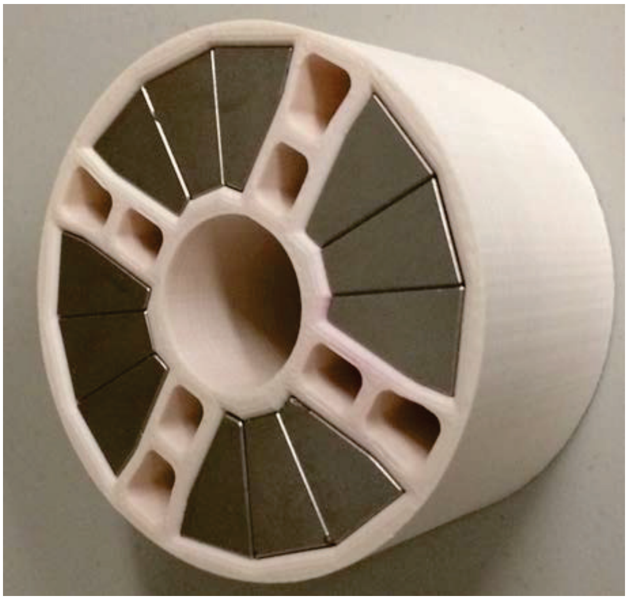

Figure 5: A picture of the modified Halbach quadrupole. The housing of the permanent magnet wedges is made by a 3D printer.

OPTICAL PROPERTIES OF THE CELL

The beam optics of the cell consists in studying the following properties of the low energy ring:

- The closed orbits of the ring for the electron bunches within the energy range 1.3 to 6.6 GeV. This study proves that the magnetic field map of a single cell allows the formation of closed orbits in the ring.
- The horizontal and vertical tunes Q_x and Q_y and the chromaticities ξ_x, ξ_y, which correspond to the closed orbits. This study provides information on the stability of the closed orbits.
- The acceptance of the ring, which is the maximum beam emittances ε_x, and ε_y, of each beam bunch that corresponds to a closed orbit of a given energy.
- The dynamic aperture for each close orbit.
- The beta functions in the cell.

The zgoubi computer code [5] has been used to calculate the optical properties.

The Closed Orbits

Figure 6 shows 42 closed orbits of electron bunches in a cell in the energy range of 1.3 GeV to 6.6 GeV. In the zgoubi code x-axis is along the beam direction and y is radial.

Tunes and Chromaticities

Figure 7 is a plot of the tunes Q_x, and Q_y, and the chromaticities ξ_x, ξ_y. The betatron tunes in combination with the chromaticities as plotted in Figure 7 indicate that the electron bunches are away from beam resonances.

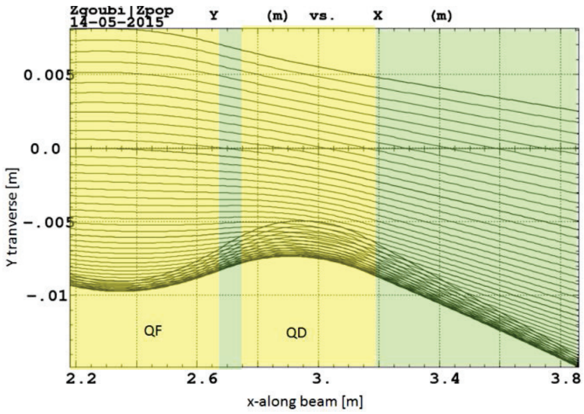

Figure 6: Closed orbits in the low energy cell of eRHIC.

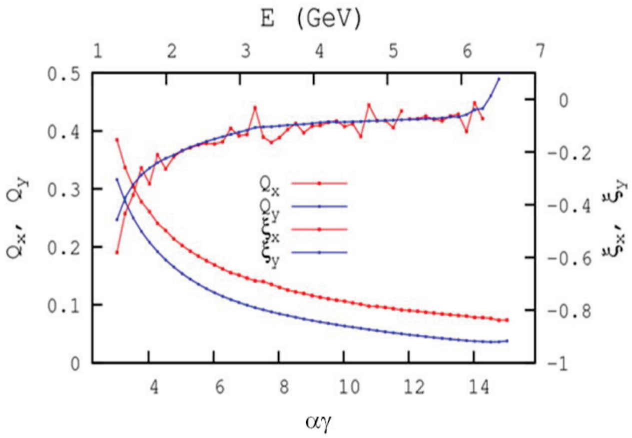

Figure 7: Plot of tunes and the chromaticities in a cell as a function of electron's kinetic energy (top scale). The symbol α=g/2-1=1.16x10^{-3} in the label of the horizontal scale and g is the g-factor of the electron.

The Acceptance of the Ring

Figures 8 and 9 show the horizontal and vertical rms acceptances of the low energy ring for five of the electron bunches.

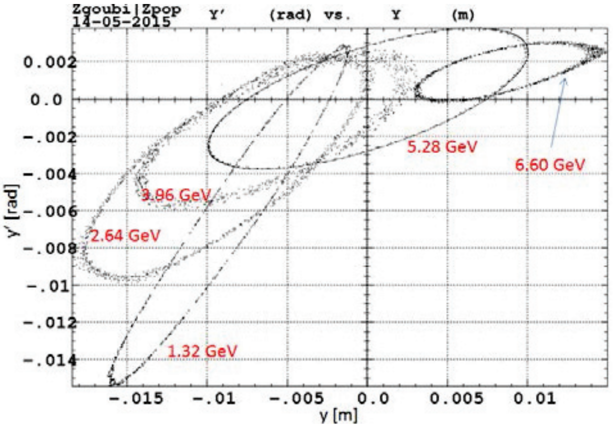

Figure 8: The horizontal rms beam acceptance for each of the five energy-bunches being transported in the ring.

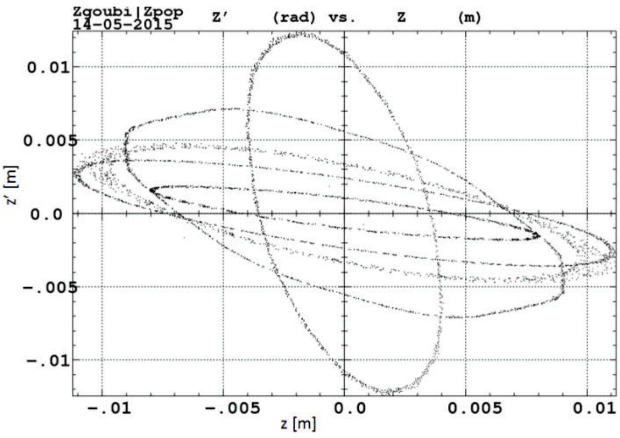

Figure 9: The vertical rms beam acceptance for each of the five energy-bunches being transported in the ring.

The minimum horizontal or vertical calculated rms value of the ring's acceptance is ~0.02 [m.rad]. This value is much larger than the required horizontal and vertical beam emittance of $30x10^{-6}$ [m.rad] to be transported in the ring.

The Dynamic Acceptance of the Ring

Starting with the maximum y and z coordinates of each of the five acceptance phase space ellipses as we calculated in the previous section, the "zgoubi" computer code calculated the maximum y and z particle-coordinates at the entrance of the ring that can be transported at the exit. Figure 10 is a plot of the dynamic aperture for the energy-bunches mentioned in this paper in the range 1.3 to 6.6 GeV.

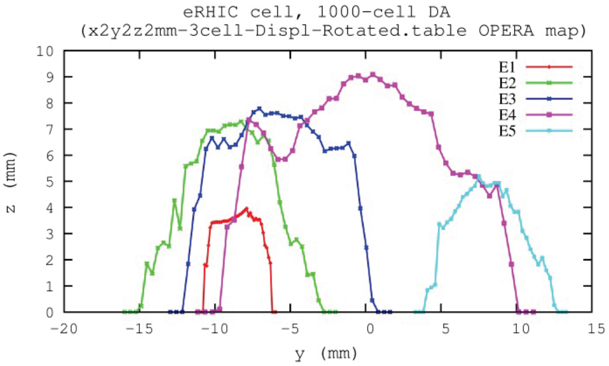

Figure 10: The dynamic acceptance of the low energy ring for the five energy bunches mentioned in the paper.

The Beta Functions of the Cell

Figure 11 plots the horizontal and vertical beta functions of the low energy FFAG eRHIC cell for three energies. The focusing and defocusing quadrupoles of the cell are highlighted.

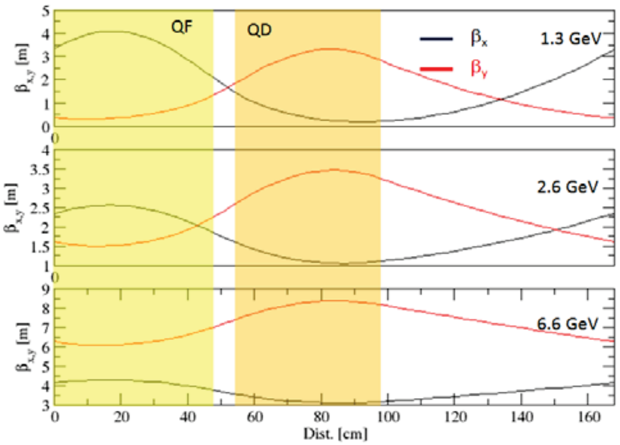

Figure 11: The horizontal and vertical beta functions of the low energy FFAG eRHIC cell for three energies. The shaded areas are the focusing and defocusing quads.

CONCLUSIONS

Using realistic field maps computed with the OPERA computer code, we calculated the optical properties of a cell to be used in the FFAG lattice of the eRHIC's recirculating electron ring. The calculated horizontal/vertical tunes, and chromaticities, indicate stability for the transported beam bunches in the required energy range. The calculated phase space for the beam acceptances and the dynamic apertures are large enough to accept the required beam emittances. The 3D calculations performed on a modified Halbach quadrupole are in agreement with the measurements thus these magnets can provide the desired magnetic fields for the cell of the FFAG lattice of the eRHIC.

REFERENCES

[1] arXiv:1409.1633
[2] K. Halbach J. Appl. Phys. 57 (1) 15 April 1985
[3] N. Tsoupas et. al. Technical Note BNL/CAD eRHIC/1 July 2015.
[4] Vector Fields Inc.
[5] F. Méot, Nuclear Instruments and Methods in Physics Research A 767 (2014) 112–125

PERFORMANCE OF THE DIGITAL LLRF SYSTEMS AT KEK cERL

F. Qiu#, D. Arakawa, Y. Honda, H. Katagiri, T. Matsumoto, S. Michizono, T. Miura, T. Obina,
H. Sakai, KEK, Tsukuba, Ibaraki 305-0801, Japan
S. B.Wibowo, SOKENDAI, The Graduate University for Advanced Studies,
Hayama, Kanagawa 240-0193, Japan

Abstract

A compact energy recovery linac (cERL), which is a test machine for the next generation synchrotron light source 3-GeV ERL, was constructed at KEK. In the cERL, a normal conducting (NC) buncher cavity and three superconducting (SC) two-cell cavities were installed for the injector, and two nine-cell SC cavities were installed for the main linac (ML). The radio-frequency (RF) fluctuations for each cavity are required to be maintained at less than 0.1% rms in amplitude and 0.1° in phase. These requirements are fulfilled by applying digital low-level radio-frequency (LLRF) systems. During the beam-commissioning, the LLRF systems were evaluated and validated. A measured beam momentum jitter of 0.006% shows that the target of the LLRF systems is achieved. To further improve the system performance, an adaptive feedforward (FF) control-based approach was proposed and demonstrated in the beam-commissioning. The current status of LLRF system and the adaptive FF approach for LLRF control in the cERL are presented in this paper.

INTRODUCTION

At KEK, a compact energy recovery linac (cERL), as a test facility for future 3-GeV ERL project, was constructed, and the first beam-commissioning was carried out at June, 2013 [1, 2]. The cERL is a 1.3 GHz superconducting radio-frequency (SCRF) machine that is operated in continuous-wave (CW) mode. As shown in Fig. 1, the cERL consists of an injector part and a main linac (ML) part. A normal conducting (NC) cavity (buncher) and three two-cell superconducting (SC) cavities (Inj. 1, Inj. 2, and Inj. 3), were installed in the injector, and two main nine-cell SC cavities (ML1 and ML2) were installed in the main linac (ML). For low-emittance beam, the requirements of the RF field stabilities are 0.1% rms in amplitude and 0.1° in phase in the cERL. This requirements are fulfilled by applying digital low-level radio-frequency (LLRF) systems.

The LLRF system in the cERL is disturbed by various disturbances include the 50-Hz microphonics, the 300-Hz high-voltage power supply (HVPS) ripples and the burst mode beam-loading [3-4]. The current LLRF system is not sufficient to reject all of these disturbances. In view of this situation, we have proposed a disturbance observer (DOB)-based approach for suppress the main disturbances in the cERL [3]. Based on this approach, the disturbances can be reconstructed by the cavity pickup signal and then removed from the feedforward (FF) table in real-time. Therefore, in terms of function, this approach is just like an adaptive FF control.

In this paper, we first introduce the LLRF system in the cERL, and then present the measured LLRF stability and beam momentum jitter during the cERL beam-commissioning. In the next stage, we describe the basic idea of the proposed adaptive FF approach for disturbances rejection. Finally, we present the preliminary result of this adaptive FF approach for microphonics rejection in the cERL commissioning.

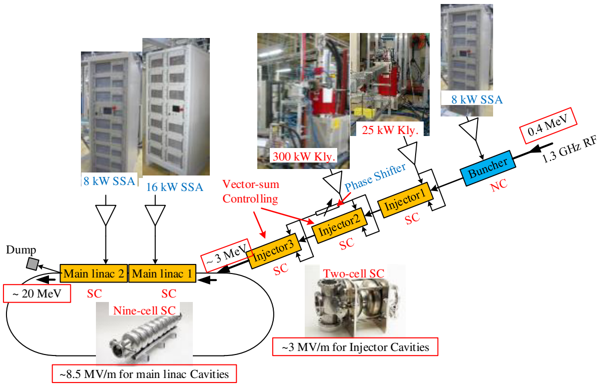

Figure 1: Layout of the cavities in the cERL. The marked values of beam energy and accelerating field indicate the current state in the cERL beam-commissioning.

HLRF SYSTEM

RF power sources including 25 kW klystron, 300 kW klystron, 8 kW solid state amplifier (SSA) and 16 kW SSA were employed in the cERL. Figure 1 shows the layout of the cavities and corresponding power sources in the cERL. Table 1 gives the loaded Q value, required RF power, and RF sources for each cavity. It should be mentioned that, in the Inj .2 and Inj .3, a vector-sum control method is applied. All of these RF sources are stable and reliable in the beam commissioning.

Table 1: Cavity Parameters of the cERL

Cav.	Q_L	$f_{1/2}$ [Hz]	RF power [kW]	RF source
Bun.	1.1×10^4	57000	3	8 kW SSA
Inj. 1	1.2×10^6	540	0.53	25 kW Kly.
Inj. 2	5.8×10^5	1120	2.4	300 kW Kly.
Inj. 3	4.8×10^5	1350		
ML1	1.3×10^7	50	1.6	16 kW SSA
ML2	1.0×10^7	62	2	8 kW SSA

[#] qiufeng@post.kek.jp

ISBN 978-3-95450-183-0

LLRF SYSTEM

A simplified schematic of the cERL LLRF system is shown in Fig. 1. The 1.3-GHz cavity pick up signal is down-converted to a 10-MHz intermediate frequency (IF) signal at first. The 10-MHz IF signal is sampled at 80-MHz by a 16-bit analog to digital converter (ADC) and then fed into a field-programmable gate array (FPGA) board. The baseband in-phase and quadrature (I/Q) components are detected from the IF signal with a non-IQ-based IQ detection method. After being filtered by infinite impulse response (IIR) filters, the detected I/Q signals are compared with their set values, and the I/Q error signals are calculated. The I/Q error signals are controlled by proportional and integrational (PI) feedback (FB) controllers and then added together with their corresponding FF tables. Finally, the combined I/Q signals are fed into an I/Q modulator via 16-bit digital to analog convertors (DACs) to regenerate the 1.3-GHz RF signal. This regulated RF signal will be used to drive the high-power RF source (e.g. klystron and SSA), which drives the cavities. It should be mentioned that, to evaluate the stability of the cavity pick-up signal, we have installed a pick-up monitor inside FPGA (see Fig. 2). An adjustable-bandwidth digital filter, aims to remove the ADC noises, is placed in front of the monitor.

A µTCA system is employed as the digital control platform. Experimental physics and industrial control system (EPICS) is selected to be the data communication system. The detailed information about that digital platform can be found in [4].

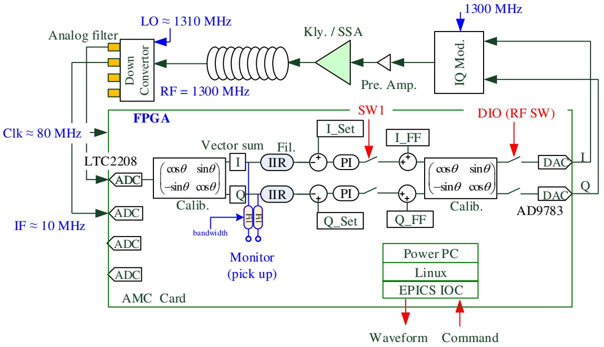

Figure 2: Schematic of the LLRF system in the cERL.

STABILITY

The typical LLRF system performance in the cERL beam-commissioning are listed in Table 2. Generally speaking, all of our LLRF systems satisfy the requirements of the cERL beam-commissioning. Disturbances in the LLRF system are suppressed well by applying high FB gains. However, some high intensity disturbances still exist in the LLRF systems. Figure 3 shows the RF performance of Inj. 2&3 and ML2. It is very clearly to see that, there is a 300-Hz fluctuation in the vector-sum RF filed of Inj. 2&3 cavities, especially in the phase. Investigations reveal that this 300-Hz ripples come from the high voltage power supply [3]. On the other hand, an approximately 50-Hz component can be observed in the phase of the ML2, this component is mainly caused by the microphonics [5].

The beam energy stability is measured by the screen monitor which is installed downstream of the bending magnet with a 2.2 m dispersion and 62.6 µm/pixel resolution. The beam momentum jitter is calculated based on the peak point of the beam projection in the screen monitor. The calibrated beam momentum jitter is about 0.006% rms as shown in Fig. 4. This value is in consistence with the measured RF stability in the LLRF system (see Table 2).

Table 2: Status of RF Systems in the Commissioning

Cavity	φ_b	V_c	**RF stability (rms)**	
			$\delta A/A$	$\delta\theta$
Buncher	-90°		0.07%	0.04°
Inj. 1	0°	0.7 MV	0.006%	0.009 °
Inj. 2	0°	0.65 MV	0.007%	0.025°
Inj. 3	0°	0.65 MV		
ML1	0°	8.56 MV	0.003%	0.010°
ML2	0°	8.56 MV	0.003%	0.007°

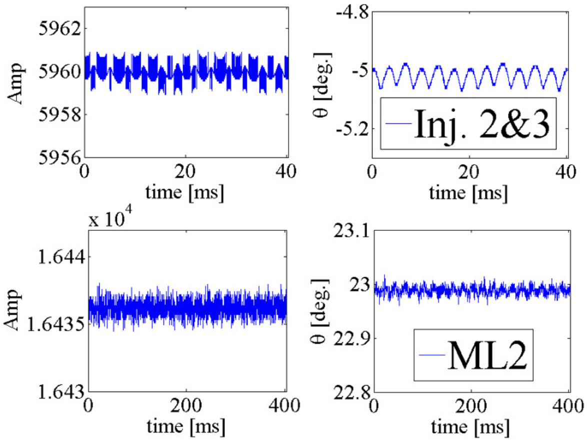

Figure 3: RF stability of the Inj. 2&3 (top) and ML2 (bottom). The 300-Hz fluctuation in the Inj. 2&3 is caused by the high voltage power supply ripples.

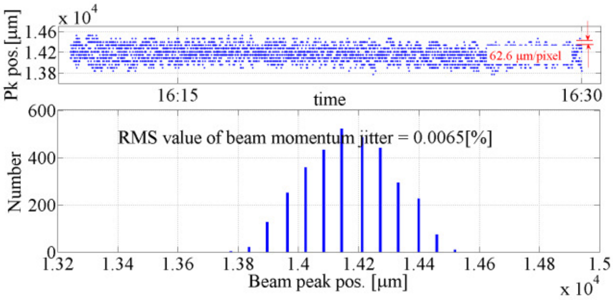

Figure 4: Beam momentum jitter measurement. The measured beam momentum jitter was 0.0065% rms, which is in agreement well with RF stability.

ISBN 978-3-95450-183-0

ADAPTIVE FF CONTROL

As depicted in Fig. 3, disturbances still exist in the current LLRF system even with high FB gains. These disturbance signals can be rejected clearly by applying an adaptive FF approach. The key idea of this adaptive FF approach is as bellow.

1. Identify the nominal system model and calculate its inverse model.
2. Estimate and rebuild the disturbance signals based on the inverse model in the step 1 from cavity pick up signal.
3. Remove the estimated disturbance in step 2 from the FF table inside FPGA.

The first step is performed off-line, whereas the next two steps are carried out in real-time. Therefore, the disturbances are removed in the cavity pickup signal. This process can be illustrated in Fig. 5. Here, $G_P(s)$ and $G_n(s)$ represent the actual plant (e.g., cavities and RF devices) and nominal model, respectively. Signals d and d_e represent the real disturbance and the disturbance estimate, respectively. Signal FF represents the FF table output. As shown in Fig. 5, the disturbance estimate d_e can be expressed by [3]

$$d_e = (\varepsilon + d) G_P(s) G_n^{-1}(s) - \varepsilon . \qquad (1)$$

If the system nominal model $G_n(s)$ is a perfect representation of real system $G_P(s)$, then according to (1), the $G_P(s)$ is perfectly cancelled by $G_n^{-1}(s)$, therefore, the disturbance estimate d_e is exactly equal with real disturbance d, that means, the disturbance d is perfectly rebuilt by disturbance estimate d_e. In practice, the system model cannot be identified perfectly, this is to say, there are some deviations between real disturbance d and d_e. Fortunately, a related analytical study reveals that the robustness of this approach is rather strong, that means the adaptive FF controller still works well even in the presence of the model mismatch.

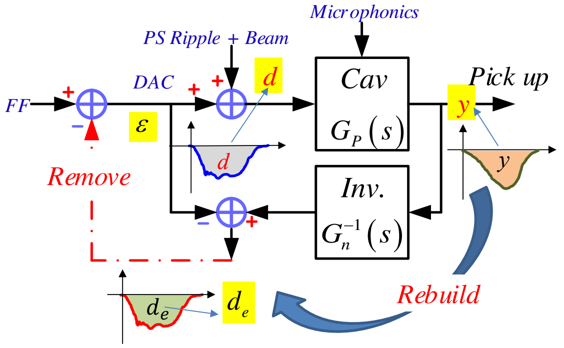

Figure 5: Basic idea of the adaptive FF approach, the key step is to reconstruct the disturbances based on the inverse system model.

We have developed and installed this adaptive FF controller in the cERL µTCA-bases LLRF systems. During the beam-commissioning, we have demonstrated this approach for disturbance rejection. As presented above, in the cERL, the main disturbances in the LLRF systems include the 300 Hz power supply ripples, the high intensity beam-loading, and the microphonics. Concerning the validation of the adaptive FF controller regards to power supply ripples rejection and beam-loading compensation, the preliminary results were already presented in [3]. For microphonics rejection for the ML2 cavity, the performance of the adaptive FF control is shown in Fig. 6. If we only use traditional PI control but without the adaptive FF control (indicated by the blue color in Fig. 6), the microphonics effect of ML2 cavity can be observed clearly in the phase of the RF field. It is clear to see that there is a 50 Hz dominant component in both waveform and spectrum in the RF phase of the ML2 cavity. After switching on the adaptive FF control, the microphonics include the 50-Hz dominant component are disappeared (indicated by the red color in the Fig. 6).

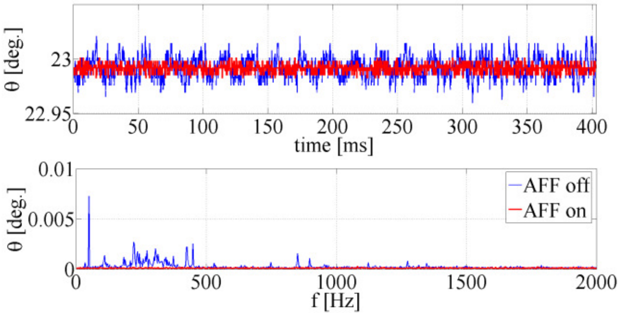

Figure 6: Measured RF phase of the ML2 cavity pickup signal in the case of with and without adaptive FF control. Both waveform (top) and spectrum (bottom) are presented.

SUMMARY

Digital LLRF systems for the injector and main linac were constructed in the cERL at KEK. During the beam-commissioning, the LLRF systems perform well and the required RF stability of the cERL (0.1% rms in amplitude and 0.1° in phase) is satisfied. Furthermore, a beam momentum jitter of approximately 0.006% was achieved. Additionally, for R&D, we have proposed an adaptive FF-based approach aims to reject the disturbances in the RF system. Results in the cERL commissioning show that this approach is very effective for the disturbance rejection.

REFERENCES

[1] N. Nakamura et al., “Present status of the compact ERL at KEK,” Proc. IPAC’14, Dresden, Germany (2014).

[2] S. Sakanaka et al., “Construction and commissioning of compact-ERL Injector at KEK,” Proc. ERL2013, Novosibirsk, Russia (2013).

[3] F. Qiu et al., “A disturbance-observer-based controller for LLRF systems”, Proc. IPAC’15, Richmond, USA (2015).

[4] T. Miura, “Low-level RF system for cERL”, Proc. IPAC’10, Kyoto, Japan (2010).

[5] M. Satoh et al., “Mechanical vibration search of compact ERL main linac superconducting cavities in crymodule”, Proc. IPAC’14, Dresden, Germany (2014).

ISBN 978-3-95450-183-0

USING A 1.3 GHz 20 kW SOLID STATE AMPLIFIER AS RF POWER SUPPLY FOR DC-SRF PHOTO-INJECTOR*

F. Wang#, L.W. Feng, J.K. Hao, L. Lin, K.X. Liu, S.W. Quan, B.C. Zhang,
Institute of Heavy Ion Physics & State Key Laboratory of Nuclear Physics and Technology,
Peking University, Beijing 100871, China

Abstract

R&D of a 1.3 GHz 20 kW CW solid state amplifier, which consists of 88 elementary modules with individual power supplies, has been carried out under the cooperation between BBEF (Beijing) and Peking University for the DC-SRF photo-injector. It has been installed and applied to the experiments of the DC-SRF photo-injector at Peking University since 2012. The structure, test with full power and full reflection, improvements and performance for long-term operation of this 20 kW solid state RF amplifier will be described in this presentation.

INTRODUCTION

The DC-SRF photo-injector which combines a DC Pierce structure and a superconducting cavity was firstly proposed by Peking University in 2001 [1]. The prototype of the DC-SRF photo-injector with a 1.3 GHz 1.5-cell superconducting cavity was constructed and preliminary experiments at 4.2 K demonstrated its feasibility in 2004 with the electron beam energy gain of about 1 MeV [2]. In the beam experiments of the prototype injector, a 4.5 kW solid state amplifier (SSA) was used. It was combined by eight unit modules and a dummy load cooled by water. Each module was supposed to deliver up to 600 W, which included four 150 W transistors. The designed output power was 4.5 kW but only 3.5 kW had been achieved finally.

After demonstrating the feasibility of prototype, we designed and constructed an upgraded DC-SRF injector with a 3.5-cell cavity. The designed beam power is 13 kW with beam current of 2.6 mA and energy gain of 5 MeV [3]. Taking into account the regulation reserve of 20% for phase and amplitude control and 6% for losses in the waveguide distribution, an amplifier with the output up to 18 kW is required. So a 20 kW CW amplifier at 1.3 GHz is needed. Table 1 shows the technical specification of the power amplifier.

There are three kinds of possible RF amplifiers, which are klystrons, IOTs and SSAs, can provide CW 20 kW RF power at 1.3GHz. The ELBE CW-LINAC employs four pairs of 10 kW SSAs to replace the 10 kW klystrons for the four superconducting 9-cell TESLA cavities in January 2012 [4]. The Cornell Energy-Recovery Linac (ERL) injector has two high power 1300 MHz RF systems, the first system is based on a 16 kW IOT transmitter to drive a normal conducting buncher cavity, and the second system employs five 120 kW klystron to feed 2-cell superconducting cavities [5]. ALICE at Daresbury Laboratory uses 5 IOTs from three different commercial suppliers [6].

Table 1: Technical Specification of the Power Amplifier

Parameter	Required
Frequency Range	1300±0.05MHz
CW & Pulsed Output Power (1dB Compression)	⩾ 20 kW
Linear Gain	⩾73dB
Output Harmonics 2nd Order	⩽-30 dBc
Output Harmonics 3rd Order	⩽-30 dBc
RF Phase Shift vs. Output	⩽10°
Gain Change vs. Output	⩽2.0 dB
Efficiency at 20kW output	⩾40%

From the experience gained from our 1.3 GHz 3.5 kW SSA, we realized the advantages of SSA for small facilities such as high modularity with the associated redundancy and flexibility, elimination of high voltage and high power circulator, and simple start-up procedures and low maintenance cost. Especially at that time transistors with CW output power more than 200 W at 1.3 GHz were available from industry and the amplifier could be made in China. So we decided to manufacture a SSA under the collaboration with BBEF by the end of 2009.

STRUCTURE OF THE 1.3 GHz 20 kW SSA

Benefitted from the transistors with output power more than 200 W, the unit module which contains two transistors, a circulator and a terminal can deliver output power up to CW 350 W after its construction. The transistors (MRF6V13250H) are from freescale, and it is claimed each one can deliver up to CW 230 W at 1.3 GHz, and a little bit higher to 250 W in pulsed mode with length of 200 μs and duty factor of 10%. The custom made circulator (VBM1387) is from VALVO in Germany, its isolation is more than 25 dB, and full reflection with the CW power of 400 W is allowed. The terminal (Series 32-1209) is from Florida RF Labs and its power capability is up to 500 W. Each unit module is powered by its own power supply with the output voltage of 50 V and the current up to 14 A. The designed efficiency of AC to DC convertor is 92%.

---

*Work supported by National Basic Research Project (973) (No. 2011CB808304 and No. 2011CB808302)

#fangwang@pku.edu.cn

ISBN 978-3-95450-183-0

Figure 1 shows the overall structure of the SSA. It consists of 8 transistor banks. Each bank generates 3 kW and is decoupled by a coaxial-waveguide transition from 1 5/8 inch rigid line to WR650 waveguide, and in which, there are 11 elementary modules with individual power supplies and one module is used as a preamplifier to drive the other ten. Figure 2 is the photograph of the SSA, the big plates cooled by water with flow rate of 4.9 m^3/h at 4 bar are the transistor banks, the 350 W unit modules are mounted on the upper side and the 700 W AC to DC convertors are on the reverse side.

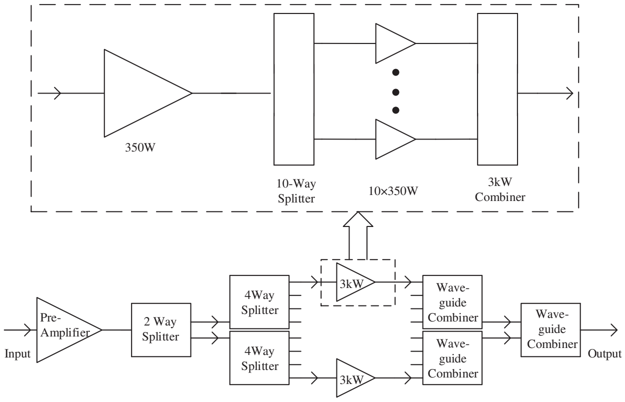

Figure 1: Structure of 20kW SSA.

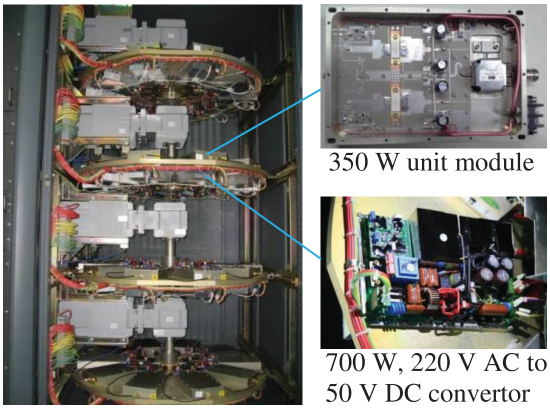
350 W unit module

700 W, 220 V AC to 50 V DC convertor

Figure 2: 1.3 GHz 20 kW SSA.

TEST AND RESULTS

After the accomplishment of the manufactory and factory test in BBEF, the SSA had been delivered to Peking University in the January of 2012. After installation, the tests of the amplifier including whether the basic parameters reach the designed values, long term performance with dummy load, full CW reflection, and the performance in pulse mode.

The results in detail are brought out in the following. The gain and output of the power amplifier is illustrated in Fig. 3, it can be seen the gain is larger than 85 dB and changes 1.6 dB from 1kW to 20kW. The phase shift changes 9.5° when the output power increased as shown in Fig. 4. The 3 dB bandwidth of the amplifier is more than 30 MHz, and it is much larger than typical 3 dB bandwidth of klystron and IOT. The drain efficiency of the SSA is 38% at 20 kW output and 25% at half power output. The efficiency of RF power, which is 34% at 20 kW output and 20% at half output, is a little lower. The second and third harmonics of the output RF signal are suppressed which are -68.9 dBc and -57.1 dBc respectively, while those of the input RF signal are -41.7 dBc and -49.7 dBc respectively. The long term stability of the amplifier was measured with the low level control system and the results of 5kW output and 17kW output are illustrated in Fig. 5 and Fig. 6 respectively. The temperature gradient of the power is ±0.8%/ °C, and we did not get the temperature gradient of the phase as the temperature of the coolant and the output power are both fluctuating during the measurements. We also measured the parameters of the amplifier in pulsed mode. The rising time of the input RF signal is about 54 ns, and the output is 64 ns. In delay measurement, the output signal is 386 ns later than the input signal, which includes the propagation time of 230 ns through coaxial cable with length of 45 m, the propagation time of 81 ns through the waveguide with the length of 17.5 m, so the delay of the amplifier is about 75 ns. The power consumed by the amplifier in pulsed mode was measured and there is a wall-plug power consuming of about 9 kW when the amplifier is only turned on but without RF output. This 9 kW is the quiescent power drain and it varies when the transistor works at different quiescent points. In our case, in order to maintain small gain fluctuation, the quiescent power drain is quite large and then limits the efficiency.

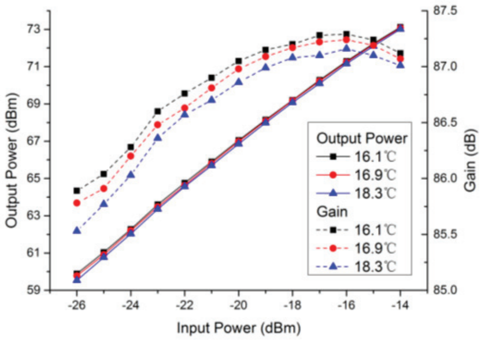

Figure 3: Output power and gain of the 20kW SSA.

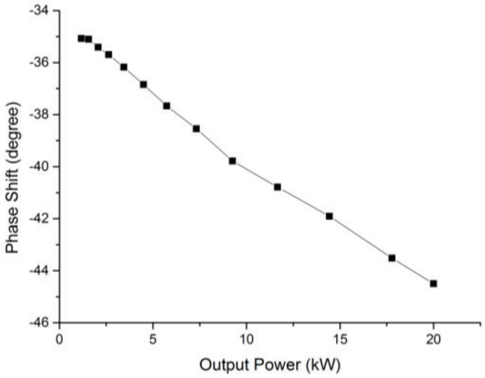

Figure 4: Phase shift of the 20kW SSA.

ISBN 978-3-95450-183-0

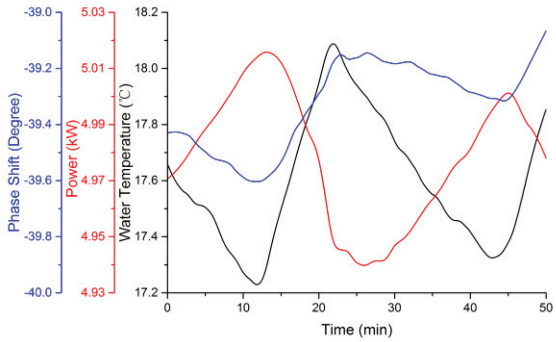

Figure 5: Stability measurements with 5 kW output.

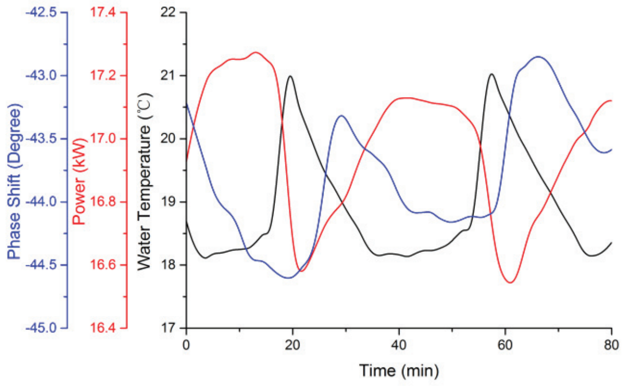

Figure 6: Stability measurements with 17 kW output.

IMPROVEMENTS AND PERFORMANCE

Because there is no large power circulator for the SSA but the full reflection may exist during the commissioning and even the operation of the DC-SRF photo-injector, we tested the SSA in full reflection with forward power of 20 kW. There were two problems during the full reflection test, one was a PTFE-support of a 1 5/8 inch rigid line was burnt and the other was one 3 kW transistor bank failed because the printed circuits near the output of the unit modules had cracked. Therefore, we realized the temperature monitoring of other components besides the unit modules is also important for the amplifier safety interlock to avoid breakdown of the SSA. And then we added temperature sensors on the eight coaxial-waveguide transitions. Stable operation of the SSA was then resumed and the amplifier sustained a test for ten minutes full reflection with CW forward power of 16 kW.

For the commissioning and operation of the DC-SRF photo-injector, a digital low level RF control system was constructed based on the FPGA and the results of the control system show the field instability is less than 0.1% (rms) for amplitude and 0.1° (rms) for phase. During the commissioning and routine operation of the DC-SRF photo-injector, the amplifier works well and has run for about 2000 hours without any big problem. Failures of a few transistors occurred (3 over 88) and the SSA was still delivering RF power. The eight spare unit modules made the replacement very easy.

CONCLUSIONS

A 1.3 GHz 20 kW CW SSA has been installed at Peking University. The efficiency of RF power is 34% with full output of 20 kW, the phase and gain various 9.5°and 1.6 dB respectively when output power changed from 1 to 20 kW and the temperature gradient of amplitude is ±0.8% / °C. Full reflection test was carried out with a short waveguide terminal, and the result is 16 kW over 16 kW in CW for ten minutes without problem. It has been used for routine operation of the DC-SRF photo-injector successfully since 2013.

REFERENCES

[1] K. Zhao et al., Nucl. Instr. and Meth. A475 (2001) 564.
[2] J. Hao et al., Nucl. Instr. and Meth. A557 (2006) 138.
[3] W. Xu et al., "Study on the 3.5 - CELL DC- SC Photo-Injector", Proceedings of SRF2007, Peking Univ., Beijing, China, 2007
[4] H. Buettig et al., Nucl. Instr. and Meth. A704 (2013) 7-13.
[5] S. Belomestnykh et al., "High Power Testing RF System Components for the Cornell ERL Injector", Proceedings of EPAC 06, 2006
[6] R. Bate et al., "Commisioning of the ERLP SRF Systems at Daresbury Laboratory", Proceedings of EPAC08, 2008

DIAGNOSTIC TEST-BEAM-LINE FOR THE MESA INJECTOR*

I. Alexander†, K. Aulenbacher, V. Bechthold, B. Ledroit, C. Matejcek
Institut für Kernphysik, Johannes Gutenberg-Universität, D-55099 Mainz, Germany

Abstract

With the test-beam-line it is possible to measure the two transverse phase-spaces and the temporal distribution of the electron bunches. It is also possible to investigate the emittance close to the source and further down stream to check the emittance evolution along the beam-line. Further more the beam halo can be studied. The beam-line components will be introduced and some preliminary results will be presented.

INTRODUCTION

MESA will be a multi-turn Energy Recovery Linac (ERL) which can be operated in two different modes. An ERL Mode (105 MeV) or an External Beam (EB) Mode (155 MeV) [1, 2]. The source will be a 100 keV dc photo gun which delivers polarized electrons with a current of 150 µA and an unpolarized electron beam with a beam current of 1 mA in stage 1 and 10 mA in stage 2. Close to the source there will be a spin manipulation section with two Wien-Filters and a solenoid followed by a chopper-buncher section consisting of four normal conducting cavities. The injector will be normal conducting with an output energy of 5 MeV. After the injector follow two superconducting linac modules which produce an energy gain of 25 MeV each. In Figure 1 a view of MESA is shown. The goal is to operate in cw-mode which means a bunch charge of 0.8 pC in stage 1 and 8 pC in stage 2.

The task of the diagnostic test-beam-line is to determine if the source can deliver a smaller emittance than the acceptance of the accelerator - for all bunch charges - which requires that the normalized emittance is $\varepsilon_n \leq 1\,\mu\mathrm{m}$. For the operation of MESA the source should be reliable and deliver a high extractable charge with a long lifetime.

Semiconductor photo cathodes have some properties that should be taken into account. Close to the band gap energy it is possible to create spin polarized electrons with circular polarized photons. However when operating in this mode one suffers from low quantum efficiency (QE) and reduced cathode lifetime. If high currents, but no spin-polarization, are desired it is advantageous to use higher photon energies, since the QE is almost an order of magnitude larger and the lifetime is longer. At around 400 nm the photo cathodes can have a QE of $10\% \triangleq 32\,{}^{\mathrm{mA}}\!/_{\mathrm{W}}$. For higher photon energies not only the QE increases but also the thermal emittance does. This is because of the fact, that the stimulated electrons have not enough time to thermalize while they are traveling through the semiconductor and end up with a wider energy distribution. This additional energy spread gets transferred into more transverse momenta which leads to a higher thermal emittance [3].

The source in the diagnostic test-beam-line has delivered 700 C within one charge-lifetime at average currents exceeding 1 mA (MESA stage-1). The experiment needs average current of $1(10)$ mA corresponding to an extracted charge of $3.6(36)\ {}^{\mathrm{C}}\!/_{\mathrm{h}}$ if a transmission of 100% is assumed. To achieve a complete transmission a RF-synchronized laser must excite photo-emission. We will capture the so-produced bunches by a harmonic buncher system which can accept bunches with an extension of about 120°. This leads to the requirement that the emitted intensity - which is the convolution of the temporal laser intensity profile and the response of the photo cathode - must fit into this interval. Tiny fractions outside the interval may be suppressed by a chopper system to provide very clean operating conditions for MESA. In the set-up described here one of the circular deflecting cavities which were developed for the chopper system of MESA is used as temporal diagnostic instrument - see below.

We estimate the space charge caused current limit of the source by $I_{sc,lim} = p_0 \frac{A}{d^2} U^{3/2}$. Here $p_0 = 2.33 \cdot 10^{-6}\,{}^{\mathrm{A}}\!/_{\mathrm{V}^{3/2}}$ is the so-called perveance, $\frac{A}{d^2} = 44.4 \cdot 10^{-6}$ is a geometric factor with the emitting area $A = 1\,\mathrm{mm}^2$ and the cathode-anode distance $d = 150\,\mathrm{mm}$. The accelerating voltage $U = 100\,\mathrm{kV}$. With all these parameters the emittance is still $< 1\,\mu\mathrm{m}$ and the current limit would be $I_{sc,lim} \simeq 3\,\mathrm{mA}$. This leads to the expectation, that the source can fulfill the requirements of MESA stage 1. This is also supported by CST-computersimulations [4]. Nevertheless a new 200 keV source is in production to increase the current limit to the requirements of MESA stage 2 [4].

COMPONENTS

Beam Line

A schematic overview of the beam-line setup is given in Figure 2. In the upper left side there is the dc photo gun with 100 kV and the electrons get accelerated in the vertical direction. After 1 m of beam-line the first analyzing stage (scanner 1) is placed followed by an α-magnet which bends the electrons 270° from the vertical to the horizontal direc-tion. Scanner 1 is positioned close to the source so that it is possible to measure the emittance without large influence of other beam manipulating elements. Between the both α-magnets the second analyzing stage (scanner 2) is mounted.

---

* Work supported by the German Science Foundation (DPG) under the Cluster of Exelence PRISMA

† alexand@kph.uni-mainz.de

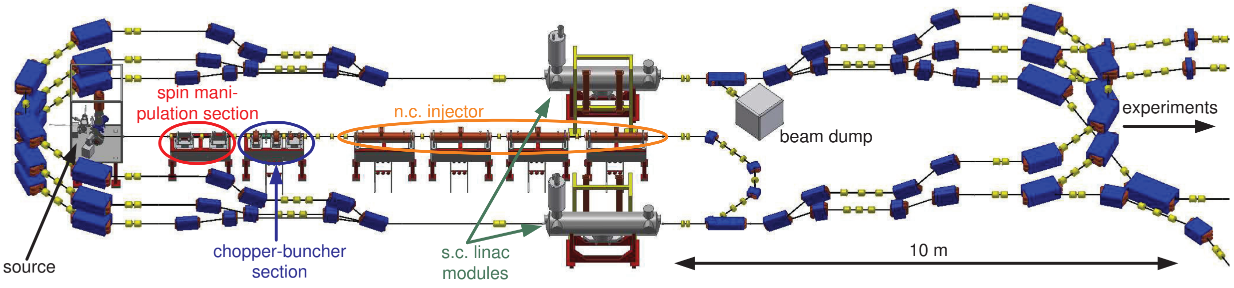

Figure 1: Floor plan of the MESA accelerator facility. In the left mid side sits the 100 keV dc photo gun, followed by some spin manipulation elements and the normal conducting injector. The main linac consists of two superconducting linac modules with two or three recirculations, depending on the operation mode. The experiments will be located further on the side and are not shown here to enhance visibility.

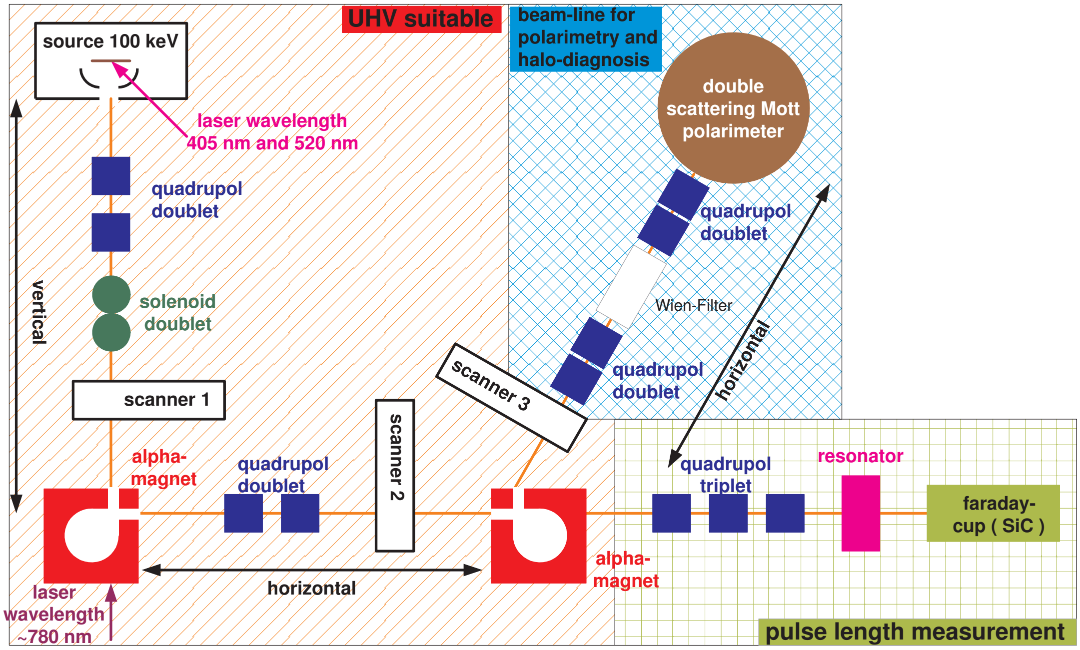

Figure 2: Schematic overview of the beam-line setup.

Here the evolution of the emittance with respect to the position of scanner 1 can be studied. If the second α-magnet is switched off investigations of the temporal distribution of the electron beam can be done with a deflecting cavity [5, 6, 7] and a Ce:YAG screen. If the second α-magnet is switched on the electrons pass by the third analyzing stage (scanner 3) where it is possible to take a closer look to the beam halo. Behind scanner 3 there is a Wien-Filter for spin manipulation and a double scattering Mott polarimeter. This device promises to yield very precise polarization measurements for the experiments foreseen at MESA. It is, however, not relevant for the contents discussed here, and we will therefore not discuss more details. All components between the source and the second α-magnet/scanner 3 are UHV compatible and bakeable. There are focusing elements like quadrupoles (blue) and solenoids (green) as well as several steering magnets which are not shown in Figure 2.

The UV-VIS laser system $(405 \,\&\, 520\,\mathrm{nm})$ is installed on the “first floor” $(2\,\mathrm{m}$ above ground) close to the source chamber to create a minimized beam spot on the photo cathode and due to the lack of space. For spin polarized electrons it is necessary to illuminate the photo cathode perpendicular to the surface with circular polarized laser light and because of that the IR laser system $(780\,\mathrm{nm})$ sits under the first α-magnet.

Laser System

The laser system consists of three laser diodes with dif-ferent wavelengths. The 405 nm and 520 nm laser diodes are mounted close to the source and illuminate the cathode through a view-port on the bottom of the source chamber. A schematic sketch is shown in Figure 3. At short distance after the two laser diodes there is an anamorphic prism pair

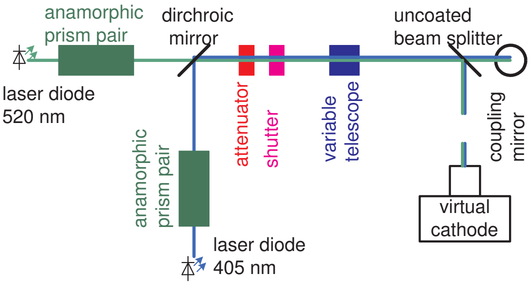

Figure 3: Overview of the UV-VIS laser system.

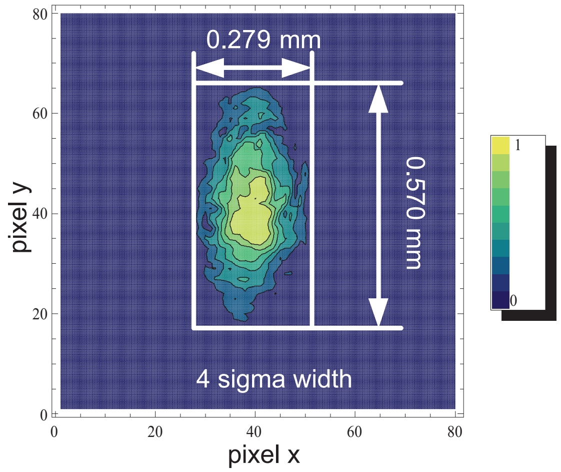

Figure 4: Example for the normalized intensity of a laser beamspot on the virtual cathode with a binning of 2 pixel in x and y.

to compensate the astigmatism of the diodes. After the prism pair a dichroic mirror to combine both wavelength is installed, followed by a remotely controlled attenuator and shutter. The next element is a variable telescope to create different beam spot sizes on the photo cathode. The penultimate element is an uncoated beam splitter which couples out 3% of the laser power and brings it onto a CCD-camera which works as virtual cathode to determine the beam spot size of the laser. The rest of the laser power gets reflected onto the photo cathode via a mirror. An example of the laser spot shape is given in Figure 4. This 2D plot shows the normalized intensity over the pixels of the camera which have a size of 6.6 μm. The IR laser system which is very similar to the UV-VIS system will be used to produce spin-polarized electron beam and is not shown here.

The laser system can be operated in three different modes. One is to create a dc beam. Here the maximum power and the average power are the same and below 300 mW. In the next mode it is possible to get dc pulse trains to decrease the thermal load on the screens. The pulses have a length of $10 - 200$ μs and a repetition rate of approximately 5 Hz. With this mode the average laser power can be decreased by a factor of 1000 but the maximum power remains the same. In the last operation mode it can produce macro pulses by the superposition of the dc-current from the laser diode driver with additional RF-power up to 1.7 W. Measurements have shown that the average power remains the same as in mode 2 but the maximum power can be increased by a factor 5, depending on the pulsing behavior of the laser diode (see Figure 7). In Figure 5 is plotted the average output power of different laser diodes over the injection current (I_{inj}). The closed data points are for the dc-current and the open data points are with RF-power. The data for the blue laser diodes belong to the left and the lower axis and for the green one to the right and the upper axis. For the blue laser diodes it can be seen, that the RF-power shifts a little the threshold current and affects slightly the slope of the output power. But for the green laser diode the difference in the threshold current and the output power with and without RF is much higher. The slope of the output power for I_{inj} above 160 mA re-mains almost the same.

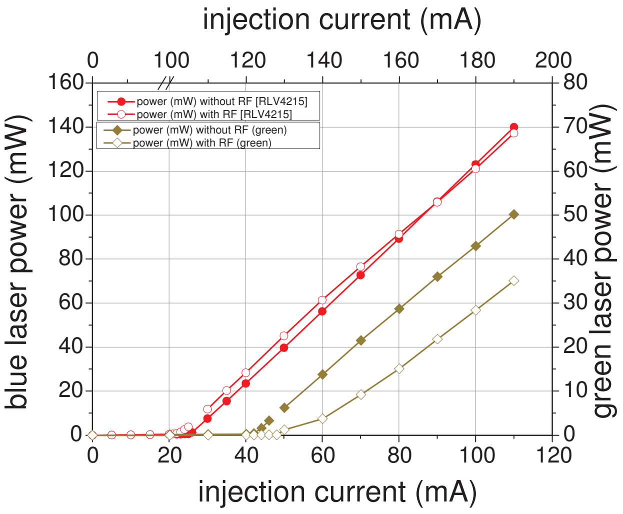

Figure 5: Average output power of a 405 nm laser diode and a 520 nm one plotted over the I_{inj}. Closed data points are for dc-current and opened ones are for dc-current and RF-power. The data for the blue laser diode belong to the left and the lower axis and for the green one to the right and the upper axis.

With this kind of measurement it can't be ensured that the laser diode is pulsing as wanted and thus, it is necessary to take a closer look to the pulse structure of the lasers. This can be done with a fast photo detector in the optical regime or with a deflecting cavity with the electron beam. The deflecting cavity transforms the longitudinal structure of the electron beam onto a transverse circle which can be observed over a screen behind the cavity. The bunch charges are too small to allow a single shot measurement, the picture represents many bunches which all impinge on the same area on the screen due to the synchronization between the cavity and the laser-system. A short description of the working principle of the deflector cavity is given in [5, 6, 7]. In Figure 6 we present two examples, one for

ISBN 978-3-95450-183-0

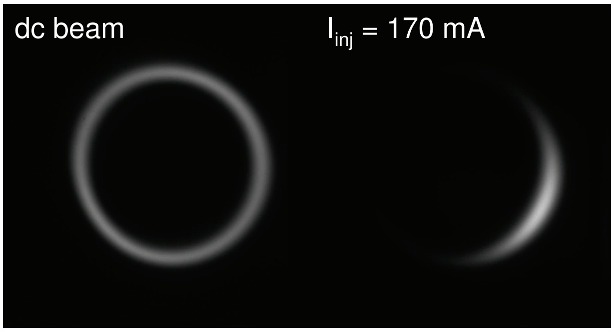

Figure 6: Example of pulse profiles behind the deflection cavity for dc beam (left) and RF-synchronized beam (right). The diameter is ˇ 30 mm with 120 W RF-power.

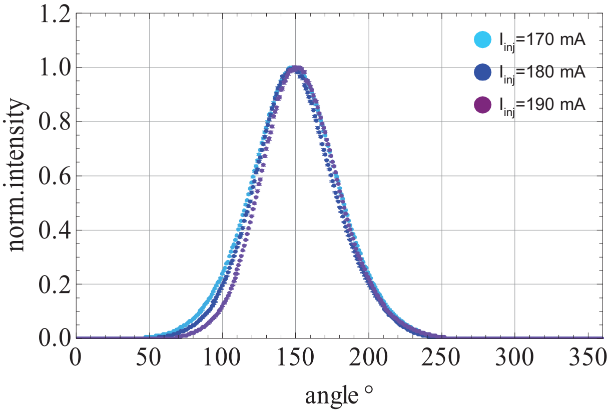

Figure 7: Normalized intensity profile for three different $Iinj$ of the green laser diode plotted over the RF-phase.

dc beam and the other one for RF-synchronized beam of the green laser diode. For this experiment a RF-power of 120 W was injected into the cavity to get a diameter of ≈ 30 mm. In Figure 7 the normalized intensity is plot-ted over the RF-phase of the cavity for three different I_{inj} (170, 180, 190 mA) of the laser diode. The peak power is more than five times larger than the the power measured at the same drive current in dc operation. All three I_{inj} deliver a transmission of 95% within a phase acceptance of 120°.

The green laser diode is mounted in the laser system to check how big the influence of the wavelength depending emittance is and if they show a better pulsing behavior than the blue ones.

Scanner Devices

All three scanners have a Ce:YAG screen with a diameter of 25 mm to optimize the beam trajectory and to make emittance measurements by quadrupole scans. Scanner 1 and 2 also contain tungsten wires with a diameter of 40 µm for emittance measurements and to investigate the halo distribution because of the higher dynamic range in comparison to the CCD-camera. Furthermore scanner 1 has two slit arrays which are oriented perpendicular to each other. They have a slit width of 25 µm and a spacing of 250 µm to make emittance measurements complementary to quad scan results. In scanner 2 the slits are replaced by a hole mask (pepper pot) with 21 x 21 holes with a diameter of 25 µm and a spacing of 250 µm in both directions. The purpose of scanner 3 is halo investigations and for that there are mounted two additional Ce:YAG screens. One with a 2 mm hole and the other one with a 3 mm hole.

RESULTS

Quad Scan

For the quadrupole scan the inverse focal length of one quadrupole is varied from $-5\,\mathrm{m}^{-1} \leq f^{-1} \leq 5\,\mathrm{m}^{-1}$ and the beam profile is obtained from a Ce:YAG screen with a CCD-camera. The squared beam diameter can be plotted over the k values of the quadrupole and on this data it is possible to fit a quadratic function which contains the TWISS parameters $(\alpha,\ \beta,\ \gamma)$. With this TWISS parameters the normalized emittance can be calculated as followed $\varepsilon_n = \beta_e \gamma_e \sqrt{\beta\gamma - \alpha^2}$ [8]. Here β_e & γ_e are the relativistic velocity and the Lorentz-factor of the electrons respectively.

This has been done for different beam alignment settings and the preliminary results are presented in Figure 8. In the upper right corner of the plot the dimensions of the used laser spot are shown and the beam profile is shown in Figure 4. With this dimensions of the emitting area $A = 0.5\,\mathrm{mm}^2$ the geometric ratio $\frac{A}{d^2} = 22.2 \cdot 10^{-6}$. The presented preliminary results are made with pulsed dc beam and without RF-synchronized pulses.

The results show large variations which may be caused by varying conditions, since they have been obtained over a long period of time. The increase in emittance can be expected because of the small perveance. However, further investigations are necessary before definitive statements can be made. In particular we will try to investigate the reason for differing values of the slit mask technique , presented below.

Slit Mask

In the slit mask emittance measurement method small slices of the beam are cut-out. More details of the slit mask method can be seen in [9]. This is presented on the left side of Figure 9 where the raw data of the measurement with 0.5 mA beam current are shown. Here the bit-value is plot-ted over the pixel position on the camera. From this data the width and the displacement of each peak are extracted and with this parameters it is possible to reconstruct the phase space distribution which can be seen on the right side of Figure 9. Here the color code and the point size indicates the normalized intensity of the slits. Furthermore with this parameters the normalized emittance can be calculated. In Figure 10 preliminary results for three different solenoid currents and a beam current of 0.1 mA to 0.5 mA are pre-sented. This data also represents the $1\sigma-$emittance. The variation of the solenoid current has been done to check

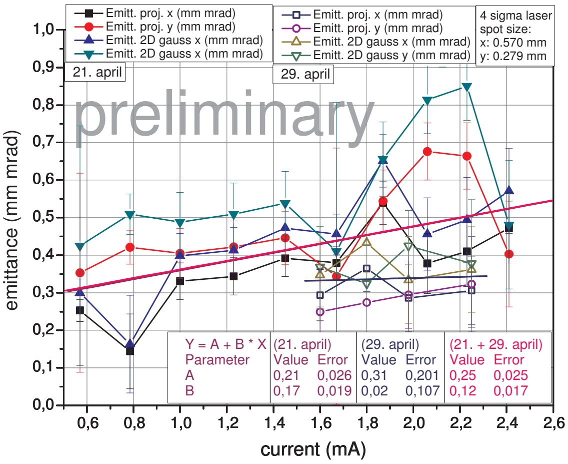

Figure 8: Preliminary emittance results from quadrupole scans are plotted over the beam current. The plot contains two different alignments and was made with pulsed dc beam. The results indicate fluctuations of the order of 30% the reasons of which are currently under investigation.

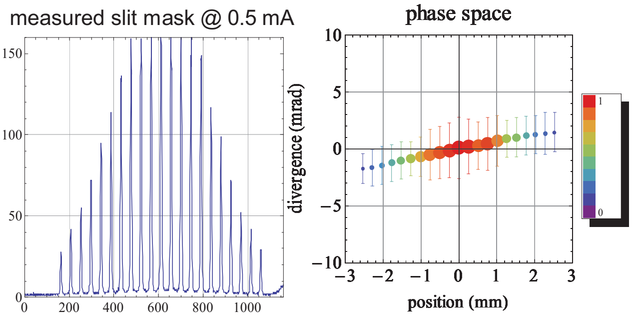

Figure 9: Raw data (left) and reconstructed phase space (right)measured with the slit mask. The color code and the point size indicates the normalized slit intensity.

if this has an influence on the emittance calculation. Up to now - unfortunately - it was not possible to measure with higher beam currents because of an accident where the photo cathode has lost a lot of QE. Nevertheless there is good reason to believe that in the near future slit mask measurements will be performed in the same current range as in Figure 8. This will clarify if the seeming increase in emittance is real and if it can be mitigated, for instance by increasing the perveance.

SUMMARY

The diagnostic test-beam-line is build up and ready to get used. Investigations of the two transverse phase-spaces with quadrupole scan technique and the determination of the beam profile with a screen or with wires are possible. The beam-line gives the possibility of a cross check between quadrupole scan and slit mask measurements. The temporal distribution can be inspected with a deflecting cavity that transforms the longitudinal distribution into an transverse one and deflects the beam onto a circle which can be observed with a Ce:YAG screen and a CCD-camera. All this can be done with three different laser wavelengths (405, 520, 780 nm) and for different laser spot sizes.

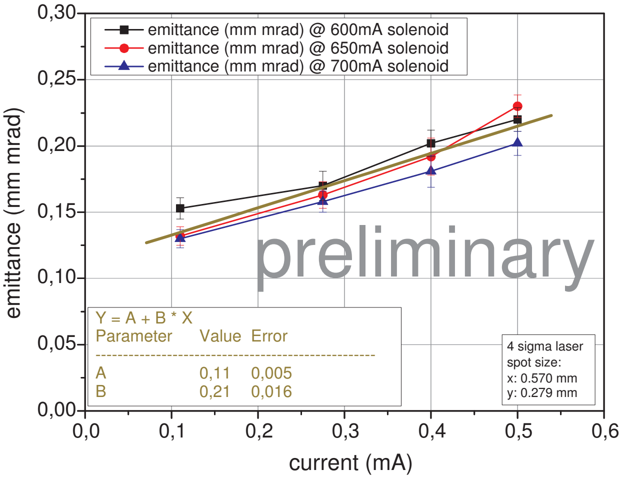

Figure 10: Preliminary emittance results from the slit mask mea-surements plotted over the beam current.

The first preliminary results of the emittance look promising to match the requirements of MESA stage 1. Further investigations of higher bunch charges etc. have to be done.

In the future it is planed to get more experience with the beam-line and the measurement techniques to characterize if the electron bunches from the source are suitable for MESA stage 1. Furthermore a closer look to helicity correlated halo effects is in preparation.

REFERENCES

[1] R. Heine, D. Simon, “Lattice and Start to End Sim-ulation of the Mainzer Energy Recovering Super-conducting Accelerator MESA”, IPAC’14, Dres-den, Germany (2014), MOPRO108

[2] D. Simon, R. Heine, “Lattice and Beam Dynamics of the Energy Recovery Mode of the Mainzer Energy Recovering Superconducting Accelera-tor MESA”, IPAC’15, Richmond, USA (2015), MOPWA046

[3] I. V. Bazarov, “Thermal Emittance And Response Time Measurement Of Negative Electron Affinity Photocathodes”, Journal Of Applied Physics 103, 054901 (2008)

[4] S. Friederich, K. Aulenbacher, “Test electron source for increased brightness emission by near band gap photoemission”, IPAC’15, Richmond, USA (2015), TUPWA044

[5] R. Heine, “Current Status Of The MESA Project", ERL2015, Stony Brook, USA (2015), WEIBLH1049

[6] V. Bechthold, “Eine Deflektor-Kavität für den MESA Beschleuniger”, Diploma thesis, JGU Mainz, Germany (2013)

[7] B. Ledroit, “Hochfrequenzmessungen am Chopperresonator für MESA”, Bachelor thesis, JGU Mainz, Germany (2014)

[8] H. Wiedemann, “Particle Accelerator Physics”, Springer, Germany (1993)

[9] M. Zhang, “Emittance Formula For Slits And Pepper pot Measurements”, FERMILAB-TM 1988

ISBN 978-3-95450-183-0

CsK_2Sb PHOTOCATHODE DEVELOPMENT FOR bERLinPro*

M.A.H. Schmeißer#, A. Jankowiak, T. Kamps, J. Kühn, Helmholtz-Zentrum Berlin, Germany

Abstract

In order to generate high brightness and high-current electron beams for bERLinPro, an SRF photoinjector is being developed at HZB. Normal conducting CsK_2Sb cathodes will be used due to their high quantum efficiency (QE) at visible wavelengths and fast response time. We report on the commissioning of a preparation and analysis system that allows investigation of the surface and near-surface chemical composition of the cathodes using XPS and ion scattering. In addition, the design of an UHV transport system for cathodes is presented.

INTRODUCTION

The ERL concept imposes strong demands on the injector. For bERLinPro [1], we intend to operate an SRF photoinjector in CW mode with high bunch charge in order to achieve an average current of 100 mA [2]. The use of CsK_2Sb photocathodes with high QE in the visible allows to drive the injector with a laser wavelength of 532 nm and average power of only 10s of Watts, thus relaxing the requirements on the cryogenic and drive laser system. The preparation of the cathodes will be performed in a dedicated growth chamber, where the cathode material is deposited on a plug that will be inserted in the back wall of the photoinjector cavity. The cathodes must be transferred between the two systems in ultra high vacuum conditions of $\leq 10^{-10}$ mbar.

Alkali antimonides have been used in phototubes and light-sensitive devices for decades and a number of empirically optimized deposition recipes are available. However, many aspects of their growth, like the diffusion of alkalis in the material and the crystallization as well as correlations between composition, crystal structure, and electronic structure and emission properties have yet to be understood. The demand from accelerator physics for highest QEs, reproducible growth, smooth surfaces, and stable operation (as desired by future user facilities) calls for dedicated investigations of these topics.

Using in-situ surface analysis with the system described below it is intended to study the influence of growth parameters on the composition of the material and find correlations with electronic structure and emission properties.

COMMISSIONING OF THE PREPARATION SYSTEM

The preparation and analysis system (see Fig. 1) was commissioned at BNL and is now back in Berlin. It consists of a preparation chamber and a surface analysis chamber which are connected via a sample manipulator. Evaporation can be performed from a thermal evaporation cell for Sb and two ports for Alkali deposition from SAES dispensers. The analysis chamber is equipped with a X-Ray source (Al and Mg anodes), an ion source and a SPECS Phoibos 100 hemispherical analyzer. Both chambers have a base pressure below $3 \cdot 10^{-10}$ mbar.

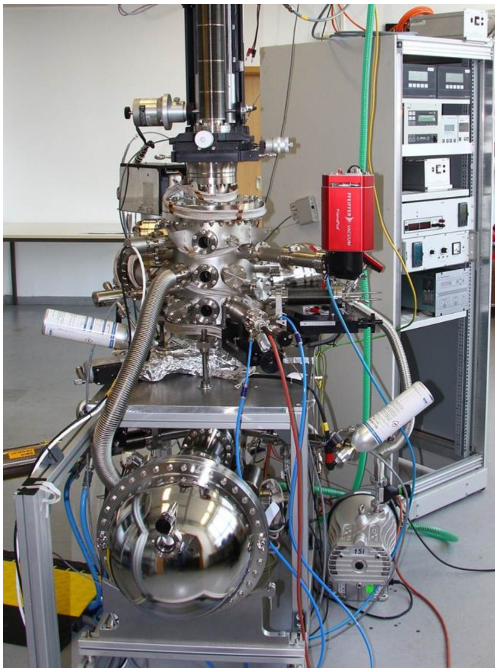

Figure 1: Photograph of the photocathode preparation and analysis (PPA) system.

PHOTOCATHODE CHARACTERIZATION

The photocurrent of a sample is collected by a biased anode and measured with a picoamperemeter. Currently, the sample is excited by a 532 nm solid state laser with 1 mW optical power. It is planned to set up a Xe-arc lamp with monochromator which would allow to resolve the spectral sensitivity of a sample. The spectral intensity of commercial tunable light sources is about 10 μW per nm bandwidth, which would allow us to measure QEs down to 10^{-5}.

A first cathode sample was prepared in April 2015 on a Mo foil (Sigma Aldrich, 99.9%). The substrate was cleaned by heating it to 450°C for 1 h and Ar^+ sputter cleaning at 3 keV for 30 min. After the cleaning procedure, only small O and C contaminations were still present. An Sb layer was deposited at a deposition rate of 0.5 Å/s, which corresponds to $1 \cdot 10^{-7}$ mbar vapour pressure. During deposition, the partial pressure of H_2O was $2 \cdot 10^{-9}$ mbar, O_2 and CO_2 were below $1 \cdot 10^{-10}$ mbar. The film proved to be very clean and no contaminations were found in the XPS spectrum.

---

* Work supported by the German Bundesministerium für Bildung und Forschung, Land Berlin and grants of Helmholtz Association.

martin.schmeisser@helmholtz-berlin.de

ISBN 978-3-95450-183-0

Following a sequential growth procedure, K and Cs were subsequently deposited. For both alkalis, the vapour pressure was very low and could hardly be resolved in the mass spectrometer ($<10^{-13}$ mbar). During the K deposition the partial pressure of H_2O was $2 \cdot 10^{-9}$ mbar, O_2 and CO_2 were below $1 \cdot 10^{-10}$ mbar. The Cs dispenser had to be heated above its specified current to obtain a reading on the quartz microbalance. A too high temperature of the dispenser led to high background pressure of atomic O and N in the 10^{-9} mbar range. An XPS spectrum was taken after the deposition of both Alkalis where traces of Cr and O are discernible. All three spectra can be compared in Fig. 2.

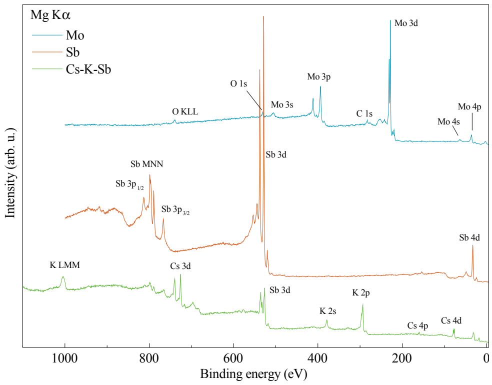

Figure 2: XPS survey spectra of three steps of a cathode preparation. The Mo substrate after cleaning (see text), after Sb deposition and after K and Cs deposition is shown.

SUBSTRATE PREPARATION AND CATHODE TRANSFER

The preparation system is located in a laboratory room apart from the injector, thus the cathodes must be transported in a movable vacuum vessel and transferred into the injector cryomodule using a load-lock. The transfer system is based on a setup that is in use at HZDR.

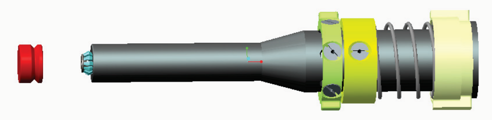

Figure 3: Drawing of the pug holder that will fit into the back wall of the gun cavity. The small CuBe spring that holds the plug is locked tightly and can be opened by a mechanism inside the holder rod.

The cathode puck (red cap in Fig. 3) can be made of copper or molybdenum. Copper plugs will be used for the commissioning of the injector with low bunch charge and molybdenum plugs will be used as substrates for the CsK_2Sb cathodes. In order to maintain the low surface resistivity of copper, but exploit the better substrate behavior of refractory metals, the use of a Cu plug with Ta or Mo evaporated on the surface as a barrier substrate layer will be investigated. Here, field emission properties need to be considered [3].

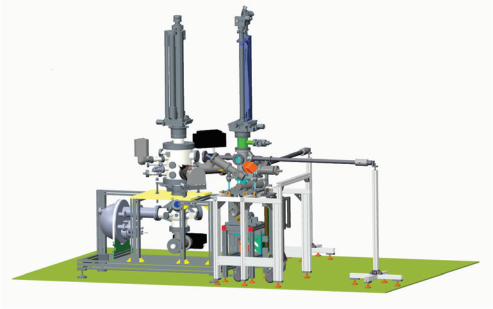

Figure 4: Drawing of the transfer system at the PPA system, as-planned.

In the preparation system and during transport the plugs will be mounted on omicron style sample holders. The transfer system (Fig. 4) at the injector allows to take the plugs off their sample holders and mount them on a cathode stalk shown in Fig. 3. Both transfer systems can handle a tray of four sample holders which can be inserted to the vacuum suitcase (Fig. 5) through a load-lock. Ongoing work will be focused on studying the QE dependence on the composition, optimization of growth procedures, photocathode life time studies and the development of a reproducible growth procedure of CsK_2Sb photocathodes with a smooth surface and high QE. A prototype of the photoinjector and a diagnostics beamline will be available in spring 2016 [4], where in-gun experiments and post-operation analysis will be performed.

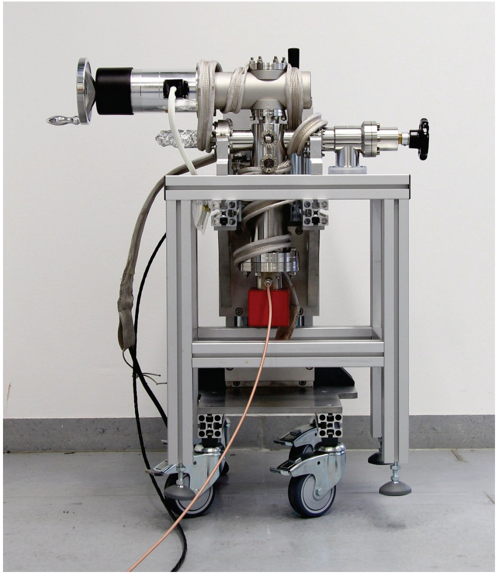

Figure 5: Photograph of the vacuum suitcase with 4 cathode positions, as recently commissioned. Base pressures in the low 10^{-11} mbar range can be maintained.

ACKNOWLEDGMENT

The authors gratefully acknowledge the engineering work of K. Martin, D. Böhlick and A. Frahm and P. Murzcek (HZDR).

REFERENCES

[1] M. Abo-Bakr et al. "Status of the HZB ERL Project bERLinPro." In: *Proceedings of IPAC 2014*. MOPRO106. Dresden, 2014, pp. 2014–2016.

[2] A. Neumann et al. "Towards a 100mA Superconducting RF Photoinjector for bERLinPro." In: *Proceedings of SRF 2013*. MOIOB02. Paris, pp. 42–49.

[3] S. Lagotzky et al. "Prevention of electron field emission from molybdenum substrates for photocathodes by the native oxide layer." In: *The European Physical Journal Applied Physics* 70.2 (2015), p. 21301. DOI: `10.1051/epjap/2015150167`.

[4] J. Völker et al. "Introducing GunLab- A Compact Test Facility for SRF Photoinjectors." In: *Proceedings of IPAC 2014*. MOPRI020. Dresden, 2014, pp. 630–632.

DEVELOPMENT OF A MULTIALKALI PHOTOCATHODE PREPARATION SYSTEM

N. Nishimori#, R. Hajima, R. Nagai, M. Sawamura, JAEA, Tokai, Naka, Ibaraki 319-1195, Japan

Abstract

We have developed a multialkali photocathode preparation system at JAEA to demonstrate high current operation of a dc photocathode gun. Quantum efficiency of 0.37% at 532 nm was obtained for a Cs_3Sb photocathode. The preparation system was connected to a photocathode gun equipped with a 250kV-50mA Cockcroft Walton high voltage power supply. The gun was high voltage conditioned up to 230 kV without a central stem electrode. Beam generation test from the multialkali photocathode is scheduled to be performed by the end of FY2015.

INTRODUCTION

A high-brightness and high-current electron gun has been developed worldwide for the next generation light sources such as an energy recovery linac (ERL) and a high-repetition rate X-ray free electron laser (XFEL). Long lifetime photocathode is important for such future light sources. Recently Cornell photoinjector demonstrated generation of record high current electron beam up to 75 mA with 1/e lifetime of 15,000 C from a multialkali photocathode dc gun [1]. High brightness specifications required for XFEL were also demonstrated at the Cornell photoinjector [2]. Thus the multialkali photocathode is anticipated as a promising photocathode for future light sources.

We have developed a 500-kV dc photocathode gun for ERL light sources in Japan and demonstrated generation of a 500-keV electron beam for high brightness beam generation [3]. The gun has been operated at the compact ERL (cERL) at KEK for more than two years and delivered CW beam up to 80 μA for laser Compton scattering experiment [4] as well as the cERL commissioning [5]. We plan to increase the beam current up to 1 mA by the end of FY2015 and to further increase the current up to 10 mA in a few years. However, the photocathode used at the cERL gun is GaAs and its lifetime is limited to a few kC [6], while that of a multialkali photocathode is measured to be greater than 15 kC [1]. Thus we have started to develop a multialkali photocathode preparation system to demonstrate high current beam generation at Japan Atomic Energy Agency (JAEA).

In this paper, our multialkali photocathode preparation system developed at JAEA is described. The system was connected to a photocathode gun equipped with a 250kV-50mA Cockcroft Walton high voltage power supply (HVPS). The gun was high voltage conditioned and beam generation test is anticipated by the end of FY2015.

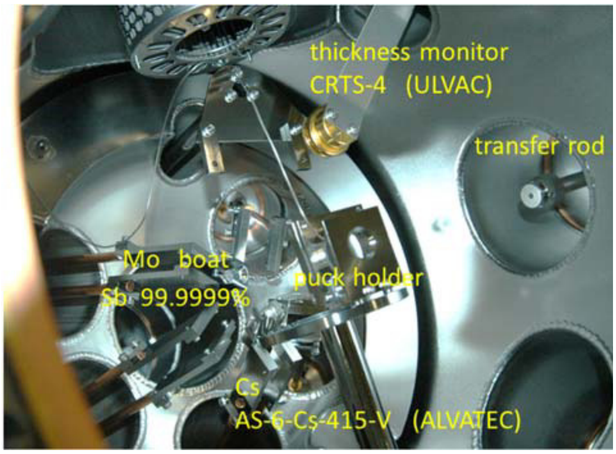

Figure 1: Inside view of multialkali photocathode preparation chamber.

MULTIALKALI PHOTOCATHODE PREPARATION SYSTEM

We have developed a multialkali photocathode preparation system following Refs. [7,8]. A silicon wafer of 0.5 mm thickness is used as a substrate. The wafer was attached on a molybdenum puck with indium seal. The puck is the same as that for GaAs photocathode used at the cERL [3] and can be installed at the cERL gun with a vacuum suitcase similar with JLab system [9]. The puck is housed in a puck holder on a rotating table and transported with a transfer rod to gun high voltage chamber for beam generation (see Fig. 1). A tungsten heater on a linear motion is used for heat cleaning of the wafer and heating the wafer during evaporation of antimony and alkali metals. The temperature is monitored with a thermocouple connected to the puck holder.

We decided to fabricate Cs_3Sb photocathode at first, because it is the simplest alkali antimony photocathode. A 99.9999% antimony bead (SB-020100: NILACO) was placed on a Mo boat. The boat was heated for evaporation. A caesium source (AS-6-Cs-415-V: ALVATEC) was placed 3 cm apart from the substrate surface. A thickness monitor (CRTS-4U: ULVAC) is used to calibrate thicknesses of both antimony and caesium. The photocathode preparation system was baked for 20 hours at 170 degree C with a 0.3 m^3/s turbo molecular pump. A 1.3 m^3/s NEG pump (SAES getters: CapaciTorr-B 1300-2) was activated after the baking. A 0.05 m^3/s ion pump (ULVAC: PST-050AU) is installed to pump noble gases and methane. The vacuum pressure of 5×10^{-9} Pa is obtained after NEG activation.

---

nishimori.nobuyuki@jaea.go.jp

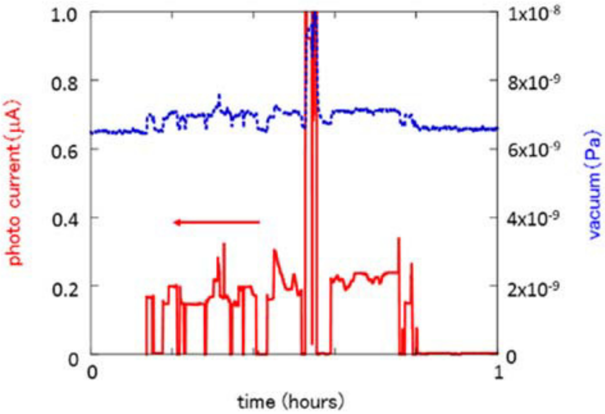

Figure 2: Photo current (red curve) measured with a Faraday cup in front of a Cs_3Sb photocathode with 532 nm laser of 125 µW. The QE is estimated to be 0.37%. The vacuum pressure rises with laser irradiation.

The wafer is heat cleaned at 550 degree C for 2 hours and then cooled to 170 degree C. The antimony was evaporated with thickness of 40 nm and the caesium was evaporated until maximum photo current is obtained. Figure 2 shows the photo current collected at a Faraday cup in front of the puck holder with 532 nm laser. The laser power is measured to be 125 µW. The QE of Cs_3Sb photocathode is estimated to be 0.37 %, which is one order of magnitude smaller than textbook [8] and recent results [7,9]. Further improvement is required for our alkali antimony preparation system.

GUN TEST STAND FOR HIGH CURRENT BEAM GENERATION

We have a dc gun with a 250kV-50mA HVPS. The gun has been originally developed as a GaAs photocathode dc gun as a test stand for future light sources. The details of the gun are described in Refs. [10,11]. The gun system consists of a SF6 tank, a high voltage chamber, a GaAs preparation chamber, a solenoid, a lightbox, and a diagnostic beam line (see Fig. 3). The multialkali photocathode preparation system was connected to the GaAs preparation chamber. The gun was used to study magnetic emittance with 1 µA beam [11]. The operational voltage at that time was limited to less than 180 kV because of field emission generated from cathode electrode. We redesigned the cathode electrode to reduce the surface electric field. Figure 4 shows the calculated surface electric field of the new cathode and anode electrodes. The maximum cathode electric field decreases from 14 MV/m to 12 MV/m. The maximum anode electric field decreases from 8 MV/m to 6 MV/m.

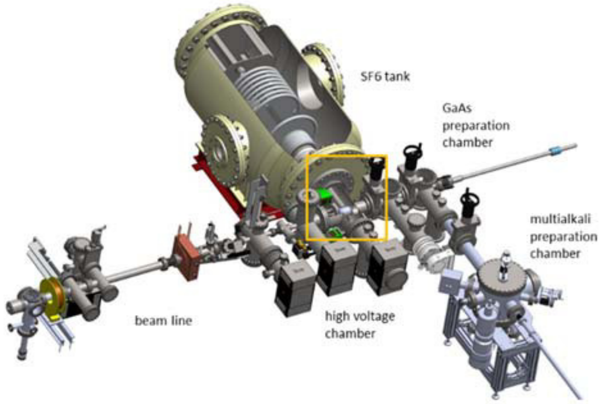

Figure 3: Gun test stand for high current beam generation at JAEA.

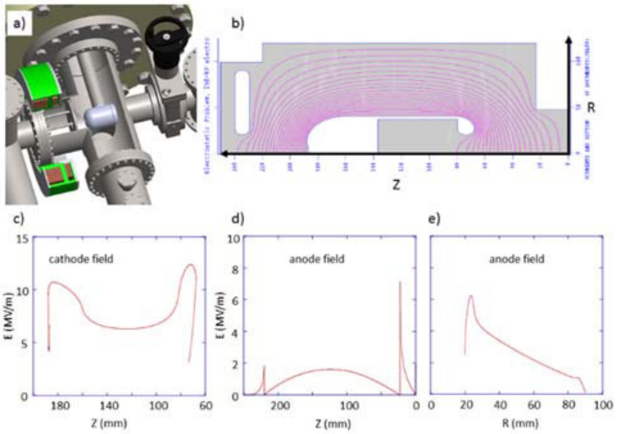

Figure 4: (a) Cutaway drawing of gun high voltage chamber and (b) radial cross section showing static electric field calculation for the gun chamber. Surface electric field distributions at 250 kV (c) of the cathode as a function of Z, (d) of the HV chamber as a function of Z, and (e) of the anode electrode as a function of R.

Before replacing the cathode electrode, we performed high voltage conditioning without central stem electrode. We had vacuum discharge at 240 kV and did not try to further push the HV processing. This is because the vacuum pressure started to increase with applied HV after the discharge event and we set our operational HV to about

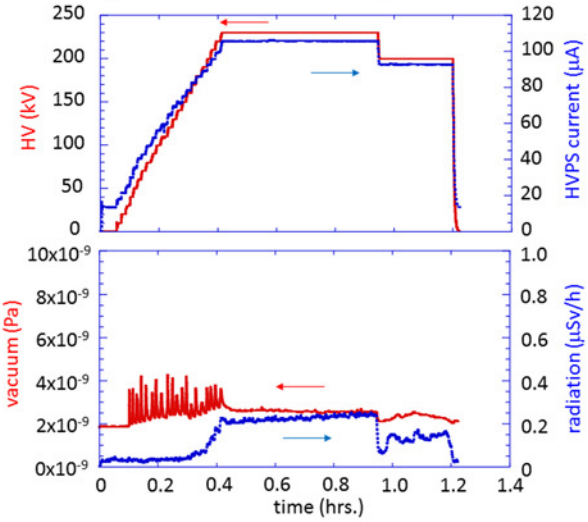

Figure 5: High voltage holding test without central stem electrode. Top shows HV (red curve) and HVPS current (blue curve). Bottom shows vacuum pressure (red curve) and radiation (blue curve). The vacuum pressure and radiation slightly increase with HV.

200 kV. The vacuum pressure recovered from 8×10^{-9} Pa to 4×10^{-9} Pa after holding HV at 230 kV for four hours. Figure 5 shows the HV holding test at 230 kV after the vacuum recovery. The top shows the gun HV (red curve) and the HVPS current (blue curve). The bottom shows the vacuum (red curve) and radiation (blue curve). The application of 200 kV on the ceramic tube leads to slight increases of vacuum and radiation. These data can be used to obtain increases of vacuum and radiation caused by central stem and cathode electrodes in the future experiment.

SUMMARY

We have developed a multialkali photocathode preparation system and obtained QE of 0.37% at 532 nm for a Cs_3Sb photocathode. The QE is one order of magnitude smaller than the textbook [8]. The system thus needs to be further improved. The system was connected to the existing dc gun equipped with a 250kV-50mA HVPS at JAEA for beam generation. The gun was high voltage conditioned up to 230 kV without a central stem electrode. Beam generation test from the multialkali photocathode is planned to be performed by the end of FY2015.

ACKNOWLEDGMENTS

This work is supported by Photon and Quantum Basic Research Coordinated Development Program from the Ministry of Education, Culture, Sports, Science and Technology, Japan and is partially supported by JSPS Grants-in-Aid for Scientific Research in Japan (15K13412).

REFERENCES

[1] L. Cultera et al., Appl. Phys. Lett. 103 (2013) 103504.
[2] C. Gulliford et al., Appl. Phys. Lett. 106 (2015) 094101.
[3] N. Nishimori et al., Appl. Phys. Lett. 102 (2013) 234103.
[4] R. Nagai et al., “Demonstration of High-flux Photon Generation from an ERL-based Laser Compton Photon Source”, in Proc. of IPAC2015, Richmond, VA, 2015.
[5] S. Sakanaka et al., “Recent Progress and Operational Status of the compact ERL at KEK”, in Proc. of IPAC2015, Richmond, VA, 2015.
[6] J. Grames et al., Phys. Rev. STAB 14 (2011) 043501.
[7] Luca Cultera, “Fabrication, characterization, and use of alkali antimonides in a dc gun”, Photocathode Physics for Photoinjectors 2012, Ithaka, NY, 2012.
[8] A. H. Sommer, “Photoemissive Materials”, John Wiley & Sons, Inc. New York (1968).
[9] R. R. Mammei et al., Phys. Rev. STAB 16 (2013) 033401.
[10] R. Nagai et al., “Development of a 250-kV Photocathode Electron Gun for the ERL Light Sources at JAEA”, in Proc. of PAC2009, p. 545-547, Vancouver, BC, Canada, 2009.
[11] R. Nagai et al., Rev. Sci. Instrum. 83 (2012) 123303.

ISBN 978-3-95450-183-0

SUMMARY OF WG1 ON INJECTORS – ERL 2015

A. Bartnik, Cornell CLASSE, Ithaca, USA
T. Kamps, Helmholtz-Zentrum Berlin, Berlin, Germany

Abstract

Here we summarize the recent progress made in injectors for high average power Energy Recovery Linacs. The progress during the past two years is discussed along with the remaining technical challenges for producing reliable, high brightness, high average-power electron sources.

INJECTOR PERFORMANCE – DC GUNS

During the plenary session results from the commissioning and measurements with the DC gun at Cornell were reported. The Cornell injector was commissioned for high bunch charge operation at 9 MeV, in order to determine whether it would be a possible design option for the proposed LCLS-II injector. Initial problems with asymmetric and poor emittance were traced to a stray quadrupole field in their solenoids, and were fixed by adding a correcting quadrupole interior to the solenoid. In the end, all major objectives were achieved, demonstrating that a DC gun at 400 kV is a viable option for high brightness with bunch charges up to 300 pC. Comparison with simulation was excellent when using a measured transverse laser profile in the simulation (Fig. 1).

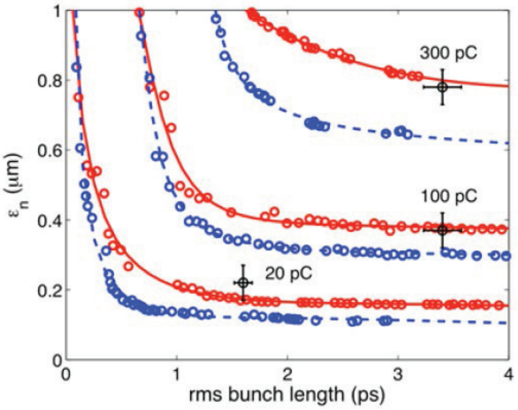

Figure 1: Cornell injector emittance results at 20, 100, and 300 pC. Black points are measured, blue points are simulated with ideal laser, red are simulated with measured laser profile.

In the first injector performance session the status and progress of the DC guns for cERL in Japan were discussed. Their gun has been designed to push the limit of the voltage possible from a DC gun. Currents up to 1.8 mA have been demonstrated, operating at the full target voltage of 500 kV, showing the benefits of the design of the guard rings on their insulating ceramic (Fig. 2). Unfortunately, two of those rings were accidentally broken during transport of the gun, resulting in performance limited to 440 kV. To regain 500 kV operation, an additional ceramic is planned to be installed.

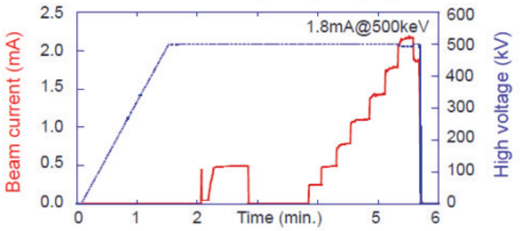

Figure 2: High current beam operation of the cERL DC gun at 500 kV.

We also heard from the status of the 70 mm DC gun at KEK. Their gun has been processed up to 550 kV, and a gradient of almost 7 MV/m—and remarkably, has shown repeatable trends in the processing (Fig. 3). A new model was presented to explain this reproducibility, explaining the mechanism as due to electron stimulated desorption (ESD). Beam operation at a more conservative voltage of 400 kV has just begun, and preparations are underway for a mA level beam test.

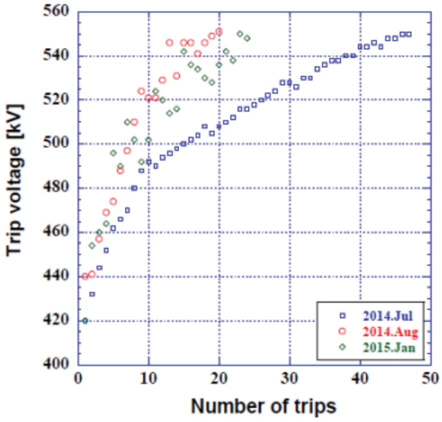

Figure 3: Processing reproducibility in the KEK DC gun.

Finally, the status of the funnelling gun at BNL was reviewed. The gun has been fabricated, assembled, and tested by industry. Importantly, a brief beam test was performed where two low current (nA) beams were correctly combined, showing that no cathode cross talk is observed at this current level. After that initial test, the system has been shipped to BNL for further high current tests.

INJECTOR PERFORMANCE – SRF GUNS

Results from commissioning activities with SRF guns were discussed in a joint session Injector and SRF for ERLs. The first session gave an update on the BNL 704 MHz SRF gun. Importantly, the new multipacting-free (MP-free) cathode stalk design has been completed (Fig. 4) and has allowed the SRF gun to operate up to 2 MV CW. A

ISBN 978-3-95450-183-0

beam test was performed with a K2CsSb cathode, which successfully demonstrated that the QE of the cathode is preserved after cryogenic cooling—no cathode degradation was observed. In addition, up to 0.55 nC per bunch was extracted from the gun, in a low-rep rate beam test at 0.85 MeV.

Figure 4: New multipacting-free cathode stalk with Ta tip, used in the BNL 704 MHz SRF gun.

Results from the recent beam measurements with the new SRF gun II at ELBE were presented. Though operating at a smaller gradient than expected due a cavity breakdown event, 7 MV/m, it should still potentially allow up to 500 pC, improving user operation. The cathode-cavity interface is the primary challenge at the moment, due to the need for high quality cleanliness. In addition, transverse emittance and longitudinal phase space measurements were performed, and agreed well with expectations from Astra simulations (Fig. 5).

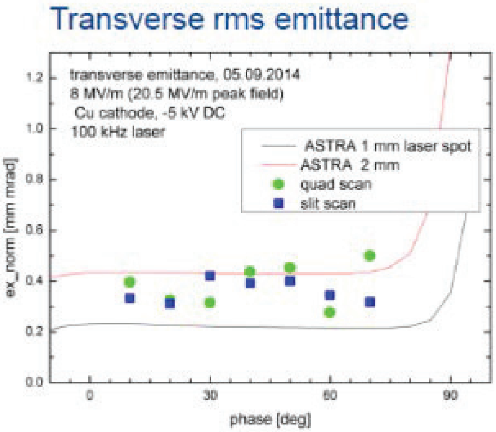

Figure 5: Transverse normalized emittance versus launch phase measurements using two methods with the SRF gun at ELBE.

CATHODES AND LASERS

Two talks were given on laser systems. First, during the plenary session, we heard a summary talk on the state of lasers for use in ERLs. Due to the existence of high quantum efficiency cathodes, drive lasers are now powerful enough for 100s of mA of beam current, and this is not a limiting factor any more. But, more work is still needed on long term stability, both in position and phase. More flexibility is also needed in the repetition rate and pulse structure, in order to have a method to raise beam current without affecting the e-beam optics.

We also saw a presentation on a new method to shape laser profiles using a spatial light modulator (SLM). Instead of making a phase grating, and exploiting diffraction to tune the shape of the laser beam, the SLM was used to manipulate the polarization of the light, on a pixel-to-pixel scale. A subsequent polarizer was then used to carve out the desired shape from the initial beam. Though inherently lossy, this method benefits from being both fast, simple, and potentially very accurate (Fig. 6).

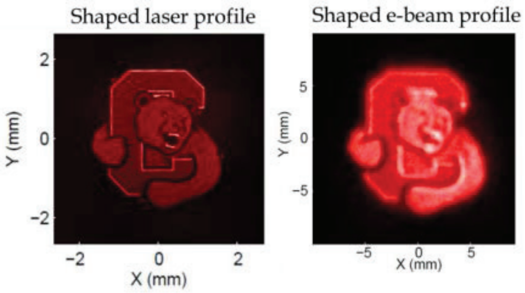

Figure 6: Example shaped laser and electron beam profile.

We heard two talks, related to an effort to understand and control the surface roughness on Alkali photocathodes. K2CsSb photocathodes have been regarded as a strong candidate for excellent electron sources. The traditional sequential growth method for this type of photocathode could result in a rough surface which will have an adverse influence on the beam emittance in the high gradient field used in most applications. Previous studies have revealed the evolution from crystalline Sb layer, to a K-Sb compound, and then to the crystalline K3Sb significantly increase the surface roughness. X-ray reflectivity (XRR) is a powerful non-destructive thin film characterization method and has been applied to the growth study of K2CsSb photocathode. In order to suppress the roughening phenomenon, they developed an alternating deposition method of Sb layer and followed by K-Cs sequential deposition, together with co-deposition of K and Cs, and sputtering. XRR analysis shows that co-evaporated K2CsSb may end up in a smoother surface with almost the same quantum efficiency compared to sequentially-evaporated photocathode (Fig. 7). Sputter deposition could result in a smooth photocathode with sub nm roughness and acceptable 1% quantum efficiency at the wavelength of green light.

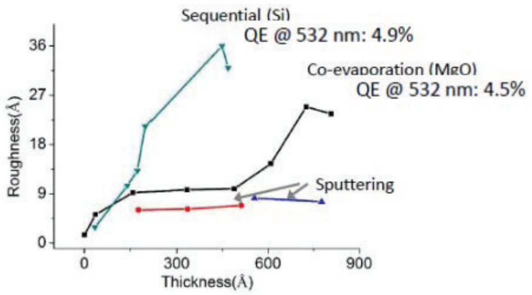

Figure 7: Cathode roughness as a function of thickness, for a variety of different growth methods.

We also heard of the development of a set of software to model the emission of electrons from an alkali photocathode. It used a 2D Monte-Carlo simulation based on Spicer's three step model. Agreement with measurement was striking (Fig. 8), and hopefully this will lead to the development of better understanding and control over these cathodes.

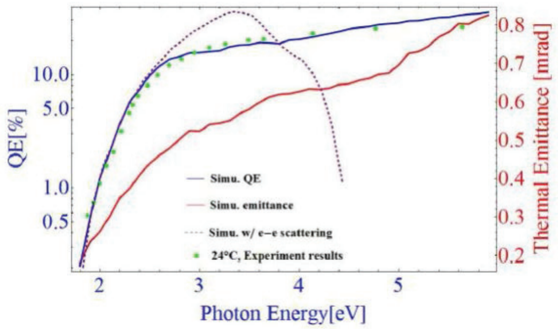

Figure 8: Simulated and measured QE and simulated thermal emittance of a K2CsSb photocathode.

There was a comparison between competing models of the activation of p-GaAs—the dipole layer model, and the heterojunction model. Longitudinal energy distribution measurements were performed periodically with a parallel plate retarding analyser during a long activation of the cathode, yielding data that agreed well with the heterojunction model (Fig. 9).

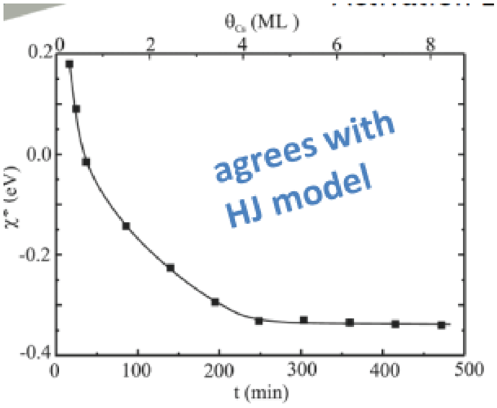

Figure 9: Effective electron affinity during cathode deposition. Measured data, and agreement with the heterojunction model.

At HZB, the commissioning of an advance photocathode preparation and analysis system is on-going. Figure 10 shows XPS spectra detected in-situ in-between sequential deposition steps of CsK2Sb photocathode.

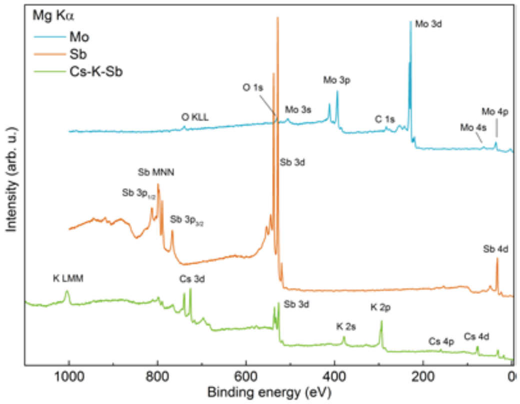

Figure 10: XPS data recorded in-situ during sequential deposition of a CsK2Sb photocathode.

Finally, Far-Tech also presented a novel design of a high peak and high average current source based on a triode-like thermionic cathode. A floating grid with a small biased dc applied field is placed inside of an RF cavity, thus preventing cathode emission during unwanted parts of the RF cycle. This electron source could potentially allow CW operation of a thermionic RF gun to generate high-peak and high-average current, small emittance beam. The source also has other potential advantages in its simplicity of structure and operation, robustness and reliability. This source is also much cheaper in fabrication and maintenance than that of a photocathode system. This source could be widely used in linac systems where high average current are needed, such as the ERL systems for electron cooling of ion beam, high average power free electron lasers, Terahertz sources.

CONCLUSION

The progress in injectors for ERLs is immense. The high average current achieved at Cornell and the high accelerating voltage achieved at JAEA and KEK is proof of the maturity of DC gun technology, and their viability for ERL use. SRF guns still need more demo and test experiments. New facilities are coming to life like the SRF gun at BNL with 200 uA average current and the new SRF gun (SRF gun II) at HZDR, but more results are needed to push the limits of the SRF gun concept. Lasers for ERLs have also become a mature field, and now mostly require further engineering to increase their stability and reliability—though the shaping of the laser, both transversely and temporally, is one important remaining area of work needed for optimal ERL operation. Photocathode R&D is now strongly benefiting from both material science methods and detailed simulation, and is using them to overcome the remaining challenges to maximizing their performance.

ACKNOWLEDGMENTS

The authors would like to thank the workshop organizers and participants of the working group for the excellent presentations and lively discussions during and in-between the sessions.

ERL BEAM DYNAMICS AND OPTICS: A SUMMARY OF WORKING GROUP 2 AT THE ERL WORKSHOP 2015

M. Abo-Bakr*, Helmholtz-Zentrum Berlin, Berlin, Germany
V. Ptitsyn#, Brookhaven National Laboratory, New York, USA

Abstract

The 45th Advanced Beam Dynamics Workshop on Energy Recovery Linacs, hosted by the Brookhaven National Laboratory, was held at the Stony Brook University Campus, June 7-12, 2015. It was the sixth in the series of international workshops covering accelerator physics and technology of Energy Recovery Linacs.

The workshop was organized into five working groups. Working group 2 (WG2) covered beam dynamics and optics issues of ERLs in operation as well as of proposed and future ones. Key aspects of some representatively selected talks together with the outcome of the working group discussion are summarized in this report.

INTRODUCTION

Energy recovery linacs enable the generation of high current beams with ultimate brilliance - lowest transverse emittance at very short pulse lengths. Several ERL demonstrator facilities have been operated so far as well as a few one, that are or had been used for light generation: ALICE [1], NovoFEL [2] and JLab FEL [3], where the latter delivered the highest ever reached average photon flux and power in the near IR. ERL operation at higher energies and highest currents (as available in 3rd generation and ultimate storage rings or required for collider experiments) still needs to be demonstrated. On this route various physical and technological problems still must be overcome to fully benefit from the potential performance of ERLs.

The ERL workshops provide the ideal stage for presentation and discussion of latest results in the community. The 45th Advanced Beam Dynamics Workshop on Energy Recovery Linacs, hosted by the Brookhaven National Laboratory, was held at the Stony Brook University Campus, June 7-12, 2015. It was the sixth in the series of international ERL workshops, proceedings of previous workshops are available [4]. Five working groups have been established for the ERL2015:

- WG1 Injectors: Injector Performance, Electron Guns, Cathodes and Lasers
- WG2 Beam Dynamics and Optics: Collective Effects, Multi-Pass Effects and Halo Simulations
- WG3 Beam Instrumentation, Controls, Beam Losses and Halo Management
- WG4 ERL and SRF: SRF System Performance, Field Stability, Synchronization, Special Requirements and HOM Damping
- WG5 Applications

For WG2, on those activities we report here, the charge has been defined in advance of the workshop as follows:

"WG2 will address the optics and beam dynamics challenges in ERLs. It will include lessons learnt from past and present ERL operation as well as issues arising during the design work on future ERL facilities. The group scope includes design approaches for one-pass and multi-pass ERL lattices, error tolerances, preserving longitudinal and transverse beam emittances during beam transport, simulation tools suitable for ERL modelling. We also will look at beam instabilities and collective effects as well as at mechanisms defining halo formation and beam losses"

Beside the plenary session with two talks assigned to WG2, three (split) sessions were dedicated to the WG2 topics. In addition there were a joint session with WG4 (SRF) and the poster session with four WG2 related posters.

A large variety of interesting and important topics has been presented in the 12 talks of the WG2 sessions. Just from the number of contribution we identified 4 "hot topics":

1. ERLs & FFAG beam transport: eRHIC (BNL), Cβ (Cornell/BNL), LHeC (CERN)
2. Microbunching Instability: simulations and μB-enhanced radiation generation
3. Beam Break Up: MESA (Mainz, Germany) , KEK
4. CSR effect on the beam

on which we will focus on in the following. At the end we will recapitulate a fruitful discussion on beam losses and halo formation & control, triggered by the presentation of recent measurement results from cERL (KEK).

ERLS & FFAG BEAM TRANSPORT

Recent results from BNL ERL Test Facility have been reported in Plenary talk by Dmitry Kayran (BNL), "Status and Commissioning Results of the R&D ERL at BNL". The first photocurrent from the ERL SRF gun has been observed in Nov. 2014 (1 uA per 500 msec RF pulse). During the spring 2015 new "multipactor free" Ta tip cathode stalks were prepared and conditioned, demonstrating 4% QE at room temperature and 1% QE in the gun. Frist beam test with the new cathode achieved the maximum average current of 4.5 μA per 3 msec RF pulse. In a mode with rare bunch pulses, the maximum bunch charge of 0.55 nC has been demosntrated. The beam parameters, such as the energy and emittance have been measured. The commissionig of beam instrumentation is underway.

The progress on the lattice development and simulations for future ERL-based collider LHeC [5] was reported by Alex Bogacz (Jefferson Lab) and Dario Pellegrini (CERN), "ERL – Design and Beam Dynamics Issues".

---

* Michael.Abo-Bakr@helmholtz-berlin.de
# vadimp@bnl.gov

ISBN 978-3-95450-183-0

The lattice of all major components of recirculating passes has been worked out and optimized. It includes isochronous arcs, detector bypasses, spreader/recombiners and SR compensation sections. The major goal of lattice optimization was the emittance preservation during the beam transport. The interaction region still needs to be integrated to complete the lattice integration. PLACET2 code is being used for beam dynamics simulations, including synchrotron radiation, beam-beam effects, cavity misalignments and long range wakefields. The importance of combined consideration of BBU and beam-beam interaction was pointed out. In near plans are studies of ion cloud effects.

Several talks were dedicated to the studies of FFAG (Fixed-Field Alternating Gradient) lattice which is considered for application in multiturn ERL-based collider eRHIC [6]. Stephen Brooks (BNL), "eRHIC: an Efficient Multi-Pass ERL based on FFAG Return Arcs" described all major features of FFAG lattice in eRHIC, where 32 of total recirculations are planned by using only two FFAG beam lines. The elementary FFAG cell contains two quadrupoles which centers are offset. Proper arrangement of the offset between quadrupole centers allows to realize various FFAG lattice components, arcs, straights, matching sections and detector bypasses. The lattice optimization was done to minimize synchrotron radiation, as well as other important values (pathlenth difference, orbit spread, ...). The FFAG lattice can be realized with permanent magnets. The design of permanent magnets for eRHIC FFAG beam lines was presented

Since the beam of multiple different energies propagating through the same FFAG beam line, the subject of the orbit control is of large importance. It was reported by Chuyu Liu(BNL), "Correction Methods for Multi-Pass eRHIC Lattice with Large Chromaticity" who concluded that the large chromaticity, intrinsically present at lower energies in the FFAG beam line, had to be included in the correction algorithm to warranty the succesful orbit correction. It may require measuring orbit response modified by large chromaticity during machine commissioning or operation. The SVD-based orbit correction algorithm includes the orbit measurements taken from several turns, with the quality of the orbit correction quickly converging with the number of turns used.

Nicholaus Tsoupas (BNL), "The optics of the eRHIC Low Energy FFAG cell with realistic field maps" showed the eRHIC simulations done with 3D-field maps of FFAG cell magnets. The field maps were calculated for Halbach-type permanent magnets. The field measurements done for short length prototypes of this magnet agreed with field calculations very well. The results for the beam transport through the FFAG beam line of low energy FFAG satisfied the machine requirement.

Simulations of beam transport in eRHIC FFAG arcs, including beam polarization, were shown by Francois Meot (BNL), "Beam and Polarization Dynamics in Electron FFAG Lattices". The ray-tracing code ZGOUBI was used for these studies. The effect of synchrotron radiation leads to small deterioration (3%) of beam polarization. The simulations with different kind of magnetic errors would help to establish the tolerances on the magnetic field errors. The effect of emittance dilution due to the orbit errors in the lattice with high chromaticity has been also studied.

Longitudinal dynamics studies for eRHIC using ELEGANT code has been presented by Yue Hao (BNL), "Aspects of eRHIC Longitudinal Dynamics". eRHIC design uses additional RF systems to compensate for energy losses caused by synchrotron radiation and to reduce the beam energy spread. In addition the proper choice of the pathlength and R_{56} parameters is required in order to minimize the energy spread of decelerated beam. Further optimization of longitudinal parameters is planned to ensure better energy recovery efficiency.

Two talks were devoted to another ERL that will use the FFAG lattice for beam recirculations. In the Plenary talk Georg Hoffstaetter (Cornell University), "A FFAG-ERL at Cornell, a BNL/Cornell Collaboration" described the future Cβ ERL-facility at Cornell University planned in a collaboration with BNL [7]. The few hundred MeV facility can be used to verify varous aspects of FFAG technology applications for ERLs as well as to carry out nuclear physics experiments with an internal target. It takes an advantage of existing Cornell high-current injector and a Linac Cryomodule. The detail of lattice components for this Cornell/BNL ERL were shown by Christopher Mayes (Cornell University), "Optics Considerations for the Cornell-BNL FFAG-ERL Test Accelerator". It included the optics for all passes through the FFAG beam line, as well as for spreader/merger and main linac. The longitudinal transport was optimized to reduce the energy spread of decelerated beam. Studies of various beam dynamics effects as well as orbit/optics correction are ongoing.

MICROBUNCHING INSTABILITY

Initial small longitudinal density modulation (even random noise) can cause momentum variations by interact with the various wakes fields in the beam pipe. On the other hand such an micro-bunching itself can drive the generation of strong wakes (e.g. SC or CSR). Under certain circumstances the momentum modulation leads to an enhanced density modulation and a resonant feedback loop - the micro bunching instability (µBI) - can build up. The density modulation is described by the Fourier-components of the longitudinal density distribution: the bunching factor $b(k)$. Its wavelength depending amplification passing a given accelerator is calculated as the bunching gain $G(k)$. µBI have been observed on linacs with strong compression but also on storage rings operating bunches with high peak current. A series of µBI dedicated workshops have been held in the past [8].

Two talks were related to µBI on the ERL2015:
Atoosa Meseck (HZB), Microbunching Instability in ERLs - a Blessing or a Curse": The µBI at bERLinPro [9] has been studied, using analytical formulas as well as the sim-

ulation code ASTRA. Amplification of initial shot noise due to LSC has been simulated, showing the most pronounced impact in the wavelength range from 1 µm to 1 mm, as expected from the applied impedance spectrum for analytical calculations. However, the longitudinal machine dispersion (R_{56}), leads to damping (instead of amplification) of the shot noise for almost the entire wavelength range. As result of the simulations no significant gain and thus µBI is expected for bERLinPro's standard mode of operation. Additional analytical 1D estimations including CSR impedance give no indication for µBI too.

As an example a test beam line including a Compact FODO Channel (CFC) has been optimized to drive the µBI: significant gains can be reached, potentially allowing the generation of at least partly coherent radiation in the EUV. Next studies will consider µBI in bERLinPro's short pulse mode and further investigations on µBI supported radiation generation.

Cheng-Ying Tsai (Virginia Polytechnic Institute and State University), "Linear Microbunching Gain Estimation Including CSR And LSC Impedances in Recirculation Machines": to investigate µBI on the CCR (Circular Cooler Ring) of JLab's proposed Medium Energy Electron Ion Collider MEIC [10], a new program, based on an extended Vlasov solver, has been written. Main program features are the implementation of horizontal & vertical bending magnets (need for spreaders and recombiners in ERLs), non ultra-relativistic, transient and steady state CSR as well as 1D LSC. The semi-analytical program uses elegant generated input and calculates gain curves for a given lattice. Calculation times for the whole gain curve correspond to those of a single elegant run. Application to a high energy arc for code testing showed very good agreement to elegant, both for a lattice developing a strong µBI as well as for one tuned to minimize the overall gain. Gain curves for MEIC CCR have been presented, indicating high gains with peak values in the order of 10^8 at 350 µm wavelength, where LSC caused even higher gains compared to CSR. Implementation of further impedance models, energy changes in the beam line and benchmarking with experiments are planned.

BEAM BREAK UP

A bunch passing a cavity off-axis excites higher order dipole modes (HOMs), where the amount of transfered energy depends on the off-axis amplitude. At the same time an already existing cavity HOM field kicks the bunch, thus changing its downstream trajectory. If the bunch's total energy transfer into the cavity HOM from all turns is not damped until the next bunch passes, a resonant loop can be formed. Especially in super conducting cavities with high quality factors, HOM amplitudes can get high enough to cause beam loss. The so called Beam Break Up (BBU) occurs in various forms - transverse and longitudinal, single and multi pass - and can severely limit the maximum machine current. The instability has been observed on many machines since the 1960ies and needs to be carefully considered in the design of high current accelerators.

In WG2 two BBU dedicated talks were given: Thorsten Kuerzeder (TU Darmstadt), "Investigations on Transverse Beam Break Up Using a Recirculated Electron Beam": observation of current limitations at the S-DALINAC facility [11]were introduces and related to the transverse BBU instability. While planning for a maximum of 20 µA no currents higher than 8 µA have been reached so far. A BBU instability, caused by the eight 3 GHz cavities, is supposed. In the design of these 1 m long, 20 cell cavities neither minimized HOMs nor HOM absorber had been considered. Several proposes to increase the BBU threshold are considered: beside the optimization of transverse tunes, 3 skew quadrupoles have been inserted into the new, second recirculation line, enabling a complete transverse phase space exchange. First test will be start in July 2015. Another approach is a massive increase of chromaticity: for large values with $|\xi \, \Delta E/E| \gg 1$ a significantly increased BBU threshold current is expected. With $\Delta E/E \; 10^{-3}$ the natural chromaticity is one order of magnitude too low. 12 sextupole magnets with an integrated sextupole strength of 10 T/m have been fabricated and will be placed at highest dispersion positions inside the arcs. Detailed BBU studies are planned for 2015/16.

Si Chen (KEK), "HOM-BBU Simulation for KEK ERL Light Source": The ERL driven photon factory [12], proposed at KEK, is planned to operate with up to 100 mA beam current. Results of latest BBU simulations, using a new 3.4 GeV lattice design together with the new HOM optimized "Model II" cavities, have been presented and compared to former calculation with the 3.0 GeV lattice and TESLA like resonators. Recirculation phase scans yields threshold currents between 220 and 300 mA, where BBU simulations for single cavities indicate lower thresholds when placed in low energy sections. Based on an FFT analysis of the simulated transverse beam motion the dominant mode at $f = 4.011$ GHz could been identified and excellently agrees with the input HOM parameter set. As expected, HOM frequency randomization studies for the 224 cavities yield higher thresholds: the average value for 1000 sets of Gaussian distributed HOM frequency shifts is 640 mA ($\sigma_f = 1$ MHz). Variation of the frequency shift showed an almost linear threshold increase from the shift-free case ($\sigma_f = 0$ MHz, 220 mA) to 940 mA at $\sigma_f = 2$ MHz. Further lattice and cavity optimization work is planned for the next time.

CSR EFFECT ON THE BEAM

Two talks were devoted to studies related with Coherent Synchrotron Radiation. Christopher Hall (Colorado State University), "Study of CSR Impact on Electron Beam in the JLab ERL", presented results of measurements which used controllable bunch compression in two locations of the JLab ERL. The resulting beam energy distribution, impacted by CSR-induced energy loss, was measured in the downstream arc. The fragmentation of the energy spectrum, enhanced by longitudinal space charge, was observed. All measured results show good qualitative agreement to 1-D CSR simulations. It was also concluded that CSR in drifts after a bunch compressor can have a large impact on the energy distribution.

Simone Di Mitri (Elettra - Sincrotrone Trieste), "Transverse Emittance Preserving Arc Compressor: Sensitivity to Beam Optics, Charge and Energy" extended the theory of CSR kick-optics balance to the case of varying bunch length. The optimal optics is based on a principle of canceling successive CSR-induced kicks to minimize CSR-induced emittance growth. The theoretical and simulation studies were presented for the arc compressor, based on DBA cells that has properly balanced optics.

BEAM LOSSES & HALO

Much of the discussion time was devoted to the topic of the beam halo and related slow beam loss. Pavel Evtushenko (Jefferson Lab) listed the major halo sources in JLab FEL injector. They include a limited extinction ratio of drive laser, stray laser light and its reflections hitting the cathode and elsewhere, and space charge dominated beam transport. There is no intentional collimation implemented in JLab ERL, but minor collimation of bunch tails is done naturally by the vacuum chamber.

cERL, which is under commissioning in KEK (Japan), carried out initial collimation studies, mentioned in the Plenary talk by Shogo Sakanaka (KEK), "Successful Result of the Commissioning on cERL in KEK". The collimated portion of beam was up to 0.1% of total beam current, but the efficiency of the collimation with respect to the radiation levels seen in recirculating arc was not very clear. It was pointed out that the collimation system has not yet been optimized, since it is not necessary at the present beam current levels ($<100\,\mu$A). Thus, much of interest will be the further experience with the collimation system at cERL, as the beam current increases. For simulation of collimation the GPT code was used with $10^5 - 10^6$ particles. It was noted that 2012 an "Unwanted Beam" workshop took place in Berlin, devoted to the topic of the beam halo, dark current and beam loss control.

REFERENCES

[1] N. Thompson et al., "First lasing of the ALICE infra-red Free-Electron Laser", NIM A **680**, 2012.

[2] O.A.Shevchenko et al., "Commissioning Status and further Development of the Novosibirsk Multiturn ERL", ERL2013, Novosibirsk, Russia.

[3] S. Benson et al., "The 4th Generation Light Source at Jefferson Lab", NIM A **582**, 2007.

[4] Previous ERL Workshops on JaCoW (www.jacow.org):
ERL2007, Daresbury, UK
http://accelconf.web.cern.ch/AccelConf/erl07
ERL2009, Cornell, USA
http://accelconf.web.cern.ch/AccelConf/ERL2009
ERL2011, Tsukuba, Japan
http://accelconf.web.cern.ch/AccelConf/ERL2011
ERL2013, Novosibirsk, Russia
http://accelconf.web.cern.ch/AccelConf/ERL2013

[5] LHeC Study Group, "A Large Hadron Electron Collider at CERN",Journal of Physics G, V.39, Number 7, Article 075001, 2012.

[6] E. Aschenauer, et al., "eRHIC Design Study", arXiv:1409.1633, 2014.

[7] I. Bazarov et al., "The Cornell-BNL FFAG-ERL Test Accelerator: White Paper", arXiv:1504.00588, 2015.

[8] Workshop Series on Micro-Bunch Instabilities:
1st µBI workshop, Trieste, 2007
XYZ/FERMI/index.php?n=Main.MicrobunchingWS
2nd µBI workshop, Berkeley, 2008
XYZ/FERMI/index.php?n=Main.MicrobunchingWS-US
3rd µBI workshop, Frascati, 2010
http://www.lnf.infn.it/conference/uBI10/
4th µBI workshop, Washington (UMER), 2012
http://www.umer.umd.edu/events_folder/uBi12/
5th µBI workshop, Pohang, 2013
http://pal.postech.ac.kr/ubi2013/
6th µBI workshop, Trieste, 2014
XYZ/Conferences/2014/MBIW6/
XYZ = https://www.elettra.trieste.it

[9] M. Abo-Bakr et al., "Progress Report of the Berlin Energy Recovery Project BERLinPro", IPAC2015, Richmond, USA.

[10] Y. Zhang et al., "Status of MEIC Design Studies", IPAC2013, Shanghai, China.

[11] Y Poltoratska et al., "Status and recent developments at the polarized-electron injector of the superconducting Darmstadt electron linear accelerator S-DALINAC", J. Phys.: Conf. Ser. 298, 2011.

[12] KEK ERL CDR:
pfwww.kek.jp/ERLoffice/detabase/ERL_CDR_full_text.pdf

SUMMARY OF WG3 ON INSTRUMENTATION, CONTROLS, AND BEAM LOSSES – ERL 2015

C. Gulliford, Cornell CLASSE, Ithaca, USA
T. Obina, KEK, Japan

Abstract

Here we summarize the work presented at the ERL 2015 concerning recent progress and issues with instrumentations, controls, and beam loss in the context of Energy Recovery Linacs.

INSTRUMENTATION, DIAGNOISTICS CONTROLS, AND BEAM LOSSES

The first talk described a non-destructive beam position monitoring method in two-beam section of KEK-cERL. The circumference about 90 m produces the time difference in pre- and post-accelerated beam. Typical macro-pulse length of 1 µs was observed as 300 ns non-overlapped signal and 700 ns overlapped signal, as seen in Figure 1. The non-overlapped part was used for beam position of two beams, as seen in Figure 2. By selecting the detection frequency, the overlapped part can be sensitive to the phase of two beams, thus the phase signal was used for path-length adjustment of the beam. The time-domain separation is also effective during the CW beam by introducing a short gap in the gun laser. This very simple method can be applied for ERL machines.

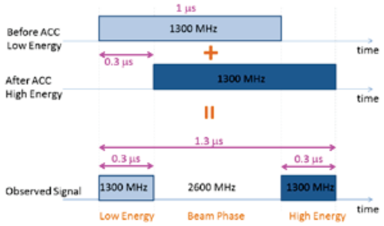

Figure 1: Principle of time separation.

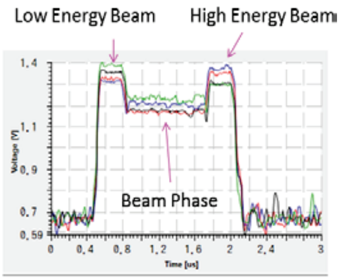

Figure 2: Measurement results for two beams.

A detailed talk concerning diagnostics at ALICE was given. The ALICE facility at Daresbury Laboratory is an energy recovery based infra-red free electron laser of the oscillator type that has been operational since 2010. Fast diagnostics have been installed to perform combined measurements on pulse-by pulse FEL pulse energy and bunch-by-bunch electron bunch position and arrival time. These measurements have highlighted and quantified fast instabilities in the electron beam and consequently the FEL output, the first observation of which is shown in Figure 3. The material presented at ERL 2015 focussed on the instabilities, rather than technical details of the diagnostic hardware and processing techniques.

The ALICE beam energy is 25-30 MeV. The ALICE beam structure has 60 pC bunches at 16.25 MHz repetition frequency (i.e. bunches separated by 62 ns) in 100 µs bunch trains (there are around 1600 bunches in each train) produced at the machine repetition rate of 10 Hz.

A fast photo electromagnetic detector (PEM) was used to measure the intensity of the individual FEL pulses and had been used since shortly after lasing in 2010, and showed immediately a pronounced variation in FEL pulse intensity at around 100 kHz (see Figure 4 and Figure 5). There were, and still are, no applications of the ALICE FEL which are sensitive to this instability.

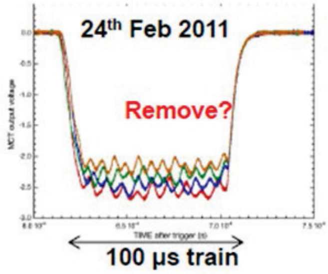

Figure 3: First observation of instability in the FEL micropulse intensity.

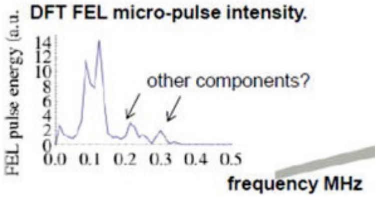

Figure 4: Frequency components of the instability.

ISBN 978-3-95450-183-0

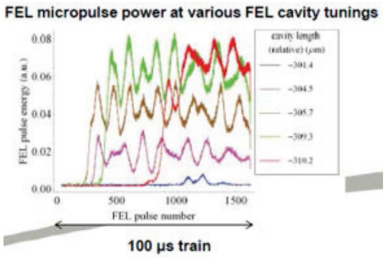

Figure 5: FEL micropulse intensity showing instability.

To investigate the source of this instability, fast BPM electronics (which had been originally developed for use on the EMMA non-scaling FFAG at Daresbury) were implemented at various locations in ALICE. They showed a pronounced instability at roughly 100 kHz in the bunch position, most clearly in the post-booster and post-linac lattice (see Figure 6). Pre-booster, the evidence for this instability was less clear. In addition, a ~300 kHz instability in the bunch charge was observed clearly at all locations; this sometimes appears in the FEL intensity at a much smaller amplitude than the 100 kHz signal.

To further investigate the root cause of the instabilities, the photoinjector laser was examined. A fast photodiode reveals a 300 kHz instability in the laser intensity, while the evidence for a ~100 kHz position instability of the laser beam is less convincing. It had in fact already been established in measurements in 2007 that the SSB spectra of the PI laser phase with respect to the RF reference showed an instability at 300 kHz.

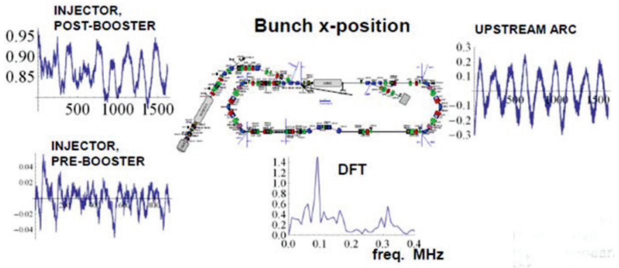

Figure 6: Position instability on fast BPMs.

In addition to the measurements described above, some measurements were performed synchronising fast PEM, BPM, and bunch time-of-arrival (TOA) measurements (using optical sampling of BPM signals) for individual machine shots. The motivation for this was as test bed for optical TOA diagnostics and as a potential source of extra information on the instabilities. The 100 kHz instability was also present in the TOA data and highly correlated with the other observables.

After presenting this material, several suggestions were made as to the root cause of the 100 kHZ instability. These included the DC gun power supply stability, stability of the PI laser power supplies, and instabilities resulting from feedback loop from the low level RF. It was noted that the bunch position stability seemed to be more pronounced as the beam moved further downstream through the machine from the gun. These suggestions will be investigated further with the relevant technical groups at Daresbury.

Similarly, diagnostic work being done on the MESA project was discussed. The diagnostic test-beam-line for MESA shown in Figure 7 is built and ready for use. Investigations of the two transverse phase-spaces with quadrupole scan technique and the determination of the beam profile with a screen or with wires are possible. The beam-line gives the possibility of a cross check between quadrupole scan and slit mask measurements. The temporal distribution can be inspected with a deflecting cavity that transforms the longitudinal distribution into an transverse one and deflects the beam onto a circle which can be observed with a Ce:YAG screen and a CCD-camera, as shown in Figure 8. All this can be done with three different laser wavelengths (405, 520, 780nm) and for different laser spot sizes.

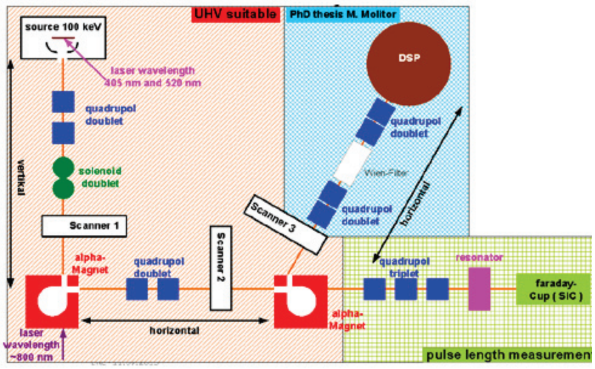

Figure 7: MESA diagnostic components.

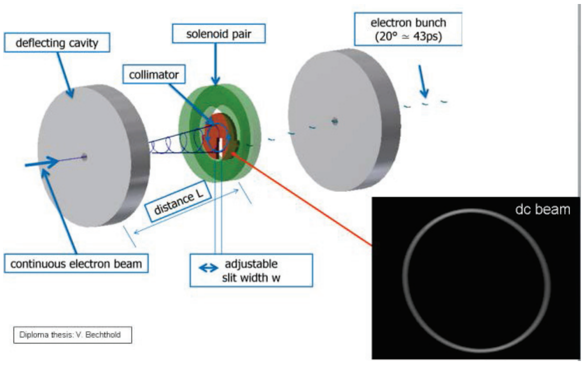

Figure 8: MESA Deflecting Cavity and Collimator Set-up.

The first preliminary results of the emittance look promising to match the requirements of MESA stage 1. Further investigations of higher bunch charges etc. have to be done.

In the future it is planned to get more experience with the beam-line and the measurement techniques to characterize if the electron bunches from the source are suitable for MESA stage 1. Furthermore a closer look to helicity correlated halo effects is in preparation.

Additionally, a presentation was given on techniques to measure the beam current in the BNL ERL. This talk focused on the techniques of current measurements associated with machine protection against over exposure of instrumentation to beam charge at BNL's ERL. The machine layout was presented with an overview of installed instrumentation, followed by the beam operating parameters and the required current measurement ranges. The measurement technique & results from the Faraday Cup measurements made with beam were presented that revealed accurate measurements of the dark current produced by the SRF cavity as well as the current pulses produced by the photocathode. The method of charge measurement was described as an in-flange integrating current transformer (ICT) from Bergoz Electronics. The beam pulse length & repetition rate limitations were discussed, followed by results of measurements of beam charge that showed good agreement with the faraday cup. This was followed by a graphical depiction of the bunch, macrobunch & bunch train structures that were implemented to tailor to the requirements of the ICT.

The use of the ICT by the machine protection system was described showing the interface electronics. The MPS logic was described to have individual charge thresholds for each insertable instrument in the beam line. These limits are enabled by the insertion of the corresponding instrument. This mode is used with short macrobunches measured directly by the ICT. For recording current from longer macro bunches, a pulse counting scheme was proposed (but not yet implemented) where the laser pulses (at 9.38MHz) in the train are counted by a high-speed counter and multiplied by the measured charge per bunch in a short "pilot macro bunch". The result is processed by the control system with the bunch train structure to record an average current.

A DCCT, also made by Bergoz Electronics, was show to be installed in two places in the ERL for average current measurement when the bunch structure is composed of trains long enough to satisfy the bandwidth requirements of the DCCT. A technique of transitioning from a bunch structure compatible with the ICT to a bunch structure compatible with the DCCT was shown in a graphical depiction, where the average train current is 50µA in both cases. A differential current measurement scheme was mentioned as being under development. Discussions that followed the talk brought out the concern for shields to be installed in the vacuum to shield the ceramic breaks from the passing beam in an effort to avoid charge being deposited on the ceramic.

ION DIAGNOSTICS AND CLEARING METHODS

Experiments were recently performed to test the effectiveness of three ion-clearing strategies in the Cornell high intensity photoinjector: DC clearing electrodes, bunch gaps, and beam shaking. The photoinjector reaches a new regime of linac beam parameters where high CW beam currents make ion trapping unavoidable. Therefore ion mitigation strategies must be evaluated for this machine and other future ERLs.

Because high beam intensities present beam diagnostic challenges, several techniques were developed to directly measure the residual trapped ions rather than the beam. Two primary indicators of successful clearing are the amount of ion current removed by a DC clearing electrode, and the absence of bremsstrahlung radiation generated by beam-ion interactions. Measurements were taken for a 5 MeV electron beam and CW beam currents in the range of 1-20 mA.

Several theoretical models have been developed to explain the data. Using them, one can estimate the clearing electrode voltage required for maximum ion clearing (see Figure 9), the creation and clearing rates of the ions while employing bunch gaps, and the sinusoidal shaking frequency necessary for clearing via beam shaking. In all cases, a maximum ion clearing of at least 70 percent or higher was achieved, and almost full ion clearing was approached in certain cases.

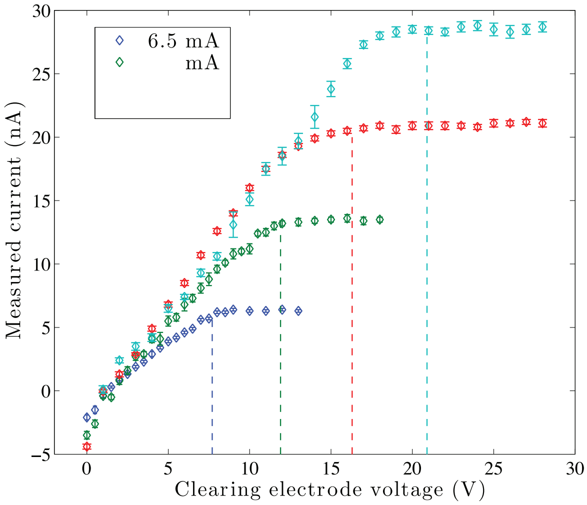

Figure 9: A picoammeter was used to measure the ion current striking the clearing electrode for different applied voltages. The vertical dotted lines mark the minimum voltage required for full ion clearing, as predicted using a simple theory.

ISBN 978-3-95450-183-0

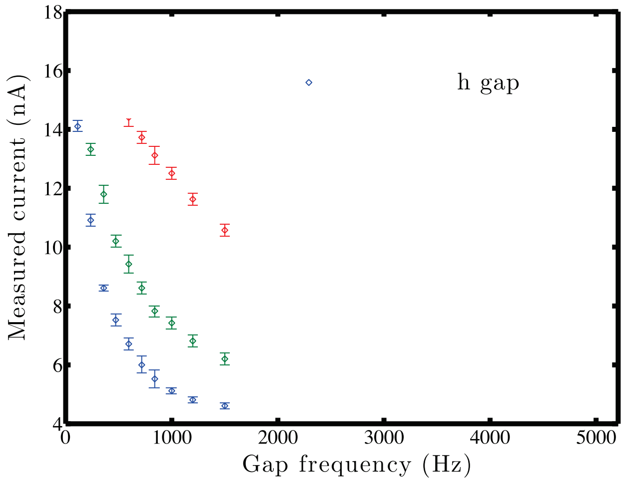

Figure 10: Increasing the frequency and duration of bunch gaps reduces the trapped ion density as shown by the residual ion current hitting a clearing electrode.

Of particular note is the finding that the total amount of clearing while employing bunch gaps does not depend strictly on the bunch gap duration and frequency. Instead, it depends only on the total time the beam is turned off, as is seen in Figure 10. This flexibility may allow it to be deployed in ERLs – a prospect previously thought too difficult to consider due to problems with beam loading.

A new diagnostic capable of surviving high intensity electron beams was discussed. It consists of a thin rotating wire that passes through the beam, and a downstream radiation detector. Together, they allow for a high current beam profile. The design was optimized to reduce the footprint of the device, while still allowing it to reach the large velocities needed to prevent it from absorbing too much heat load from the beam. It was installed in the Cornell injector, and tested at moderately high beam currents up to 20 mA, though at the relatively low energy and correspondingly large beam width inherent in injectors. Depending on the gain in the PMT radiation monitor, it could also be used at a much lower average current, and at these currents it was compared to a measurement on a viewscreen. Above a certain speed, which supressed the error from wire vibration, the two measurements were found to agree well, as in Figure 11.

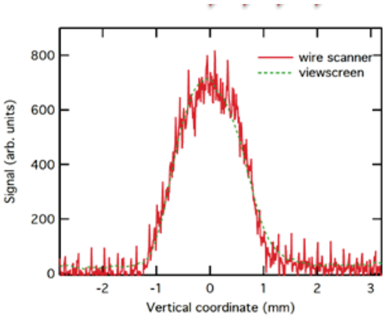

Figure 11: Comparison of the beam profile using the wire-scanner vs. viewscreen.

CONCLUSION

Progress continues to be made in the development of diagnostics suitable for the high intensity beams produced in Energy Recovery Linear accelerators. Instabilities were investigated at ALICE using various diagnostics including fast BPMs. The diagnostic beamline for MESA was discussed. The applicable range and performance benefits of competing designs for measuring beam current were covered, including ICTs and DCCTs. Finally, a report on effective methods of ion clearing as well as a new diagnostic for transverse beam profiles was given.

ACKNOWLEDGMENT

The authors would like to thank the workshop organizers and participants of the working group for the excellent presentations and discussions during and in-between the sessions.

ERL2015 SUMMARY OF WORKING GROUP 4 RF AND SUPERCONDUCTING RF

H. Sakai[#] ,KEK, Tsukuba, Ibaraki, Japan
E. Jensen[*], CERN, Geneva, Switzerland

Abstract

The 50th ICFA Advanced Beam Dynamic Workshop on Energy Recovery Linac (ERL2015) was held on June 7-12, 2015 at Stony Brook University in U.S.A. Working Group 1-5, were organized in the workshop. Working Group 4 mainly covered the topics and issues about RF and Superconducting RF cavity for ERLs. This paper summarizes WG4 presentation and activities.

INTRODUCTION

The WG4 charge is to identify the critical issues of each component in cryomodule construction, assembly works and beam operation for ERL. Especially, we need to evaluate what is the critical issues of SRF cryomodules for high current and high charge with low emittance beam operation. Following themes was discussed in WG4.

A) Recent progress of each laboratory for ERL from ERL2013.
B) Cavity and cryomodule design for ERL.
C) Cavity fabrication technique and cavity testing.
D) HOM damping design/simulation and HOM damper/coupler development.
E) RF control for stable beam operation.
F) SRF Gun.
G) High Q R&D for SRF challenge.

18 oral presentations were contributed to WG4 in total. The topics of SRF Gun were discussed at joint session of WG1 and WG4. The topics of HOM BBU simulation and impedance issues were discussed at joint session of WG2 and WG4. The topics of RF control were discussed at joint session of WG3 and WG4.

Among these WG4 presentation and discussion, we pick up the critical issues and progresses in this paper.

SRF CHALLENGE

Recent most interesting and exciting topic about SRF field is to study new approaches for obtaining higher-Q of more than $1x10^{10}$. Fumio review the recent progress to obtain higher Q-value about SRF cavities all over the world in this plenary session.

High-Q R&D for SRF Challenge for ERL (Fumio Furuta, Cornell Univ.)

The two approaches to obtain the higher-Q value of SRF cavities were presented. One is done by Cornell Univ. for ERL project; the other is by FNAL for LCLS-II project. Table 1 shows the summary of two approaches. The former surface treatment was based on the normal cavity treatment. But by applying the slow cooling to 2 K, we would reduce the thermo-current in Nb and the higher-Q was achieved. The latter case is the new approach for SRF challenge to get higher-Q. Nb surface properties was changed by adding N2 gas with optimum pressure in a few minutes when Nb cavity was annealed in furnace; this procedure was named as "N2-dope". It is recently found that this "N2-dope" procedure tend to increase the unloaded-Q of Nb cavity [1]. Comparing with former approach, this "N2-doped" cavity do not need slow cooling but fast cooling because the magnetic flux was easily trapped so that residual loss was increased.

Finally, it was concluded that higher-Q of more than $3x10^{10}$ at 2 K in medium field is in hand now with high yield at horizontal test by recent dramatic high-Q study of both procedures in this plenary talk.

Table 1: Summary of High-Q Approaches

R&D program	Cornell ERL	LCLS-II
SRF cavity	1.3GHz 7-cell	1.3GHz 9-cell
Highest Q0 in HT at 16MV/m,2K	$3.5x10^{10}$	$3.2x10^{10}$
Surface finish	120C bake + HF rinse	N2-dope
Cool down	Slow cool	Fast cool
Trapped flux effect	Not sensitive	High sensitive

PROGRESS FROM ERL2013 AT EACH SRF FACILITY FOR ERL

In this session, we review the recent progress at each laboratory and company.

Completion of the Cornell High Q CW Full LINAC Cyromodule (Ralf Eichhorn, Cornell Univ.)

Cornell University has finished building a 10 m long superconducting accelerator module as a prototype of the main linac of a proposed ERL facility. This module houses 6 superconducting cavities- operated at 1.8 K in continuous wave (CW) mode - with individual HOM absorbers and one magnet/ BPM section [2].

Cavity Production and Results: For the cavities, a 7-cells, 1.3 GHz design was made while an envisaged Q of $2x10^{10}$ was targeted at a gradient of 16 MV/m. All 6 cavities for the MLC module have been produced in-house starting from flat metal niobium sheets. All cavities were tested vertically, the summary of these test are given in Figure 1. All six cavities exceeded the design quality

---

[#] hiroshi.sakai.phys@kek.jp,
[*] Erk.Jensen@cern.ch

factor, averaging to 2.9x10^{10} at 1.8 K. At 2 K, the average Q was 1.8x10^{10}, at 1.6 K we found 4.3x10^{10}[3].

The reproducibility of the Q versus E curves for all cavities is remarkable, also the fact that none of the cavities needed additional processing- giving a 100 % yield.

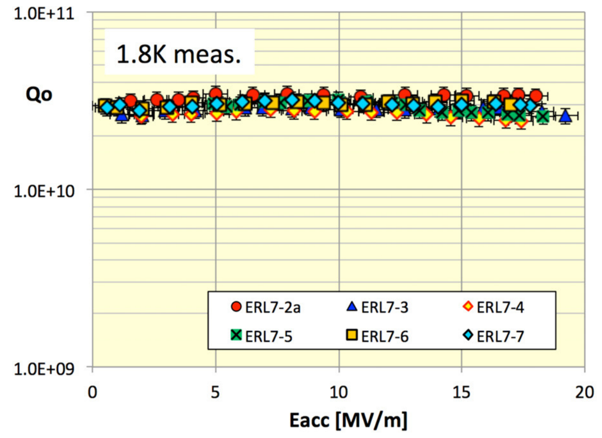

Figure 1: Vertical test results for all 6 ERL cavities. All cavities exceeded the design specifications for the ERL (Q=2x10^{10} at 1.8 K). The reproducibility of the results, gained without any reprocessing of a cavity, is remarkable. The cavities were not N2-doped!

Preparation for Testing: In preparation for the testing of the MLC, the module was transported across the Cornell campus (Figure 2). Currently, cryogens and instrumentation is getting connected and the first cool-down is scheduled for early July.

Figure 2: The MLC crossing Cornell campus on a truck in preparation for testing at Wilson Lab.

Operational experience of CW SRF injector and Main-linac cryomodules at the Compact ERL (Hiroshi Sakai, KEK)

CW injector and main linac cryomodules were developed for Compact ERL (cERL) project [4] and constructed at 2012. The injector cryomodule [5] includes three 2-cell 1.3 GHz superconducting cavities. The main linac cryomodule [6] includes two 9-cell 1.3 GHz superconducting cavities. After construction of the injector and the recirculation loop, the CW operation was started with 20 MeV beam in Dec. 2013 [7]. After precise beam tuning, energy recovery operation was achieved with more than 90 uA at present. Injector and main linac cavity were stable for ERL beam operation with Digital LLRF system, which stability has $\Delta A/A < 0.01\%$ and $\Delta\theta < 0.01$ degree.

Q-values of Main-linac cavities were several times measured. Results are shown in Figure 3. Although radiation existed and Q-values were low from the first high power test at 2012, after some period of beam operation, Q-values became further worse. However, pulse processing method worked effectively to suppress field emissions. Finally, we kept same performance within error-bars after degradation from May 2014 to Mar. 2015. At present, Reason why field emission became worse and stopped is not clear. We will continue measuring the cavity performances.

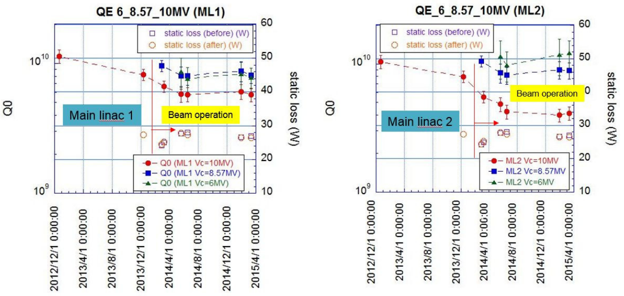

Figure 3: Measurement of the cavity performances of 6, 8.57 and 10 MV cavity voltage, which almost equals with MV/m, during long-term beam operation including high power test of Main linac 1(left) and 2 (right).

The Development of the High Current Superconducting Cavity at IHEP (Zhenchao Liu, IHEP)

High current superconducting cavity, slotted cavity, was developed at IHEP [8]. The aim of the cavity is delivering ampere-class beam current for the GeV ERLs [9]. Although the fabrication of the cavity is challenging, we have fabricated a 1.3 GHz 3-cell slotted cavity. The room temperature RF test and the vertical test at 4.2 K were taken and the results show that the cavity is available to reach the design goal. Figure 4 shows the 1.3 GHz 3-cell slotted cavity. The heavy damping of the slotted cavity for dipoles were performed in low level RF test up to 2.5 GHz. The cavity has extremely low HOM impedance and the HOMs power can be easily extracted from the waveguide structure.

The cavity has few hard multipacting barriers, however, the gradient is limited by the RF power. The gradient of the cavity reached 2.4 MV/m at 4.2 K with a Q_0 of 1.4x10^8 limited by power. 2K vertical test will be done soon. And further study will begin. The cavity shows a great potential in the high current and high HOM damping application such as ERL and circular collider.

Figure 4: 1.3GHz 3-cell slotted cavity.

Development for Mass Production of Superconducting Cavity by MHI
(Kohei Kanaoka, Mitsubishi Heavy Industry)

MHI has improved our superconducting technology to take part in the production design and manufacturing of the cryomodules including the superconducting cavities. MHI produced the injector module of cERL shown in Figure 5(right) which contains three 9-cell cavities. We performed the production design and fabrication of the parts and assembly of the cryomodule at KEK. We also fabricated the main accelerator module for cERL shown in Figure 5 (left) [10,11].

We designed the 1.3GHz 1.5-cell elliptical cavity for the superconducting RF electron gun and fabricated the Prototype#1.

MHI has developed the manufacturing process of superconducting cavities for a long time. For example, we perform the welding of the stiffener rings by the laser welding. The 2-cell cavity shown in Figure 6(left) was fabricated by using the seamless dumbbell. MHI has the EBW machine which can contain four 9-cell cavities by vertical position and weld them in one batch. We succeeded in welding all seams of equator of four cavities in one batch shown in Figure 6(right)[12].

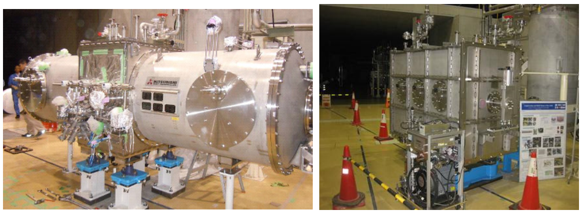

Figure 5: Main accelerator module(left), Injector module of cERL (right).

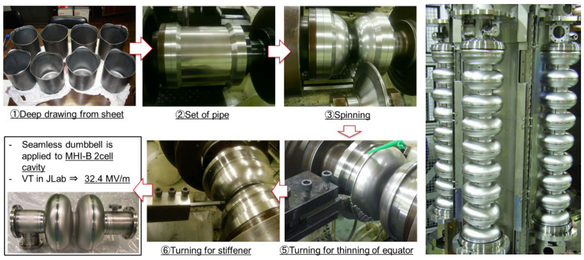

Figure 6: Process of the manufacture of the seamless dumbbell and 2-cell cavity (left), batch process (right).

Ultra-Fast Harmonic Resonant Kicker Design for the MEIC Electron Circular Cooler Ring
(Yulu Huang, IMP (Jlab))

Electron cooling is essential for the proposed MEIC to attain low emittance and high luminosity [13].The present MEIC design utilizes a scheme of multi-stage cooling, a DC cooler in the booster and bunched electron beam cooler ERL in the collider ring. To achieve a very high electron beam current for bunched beam cooling in the future high luminosity upgrade, we adopt a circulator ring to reuse the electron bunches. The electron bunches will recirculate for 25 turns, thus the current in the ERL can be reduced by a factor of 25. An ultra-fast kicker is required for this circulator ring, with a pulse width less than 2.1ns (1/476.3MHz) and a high repetition frequency of 19.052MHz (1/25 of 476.3MHz). JLab started an LDRD proposal to develop such a kicker. Our approach is to generate a series harmonic mode with RF resonant cavities [14], electron bunches passing through the cavity will experience an integral effect of all the harmonic field, thus every 25th bunch will be kicked while all the other bunches un-kicked.

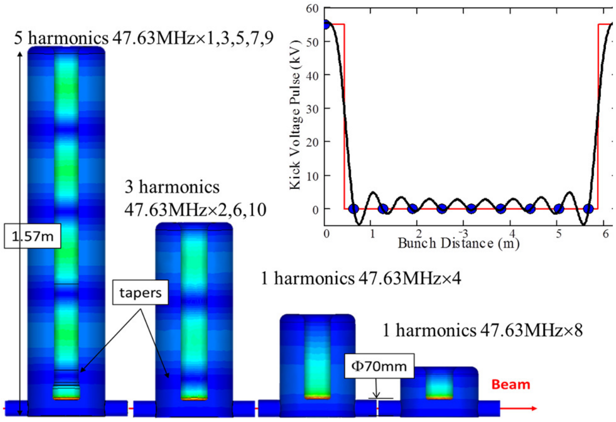

Figure 7: Harmonic modes in four cavity system with the highest harmonic electric field distribution shown in each cavity. Ideal kick voltage pulse (red square pulse) and bunch train scheme (blue point) to kick every 10th bunch, and the reconstructed kicker pulse with the first 10 harmonic modes (black).

ISBN 978-3-95450-183-0

Here we present a design of a simplified prototype with every 10th bunch kicked, using four Quarter Wave Resonator based cavities to generate 10 harmonic modes, as shown in Figure 7. Cavity structure is optimized to get the highest shunt impedance, and the total power dissipated on the four cavities for copper material is 87.72W, two to three orders of magnitude lower than a strip-line kicker [15].

Recent progress of PKU DC-SRF gun and future prospect were also presented. Furthermore, design work for SRF cavities for high current ERLs at BNL were also presented in this session

RF CONTROL OF SRF CAVITIES FOR STABLE BEAM OPERATION

The joint session with WG3 were held to discuss the RF control for SRF cavities and RF sources.

Performance of Digital LLRF System at cERL (Feng Qiu, KEK)

A compact energy recovery linac (cERL), which is a test machine for the next generation synchrotron light source 3-GeV ERL, was constructed at KEK [7]. In the cERL, a normal conducting (NC) buncher cavity and three superconducting (SC) two-cell cavities were installed for the injector, and two nine-cell SC cavities were installed for the main linac (ML). The radio-frequency (RF) fluctuations for each cavity are required to be maintained at less than 0.1% rms in amplitude and 0.1° in phase. These requirements are fulfilled by applying digital low-level radio-frequency (LLRF) systems. During the beam-commissioning, the LLRF systems were evaluated and validated. A measured beam momentum jitter of 0.006% indicates that the target of the LLRF systems is achieved (see Figure 8). To further improve the system performance, an adaptive feedforward (FF) control-based approach was proposed and demonstrated in the beam-commissioning as well [16]. Based on the new adaptive FF approach. The microphonics in the cavity of the ML has been rejected successfully as shown in Figure 9. The current status of LLRF system and the adaptive FF approach for LLRF control in the cERL are presented in this paper.

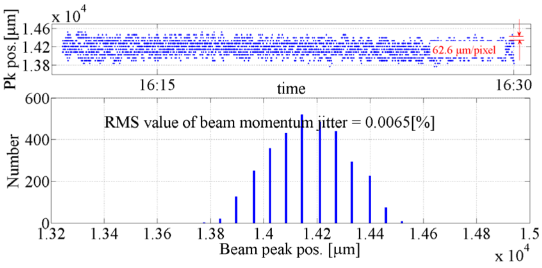

Figure 8: Beam momentum jitter measurement. The measured beam momentum jitter was 0.0065% rms, which is in agreement well with RF stability.

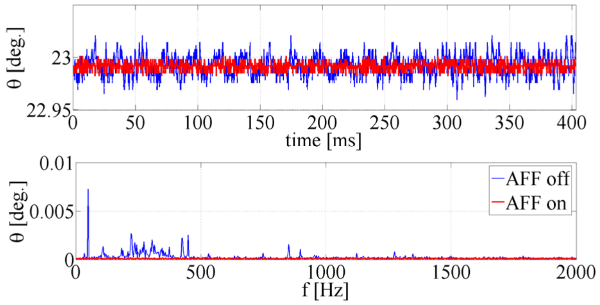

Figure 9: Measured RF phase of the ML2 cavity pickup signal in the case of with and without adaptive FF control. Both waveform (top) and spectrum (bottom) are presented.

Resonance Control for Narrow-Bandwidth, Superconducting RF Applications (J. P. Holzbauer, FNAL)

Many of the next generation of particle accelerators (ERLs, XFELs) are designed for relatively low beam loading. The cavities are designed to operate with narrow cavity bandwidths to minimize capital and operational costs of the RF plant. With such narrow bandwidths, cavity detuning from microphonics becomes a significant factor, and in some cases can drive the cost of the machine [17]. Piezo actuators have been successfully used to actively stabilize cavity resonant frequencies. This paper will present the results of ongoing detuning compensation efforts at FNAL using prototype 325 MHz SRF single spoke resonators designed for the PIP-II project at Fermilab [18].

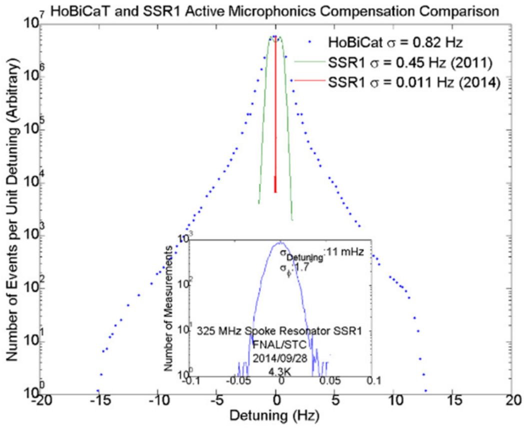

Figure 10: A comparison detuning distributions following active compensation at HoBiCaT and FNAL.

Using an FPGA system developed at FNAL, the cavity was controlled and calibrated on-line. Static and dynamic measurements were used to calibrate relative gains and phases of cavity signals along with cavity Lorentz Force Detuning coefficients. This coefficient was used to correct this detuning in a feedforward configuration on the piezo. Careful calculation of cavity detuning was calculated online and feed into the piezo for active compensation of fast cavity detuning. Over a two hour run, the cavity resonance was stabilized to an RMS detuning of 11 mHz with a peak to RMS ratio of 6 as shown in Figure 10. Active efforts to improve this and include amplitude and phase stability are ongoing.

Using a 1.3 GHz 20 kW Solid State Amplifier as RF Power Supply for DC-SRF Photo-Injector (Fang Wang, Peking Univ.)

An upgraded DC-SRF injector with a 3.5-cell cavity was designed and constructed at Peking University [19]. Taking into account the regulation reserve for phase and amplitude control and losses in the waveguide distribution, a 20 kW CW amplifier at 1.3 GHz is needed and we manufactured a solid state amplifier (SSA) under the collaboration with BBEF.

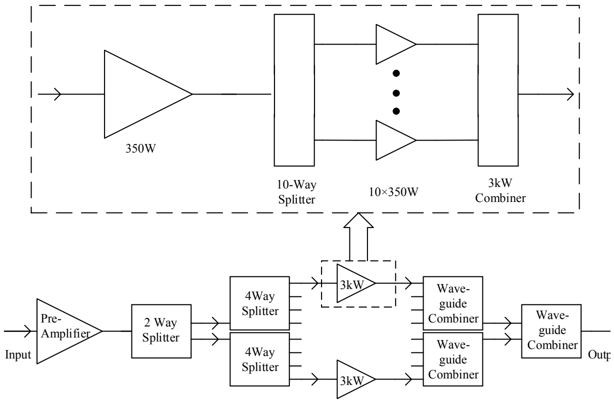

Figure 11 : Structure of 20kW SSA.

Table 2: Technical Specification of the Power Amplifier

Parameter	Required	Results
Frequency Range /MHz	1300±0.05	1300±0.05
CW & Pulsed Output Power (1dB Compression) /kW	≥ 20	20
Linear Gain /dB	≥73	~85
Output Harmonics $2^{nd}/3^{rd}$ Order /dBc	≤-30 ≤-30	-70 -57
RF Phase Shift vs. Output/°	≤10	9.5
Gain Change vs. Output/ dB	≤2.0	1.6
Efficiency at 20kW output	≥40%	34%

The overall structure of the SSA is illustrated in Figure 11. It consists of 8 transistor banks. Each bank generates 3 kW and in which, there are 11 elementary modules with individual power supplies and one module is used as a preamplifier to drive the other ten.

It has been tested after the installation. The technical specification is shown in Table 2. Full reflection test was carried out with a short waveguide terminal, and we got 16 kW over 16 kW in CW for ten minutes without problem. It has been used for routine operation of the DC-SRF photo-injector successfully since 2012.

DISCUSSION

To clarify the present status and future prospect for establishing the high current and high charge with low emittance ERL beam operation. We discuss the following subjects.

A) How is the present status for high current ERL of each component ?
  i. Cavity design and test results are OK to meet the more than 100mA operation. However, we need to care not to contaminate the field emission source in string assembly especially for mass production phase.
  ii. HOM damper/coupler development for high current beam operation were continuously proceeded at each labs. Recently, HOM damper works well with CW 40 mA of 2.7 ps bunch length at Cornell injector beam line.
  iii. Fundamental power coupler (FPC) gives the transmitted more than CW 40kW of 1.3 GHz at Cornell Univ and KEK. BNL FPC give the CW 500 kW of 700 MHz. These results enable CW beam operation 100mA at injector.

B) How to obtain and keep the optimum and stable CW operation field with High-Q for a long time for beam operation ?
  i. Recent high-Q R&D including “N2 doped” cavity gives the Q0 > $3x10^{10}$ at 16 MV/m. We need to push high-Q R&D more.
  ii. Degradation during beam operation is one of the problem for stable beam operation. KEK cERL main linac cavities met the degradation come from field emission (FE) during beam operation at 8.3MV/m field. Furthermore, CEBAF and SNS also meet the degradation during beam operation. We need to keep measuring the cavity performance and collect the experience of degradation of cavities with long-term beam operation.
  iii. We discuss about how to stop the FE (Dark) current from cavity in operation. By using collimator and Q-magnet between cryomodule, we can separate the dark current and main beam. However, we conclude that we need the careful simulation and discuss with beam dynamics group (WG2) more.

C) RF and beam control issues. (WG3/4 joint session)
  i. By using Digital LLRF system, stability has $\Delta A/A < 0.01\%$ and $\Delta\theta < 0.01$ degree at KEK cERL. And tuner control with 0.011Hz was

satisfied by cautious optimism by FPGA at FNAL. These are encouraging results, which satisfy our ERL requirements.

ii. We discuss the strategy to reach the high current beam more than 100 mA. By considering the space charge effects at injector parts, we support starting the beam tuning with nominal bunch charge and increase the beam current by changing the repetition ratio of beam. In reality, more discussion is needed.

iii. When we hit the worse HOM's, we basically need to detune the one cavity. We also discuss the possibility about de-Qing and feedback to HOM suppression.

iv. What we need to do and care if we met the failure during beam operation with high current beam ? Failure modes, which gives the not only stopping the injector beam but also ejecting beam, must to be considered before the beam operation. Clearing gap with beam was also suggested not to increase the beam instability and to identify the bunch train information.

SUMMARY

From ERL2013, the positive and steady advances are seen at every laboratories in these two years as follows.

A) Recent high-Q R&D including the "N2 dope" at FNAL, Cornell Univ. is a great work. This lead us to reach more higher gradient CW operation of ERL.

B) Cavity performance including cryomodule test has reached the ERL level and meet reququirments. On the other hand, we met the degradation with FE during long-term beam operation at KEK cERL main-linac.

C) HOM damper was performed with real high current beam with CW 40 mA at Cornell injector and gave the good performance.

D) More than 100 mA was achieved with BBU suppressed cavity design, which was done at BNL, Cornell, KEK, HZB, in the elaborate simulation work.

E) Cavity fabrication technique catch up with the mass production phase now.

F) LLRF with tuner control of stable power source reach the very high stability of $\Delta A/A < 0.01\%$ and $\Delta\theta < 0.01$ degree, which satisfy our ERL requirements.

G) New SRF guns starts in operation at HZDR and BNL. Dark current is severe problem at present.

All key components are in the level of practical use expect for HOM damper. Furthermore, we understand the difficulty of SRF operation with high gradient in CW mode because of FE and other disturbance. We note that construction of new ERLs like BERLinPro is underway and new test facility of FFAG-ERL at Cornell/BNL and CERN are proposed. As the next step, we will accumulate the cavity & cryomodule test including new ERL facility and operation experiences so that we can meet for stable operation at the next ERL2017.

ACKNOWLEDGMENTS

We would like to thank all ERL2015 committee's members, all contributors to the presentation and discussions in WG4, and those who provide material for this paper.

REFERENCES

[1] A. Grassellino *et al.*, 2013 Supercond. Sci. Technol. 26 102001.

[2] R. Eichhorn, B. Bullock, B. Elmore, B. Clasby, F. Furuta, Y. He, G. Hoffstaetter, M. Liepe, T. O'Connell, J. Conway, P. Quigley, D. Sabol, J. Sears, E. Smith, V. Veshcherevich, "The Cornell Main Linac Cryomodule: a Full Scale, High Q Accelerator Module for cw Application", Physics Procedia (2014), accepted

[3] R. Eichhorn, et. al. "Cornell's ERL Cavity Production", Proc. of the 2013 Int. Conf. on RF Supercond., Paris, France (2013) 909.

[4] R. Hajima *et al.* (ed.), KEK Report 2007-7/ JAEA-Research 2008-032 (2008) [in Japanese]

[5] E. Kako *et al.*, "High power tests of Injector Cryomodule for Compact-ERL", IPAC'13, Shanghai, China, May 2013, p.2340 (2013)

[6] K. Umemori *et al.*, "Construction of main linac cryomodule for Compact ERL project", IPAC'13, Shanghai, China, May 2013, p.2349 (2013)

[7] N. Nakamura *et al.*, "Present Status of the Compact ERL at KEK", IPAC'14, Dresden, Germany, June 2013, p.353 (2014)

[8] Z.C. Liu et al., New way to accelerating high current beam in ERL, in Proceedings of ERL2013, Novosibirsk, Russia, WG303

[9] Z. Liu and A. Nassiri, Novel Superconducting rf Structure for Ampere-Class Beam Current for Multi-GeV Energy Recovery Linacs, Phys. Rev. ST Accel. Beams 13, 012001 (2010)

[10] F. Inoue, et al., "The Development of Cryomodule for c-ERL at MHI", ERL2013, Novosibirsk, Russia, 2013, PS15.

[11] H. Hara, et al., "SRF activities at MHI," TTC Meeting, Tsukuba, Japan, December 2014, WD4 Id86.

[12] T. Yanagisawa, et al., "Development for Mass Production of Superconducting Cavity by MHI" IPAC2015, Richmond, VA, USA, July 2015, WEPMA048.

[13] MEIC Design Summary. January 12, 2015.

[14] B. Roberts et al, Phys. Rev. ST Accel. Beams 15, 122802 (2012).

[15] J. Guo, H. Wang, First Estimate of the Require Power for the Stripe-line RF Kicker, JLAB-TN-15-020

[16] F. Qiu., "A disturbance-observer-based controller for LLRF systems", Proc. IPAC'15, Richmond, USA (2015).

[17] S. Nagaitsev, "Project X, new multi megawatt proton source at Fermilab", Invited talk, PAC 2011, New York.

[18] L. Ristori, "Status of SSR1 Cryomodule Development", PIP-II Meeting, Feb 3rd, 2015.

[19] W. Xu et al., STUDY ON THE 3.5-CELL DC-SC PHOTO-INJECTOR, Proceedings of SRF2007, Peking Univ., Beijing, China, 2007.

SUMMARY OF WG5 ON ERL APPLICATIONS– ERL 2015

V. Litvinenko, Stony Brook University, Stony Brook, NY, USA
O. Brüning, CERN, Geneva, Switzerland

Abstract

In this paper we present a brief summary of material presented and discussed at ERL 2015 workshop, Working Group 5 (WG5), Applications. Because of the brevity of the paper we can only scratch the surface of the material covers in many excellent presentations. The goal of the WG5 was to discuss applications, which require an ERL or can benefit from an ERL. We also aimed to discuss strengths and weaknesses of ERLs as accelerator used for those applications.

As examples of possible weaknesses we identified the difficulty with radiation protection/beam loss monitoring (when ERLs compared with storage rings) and the need to bend electrons and suffer SR losses and effects (when ERLs compared with straight linacs).

As example of obvious advantages we identified the ERL's energy efficiency, its ability of providing fresh beam with very high power as well as to preserve polarization of the accelerated beam.

We also discussed a set of critical parameters, which ERLs should demonstrate to become of interest for various applications.

INTRODUCTION

The list of applications, which were presented as part of WG5 thematic (e.g. some of them were presented as plenary talks) included the following [1-16]:

- High energy and nuclear physics, including γ-ray sources;
- Light sources and FELs;
- Material science and technology;
- Industry, including XUV lithography.

First, we have heard about three operational ERLs. JLab ERL after operating record breaking high power IR and UV FELs [17] continues to have user applications including THz radiation and the dark photon search. A detailed review [3] of ALICE ERL operation and user program – THz radiation, IR FEL, Thomson scattering, injector in FFAG ring EMMA - was a clear demonstration of the usefulness of ERL, which was initially built as a test facility. Unique four-pass ERL at Novosibirsk did not have a dedicated presentation at the workshop. Nevertheless its user program using high power THz and FIR FEL radiation [18] is well known and was acknowledged in a number of talks. In addition, a lot of excitement came from the KEK, where a commissioning of ERL prototype is in full swing [19] and BNL, where SRF gun became operational initiating the R&D ERL commissioning program [20].

Most of the WG5 talks were focusing on the future accelerators and applications.

LIGHT SOURCES AND FELS

H. Kawata from KEK presented an illuminating talk [5] on scientific potential of the ERL based (both incoherent and coherent) light sources. He presented a compelling case that ERLs would offer far superior performance when compared with existing storage ring-based light sources. In ERL based-light sources, the high repetition rate, short pulse, high spatial coherence and high brightness will enable the filming of ultrafast atomic-scale movies and determination of the structure of heterogeneous systems at a nano-scale. He concluded that unique capabilities of ERL-based light sources will drive forward a distinct paradigm shift in X-ray science from *"static and homogeneous"* systems to *"dynamic and heterogeneous"* systems. In other words, ERL can provide a conceptual change in X-ray science from *"time- and space-averaged"* to *"time- and space-resolved"* analysis.

T. Atkinson from HZB presented design of ERL-based Femto-Science Factory [2], which promised outstanding performance (see Fig. 1) while operating very short electron bunches (from 5.6 fsec upwards).

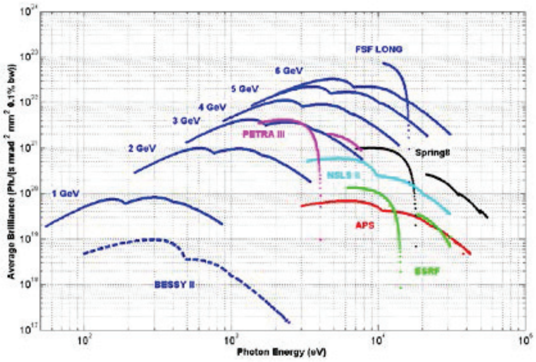

Figure 1: Spectral brightness of various light sources [2].

N. Nakamure (KEK) presented a very interesting design of 800-MeV ERL based FEL, which would serve as a new generation 13.5 nm light source for a chip-production industry [4]. Such facility (see Fig. 2) would generate 10 kW of average power in a 100-meter long SASE FEL with tapered undulator. The EUV FEL power would be split and delivered to chip manufacturing stations. Potentially this ERL technology can revolutionize the chip industry and become one of the main ERL usages.

Y. Jing (BNL and Stony Brook University), presented an overview of existing/past ERL-based FELs (JLAb, ALICE, Novosibirsk and JAERY) and discussed their future potential of ERL-based X-ray FELs [6]. He discussed challenges of preserving the beam quality while propagating the beam through the ERL arcs, as well as

ISBN 978-3-95450-183-0

design of bunch of compressors which minimize damage to the beam from coherent synchrotron radiation (CSR).

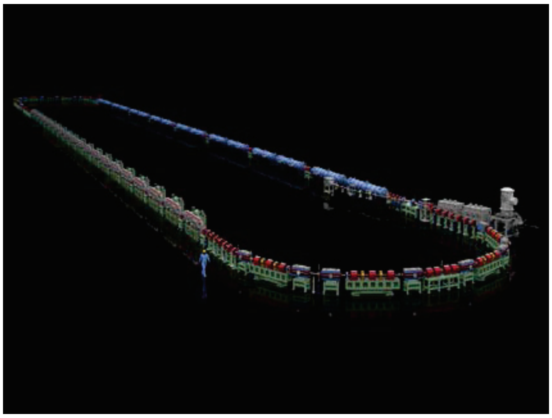

Figure 2: 3D-rendering of EUV source design [4] for industrial applications.

Using an example of an ERL designed for the eRHIC electron-ion collider, he showed that the electron bunch can be accelerated, compressed and used in a single path SASE FEL [6,21 (see Fig. 3). Furthermore, he illustrated how ERL driven FEL can be used for X-ray FEL oscillators [22,23].

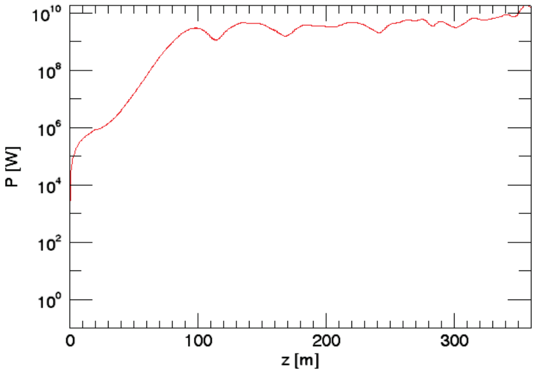

Figure 3: Power evolution in ERL driven SASE FEL operating at 1 Å. Such FEL saturates after 100 m of the FEL wiggler.

I. Konoplev (JAI) presented a concept of a compact ultra-high flux X-ray and THz source [13], based on unique two-cavity SRF system strongly coupled at fundamental frequency (Fig. 4). One of the cavities is used for accelerating the beam and the other is for decelerating. A unique feature of this design is that HOMs of two cavities are intentionally detuned to suppress TBBU instability. The X-ray radiation in such ERL system will be generated using Compton scattering of a laser light, while THz radiation will use a Smith-Purcell type.

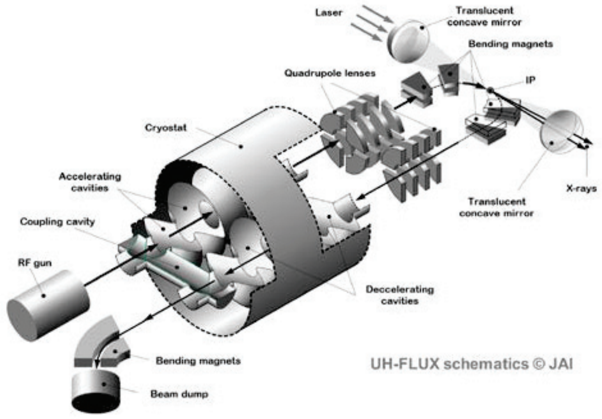

Figure 4: Conceptual layout of uh-flux system [13].

HIGH ENERGY AND NUCLEAR PHYSICS, INCLUDING γ-RAY SOURCES

V. Ptitsyn presented two compelling designs of high energy ERL-based electron-hadron colliders [1]: eRHIC [21] and LHeC [22]. In eRHIC (Fig. 5), 21.2 GeV 16-pass ERL would be used to collide polarized electrons with 250 GeV polarized proton or 100 GeV heavy ion circulating in one of RHIC super-conducting rings. This next generation QCD-facility promises a range of discoveries ranging from observing gluon saturation to solving proton spin puzzle. [21]

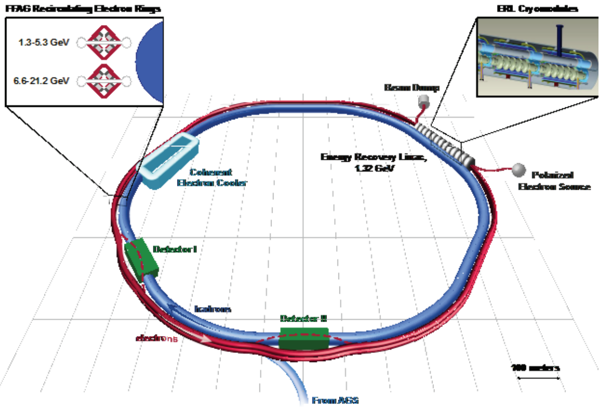

Figure 5: Layout of eRHIC collider.

LHeC would use a 3-pass 60 GeV ERL (see Fig. 6) to accelerate and to collide polarized electrons with one of he 7 TeV proton beams circulating the LHC. This collider program aims at the energy frontier of high-precision physics and beyond-the-standard-model physics [22]. It also would allow high precision studies of Higgs properties.

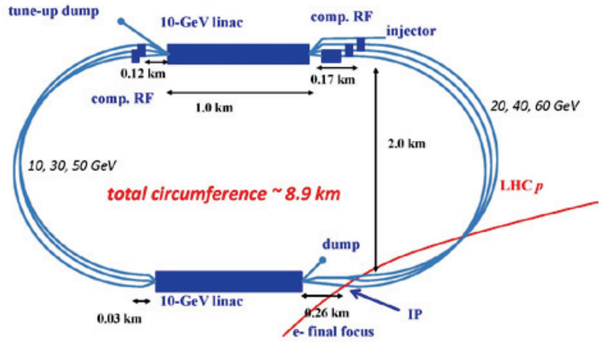

Figure 6: Layout of LHeC ERL.

One of the co-authors from this summary presented a concept of lepton ERL scalable to TeV energies using proton beam for transporting the energy from decelerating linac to an accelerating one [8] (see Fig. 7). Such scheme allows to practically eliminating losses for synchrotron radiation, which limit traditional lepton ERL schemes to few tens of GeV.

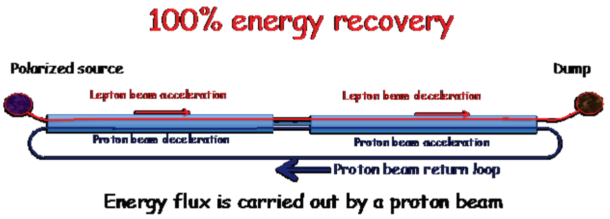

Figure 7: Schematic of TeV-scale lepton ERL.

E. Jensen (CERN) presented plans for 900 MeV three-path ERL facility at CERN (Fig. 8), which would be used for a number of applications beyond serving as a test bed for LHeC [7]: quench test of the superconducting magnets, testing beam instrumentation for future accelerator facilities, and generating γ-ray beams.

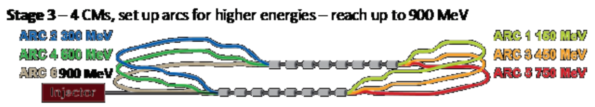

Figure 8: Schematic of CERN ERL facility.

There were two talks on how ERL can be used for cooling hadron beams. I. Pinayev (BNL) presented talk on using an ERL for coherent electron cooling (CeC) on hadron beam in eRHIC, which had to increase the RHIC hadron beams' brightness by about three orders of magnitude [11]. He also presented the Proof-of-Principle CeC experiment system (see Fig. 9), which is under commissioning at RHIC IP2 straight section [23].

J. Kewisch presented a concept of low energy (2.7 to 5 MeV) ERL for cooling RHIC ion beams when operating at low energies below 10 GeV/u [14] (see Fig. 10).

R.Heine described a 155 MeV MESA ERL/RL, which is under construction at Mainz, Germany [9] under the nuclear physics research program. This facility will operate both in ERL and RL (recirculating linac) modes accelerating polarized electron beam (see Fig. 11).

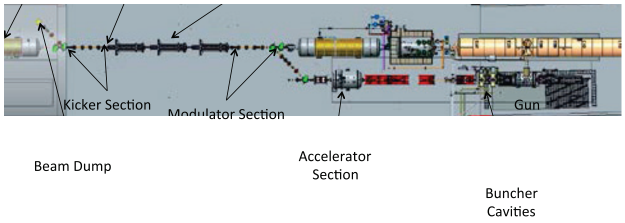

Figure 9: CeC Proof-of-Principle system at IP2 of RHIC.

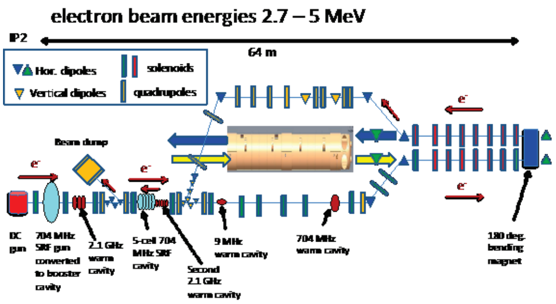

Figure 10: CeC Proof-of-Principle system at IP2 of RHIC.

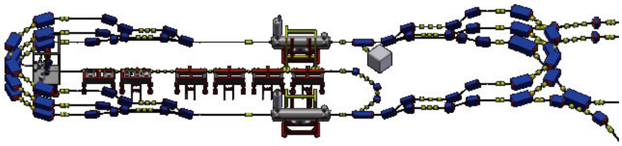

Figure 11: Layout of MESA ERL.

Generating Compton back-scattered γ-ray beams using ERLs was a prominent theme in many presentations. ERL-based Compton γ-ray sources [24] have significant advantage when compared with that based on storage rings [25] or linacs [26]. R. Hajima (JAEA) presented a detailed design as well as a first experiment on ERL-based γ-ray source at KEK [10] (see Fig. 12). He presented an example of how such sources can be used for detection of illicit radioactive materials using existing HIγS facility at Duke University [24].

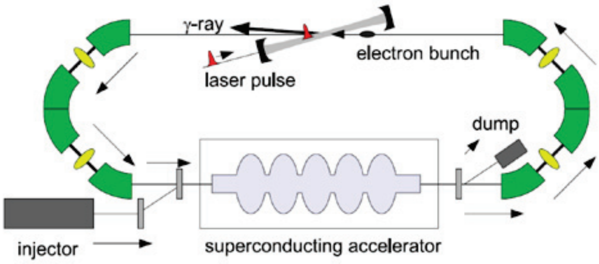

Figure 12: ERL based Compton γ-ray source.

ISBN 978-3-95450-183-0

V. Yakimenko gave an overview talk on ERL-based intense mono-energetic γ-ray sources [12]. He presented quite an exhausting list of potential applications for such sources ranging from security applications and isotope production to generating polarized positron beams for colliders (see Fig. 13).

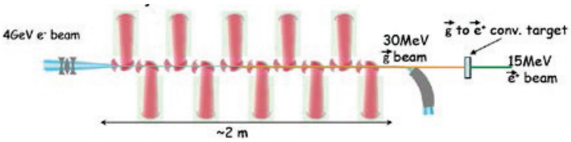

Figure 13: Possible scheme for generating polarized positrons using polarized Compton γ-ray source.

B. Dunham (Cornell U) continued the trend describing how they would use a proposed 4-path ERL for generating intense beams of 50-200 KeV Compton X-rays for material studies and structural engineering [15]. M. Perelstein (also Cornell U) continued discussion of potential application of the propose ERL and shared with us his opinion that such ERL with 300 MeV electron beams can be used in search for dark photon search and used for discoveries in physics beyond the standard model [16].

TABLE OF PARAMETERS

We asked participants of WG5 to send us list of ERL parameters, which are either critical or sufficient for specific application. We have a number of responses and results that are presented in the table below. We want to thanks everybody who responded to our call for information. *Important disclaimer: this table by no means is representative of the whole set of parameters needed for the specific application – it is just a snap-shot of a public opinion represented in WG5.*

Table 1: Range ERL and Beam Parameters Important for Various Applications

Application/ ERL parameter	eA/ep colliders	XUV/XRay FELs	γ-ray sources	SR sources	Nuclear Physics	THz/IR FELs	Electron cooling	CeC
Energy, GeV	20-60	0.65-10	0.1-10	3-7	0.2	0.01 – 0.2	1.6-5 MeV	0.1-0.2
# of passes	3-16	1-4	x	1-2, 12	3	1-3	1	3
Beam current, mA	5-50	10-50	100	10- 100+	1	2-20 (within macropulse if pulsed)	50	100
Peak current, A		500 - 5000	1000	~ 100	?	20-200	0.35	10
Charge per bunch, nC	1-5	0.05 – 1	~ 1	0.01-1	pC	0.05-0.2	100	10
Norm Emittance, mm mrad	5-50	0.1 – 1	~ 1	0.1-1		2-20	2.5	<5
Bunch length, mm	4-10 mm	10– 100 µm	100 µm	3-100µm		0.1 – 0.5	15-35	200
Energy spread	10^{-3} 10^{-4}	10^{-3} – 10^{-4}	10^{-3} – 10^{-4}	10^{-4}		10^{-2} – 10^{-3}	$5\cdot10^{-4}$	$5\cdot10^{-4}$
Electron Polarization	>80%	No	?	No	Yes	No	No	No
Return arc energy acceptance		1-5%	10%	10-3		Few percent		

CONCLUSIONS

Presentations and discussions at WG5 clearly demonstrated that ERL brings new and unique capabilities in many application areas: from fundamental science to industry and national security. With ERL technology maturing, we expect more and more application area to pop-up in near future. The fact that a number of ERL are either under construction, commissioning or in other advanced development phases, makes this period very exciting but also very raveling of real challenges posed by ERL technology.

ACKNOWLEDGMENTS

The authors would like to thank the workshop organizers and participants of the working group for the excellent presentations and lively discussions during and in-between the sessions.

REFERENCES

[1] ERL-based Electron-Ion Colliders, V. Ptitsyn, these proceedings

[2] The Femto-Science Factory: A Multi-turn ERL-based Light Source, T. Atkinson, these proceedings

[3] 10 Years of ALICE: From Concept to Operational User Facility, P. Williams, these proceedings

[4] Design work of the ERL-FEL as the high intense EUV light source, N. Nakamura, these proceedings

[5] Science cases on ERL as a synchrotron light source, H. Kawata, these proceedings

[6] ERL as FEL driver, Y.Jing, these proceedings

[7] ERL facility at CERN for applications, E. Jensen, these proceedings

[8] A Lepton Energy Recovery Linac Scalable to TeV, V. N. Litvinenko, these proceedings

[9] Current Status of the MESA Project, R.Heine, , these proceedings

[10] Laser Compton Sources Based On Energy Recovery Linacs, R. Hajima, , these proceedings

[11] Using ERLs for Coherent electron Cooling, I.Pinayev, these proceedings

[12] ERL as high intensity mono-energetic γ-ray sources, V. Yakimenko, these proceedings

[13] Ultra-High Flux of X-ray/THz Source based on Asymmetric Dual Axis Energy Recovery Configuration, I. Konoplev, these proceedings

[14] ERL for low energy electron cooling at RHIC (LEReC), J.Kewisch, these proceedings

[15] An Inverse Compton Scattering Beamline for High-Energy, Time-Resolved X-ray Scattering Studies of Materials, B. Dunham, these proceedings

[16] Nuclear and High-Energy Physics Experiments with Cornell's FFAG ERL, M. Perelstein, these proceedings

[17] G. R. Neil et al., Phys. Rev. Lett. 84, 662, 2000

[18] O.A. Shevchenko et al.," The Novosibirsk terahertz FEL facility – current status and future prospects", Proc. of FEL 2012, Nara, Japan (2012)

[19] Successful Result of the Commissioning on cERL in KEK, S. Sakanaka, these proceedings

[20] Status and Commissioning Results of the R&D ERL at BNL, D. Kayran, these proceedings

[21] eRHIC Design Study: An Electron-Ion Collider at BNL, E.C.Aschenauer et al., arxiv.org/abs/1409.1633, 2014

[22] A Large Hadron Electron Collider at CERN, J. L. A. Fernandez et al., Journ. Of Physics G: Nuclear and Particle Physics, **39**, 2012, p. 75001

[23] First 1.6 MeV electron beam with 3 nC per bunch was generated from its 112 MHz SRF gun in June 2015.

[24] Potential uses of ERL-based γ-ray sources, V.N. Litvinenko et al., IEEE Trans. Plasma Science **36**, 2008, p. 1799

[25] Recent Results with the High Intensity γ-ray Facility, V.N. Litvinenko, NIM **A507** (2003) 527

[26] Electron Linac design to drive bright Compton back-scattering gamma-ray, A. Bacci et al., J. Appl. Phys. 113, 194508 (2013)

ISBN 978-3-95450-183-0

List of Authors

Bold papercodes indicate primary authors

— A —

Abo-Bakr, M. **TUPATH020**, **THPCTH076**
Ackeret, M.A. TUIBLH1023
Agladze, N.I. THIALH2070
Ainsworth, R. WEICLH1057
Alexander, I. **THIALH2069**
Altinbas, Z. MOPDTH014
Arakawa, D.A. WEIDLH2066
Arnold, A. **TUIDLH1037**, TUIDLH1038
Arnold, M. TUICLH2032
Atkinson, T. **MOPBTH003**
Attenkofer, K. TUICLH1030
Aulenbacher, K. THIALH2069

— B —

Bakin, V.V. THIALH2072
Bartnik, A.C. **MOPCTH008**, **TUPATH019**, TUICLH1024, THIALH2070, THIALH2071, **THPCTH075**
Bazarov, I.V. MOPBTH005, MOPCTH008, TUICLH1024, THIALH2070, THIALH2071
Beavis, D.R. MOPDTH014
Bechthold, V. THIALH2069
Belomestnykh, S.A. MOPDTH014, TUICLH1027, TUIDLH1036, WEICLH2061
Ben-Zvi, I. MOPBTH005, MOPDTH014, TUIBLH1023, TUICLH1027, TUIDLH1036, WEICLH2061
Berg, J.S. MOPBTH005, TUIBLH2024
Bhandari, H. TUICLH1030
Blaskiewicz, M. MOPBTH005, WEICLH1058
Bogacz, S.A. MOPBTH004, **TUIBLH2026**, WEIALH1043
Bondarenko, A.V. MOPBTH003
Brock, J.D. **WEICLH1059**
Brooks, S.J. MOPBTH005, **TUIBLH2024**, TUIBLH2027, WEIDLH1002
Brown, K.A. MOPBTH005
Brüning, O.S. MOPBTH004, TUPATH023, WEIALH1043, THPDTH079
Bullock, B. WEIBLH2053
Burt, G. WEICLH1057

— C —

Calaga, R. WEIALH1043
Cenni, E. WEIBLH2054
Chang, X. **TUIBLH1022**
Chen, J.E. WEIBLH2056
Chen, S. MOPCTH010, **TUICLH2033**
Ciovati, G. TUIDLH1037
Clasby, B. WEIBLH2053
Conway, J.V. WEIBLH2053
Cultrera, L. MOPCTH008

— D —

Dai, J. WEIBLH2055
Deonarine, S. MOPDTH014
Di Mitri, S. **TUIDLH2040**
Ding, Z. **TUICLH1030**
Dobbins, J. MOPBTH005, THIALH2070, THIALH2071
Dobrin, E. TUIBLH1023
Douglas, D. TUICLH2034
Dunham, B.M. MOPBTH005, MOPCTH008, WEICLH1059, THIALH2070, THIALH2071

— E —

Eichhorn, R.G. **WEIBLH2053**
Elmore, B. WEIBLH2053
Enami, K. WEIBLH2054

— F —

Fan, P.L. WEIBLH2056
Fedotov, A.V. WEICLH1058
Feng, L.W. WEIBLH2056, WEIDLH2068
Fischer, W. MOPBTH005
Freitag, M. TUIDLH1037
Frisch, H.J. TUICLH1030
Full, S.J. THIALH2070, **THIALH2071**
Furuta, F. **MOPDTH012**, WEIBLH2053
Furuya, T. MOPCTH010, WEIBLH2054

— G —

Gao, J. WEIBLH2055
Gaowei, M. TUICLH1030
Gassner, D.M. MOPDTH014, TUIBLH1023, WEIALH2048
Gros, M. TUICLH2032
Gulliford, C.M. MOPCTH008, TUPATH021, **THPCTH077**
Guo, J. WEICLH2063
Gupta, R.C. MOPDTH014

— H —

Haga, K. MOPCTH010
Hahn, H. MOPDTH014, WEICLH2061
Hajima, R. MOPCTH010, TUIBLH1020, TUIBLH1021, **WEIBLH1050**, THPTHL073
Hall, C.C. **TUICLH2035**
Hammons, L.R. MOPDTH014

ISBN 978-3-95450-183-0

Hanyu, I. MOPCTH010
Hao, J.K. WEIBLH2056, WEIDLH2068
Hao, Y. MOPBTH005, TUIBLH2024, TUIBLH2025, **TUIDLH2041**
Hara, H. WEICLH2062
Harada, K. MOPCTH010
He, F.S. WEIBLH2055
He, Y. WEIBLH2053
Heine, R.G. **WEIBLH1049**
Ho, C. MOPDTH014
Hoffstaetter, G.H. **MOPBTH005**, WEIBLH2053, WEICLH1059, WEICLH1060, THIALH2071
Holzbauer, J.P. **WEIDLH2067**
Honda, T. MOPCTH010
Honda, Y. MOPCTH010, TUIBLH1020, TUIBLH1021, WEIDLH2066
Huang, S. WEIBLH2056
Huang, Y.L. **WEICLH2063**
Hug, F. TUICLH2032
Hulsart, R.L. WEIALH2046

— J —

Jackson, F. **WEIALH2047**
Jain, A.K. WEIDLH1002
Jamilkowski, J.P. MOPDTH014, WEIALH2048
Jankowiak, A. THPTHL072
Jensen, E. MOPBTH004, **TUPATH022**, **WEIALH1043**, THPDTH078
Jin, S. WEIBLH2055
Jin, X.J. TUIBLH1020, TUIBLH1021
Jing, Y.C. **WEIALH1042**
Jones, L.B. **THIALH2072**
Jürgensen, L.E. TUICLH2032

— K —

Kako, E. MOPCTH010, WEIBLH2054
Kamiya, Y. MOPCTH010
Kamps, T. TUPATH019, THPTHL072, THPCTH075
Kanaoka, K. **WEICLH2062**
Kankiya, P. K. MOPDTH014
Katagiri, H. WEIDLH2066
Kato, R. MOPCTH010
Kawata, H. MOPCTH010, **WEIALH1041**
Kayran, D. **MOPDTH014**, TUICLH1027, TUIDLH1036, WEIALH2048, WEICLH1058
Kewisch, J. **WEICLH1058**
Klein, M. MOPBTH004, WEIALH1043
Kneisel, P. TUIDLH1037
Knobloch, J. **MOPBTH006**
Kobayashi, M. TUIBLH1021
Kobayashi, Y. MOPCTH010
Kondo, Y. WEIBLH2054
Konomi, T. MOPCTH010
Konoplev, I.V. **WEICLH1057**
Kostroun, V.O. WEICLH1059
Kubo, T. MOPCTH010
Kühn, J. TUICLH1030, THPTHL072
Kürzeder, T. **TUICLH2032**
Kuriki, M. TUIBLH1021, TUIBLH1020
Kurisu, H. TUIBLH1021

— L —

Laloudakis, N. MOPDTH014
Lambiase, R.F. MOPDTH014, TUIBLH1023
Latina, A. TUIBLH2026
Ledroit, B. THIALH2069
Li, R. TUICLH2034
Li, Y. THIALH2070
Liepe, M. WEIBLH2053
Lin, L. WEIBLH2056, WEIDLH2068
Litvinenko, V. MOPDTH014, **TUPATH023**, TUIBLH2024, TUIBLH2025, TUIDLH2041, **WEIALH1044**, **THPDTH079**
Liu, C. TUIBLH2024, **TUIBLH2025**
Liu, K.X. WEIBLH2056, WEIDLH2068
Liu, X. THIALH2070
Liu, Z.C. **WEIBLH2055**
Lu, P.N. TUIDLH1038

— M —

Mahler, G.J. MOPDTH014, WEIDLH1002
Masi, L. MOPDTH014
Matejcek, C. THIALH2069
Matsuda, R. WEICLH2062
Matsumoto, T. WEIDLH2066
Matveenko, A.N. MOPBTH003
Maxson, J.M. MOPCTH008, **TUICLH1024**
Mayes, C.E. MOPBTH005, **WEIDLH1001**
McIntyre, G.T. MOPDTH014, TUICLH1027
Meng, W. MOPBTH005, TUIBLH1023
Méot, F. MOPBTH005, **TUIBLH1019**, TUIBLH2024, **TUIBLH2027**, WEIDLH1002
Mi, Z.H. WEIBLH2055
Michel, P. TUIDLH1038
Michizono, S. MOPCTH010, WEIBLH2054, WEIDLH2066
Michnoff, R.J. WEIALH2046
Militsyn, B.L. THIALH2072
Miller, R.C. TUIBLH1023
Miller, T.A. MOPDTH014, **WEIALH2048**
Minty, M.G. MOPBTH005, TUIBLH2024, TUIBLH2025, WEIALH2048
Miura, T. WEIBLH2054, WEIDLH2066
Miyajima, T. MOPCTH010, TUIBLH1020, TUIBLH1021
Montag, C. WEICLH1058
Moore, T.P. **THIALH2070**

Morris, J. MOPDTH014, WEIALH2048
Muller, E.M. TUICLH1030
Murcek, P. TUIDLH1037, TUIDLH1038

— N —

Nagai, R. TUIBLH1020, TUIBLH1021, THPTHL073
Nakai, H. MOPCTH010
Nakamura, N. **MOPCTH010**, TUICLH2033
Nishimori, N. MOPCTH010, TUIBLH1021, **THPTHL073**, **TUIBLH1020**
Noakes, T.C.Q. THIALH2072

— O —

O'Connell, T.I. WEIBLH2053
Obina, T. MOPCTH010, **TUPATH021**, TUIBLH1020, **WEIALH2045**, WEIDLH2066, THPCTH077
Oide, K. MOPCTH010
Okihira, K. WEICLH2062

— P —

Padmore, H.A. TUICLH1030
Patterson, J.R. MOPBTH005, WEICLH1060
Peggs, S. MOPBTH005
Pellegrini, D. MOPBTH004, TUIBLH2026
Perlstein, M. **WEICLH1060**
Petenev, Y. MOPBTH003
Pforr, J. TUICLH2032
Phillips, D. MOPDTH014
Pietralla, N. TUICLH2032
Pietz, J.R. TUIBLH1023
Pinayev, I. **WEIALH2046**, **WEIBLH1051**
Pischalnikov, Y.M. WEIDLH2067
Ptitsyn, V. **MOPATH001**, MOPBTH005, MOPDTH014, TUPATH020, TUIBLH2024, TUIBLH2025, TUIBLH2027, TUIDLH2041, WEIDLH1002, THPCTH076

— Q —

Qiu, F. WEIBLH2054, **WEIDLH2066**
Quan, S.W. **WEIBLH2056**, WEIDLH2068
Quigley, P. WEIBLH2053

— R —

Rahman, O.H. TUIBLH1023
Ranjbar, V.H. WEICLH1058
Rao, T. MOPDTH014, TUIBLH1023
Rimmer, R.A. WEICLH2063
Roser, T. MOPBTH005, TUIBLH2024

— S —

Sabol, D.M. WEIBLH2053
Sagan, D. MOPBTH005
Sakai, H. MOPCTH010, **WEIBLH2054**, **THPDTH078**
Sakai, H. TUPATH022, WEIDLH2066
Sakanaka, S. **MOPCTH007**, MOPCTH010
Sato, M. WEIBLH2054
Savino, J.J. THIALH2070
Sawamura, M. WEIBLH2054, THPTHL073
Schappert, W. WEIDLH2067
Scheibler, H.E. THIALH2072
Schirm, K.M. WEIALH1043
Schmeißer, M. **THPTHL072**
Schubert, S.G. TUICLH1030
Schulte, D. TUIBLH2026
Sears, J. WEIBLH2053
Seda, T. MOPDTH014
Sennyu, K. WEICLH2062
Seryi, A. WEICLH1057
Severance, M. WEIDLH1002
Sheehy, B. MOPDTH014, TUIBLH1023, TUICLH1027, WEIALH2048
Shimada, M. MOPCTH010, TUICLH2033
Shinoe, K. WEIBLH2054
Shishido, T. WEIBLH2054
Sinsheimer, J. TUICLH1030
Skaritka, J. TUIBLH1023
Smart, L. MOPDTH014
Smedley, J. TUICLH1030
Smith, E.N. WEIBLH2053
Smith, K.S. MOPDTH014
Smolenski, K.W. THIALH2070
Srinivasan-Rao, T. MOPDTH014
Steszyn, A.N. MOPDTH014

— T —

Takai, R. WEIALH2045
Teichert, J. TUIDLH1037, **TUIDLH1038**
Tennant, C. TUICLH2034
Terekhov, A.S. THIALH2072
Than, R. MOPDTH014, TUICLH1027
Thieberger, P. MOPBTH005, TUIBLH2024
Thompson, K.A. TUIBLH1023
Tigner, M. **MOPATH002**
Torres-Sanchez, R. WEIALH1043
Trbojevic, D. MOPBTH005, TUIBLH2024, TUIBLH2025, TUIBLH2027, WEIDLH1002
Tsai, C.-Y. **TUICLH2034**
Tsoupas, N. MOPBTH005, TUIBLH2024, TUIBLH2027, **WEIDLH1002**
Tsuchiya, K. MOPCTH010
Turlington, L. TUIDLH1037

— U —

Uchiyama, T. TUIBLH1020, TUIBLH1021
Umemori, K. MOPCTH010, WEIBLH2054

— V —

Valloni, A. **MOPBTH004**, WEIALH1043
Vennekate, H. TUIDLH1037, TUIDLH1038
Veshcherevich, V. WEIBLH2053

— W —

Walsh, J. TUICLH1030
Wang, E. MOPDTH014, **TUIBLH1023**, TUICLH1027
Wang, F. WEIBLH2055, WEIBLH2056, **WEIDLH2068**
Wang, G.W. WEIBLH2055
Wang, H. WEICLH2063
Wang, Q.Y. WEIBLH2055
Wang, S. WEICLH2063
Wang, Zh.W. WEIBLH2056
Watanabe, K. WEIBLH2054
Weiss, D. MOPDTH014, TUICLH1027
Wen, X.D. WEIBLH2056
Wibowo, S.B. WEIDLH2066
Williams, P.H. **MOPCTH009**
Wong, J.J. TUICLH1030

— X —

Xiang, R. TUIDLH1037, TUIDLH1038
Xie, H. MOPDTH014
Xie, H.M. **TUICLH1027**, WEIBLH2056
Xie, J. TUICLH1030
Xu, W. MOPDTH014, TUICLH1027, **TUIDLH1036**, **WEICLH2061**

— Y —

Yakimenko, V. **WEIBLH1052**
Yamamoto, M. MOPCTH010, TUIBLH1020, **TUIBLH1021**
Yamamoto, Y. WEIBLH2054
Yanagisawa, T. WEICLH2062
Yeckel, C. TUIBLH1023

— Z —

Zaltsman, A. MOPDTH014
Zhai, J.Y. WEIBLH2055
Zhang, B.C. WEIDLH2068
Zhao, K. WEIBLH2056
Zhao, T.X. WEIBLH2055
Zheng, H.J. WEIBLH2055
Zhu, F. WEIBLH2056
Zimmermann, F. MOPBTH004

Institutes List

ANL
Argonne, Illinois, USA

- Xie, J.

BNL
Upton, Long Island, New York, USA

- Altinbas, Z.
- Attenkofer, K.
- Beavis, D.R.
- Belomestnykh, S.A.
- Ben-Zvi, I.
- Berg, J.S.
- Blaskiewicz, M.
- Brooks, S.J.
- Brown, K.A.
- Calaga, R.
- Deonarine, S.
- Fedotov, A.V.
- Fischer, W.
- Gaowei, M.
- Gassner, D.M.
- Gupta, R.C.
- Hahn, H.
- Hammons, L.R.
- Hao, Y.
- Ho, C.
- Hulsart, R.L.
- Jain, A.K.
- Jamilkowski, J.P.
- Jing, Y.C.
- Kankiya, P. K.
- Kayran, D.
- Kewisch, J.
- Laloudakis, N.
- Lambiase, R.F.
- Litvinenko, V.
- Liu, C.
- Mahler, G.J.
- Masi, L.
- McIntyre, G.T.
- Meng, W.
- Méot, F.
- Michnoff, R.J.
- Miller, T.A.
- Minty, M.G.
- Montag, C.
- Morris, J.
- Peggs, S.
- Phillips, D.
- Pinayev, I.
- Ptitsyn, V.
- Ranjbar, V.H.
- Rao, T.
- Roser, T.
- Seda, T.
- Sheehy, B.
- Sinsheimer, J.
- Skaritka, J.
- Smart, L.
- Smedley, J.
- Smith, K.S.
- Srinivasan-Rao, T.
- Steszyn, A.N.
- Than, R.
- Thieberger, P.
- Trbojevic, D.
- Tsoupas, N.
- Walsh, J.
- Wang, E.
- Weiss, D.
- Xie, H.
- Xu, W.
- Zaltsman, A.

CERN
Geneva, Switzerland

- Brüning, O.S.
- Jensen, E.
- Klein, M.
- Latina, A.
- Pellegrini, D.
- Schirm, K.M.
- Schulte, D.
- Torres-Sanchez, R.
- Valloni, A.
- Zimmermann, F.

Cockcroft Institute, Lancaster University
Lancaster, United Kingdom

- Burt, G.

Cornell University (CLASSE), Cornell Laboratory for Accelerator-Based Sciences and Education
Ithaca, New York, USA

- Agladze, N.I.
- Bartnik, A.C.
- Bazarov, I.V.
- Brock, J.D.
- Bullock, B.
- Clasby, B.
- Conway, J.V.
- Cultrera, L.
- Dobbins, J.
- Dunham, B.M.
- Eichhorn, R.G.
- Elmore, B.
- Full, S.J.
- Furuta, F.
- Gulliford, C.M.
- He, Y.
- Hoffstaetter, G.H.
- Kostroun, V.O.
- Li, Y.
- Liepe, M.
- Liu, X.

ISBN 978-3-95450-183-0

- Maxson, J.M.
- Mayes, C.E.
- Moore, T.P.
- O'Connell, T.I.
- Patterson, J.R.
- Quigley, P.
- Sabol, D.M.
- Sagan, D.
- Savino, J.J.
- Sears, J.
- Smith, E.N.
- Smolenski, K.W.
- Tigner, M.
- Veshcherevich, V.

Cornell University
Ithaca, New York, USA
- Furuta, F.
- Perlstein, M.

CSU
Fort Collins, Colorado, USA
- Hall, C.C.

Elettra-Sincrotrone Trieste S.C.p.A.
Basovizza, Italy
- Di Mitri, S.

Enrico Fermi Institute, University of Chicago
Chicago, Illinois, USA
- Frisch, H.J.

EPFL
Lausanne, Switzerland
- Pellegrini, D.

Far-Tech, Inc.
San Diego, California, USA
- Chang, X.

Fermilab
Batavia, Illinois, USA
- Holzbauer, J.P.
- Pischalnikov, Y.M.
- Schappert, W.

Hiroshima University, Graduate School of Science
Higashi-Hiroshima, Japan
- Kuriki, M.

HU/AdSM
Higashi-Hiroshima, Japan
- Kuriki, M.

HZB
Berlin, Germany
- Abo-Bakr, M.
- Atkinson, T.
- Bondarenko, A.V.
- Jankowiak, A.
- Kamps, T.
- Knobloch, J.
- Kühn, J.
- Matveenko, A.N.
- Petenev, Y.
- Schmeißer, M.

HZDR
Dresden, Germany
- Arnold, A.
- Freitag, M.
- Lu, P.N.
- Michel, P.
- Murcek, P.
- Teichert, J.
- Vennekate, H.
- Xiang, R.

IHEP
Beijing, People's Republic of China
- Dai, J.
- Gao, J.
- He, F.S.
- Jin, S.
- Liu, Z.C.
- Mi, Z.H.
- Wang, G.W.
- Wang, Q.Y.
- Zhai, J.Y.
- Zhao, T.X.
- Zheng, H.J.

IKP
Mainz, Germany
- Alexander, I.
- Aulenbacher, K.
- Bechthold, V.
- Heine, R.G.
- Ledroit, B.
- Matejcek, C.

IMP/CAS
Lanzhou, People's Republic of China
- Huang, Y.L.

ISP
Novosibirsk, Russia
- Bakin, V.V.
- Scheibler, H.E.
- Terekhov, A.S.

JAEA/FEL
Ibaraki-ken, Japan
- Nishimori, N.

JAEA
Ibaraki-ken, Japan
- Hajima, R.
- Nagai, R.
- Nishimori, N.
- Sawamura, M.

JAI
Egham, Surrey, United Kingdom
- Ainsworth, R.
- Konoplev, I.V.
- Seryi, A.

JLab
Newport News, Virgina, USA
- Bogacz, S.A.
- Ciovati, G.
- Douglas, D.
- Guo, J.
- Kneisel, P.
- Li, R.
- Rimmer, R.A.
- Tennant, C.
- Turlington, L.
- Wang, H.
- Wang, S.

KEK
Ibaraki, Japan
- Arakawa, D.A.
- Chen, S.
- Enami, K.
- Furuya, T.
- Haga, K.
- Hanyu, I.
- Harada, K.
- Honda, T.
- Honda, Y.
- Jin, X.J.
- Kako, E.
- Kamiya, Y.
- Katagiri, H.
- Kato, R.
- Kawata, H.
- Kobayashi, M.
- Kobayashi, Y.
- Kondo, Y.
- Konomi, T.
- Kubo, T.
- Matsumoto, T.
- Michizono, S.
- Miura, T.
- Miyajima, T.
- Nakai, H.
- Nakamura, N.
- Obina, T.
- Oide, K.
- Qiu, F.
- Sakai, H.
- Sakanaka, S.
- Sato, M.
- Shimada, M.
- Shinoe, K.
- Shishido, T.
- Takai, R.
- Tsuchiya, K.
- Uchiyama, T.
- Umemori, K.
- Watanabe, K.
- Yamamoto, M.
- Yamamoto, Y.

LBNL
Berkeley, California, USA
- Padmore, H.A.
- Schubert, S.G.
- Wong, J.J.

MHI
Hiroshima, Japan
- Hara, H.
- Kanaoka, K.
- Okihira, K.
- Sennyu, K.
- Yanagisawa, T.

Mitsubishi Heavy Industries Ltd. (MHI)
Takasago, Japan
- Matsuda, R.

PKU
Beijing, People’s Republic of China
- Chen, J.E.
- Fan, P.L.
- Feng, L.W.
- Hao, J.K.
- Huang, S.
- Lin, L.
- Liu, K.X.
- Quan, S.W.
- Wang, F.
- Wang, Zh.W.
- Wen, X.D.
- Xie, H.M.
- Zhang, B.C.
- Zhao, K.
- Zhu, F.

Radiation Monitoring Devices
Watertown, USA
- Bhandari, H.

SBU
Stony Brook, New York, USA
- Ding, Z.
- Muller, E.M.

SLAC
Menlo Park, California, USA
- Yakimenko, V.

Sokendai
Ibaraki, Japan
- Cenni, E.
- Wibowo, S.B.

Stangenes Industries
Palo Alto, California, USA
- Dobrin, E.
- Miller, R.C.
- Thompson, K.A.
- Yeckel, C.

STFC/DL/ASTeC
Daresbury, Warrington, Cheshire, United Kingdom
- Jackson, F.
- Jones, L.B.
- Militsyn, B.L.
- Noakes, T.C.Q.
- Williams, P.H.

Stony Brook University
Stony Brook, USA
- Belomestnykh, S.A.
- Ben-Zvi, I.
- Hammons, L.R.
- Kayran, D.
- Litvinenko, V.
- Ptitsyn, V.
- Rahman, O.H.
- Severance, M.

Transfer Engineering and Manufacturing, Inc
Fremont, California, USA
- Ackeret, M.A.
- Pietz, J.R.

TU Darmstadt
Darmstadt, Germany
- Arnold, M.
- Gros, M.
- Hug, F.
- Jürgensen, L.E.
- Kürzeder, T.
- Pforr, J.
- Pietralla, N.

Virginia Polytechnic Institute and State University
Blacksburg, Virginia, USA
- Tsai, C.-Y.

Yamaguchi University
Ube-Shi, Japan
- Kurisu, H.